Microwave and Superconducting Techniques for Measurements on Unconventional Josephson Junctions

Georgina Marie Klemencic

Thesis submitted for the degree of
Doctor of Philosophy

Condensed Matter Group,
School of Physics and Astronomy,
University of Birmingham.

June 4, 2013

Acknowledgments

Many people have helped me to complete this work.

First, massive thanks to members of the Condensed Matter group at the University of Birmingham past and present. Extra special thanks to Mark for putting up with me for so long, and Chris for dealing with quite a large number of stupid questions with the patience of a saint. Special mentions go to Gary, who can make anything from anything else, and Michael for the constant and quick supply of the 'cold stuff'.

I would like to thank all of the friends and acquaintances who made being in Birmingham so much fun. Life would have been much less fun without regular trips to Staff House and quiz nights at the Selly Park Tavern. Housemates of the Cottage/Mansion of Rock provided an interesting and lively home that made a welcome break from the lab. Special thanks also go to Angela and Brette (and all of those in Nuneaton) for dealing with The Write Up, feeding me on a regular basis and providing a sympathetic ear when it was most needed.

Most of all, I could not have done this without my family egging me on, being on the other end of the phone or racing up the M40 whenever I've needed them. Thank you, I hope it wasn't too traumatic. Finally, I really could not have done this without the love and support of my partner in crime, Jonathan Fellows. Thank you.

Abstract

The first part of the thesis describes the instrumentation, testing and analysis of a planar circuit designed for the measurement of the current-phase relationship of niobium-cobalt-insulator-niobium Josephson junctions. A detailed analysis method and fitting routine was developed but the results show that an irreducible mutual inductance places a limit on the accuracy of the chip for the intended measurement.

The second part describes a study of the magnetic and microwave properties of a range of thin film niobium coplanar resonators with cobalt and normal metal layers. Magnetic measurements show a magnetic dead layer of 1.3 nm. The observed microwave losses are found to be two orders of magnitude higher than for high quality niobium films. Computer simulation shows that this is mainly due to conductive, rather than magnetic losses, and is in good agreement with the observed proportionality to cobalt thickness. Measurements of the temperature and magnetic field dependence of the losses and resonant frequency as a function of the cobalt thickness show no signs of the oscillatory thickness dependence reported in a number of other experiments. The temperature dependence of all films is found to be in good agreement with Mattis-Bardeen theory.

Contents

List of Tables

List of Figures

CHAPTER 1

INTRODUCTION

Devices made of superconductors exploit the quantum mechanics that underpin their operation, for example the Josephson junction. The Josephson junction is made from two superconducting electrodes that are spatially separated by a barrier to allow weak coupling between them. The current through the device is functionally dependent on the phase difference across it – called the Current-Phase Relationship (CPR). One practical application of Josephson junctions of interest is their inclusion in superconducting Quantum Bits – qubits – the building block of quantum computers [1–3]. Many properties of Josephson junctions are often investigated experimentally but measurement of the CPR is less widely attempted due to the difficulty of sample preparation and the sensitivity required to make the measurement. As a result, much of the literature in the field is theoretical. Despite the technical challenge, it is a worthwhile measurement to make; firstly to test theoretical predictions, and secondly to aid large scale modeling of complex Josephson junction systems.

The work presented in this thesis comprises two experimental projects conducted to explore potential methods of measuring the CPR of exotic Josephson junctions, specifically those containing a ferromagnetic barrier. The first project is based on a

method used by Waldram and Lumley in 1975 [4]. This method measures the CPR under static conditions and has since been implemented by other research groups to investigate a variety of junction types [5–7]. It will be shown that there is a serious flaw in the planar device design presented here that may potentially throw some doubt on other CPR measurements made using planar circuits in this way. A second CPR measurement device is proposed that operates at microwave frequencies and shares some similarities with a method first proposed by Rifkin and Deaver in 1976 [8]. The organisation of content is as follows:

- Chapter 2 begins with a brief introduction to concepts and terms used from the fields of superconductivity and ferromagnetism that are universal to all work presented in this thesis. The chapter ends with a discussion of the proximity effect for superconductor-ferromagnet interfaces.

- Chapter 3 presents a more detailed discussion of the physics of Josephson junctions. A method for CPR under static conditions is presented. The results of extensive circuit characterisation are described and it will be shown that there are serious problems associated with the particular chip design used.

- Following the issues raised in chapter 3, a method in the microwave regime using coplanar resonators is proposed at the end of chapter 4. To facilitate the proposal, a discussion of the high frequency electrodynamics of superconductors is provided.

- Chapter 5 describes the preparation and material characterisation of coplanar resonator samples fabricated from superconductor-ferromagnet thin film multilayers intended to assess the suitability of the proposed materials – niobium and cobalt – to the device described at the end of chapter 4.

- The experimental and data anaylsis techniques used to perform microwave measurements on the coplanar resonator samples are outlined in chapter 6. A method of extracting the resonant frequency and quality factor from asymmet-

ric lineshapes is presented along with a method of comparing the experimental results with Mattis-Bardeen theory.

- Chapter 7 contains the experimental results and discussion of the implications relating to the proposed device. A study of the microwave losses of the structure as a function of the ferromagnetic layer thickness is presented together with computational simulation of the thin film system. The temperature and field dependence of the resonant frequency is presented and the observed behaviour is discussed for both magnetically unsaturated and saturated samples. Finally, preliminary results for microwave devices made from superconductor-ferromagnet-superconductor films are presented and discussed.

- To finish, chapter 8 will draw together the results of both projects and conclude the thesis.

CHAPTER 2

SUPERCONDUCTIVITY, FERROMAGNETISM AND THEIR INTERACTION

The first section of this chapter will introduce some of the key ideas from the field of superconductivity that are essential for understanding the experimental results presented in chapters 3 and 7. More detailed material will be highlighted in later chapters as necessary. For a more in depth discussion of the theoretical background, there are many textbooks that provide a thorough treatment of the field; good examples are *Superconductive Devices and Circuits* by T. Van Duzer and C. W. Turner [9] and *Introduction to Superconductivity* by M. Tinkham [10].

The results presented in chapter 7 show only very weak dependences on the magnetism of the samples. The second section will therefore give a very brief introduction to the terms and concepts that will be used from the very wide field of magnetism. Finally, the last section will discuss behaviour that can be observed as a consequence of interactions between superconducting and ferromagnetic materials.

2.1 Superconductivity

Observations of the Superconducting State

As a normal metal is cooled, a general decrease in the resistivity is observed that is associated with a reduction in lattice vibrations. For the majority of simple metals, the resistivity eventually levels out at a finite value determined by the purity of the material. For a superconducting material, however, a drop in the electrical resistance to a dc current to an immeasurably small value is observed with a sudden onset below a critical temperature, T_C.

It was over twenty years after the discovery of the transition to a zero-resistivity state was made [11] that a second phenomenon associated with superconductors was discovered. Meissner and Ochsenfeld [12] observed that a superconductor below T_C actively expels small magnetic fields from the material interior, i.e. the superconductor behaves as a perfect diamagnet where the behaviour is supported up until a critical field strength, H_C. A magnetic field is expelled from the bulk by the creation of persistent currents that flow within a small distance of the material surface. In this way, the field is restricted to a small depth, λ_L – the London penetration depth. This behaviour is termed the Meissner effect and cannot be explained by perfect metallic conductivity alone.

The London Equations

The first theoretical treatment of perfect conductivity and the Meissner effect in superconductors was the phenomenological theory proposed by Fritz and Heinz London in 1935 [13]. Starting from the Drude model and assuming an infinite time between collisions, one can relate the current density, $\mathbf{j}$, to the electric, $\mathbf{E}$, and magnetic, $\mathbf{B}$, fields as

$$\frac{d\mathbf{j}}{dt} = \frac{n_s e^2}{m}\mathbf{E} \tag{2.1}$$

and

$$\nabla \times \mathbf{j} = -\frac{n_s e^2}{m}\mathbf{B} \tag{2.2}$$

where n_s is the number density of the superconducting charge carriers, and e and m are the electron charge and mass respectively. These are the first and second London equations respectively; the first London equation describes perfect conductivity and the second London equation describes the Meissner effect.

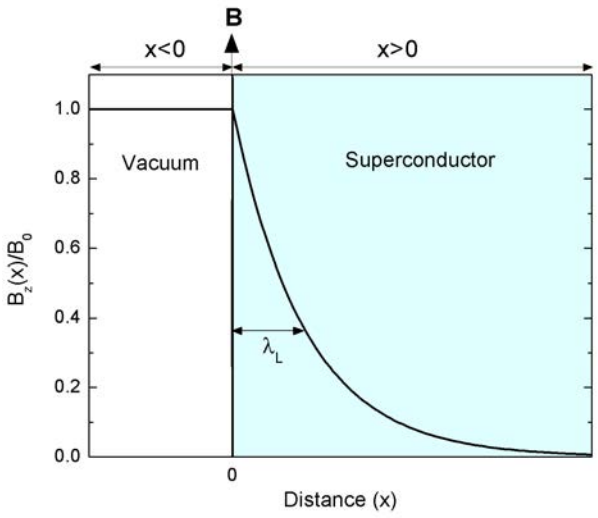

Figure 2.1: Magnetic field $\mathbf{B}$ applied parallel to the boundary ($x = 0$) between a superconductor and a vacuum. The field is restricted to a distance λ_L within the superconductor. Adapted from Ref. [14].

It has already been noted that flux expulsion from the bulk arises from persistent screening currents on the surface; the London equations allow calculation of the extent of flux penetration into the superconductor. Consider a superconductor in an external field $\mathbf{B} = B_0\hat{\mathbf{z}}$ that is applied parallel to the boundary between the superconductor and a vacuum, as shown in Fig. 2.1. Solving equation (2.2) for the field inside the superconductor gives

$$B_z(x) = B_0 e^{-x/\lambda_L} \tag{2.3}$$

where

$$\lambda_L(0) = \left(\frac{m}{\mu_0 n e^2}\right)^{1/2} \tag{2.4}$$

is the London penetration depth at zero temperature. By putting equation (2.3) into the Maxwell equation $\nabla \times \mathbf{B} = \mu_0 \mathbf{j}$, the spatial variation of the screening current density is given by

$$j_y(x) = j_0 e^{-x/\lambda_L}. \tag{2.5}$$

The temperature dependence of the London penetration depth is given by

$$\lambda_L(T) = \frac{\lambda_L(0)}{\sqrt{1-(T/T_C)^4}} \tag{2.6}$$

which follows from the temperature dependence of the number density of superconducting charge carriers according to the two-fluid model proposed by Gorter and Casimir [15] and will be discussed further in chapter 4.

Cooper Pairs

The microscopic origin of superconductivity was first proposed by Bardeen, Cooper and Schrieffer in 1957 [16], now called BCS theory. This theory describes how electrons in a superconductor couple together and condense into the same low energy state by the formation of so-called Cooper pairs.

The mechanism by which Cooper pairs are formed was first suggested by Fröhlich

in 1950 [17], which predated BCS theory. The hypothesis was that electrons could couple together via an electron-phonon interaction with the material crystal lattice. A simple picture is to consider two electrons moving through an ionic lattice. The first electron to move through the lattice will cause a slight distortion in the ion spacing which leads to an excess of positive charge in this region even after the electron has moved on. This charge will then attract the second electron in such a way that the motion of the two electrons is correlated over a distance, ξ_0. This is the BCS coherence length and can be thought of as the average 'size' of a Cooper pair. A Cooper pair (with s-wave pairing) is comprised of two electrons with equal and opposite spin and momenta.

Since Cooper pairs have zero spin they are bosons and as such they obey Bose rather than Fermi statistics. It is this property that allows Cooper pairs to condense into the same quantum state. Typical coherence lengths are $10^2 - 10^3$ nm such that there is a strong overlap of many pairs. To this end, the entire system can be represented by a single coherent wavefunction, known as the superconducting order parameter:

$$\Psi(\mathbf{r}) = \Psi_0(r)e^{i\theta(\mathbf{r})} \tag{2.7}$$

where θ is the phase of the macroscopic wavefunction and $|\Psi_0(\mathbf{r})|^2 = n_s$, the Cooper pair density.

The Cooper pair condensate is protected from excitations from the ground state (called quasiparticles) by an energy gap, 2Δ; i.e. for an input energy less than 2Δ, Cooper pairs are not broken into their constituent parts. The energy gap has a temperature dependence as shown in Fig. 2.2 such that $2\Delta(T = 0)$ is at a maximum and $2\Delta(T = T_C) = 0$. This will be returned to in section 6.2.3.

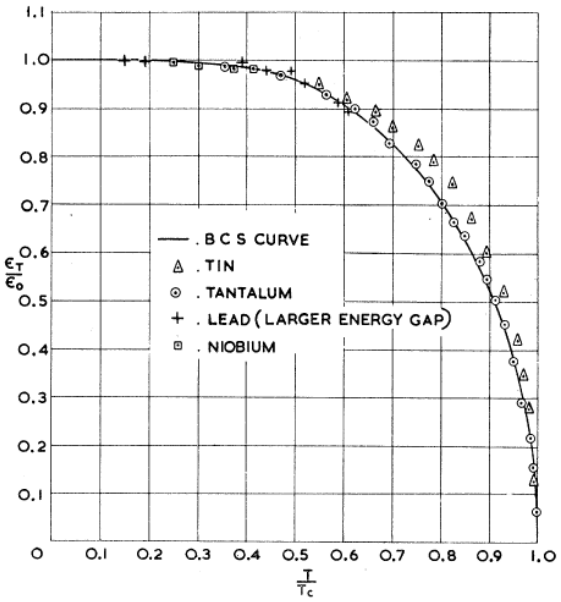

Figure 2.2: Temperature dependence of the energy gap for a variety of materials as measured by Townsend and Sutton [18].

Flux Quantisation

The existence of a single quantum mechanical wavefunction given by equation (2.7) has an important consequence that is exploited by the device concepts presented in this thesis: the total magnetic flux that threads a complete superconducting ring that is thick compared with the penetration depth is quantised in integer multiples of the flux quantum, Φ_0.

To see how this works one can first consider the current density in a ring of superconductor at $T < T_C$. The current density, $\mathbf{j}(\mathbf{r})$, associated with the macroscopic wavefunction is defined as

$$\begin{aligned}\mathbf{j}(\mathbf{r}) &= \frac{i\hbar e}{2m}(\Psi^*\nabla\Psi - \Psi\nabla\Psi^*) - \frac{2e^2}{m}\Psi^*\Psi\mathbf{A} \\ &= -\frac{e}{m}|\Psi(\mathbf{r})|^2(\hbar\nabla\theta + 2e\mathbf{A}) \end{aligned} \tag{2.8}$$

where e is the electron charge, m is the electron mass, and $\mathbf{A}$ is the vector potential. Away from the surface of the ring, $\mathbf{j}(\mathbf{r}) = 0$ since $T < T_C$. Therefore,

$$\hbar \nabla \theta = -2e\mathbf{A}. \tag{2.9}$$

Integrating this expression around a closed curve through the superconductor bulk gives

$$\hbar \oint_C \nabla\theta \cdot d\mathbf{l} = \hbar\Delta\theta = -2e \oint_C \mathbf{A} \cdot d\mathbf{l} = -2e\Phi \tag{2.10}$$

where Φ is the magnetic flux through the the curve defined by C and $\Delta\theta$ is the phase change of the wavefunction around the curve, which must be equal to $2\pi n$ where n is an integer. From this it is seen that

$$\Phi = \frac{2\pi n\hbar}{2e} = n\Phi_0. \tag{2.11}$$

This shows that the flux threading a complete ring of superconducting material is quantised in integer units of the flux quantum, Φ_0. This is a well known result [19] and will be shown to be important for the devices described in chapter 3.

Flux Lines and Type II Superconductors

The discussion until now has focused on the complete Meissner state in which an applied magnetic field is completely excluded from the superconducting interior, called 'type I superconductivity'. There exists another type of superconductor that presents the complete Meissner state up to a lower critical field, H_{C1}. Beyond this field, quantised magnetic flux lines are allowed into the interior until a second critical field, H_{C2}, above which the superconductivity is completely destroyed. This is 'type

II superconductivity' in which the state where $H_{C1} < H < H_{C2}$ is called the mixed state.

To see why quantised flux lines occur in type II superconductors, first consider the argument of flux quantisation for a superconducting ring given above but this time the closed curve C encloses a region filled with superconducting material. Here, the total phase change around the loop is still quantised in integer units of 2π and therefore, if the phase change is non-zero, there will be some point enclosed by the loop which will have all values of phase around the loop simultaneously. This is inconsistent with a single-valued wavefunction *unless* $|\Psi| = 0$ at some point enclosed by the curve. This argument holds not just for a single plane in the material but all planes, which leads to filaments of flux that run through the whole of the superconductor. Circulating currents pass around the closed curve C to generate a magnetic field associated with flux lines quantised in units of Φ_0.

There are two length scales that determine the type of superconductivity – the London penetration depth, λ_L, and the Ginzburg-Landau coherence length, ξ_{GL}, which characterises the distance over which the superconducting wavefunction can change. It is the ratio of these length scales that defines the Ginzburg-Landau parameter, $\kappa = \lambda_L/\xi_{GL}$, which determines the particular superconductor's response to an increasing magnetic field. If $\kappa < 1/\sqrt{2}$, the superconductor shows the complete Meissner effect for all values of applied field up to H_C (type I); if $\kappa > 1/\sqrt{2}$, type II superconductivity is observed such that flux lines may enter the superconductor for applied magnetic fields $H_{C1} < H < H_{C2}$.

In practice, in the absence of a current flow through the material, flux lines that enter the superconducting bulk spread out to form a spatially ordered flux line lattice due to a mutual repulsion between the lines. If a transport current is now passed through a superconductor in the mixed state, the flux lines will move perpendicular to the direction of the current under the influence of a Lorentz force causing a potential gradient along the sample. The movement of flux lines is a dissipative process – this effect will be seen to be important in chapter 7.

The Superconducting Properties of Niobium

The superconducting material used for the work presented in this thesis was niobium; table 2.1 gives some of the superconducting properties of this material.

Table 2.1: Superconducting properties of niobium [20].

Property	Value
T_C	9.2 K
ξ_0	38 nm
λ_L	39 nm
$2\Delta(0)/k_BT_C$	3.8

2.2 Ferromagnetism

As stated in the introduction to this chapter, this section will give only a very brief overview of the wide field of magnetism and is only intended to introduce the terms and concepts that will be used later in the thesis. An in depth treatment of the field can be found in *Magnetism in Condensed Matter* by S. Blundell [21] or *Electricity and Magnetism* by B. I. Bleaney and B. Bleaney [22], for example.

Spontaneous Magnetism

At sufficiently low temperatures, many materials exhibit a spontaneous magnetisation in the absence of an applied magnetic field. This spontaneous magnetisation arises due to the preferential alignment of the permanent dipole moments within the material, where the alignment type determines the nature of the magnetism. The fact that these dipoles align into an ordered configuration indicates that they are aware of the orientation of neighbouring moments and that they interact. It can be shown that the strength of magnetic interactions between the dipoles alone is too weak to account for magnetic ordering above $\sim$0.03 K. This indicates that there is another mechanism that causes long-range order that exceeds the strength

of magnetic interactions alone. This interaction is called the quantum mechanical 'exchange interaction' and the combined result of the individual interactions gives rise to an overall effective 'exchange field'.

Types of magnetic ordering include antiferromagnetism, where identical dipoles located on different sublattices anti-align to produce a zero net magnetisation, and ferrimagnetism, where the dipoles of anti-aligned sublattices have different moments to produce a finite net magnetisation. The form of magnetism relevant to the work presented in this thesis is *ferromagnetism*, in which the moments are aligned parallel to their neighbours to create a finite spontaneous magnetisation. The effect of increasing temperature on a ferromagnet is to disrupt the spontaneous ordering and cause the dipole moments to become randomly orientated. The temperature at which this happens is called the Curie temperature, T_{Curie}, where the magnitude of T_{Curie} is proportional to the strength of the exchange interaction.

The Exchange Interaction

The magnetic properties of a material are directly related to the quantum mechanical spin and the Pauli exclusion principle. The quantum mechanical origin of the exchange interaction is a result of the fact that, although the Coulomb interaction has no explicit dependence on the electron spin, there is an implicit dependence due to the antisymmetry of the electron wavefunction. The quantum mechanical description of two neighbouring electrons that interact via a Coulomb potential gives the interaction energy of the singlet state, E_S, as

$$\Delta E_S = E_C + E_{\text{ex}} \tag{2.12}$$

where E_C is the energy due to density-density interactions and E_{ex} is the exchange energy. The interaction energy of the triplet state, E_T, is given by

$$\Delta E_T = E_C - E_{\text{ex}} \tag{2.13}$$

as shown in Ref. [14]. Therefore, the energy difference between a parallel and an antiparallel alignment of neighbouring spins is

$$\Delta E_T - \Delta E_S = -2E_{\text{ex}}. \tag{2.14}$$

Macroscopically, it is the difference in energy for the two pairing arrangements that is relevant as it is the determining factor for the preferred orientation of neighbouring moments. The exchange interaction between two moments can be written as

$$-2E_{\text{ex}}\mathbf{s}_1 \cdot \mathbf{s}_2 \tag{2.15}$$

where $\mathbf{s}_i$ is the direction of the i^{th} moment such that the energy for parallel moments is $2E_{\text{ex}}$ less than for anti-parallel moments. It is the overlap of electron wavefunctions in a material that is responsible for the exhibited magnetic properties; the distance between nearest neighbours has important consequences in terms of magnetic behaviour. The Hamiltonian for this model, called the Heisenberg model, can be written as

$$H = -\sum_{i,j\neq i} E_{\text{ex}}(ij)\mathbf{s}_i \cdot \mathbf{s}_j. \tag{2.16}$$

The direct exchange described here is the simplest process that can cause spontaneous magnetic ordering. In reality, there are often indirect exchange processes that may change the sign of E_{ex} and lead to other forms of magnetic ordering.

The Exchange Field

Within a ferromagnet, the dipole moments align spontaneously as if the material were a paramagnet under the influence of an externally applied magnetic field. The overall effect can be thought of as exactly this; the exchange interaction produces an effective internal field, $\mathbf{B}_{\text{ex}}$. This can be called the exchange field, also referred to as the Weiss molecular field. The exchange field is proportional to the magnetisation, $\mathbf{M}$:

$$\mathbf{B}_{\text{ex}} = \mu_0 \lambda \mathbf{M}, \tag{2.17}$$

where λ is a dimensionless constant that is directly proportional to the exchange energy. Thus a ferromagnet with a larger exchange energy brought about by a greater overlap of the nearest-neighbour wavefunctions will have a proportionally larger exchange field. The consequence of this with regards to a superconductor-ferromagnet interface will be seen in section 2.3.

Ferromagnetic Domains

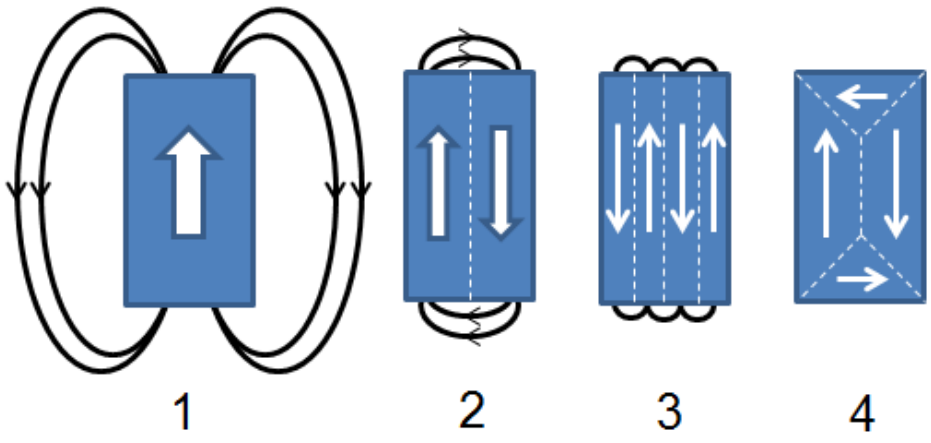

Figure 2.3: Diagram to show the reduction of magnetic field energy by the formation of magnetic domains within a ferromagnetic sample. The white arrows show the direction of magnetisation for each domain.

If all of the individual moments in a ferromagnetic sample are aligned in the same direction, illustrated by *(1)* in Fig. 2.3, the sample will have a total *saturation* magnetisation, M_S. In reality, in the absence of an externally applied magnetic field, ferromagnetic materials often exhibit a total magnetisation that is much less than M_S. This is due to the tendency of the material to form many small domains which individually display saturated ferromagnetic ordering but collectively point in different directions. This reduces the total magnetisation of the sample (shown by *(2-4)* in Fig. 2.3).

The formation of these domains arises from competition between the exchange energy and the magnetic energy that is stored in the field outside the sample. Fig. 2.3 *(1)* shows that if $M = M_S$, the sample has a correspondingly large magnetic energy which may exceed the energy saving acquired by aligning all moments in the sample. The competition is resolved by a large area with parallel aligned spins dividing into differently orientated domains, the shape and size of which are determined by minimising the energy required to form a domain wall. Despite a domain wall being costly from an energetic point of view due to the exchange interaction, there is an overall 'saving' when compared to the reduction in the magnetic energy. For the case shown in Fig. 2.3 *(4)*, the external field is almost eliminated by forming closure domains.

In zero applied field a ferromagnetic sample can show a small, or even zero, magnetisation. However, a large magnetisation can be produced through the application of a relatively small external magnetic field. Fig. 2.4 shows a cartoon graph of a ferromagnetic magnetisation curve which shows hysteresis in the sample response to an applied field. Initially, $M = 0$ at $H = 0$ since the sample contains many small domains that act to reduce the magnetic energy stored outside of the sample. As H is increased in a positive direction, irreversible changes to the sample magnetisation are caused by the shrinking of the domains that oppose the applied field by movement of the domain walls. This is because it is energetically favourable for the individual moments within the sample to align with the magnetic field, which

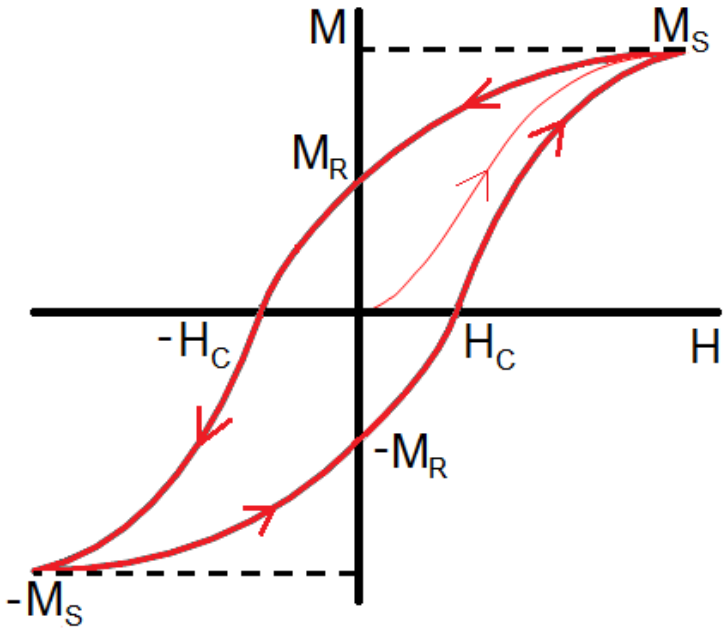

Figure 2.4: Ferromagnetic $M(H)$ curve. The saturation magnetisation, M_S, remanence, M_R, and the coercive field, H_C are indicated on the graph.

penalises the anti-aligned domains. The saturation magnetisation, M_S, is reached when the sample becomes a single domain where all of the dipole moments align with the applied field. If H is now reduced back to zero from this point, a finite magnetisation remains (the remanence, M_R) and if H is reduced further still, M will eventually return to zero at a point H_C, the coercive field. The hysteresis results from domain walls moving and becoming trapped on impurities or lattice defects. From $H = 0$, the field could then increased in the negative direction until $-M_S$ is achieved. By reversing the field direction and repeating the process, the characteristic hysteresis loop is traversed.

The Magnetic Properties of Cobalt

The ferromagnetic material used for in work presented in this thesis was cobalt; table 2.2 gives some of the magnetic properties of this material.

Table 2.2: Magnetic properties of cobalt [21].

Property	Value
T_{Curie}	1388 K
Spontaneous magnetisation	1.72 μ_B/atom

2.3 The Proximity Effect

The proximity effect will now be discussed for Superconductor-Normal metal (SN) and Superconductor-Ferromagnet (SF) interfaces. It will be seen in chapter 7 that the proximity effect for the case of an SN interface is observable in the measurement of microwave losses for multilayered systems but that the SF proximity effect was not observed. The discussion presented here will therefore be kept at a general level but a more detailed treatment of these effects can be found in Ref. [23].

2.3.1 Superconductor-Normal Metal Interface

For an SN bilayer, the respective charge carriers can diffuse across the interface in both directions. The superconductor wavefunction decays exponentially over a distance ξ_N (the coherence length in the normal metal), known as the proximity effect, and the superconducting properties are suppressed in the region near the interface over a distance ξ_0, known as the inverse proximity effect. An example of the observation of the proximity effect is shown in Fig. 2.5. The first observation of the proximity effect predates the discovery of the Josephson effects (to be discussed in chapter 3) but contributes to the phenomenon in SNS junctions.

2.3.2 Superconductor-Ferromagnet Interface

The previous sections show that superconductivity and ferromagnetism are states of matter that are generally considered to be antagonistic in nature. Superconductors display ideal diamagnetism and the state can be destroyed by the presence of

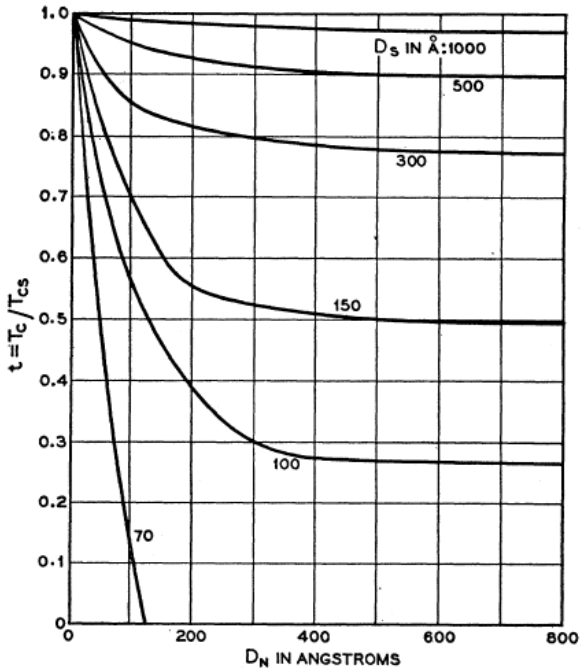

Figure 2.5: Data showing the weakening of superconductivity in a SN (lead-copper) film as a function of the normal metal layer thickness [24]. Here T_{CS} is the transition temperature of the superconductor alone, and D_S and D_N are the superconductor and normal metal layer thicknesses respectively.

a sufficiently large magnetic field or magnetic impurities within the material. Antiparallel spin Cooper pairs are incompatible with the parallel spin alignment within a ferromagnet. There is much evidence, however, which shows that superconductivity and ferromagnetism can coexist in the region surrounding an SF interface and furthermore that systems incorporating the two types of electronic ordering could be utilised in technologies such as Rapid Single Flux Quantum (RSFQ) and qubit technology [25].

An SF interface exhibits a similar proximity effect to that found at an SN interface but with an important difference that arises from the electronic properties of the ferromagnet. There is still an exponential decay of the magnitude of superconducting wavefunction in the ferromagnet, but it is accompanied by sign-reversing spatial oscillations of the phase. This is somewhat analogous to the Larkin-Ovchinnikov-Fulde-Ferrel (LOFF) state predicted for magnetic superconductors [26, 27].

An explanation of this behaviour given by Demler et al [28] considers a conventional superconductor where the composite electrons of the Cooper pairs have opposite spin and momentum. This superconductor is brought into close proximity with a ferromagnetic material with an exchange energy E_{ex}. As the Cooper pairs move into the ferromagnet as per the proximity effect, the spin up and spin down electrons experience an energy splitting of $2E_{\text{ex}}$ due to the different energies of the spin bands within the ferromagnet. To maintain energy conservation, changes in potential energy are compensated by an adjustment of the kinetic energy and therefore the momentum; positively for the spin direction parallel to the exchange field and negatively for the antiparallel spin.

The result is that the Cooper pair obtains a nonzero momentum $Q = 2E_{\text{ex}}/\nu_F$, where ν_F is the Fermi velocity. There are, however, two possible spin configurations in the singlet state, $\uparrow\downarrow$ and $\downarrow\uparrow$, and the sign of the centre of mass momentum change depends on whether it is the up- or down-spin which has positive momentum. The singlet state $(\uparrow\downarrow - \downarrow\uparrow)$ centre of mass wavefunction in the ferromagnet, accounting for the proximity effect at an SN interface, is given by

$$\Psi(x) = \Psi(0)\cos(Qx/\hbar)\exp(-x/\xi_N). \tag{2.18}$$

This simplified treatment assumes that Cooper pairs are traveling normal to SF interface, but the qualitative behaviour does not change for a more thorough treatment [28]. More generally, Ryazanov [6, 29–33] showed that the wavefunction in the ferromagnet can be written

$$\Psi(x) \propto \exp(-x/\xi_F) = \exp(-x/\xi_{F1} - ix/\xi_{F2}) \tag{2.19}$$

where the complex coherence length is given by

$$\xi_F = \sqrt{\frac{\hbar D}{2(\pi k_B T + iE_{\text{ex}})}}. \tag{2.20}$$

where D is the diffusion constant for electrons in the ferromagnet.

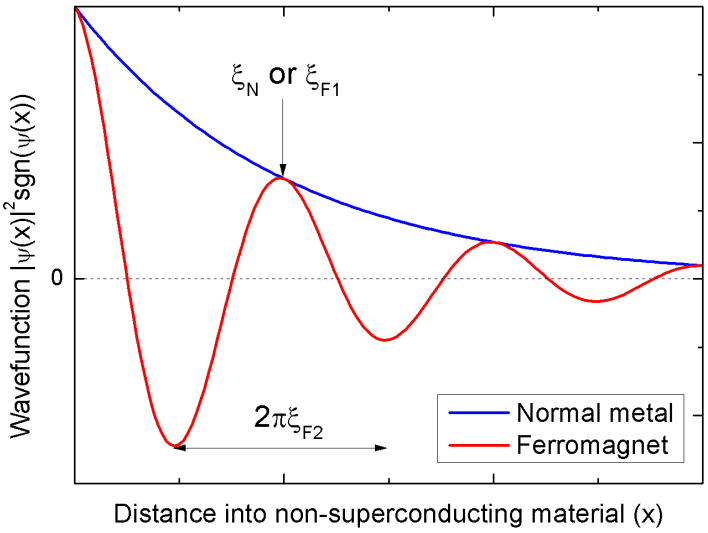

Figure 2.6: Decay of the superconducting wavefunction for SN and SF bilayer structures.

The difference between the wavefunction decay in a normal metal and in a ferromagnet is shown in Fig. 2.6. Here, ξ_{F1} and ξ_{F2} are the real and imaginary parts respectively, given by

$$\xi_{F1,2} = \sqrt{\frac{\hbar D}{[E_{\text{ex}}^2 + (\pi k_B T)^2]^{1/2} \pm k_B T}} \tag{2.21}$$

where ξ_{F1} is responsible for the decay and ξ_{F2} determines the oscillation period. For strong ferromagnets with $E_{\text{ex}} \gg k_B T_C$, $\xi_{F1} \approx \xi_{F2}$ and the predicted behaviour is insensitive to changes in temperature. For the case where $E_{\text{ex}} \sim k_B T_C$, ξ_{F1} decreases and ξ_{F2} increases as the temperature is raised. The ferromagnetic material used for the work presented in this thesis has $T_{\text{Curie}} = 1388$ K ($E_{\text{ex}} \gg k_B T_C$) and therefore is in the regime where $\xi_{F1,2}$ do not change with temperature.

Experimental Observations of Wavefunction Oscillations in SF Bilayers

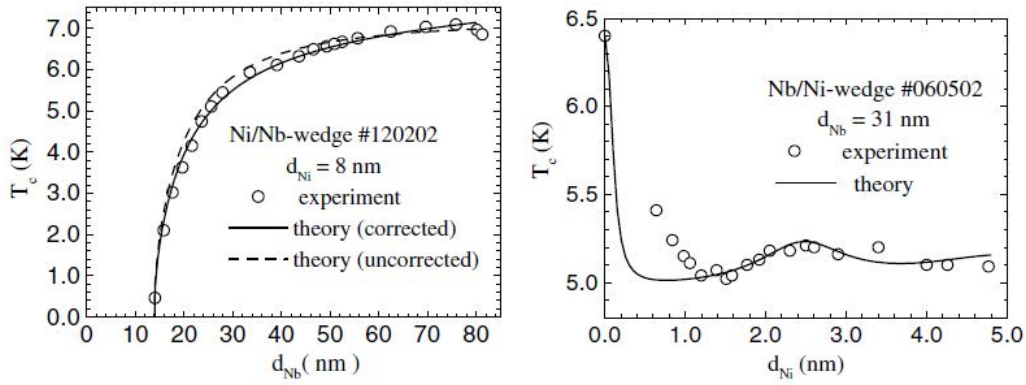

Figure 2.7: Oscillatory behaviour in T_C measured for two sample sets of Nb/Ni bilayers by Sidorenko et al [34].

As will be shown in section 3.1.2, by sandwiching a ferromagnet with a carefully chosen thickness between two superconductors, a phase difference of π can be maintained across the structure in the ground state. The work presented in chapter 7 uses samples with a bilayer structure. For this geometry, π-coupling between layers is clearly impossible and yet a nonmonotonic dependence of T_C on d_{FM} was predicted [35] (where d_{FM} is the ferromagnetic layer thickness). This behaviour was subsequently observed by Wong et al in V/Fe superlattices [36], and improvements in deposition techniques has enabled the unambiguous demonstration of this effect in many other material combinations and sample structures (for example V/Co and Nb/Co multilayers by Obi et al [37], Nb/$Cu_{1-x}Ni_x$ bilayers by Zdravkov et al [38], and Nb/Ni bilayers by Sidorenko et al [34] (shown in Fig. 2.7)).

A qualitative analogy for the mechanism causing T_C oscillations in bilayer structures was proposed by Sidorenko et al [34]. The ferromagnetic layer was likened to a Fabry-Pérot interferometer, in that the pairing function flux through the SF interface is modulated by constructive or destructive interference of the oscillating wavefunction as a result of reflections that occur at both boundaries. In this way, T_C is sensitively dependent on the ferromagnet thickness. An explanation for the large initial decrease of T_C in bilayers was also proposed by Mühge et al [39] following measurements made on sputtered Fe/Nb/Fe trilayers. They argue that the presence

of a magnetic 'dead layer' is critical for the observation of reentrant superconductivity and further investigated this hypothesis in Nb-Fe bilayers [40] prepared by molecular beam epitaxy. The dependence of the observation of an oscillating T_C on the deposition conditions was later studied in the literature by Sidorenko et al [34]; they noted that the reduction in the dead layer thickness was coincident with a reduction or absence of the pronounced oscillatory behaviour that is seen for sputtered samples. This will be discussed further in chapter 7 where it will be shown that the superconductor thickness, as in Fig. 2.5, is also an important parameter.

Part I

Experimental Measurement of the Current-Phase Relationship of a Josephson Junction

CHAPTER 3

MEASUREMENT OF THE CURRENT-PHASE RELATIONSHIP OF JOSEPHSON JUNCTIONS IN A PLANAR GEOMETRY

This chapter covers phase sensitive measurements made on a conventional Josephson junction and the characterisation of the measurement circuit used to do this. The circuit was designed to be a general purpose measurement device that could be used to measure any junction deposited into a small window. It was necessary to have a good understanding of circuit parameters, such as on-chip inductances. It will be shown that the circuit design presented here has insurmountable problems that arise from parasitic mutual inductances which place a limit on this method of CPR measurement, but serves as motivation for the alternative measurement circuit that will be presented in chapter 4. Before a detailed account is given of the experimental method and the resulting data it is first necessary to build upon the general theory provided in the previous chapter to provide a more specific background relating to Josephson devices.

3.1 Josephson Devices

3.1.1 Josephson Junctions

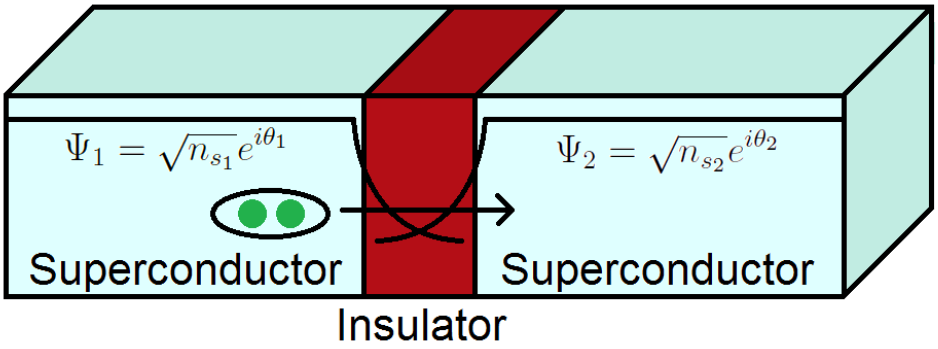

Figure 3.1: Schematic representation of a superconducting weak link. The magnitude of each superconducting electrode wavefunction is represented by the black line that falls away exponentially in the barrier region. When the wavefunction of each electrode overlaps, dissipationless tunneling can be observed (see text).

Further to the discussion of superconductivity in chapter 2, the situation illustrated by Fig. 3.1 is now discussed. Behaviours known as the Josephson effects are observed in systems that allow the wavefunction of two spatially separated regions of superconductor to overlap in an intermediate 'barrier' region. Briefly, there are two main consequences of this; firstly, a small zero voltage dc supercurrent can flow across the barrier where the current, I, is functionally related to the phase difference across the junction such that

$$I = I_C \sin\theta \tag{3.1}$$

where

$$\theta = \theta_2 - \theta_1. \tag{3.2}$$

Equation (3.1) is known as the dc Josephson equation and describes the Current-

Phase Relationship (CPR) of the junction. The current that can flow through the junction is related to the critical (i.e. maximally supported) current, I_C, modulated sinusoidally by the phase difference across the junction. Here, I_C contains information about the coupling strength and is temperature dependent since $I_C \propto \sqrt{n_{s_1} n_{s_2}}$ [41]. According to equation (3.1), I_C is reached at $\theta = \pm\pi/2$.

The second consequence of the geometry shown in Fig. 3.1 is that if a dc potential difference is maintained across the barrier, an ac current will flow. This behaviour is described by the ac Josephson equation

$$\frac{d\theta}{dt} = \frac{2eV}{\hbar} \tag{3.3}$$

where e is the charge of an electron and $\hbar$ is the reduced Planck constant. A voltage across the junction results in a phase difference that evolves with time and provides a relationship between the voltage, V, and the frequency given by $f = 2eV/h$. Electromagnetic radiation is produced with $f = 483.6$ GHz/mV and can be used as an accurate voltage standard.

In Fig. 3.1 the barrier is shown as an insulator but in practice this is not the only material to allow the Josephson effects to be observed; any region that allows a weak coupling between superconducting electrodes should suffice. There are a number of good review articles that describe different junction arrangements and their properties [3, 30], but the first prediction of the Josephson effect was made for a superconductor-insulator-superconductor (SIS) junction [42] and were observed experimentally soon after [43,44]. There are many types of junction that do not follow the sinusoidal behaviour predicted by the CPR given in equation (3.1). This will be discussed further in section 3.1.4. The general criteria to allow these effects to occur are that the coupling between the electrodes should be strong enough that the phases of the wavefunctions should be correlated yet weak enough that perturbation by external electromagnetic fields is allowed.

Josephson Energy

The overlap of the superconducting electrode wavefunctions reduces the energy of the Josephson junction below that of two uncoupled islands of superconducting material. For a phase difference $\theta = 0$, the so-called coupling energy is maximal and is reduced as the current through the junction is increased. At $\theta = \pi/2$ ($I = I_C$) the coupling energy becomes zero.

Given equations (3.1) and (3.3), the energy stored by the junction due to the coupling can be calculated by evaluating the work done in bringing about a phase change from $\theta = 0$ at time $t = 0$ to $\theta = \theta$ at time $t = t$. The work done is

$$E(\theta) = \int_0^t IV dt = \int_0^t I_C \sin\theta \frac{\hbar}{2e}\frac{d\theta}{dt} dt = \frac{\hbar I_C}{2e}(1 - \cos\theta) \tag{3.4}$$

where the Josephson coupling energy, E_J, is defined as

$$E_J = \frac{\hbar I_C}{2e}. \tag{3.5}$$

Assuming a positive value for I_C, the energy is minimised for the case where $\theta = 0$, as shown in Fig. 3.2. Should the junction be incorporated into a superconducting loop, in the absence of a method of driving the two sides of the junction out of equilibrium, no current will flow since the minimum energy corresponds to the case of no phase gradients. A phase difference of $\theta = \pi$ also gives zero current but, according to this graph, this value of phase difference corresponds to a maximum Josephson coupling energy and therefore is unstable.

Josephson Inductance

It can be shown by combining the dc and ac Josephson equations that the Josephson junction has a highly nonlinear inductance. The inductance can be written in terms

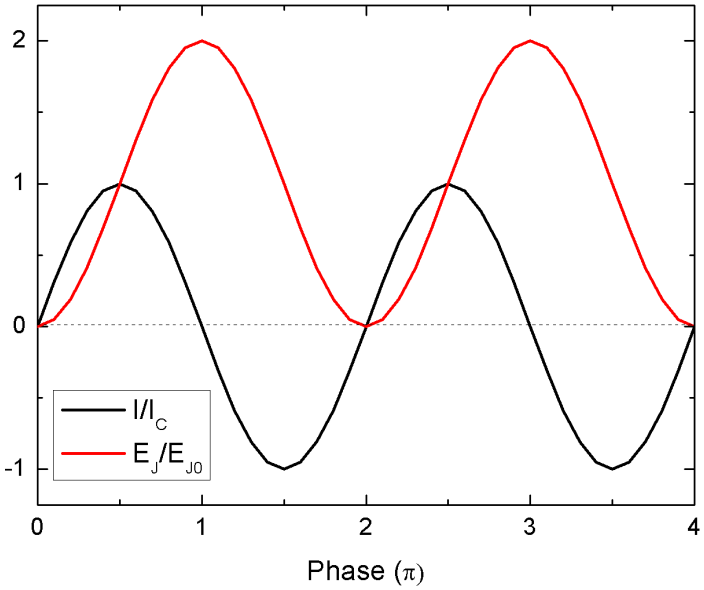

Figure 3.2: The dc Josephson relationship and the Josephson coupling energy as a function of the phase difference across the junction.

of the phase difference as

$$L_J(\theta) = \frac{\Phi_0}{2\pi I_C \cos(\theta)} = \frac{L_{J0}}{\cos(\theta)}, \tag{3.6}$$

where L_{J0} is the Josephson inductance at $\theta = 0$. It can be noted that E_J in equation (3.4) can be replaced with $L_{J0}I_C^2$ such that, although there are no magnetic fields involved, the potential energy of the junction can be considered as being stored by the Josephson inductance. The Josephson inductance can also be written in terms of the current as

$$L_J(I) = \frac{I_C L_{J0}}{\sqrt{{I_C}^2 - I^2}}. \tag{3.7}$$

This is plotted in Fig. 3.3 where it is shown that for small currents the junction retains an approximately constant value of inductance before diverging as $I \to I_C$.

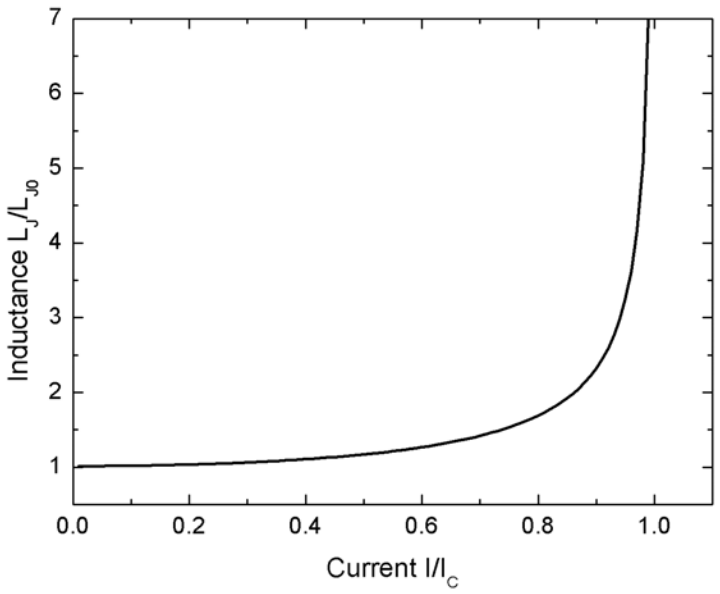

Figure 3.3: The Josephson inductance normalised to the zero-current Josephson inductance as a function of the current through the junction.

3.1.2 π-junctions

The term 'π-junction' refers to a junction where the CPR is sinusoidally dependent on a *negative* critical current:

$$I = -I_C \sin\theta = I_C \sin(\theta + \pi). \tag{3.8}$$

For a negative I_C, the CPR and the Josephson energy are shown graphically in Fig. 3.4. Here, the Josephson energy is now minimised when a phase difference of π is maintained across the junction. π-junctions have been proposed and demonstrated [25] as complementary circuit elements in digital and quantum circuits and will be discussed further for the case of a multiply connected geometry in section 3.1.3.

The first prediction of the existence of a π-junction was presented by Bulaevskii, Kuzii and Sobyanin [45] for a tunnel junction with an insulating barrier containing magnetic impurities. Along with superconductor-ferromagnet-superconductor (SFS)

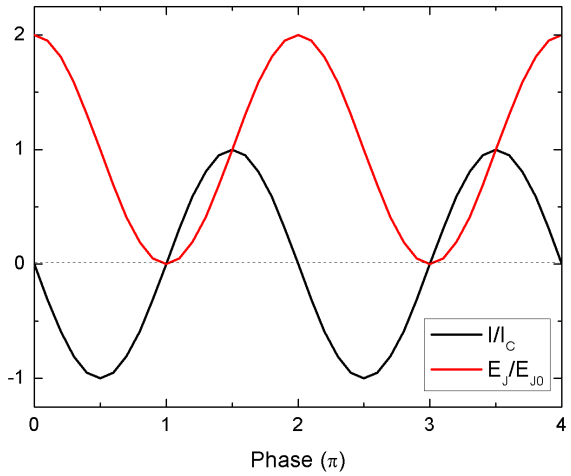

Figure 3.4: The dc Josephson relation and Josephson coupling energy as a function of the phase difference across the junction where the junction now has a negative I_C.

junctions (discussed further below), there are other proposed methods for creating π-junctions [46]. Some examples of structures that can possess a negative I_C include junctions containing quantum dots [47], non-equilibrium effects brought about by controlling the state of the N-layer in SNS junctions [48], and junctions fabricated from unconventional superconductors [49, 50].

SFS Junctions

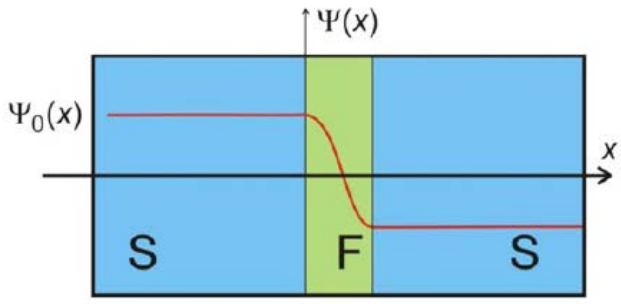

Figure 3.5: Schematic diagram of an SFS π-junction (taken from Ref. [46]).

To create the π-phase shift across a junction described by equation (3.8), a ferromagnetic barrier between superconducting electrodes can be used. The principle of an SFS Josephson junction is to make use of the progressive phase shift of the

wavefunction through the barrier that was described in section 2.3.2 for the case of a superconductor-ferromagnet bilayer. Through knowledge of the properties of the ferromagnetic barrier layer, a junction can be engineered such that the sign of the wavefunction differs at each electrode in the ground state, as illustrated schematically by Fig. 3.5.

As stated above, the first prediction of a π-junction was for a Josephson junction with magnetic impurities in the barrier layer [45]. There are many technical challenges related to the fabrication of SFS π-junctions that currently prevent their use in large-scale superconducting electronic systems. This is evidenced by the fact that after the initial prediction, it was not until 2001 that Ryazanov et al [29] published the first experimental evidence of a π-junction; they observed a nonmonotonic dependence of I_C on the sample temperature for a range of barrier thicknesses. Their result provided a more conclusive body of evidence for the oscillatory decay of the wavefunction inside the ferromagnet than some previous experiments involving bilayers [39].

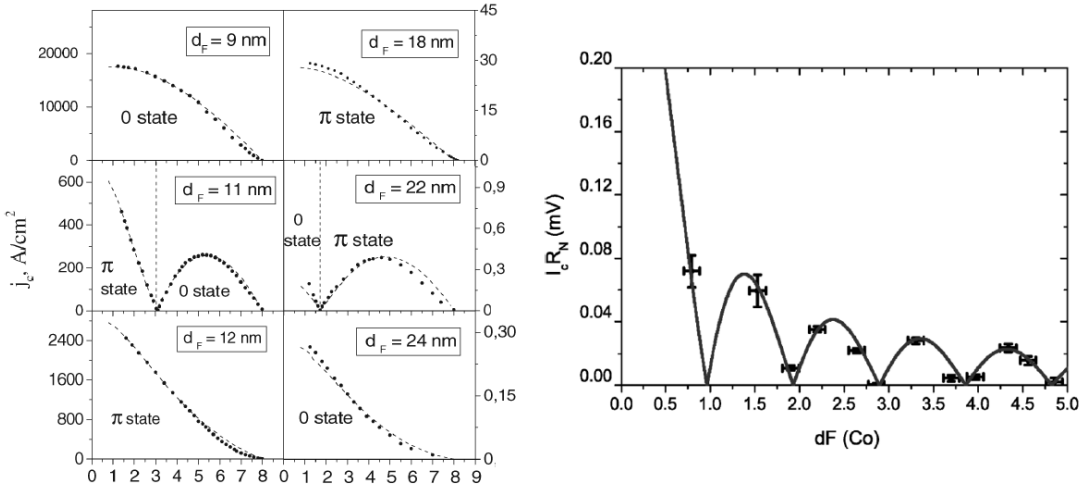

Figure 3.6: Examples of 0-π transitions in SFS junctions as a function of temperature (left) and barrier thickness (right). Left: $I_C(T)$ for junctions with a $Cu_{0.48}Ni_{0.52}$ barrier made by Ryazanov et al [29] (image adapted from [51]). Right: I_C as a function of cobalt barrier thickness from Robinson et al [52].

One of the challenges involved in SFS junction fabrication is the fine control of

the ferromagnet deposition needed to create a 0-π transition as a function of barrier thickness only. For ferromagnets with a large exchange energy, control in the angstrom range is often required. Ryazanov et al [29, 51] and other research groups [6, 25, 53–58] have been able to circumvent this problem by using a dilute ferromagnetic alloy [59] to reduce the exchange energy such that $E_{\rm ex} \approx k_B T_C$. As shown in section 2.3.2, this enables the 0-π transition to be induced by a change in temperature for a single sample rather than careful fabrication of a set of junctions (as the temperature is decreased, ξ_{F1} increases while ξ_{F2} decreases). An example of the 0-π transition for a Josephson junction with a weak ferromagnetic barrier is shown in Fig. 3.6 (left). The ferromagnetic barrier thickness in these experiments can be many tens of nanometers and despite this, there was some initial difficulty reported in achieving reproducible devices.

Although precise control over the barrier thickness is difficult, later work on SFS π-junctions has made use of undiluted ferromagnets to demonstrate 0-π transitions as a function of the barrier thickness alone. Notable measurements of I_C as a function of a cobalt barrier thickness were made by Robinson et al [52], who were collaborators for the experiments described in this thesis, where selected results are shown in Fig. 3.6 (right). The results can be interpreted as showing *multiple* 0-π and π-0 transitions as a function of barrier thickness for $d_F(Co) < 5$ nm, which clearly shows the need for extreme control needed in the junction fabrication. Other barrier materials that have been studied include $Fe_{20}Ni_{80}$ [31, 32, 60], Ni_3Al [33], Ni [31, 32, 61, 62], Fe [31, 32], and Co [31, 32].

There are other technical challenges to be addressed before these structures can be implemented in large scale systems. From an applications perspective, it has been shown that for long decoherence times in quantum circuits containing Josephson junctions, a high normal resistance is required [63]. This criterion is difficult to fulfill in trilayer SFS junctions owing to the naturally low resistivity of the metallic ferromagnetic layer. To combat this, the addition of an insulating layer has been proposed to give an SIFS junction structure in order to increase the $I_C R_n$ product

and has been successfully demonstrated by Kontos et al [56] amongst others [53, 64, 65].

0-π transitions in SFS junctions are often 'identified' in the literature by measuring the absolute value of I_C as a function of the barrier thickness or temperature. The observation of a nonmonotonic change in I_C, as illustrated by Fig. 3.6, is interpreted as alternating 0- and π-phase shifts across the junction. While this is a convenient measurement, a more convincing experiment that reveals the change of sign of I_C as well as the magnitude is the measurement of the CPR of the Josephson junction. This will be discussed further in section 3.1.4.

3.1.3 SQUID Devices

A Superconducting QUantum Interference Device (SQUID) incorporates weak links in otherwise complete loops of superconducting material, thereby creating a device that combines flux quantisation with the Josephson effects. The circuit used here to determine the CPR uses a dc SQUID (a loop containing two junctions) to monitor the current flowing through an inductor by sensitive measurement of the magnetic field produced. As will be seen, the loop containing the junction under measurement has the same structure as an rf SQUID (a loop containing a single junction), therefore much of its behaviour can be explained in this context.

The dc SQUID

The dc SQUID is a loop of superconducting material interrupted by two weak links in a parallel configuration, as shown in Fig. 3.7 (left) where the system output behaves analogously to a two-slit interferometer and is used to measure small changes in applied magnetic fields. A constant bias current, I_B, is passed through the configuration such that $I_B > 2I_C$ and a voltage is maintained across the device according to the ac Josephson relationship. This voltage varies in response to an externally

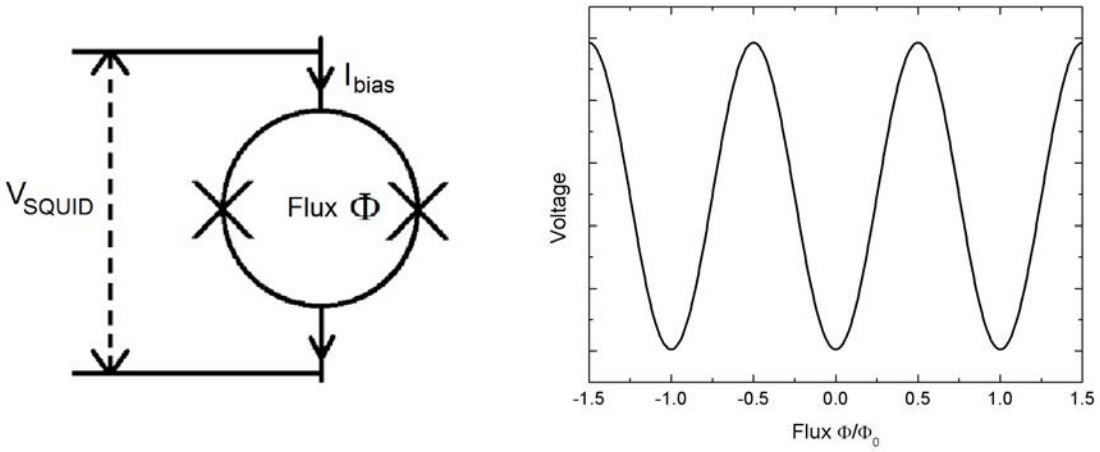

Figure 3.7: Left: Schematic diagram of a dc SQUID. Right: Voltage response of a dc SQUID to an applied magnetic field.

applied magnetic field with a period of Φ_0, as shown in Fig. 3.7 (right).

For the circuit used to measure the CPR, a dc SQUID was simply used to measure the magnetic field produced by a current flowing through a coupled inductor. As such, detailed discussion will not be made here but further information can be found in Ref. [66].

The rf SQUID

The rf SQUID is a loop of superconducting material interrupted by a single weak link. The CPR measurement device to be presented in section 3.2 shares this configuration and therefore much of the circuit behaviour can be understood in terms of the rf SQUID.

As was discussed in section 2.1, the flux through a complete thick (i.e. $t \gg \lambda_L$) ring of superconductor must be quantised in units of the flux quantum, Φ_0. A phase difference can be maintained in the wavefunction across the electrodes of a Josephson junction, as discussed in section 3.1.1. Combining the two phenomena by interrupting a complete loop with a junction, the following condition must then be satisfied

$$\theta + 2\pi\frac{\Phi}{\Phi_0} = 2\pi n \tag{3.9}$$

where θ is the phase difference across the junction, Φ is the total magnetic flux in the loop, and n is an integer. The total current that flows around the loop can then be found by combining equations (3.1) and (3.9) to give

$$I = -I_C \sin\left(2\pi\frac{\Phi}{\Phi_0}\right). \tag{3.10}$$

The total current can also be expressed in terms of the geometric inductance of the loop, L. Equating the two gives an expression for the total flux threading the loop as

$$\Phi = \Phi_{\text{ext}} - LI_C \sin\left(2\pi\frac{\Phi}{\Phi_0}\right) \tag{3.11}$$

where Φ_{ext} is the flux due to an external magnetic field applied to the loop which the supercurrent will oppose. This equation shows two possible behaviours depending on the hysteresis parameter

$$\beta_L = \frac{2\pi LI_C}{\Phi_0}, \tag{3.12}$$

the origin of which can be seen by taking the derivative of equation (3.11) with respect to Φ and calling the coefficient of the cosine β_L, which gives

$$\frac{d\Phi}{d\Phi_{\text{ext}}} = \frac{1}{1 + \beta_L \cos\left(2\pi\frac{\Phi}{\Phi_0}\right)}. \tag{3.13}$$

The potential energy of the rf SQUID is a sinusoidally modulated quadratic function given by the sum of the energies stored in the Josephson junction and the magnetic

field produced by the circulating current:

$$U = \frac{(\Phi - \Phi_{\text{ext}})^2}{2L} - E_J \cos\left(2\pi \frac{\Phi}{\Phi_0}\right). \tag{3.14}$$

Φ and U are plotted in Fig. 3.8 for $\beta_L = 0.9$ and $\beta_L = 9$ to illustrate the importance of the value of this parameter. For Φ, if $\beta_L < 1$, $d\Phi/d\Phi_{\text{ext}}$ is always positive and nonhysteretic, and in the potential energy picture, there is a single stable state. If $\beta_L > 1$, equation (3.11) describes a reentrant curve where $d\Phi/d\Phi_{\text{ext}}$ can now be positive, negative or infinite. The potential energy picture now shows multiple 'wells' that the rf SQUID can exist in.

Starting at $\Phi_{\text{ext}} = 0$, for a small increase in Φ_{ext}, Fig. 3.8 (top) shows that the effect is to reduce the total flux threading the loop compared to the applied flux. In the potential energy description of the rf SQUID with $\beta_L = 9$ (bottom), the effect is to decrease the barrier on one side of the lowest energy well. Eventually, the circulating current reaches I_C of the junction at $\Phi_{\text{ext}} = n\Phi_0/4 + LI$ and a sudden transition occurs; the junction momentarily enters the finite voltage regime and makes a quantum transition from n to $n+1$ accompanied by an increase in the flux in the loop by Φ_0. In the potential picture, the phase 'particle' is able to overcome the barrier and roll into the next well. Similarly, if the external flux is decreased, I_C will be reached in the negative direction and the number of flux quanta in the loop is decreased; as the system makes a series of flux state transitions, a hysteresis loop is followed.

Fig. 3.8 (bottom) shows that for $\Phi_{\text{ext}} = 0.5$, a double-well potential exists which has made the rf SQUID an attractive candidate for quantum bit technology [1, 2, 67]. The creation of this doubly degenerate ground state requires the introduction of the aforementioned flux-bias, which creates experimental difficulty for large scale systems. The first theoretical π-junction proposal was of a tunnel junction with magnetic impurities in the barrier in a multiply connected geometry where Bulaevskii et al predicted the existence of a spontaneous supercurrent that would cir-

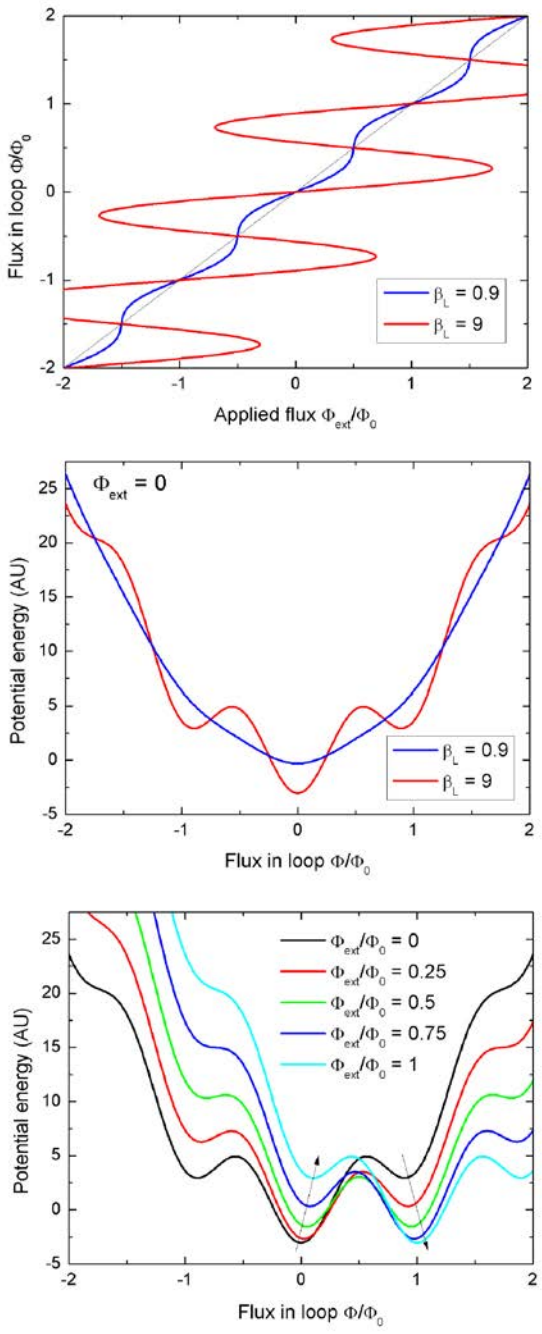

Figure 3.8: Top: Dependence of the total flux in the rf SQUID loop, Φ, on the applied flux, Φ_{ext} for $\beta_L = 0.9$ and 9 (black line indicates $\Phi/\Phi_0 = \Phi_{\text{ext}}/\Phi_0$). Middle: Potential energy of the rf SQUID for $\Phi_{\text{ext}} = 0$ for the same values of β_L. Bottom: Potential energy for $\beta_L = 9$ for a series of values of Φ_{ext} where the arrows indicate the barrier movement with increasing Φ_{ext}.

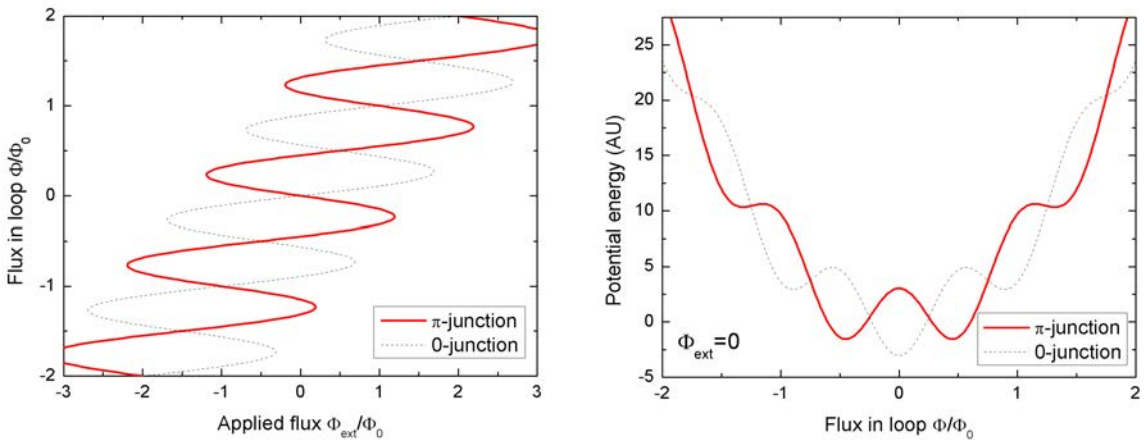

Figure 3.9: Φ/Φ_{ext} (left) and potential energy (right) for an rf SQUID containing a π-junction where $I_C L \geq \Phi_0/2\pi$ and $\beta_L = 9$.

culate around the ring in the absence of an applied magnetic field [45]. This has been notably demonstrated experimentally by Frolov et al [68] and Bauer et al [69]. The result of a negative critical current in a multiply-connected geometry is shown in Fig. 3.9 for the flux in the loop and the potential energy under the condition $I_C L \geq \Phi_0/2\pi$ where L is the inductance of the loop. Clearly, the spontaneous generation of this degeneracy is advantageous in that it not only reduces the technical challenge of introducing extra bias lines into the system but also reduces the amount of noise entering the system as a consequence of the flux-biasing.

The rf SQUID is an important concept for the work presented in this thesis as it forms the basis for observing the CPR of the Josephson junction that interrupts the complete superconducting loop. In practice, an rf SQUID used in the context of magnetic field sensing is read out by monitoring the periodic losses across a resonant circuit [66]; this idea will be returned to in section 4.3.

3.1.4 The Current-Phase Relationship

Non-sinusoidal current-phase relationships

The discussion of Josephson devices thus far has assumed a sinusoidal CPR as given by equation (3.1). In general, however, the current need not be sinusoidally dependent on the phase; the key requirement is only that it is an odd 2π periodic function. While the ideal dc Josephson equation is often used and has been shown to accurately describe SIS junctions [70,71], it has also been shown that deviations can occur for other junctions types where microscopic processes in the barrier influence the form of the CPR. Deviations are noted to occur in SNS junctions and point contacts, amongst others [3,30,72]. The microscopic detail for individual cases will not be discussed here but a more general way of expressing the CPR, given that it is an odd 2π periodic function, is

$$I = I_C f(\theta) = \sum_n I_n \sin(n\theta) \tag{3.15}$$

i.e. there may be higher harmonic components in the CPR which means that I_C may not be reached at exactly $\theta = \pi/2$. Golubov et al [30] have published an extensive review that covers the many cases where $f(\theta) \neq \sin(\theta)$.

A summary of other possible types of CPR are shown in Fig. 3.10 as presented by Golubov et al [30]. Commonly observed deviations include a skewness in the CPR [7,73], higher order components of the supercurrent [74] and, as was discussed in section 3.1.2, conclusive evidence of a transition from a 0- to $\pi-$phase difference across the junction [6]. Phase sensitive measurements have also been used to study the pairing symmetry of unconventional superconductors [75].

Junctions that show deviation from ideal behaviour are interesting not only as they allow insight into the microscopic processes that affect the supercurrent, but also from an applications point of view. For example, by observing the detailed shape of

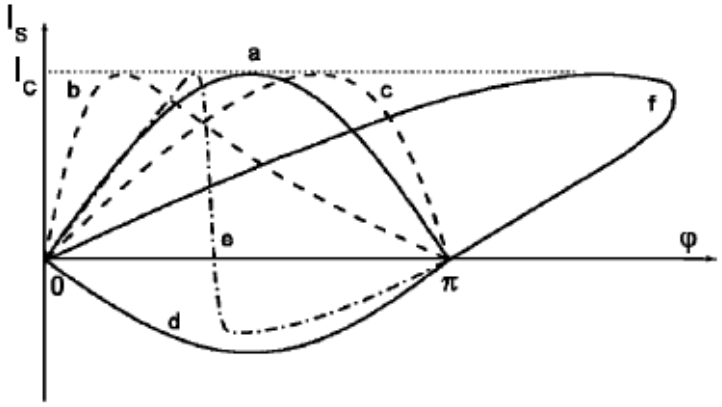

Figure 3.10: Other possible types of CPR. Curve (a) shows the ideal sinusoidal CPR. Curves (b) and (c) show a skewed CPR where I_C is reached at $\theta \leq \pi/2$ and $\theta \geq \pi/2$ respectively. (d) shows π-junction behaviour. (e) shows the current crossing the horizontal axis for $0 \leq \theta\pi$. Curve (f) shows a multivalued CPR. Image taken from Ref. [30].

the CPR, more accurate modelling of the dynamics of large-scale Josephson junction systems is afforded. Much of the work in the literature that has documented deviations from the ideal CPR has been theoretical. In practice, it is difficult to fabricate non-ideal junctions and perform phase-sensitive measurements to observe the exact form of the CPR. A brief review of methods that have been employed to do this will now be presented.

CPR measurements in the literature

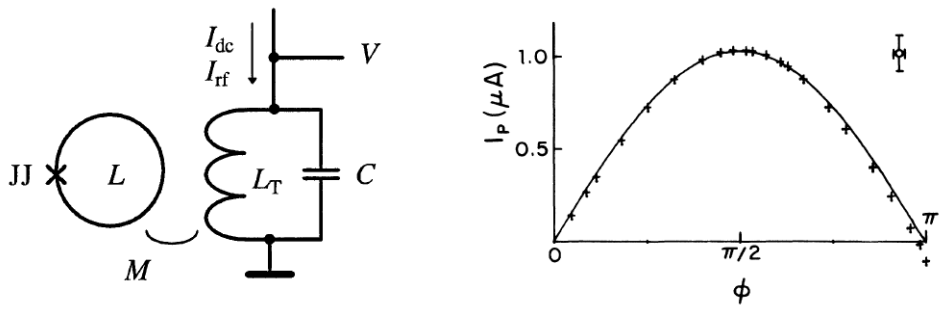

Figure 3.11: Left: Schematic circuit diagram of the Rifkin-Deaver method of observing the CPR (image taken from Ref. [72]). Right: Observation of the CPR of a niobium point contact made by Rifkin and Deaver [8].

In practice, it is difficult to measure the quantum mechanical phase across the junction directly; some proposed methods of measurement rely on measuring a junction parameter that is dependent on the phase in some way. An early measurement of the CPR was made by Rifkin and Deaver [8] in 1976 where the phase-dependent variable from which the CPR was deduced was the Josephson inductance (c.f. equation (3.6)). To achieve this, an rf SQUID structure was coupled to a tank circuit, shown in Fig. 3.11. The impedance of the rf SQUID, and hence the tank circuit, is a periodic function of the applied field. From this, the complete CPR can be mathematically reconstructed [8, 30, 72] provided that $\beta_L < 1$ for the rf SQUID.

The Rifkin-Deaver method has since been used in the measurement of other more exotic junctions. For example, Il'ichev et al [72] implemented this method to observe the nonsinusoidal CPR of grain boundary junctions. The method was also employed by Ebel et al [76] to observe low temperature deviations from ideal behaviour in Nb/InAs(2DES)/Nb junctions. It seems to the author that the disadvantage of the Rifkin-Deaver method is the rather indirect manner in which the CPR is obtained.

Another approach, from which the inspiration for the circuit design presented in this chapter is drawn, is similar to a dc method used by Jackel et al [70] as adapted by Waldram and Lumley in 1976 [4]. The phase-dependent variable to be measured in the Jackel method is the current through the junction (c.f. equation (3.1)). Briefly, this is a static method that also makes use of the rf SQUID configuration. The induced current in the rf SQUID in response to an applied field is monitored directly using a coupled dc SQUID. The Waldram-Lumley method builds upon the Jackel method to make a more direct measurement of the CPR by the inclusion of additional current sources to the rf SQUID such that the dc SQUID can be used as a null-detector. The approach taken with the design presented in this chapter will be described in greater detail in section 3.2.

The static method of CPR measurement has been used by a number of groups [5–7] due to its versatility. A notable experiment conducted by Frolov et al [6] used the Jackel method to measure the CPR of a Josephson junction with a weak ferromag-

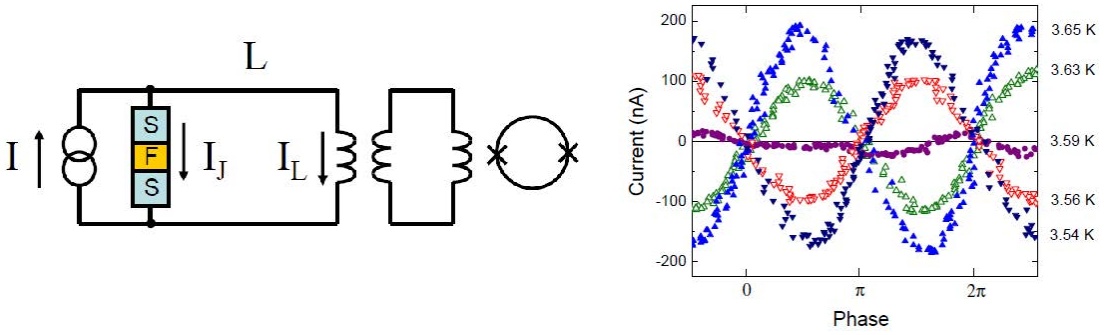

Figure 3.12: Left: Schematic circuit diagram of the CPR measurement device used by Frolov et al. Right: Observed CPR of an SFS Josephson junction for a variety of temperatures showing a 0- to π-transition at $T = 3.59$ K (both images taken from Ref. [6]).

netic barrier as a function of temperature. The experimental design and selected results are shown in Fig. 3.12 which shows the change in junction behaviour either side of $T = 3.59$ K. A similar method was used by Chialvo et al [7] to measure the CPR in Josephson junctions with a graphene barrier. The Jackel method relies upon the subtraction of a linear background in the dc SQUID response equal to the loop inductance. The Waldram-Lumley method allows a more direct measurement of the CPR and as such does not require the same level of analysis as the Rifkin-Deaver method.

Other phase sensitive experiments have been conducted that have not necessarily focused on the exact shape of the CPR. Guichard et al [57] fabricated a series of dc SQUIDs where the two junctions were either 0-0, 0-π or π-π to firmly establish the crossover from 0- to π coupling in SFS Josephson junctions with a weak ferromagnetic barrier. By plotting the SQUID I_C as a function of the applied magnetic field for a simultaneous measurement of the 0-π SQUID with a 0-0 or π-π SQUID they proved negative coupling across the SFS junctions. In principle, this experiment does contain some information about the CPR though this kind of measurement is not fit for a detailed study.

Section 3.1.2 showed that much work has been undertaken in the study of the magnitude of I_C for SFS junctions but there have been relatively few experiments

that focus on the detailed shape of the supercurrent's dependence on the phase difference across the junction. As discussed, this measurement provides important information about the microscopic processes contributing to the current through the junction and therefore the work presented in this thesis is focused on methods of extracting this information.

3.2 The Measurement Circuit

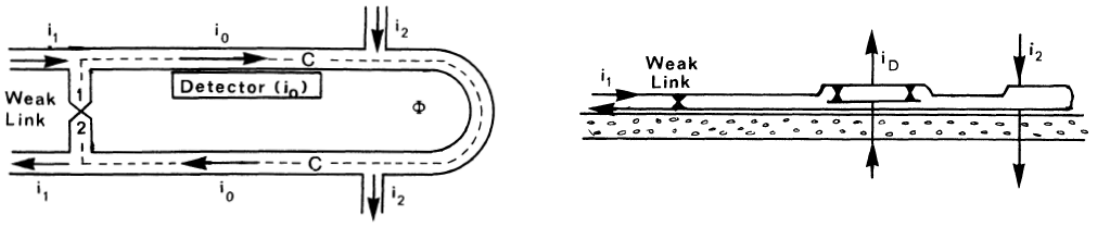

Figure 3.13: Schematic diagram of the Waldram-Lumley measurement circuit taken from Ref. [4] (left) with a cross sectional view to show the stacked geometry of the device (right).

The circuit that was designed to measure the CPR is based on a device made by Waldram and Lumley in 1976 also at the University of Birmingham [4]. The Waldram-Lumley device is shown schematically in Fig. 3.13 (left) and as a cross section through the device (right). This device uses a stacked geometry to minimise stray fields from current flow in the circuit and the Josephson junction fabrication must occur with the measurement device fabrication.

The operation of this measurement scheme is more clearly explained in the context of the planar device geometry used here. The circuit was designed by Dr E. Tarte of the Electronic, Electrical and Computer Engineering Department at the University of Birmingham and Dr T. Ortlepp of the Department of Advanced Electromagnetics at Ilmenau University of Technology. The chips were made at the Institute of Photonic Technology by Dr J. Kunert and contain a high-I_C Josephson junction in the measurement loop for test purposes. A photograph of the measurement circuit is shown in Fig. 3.14 (left) and shown schematically for clarity (right). Inductors are

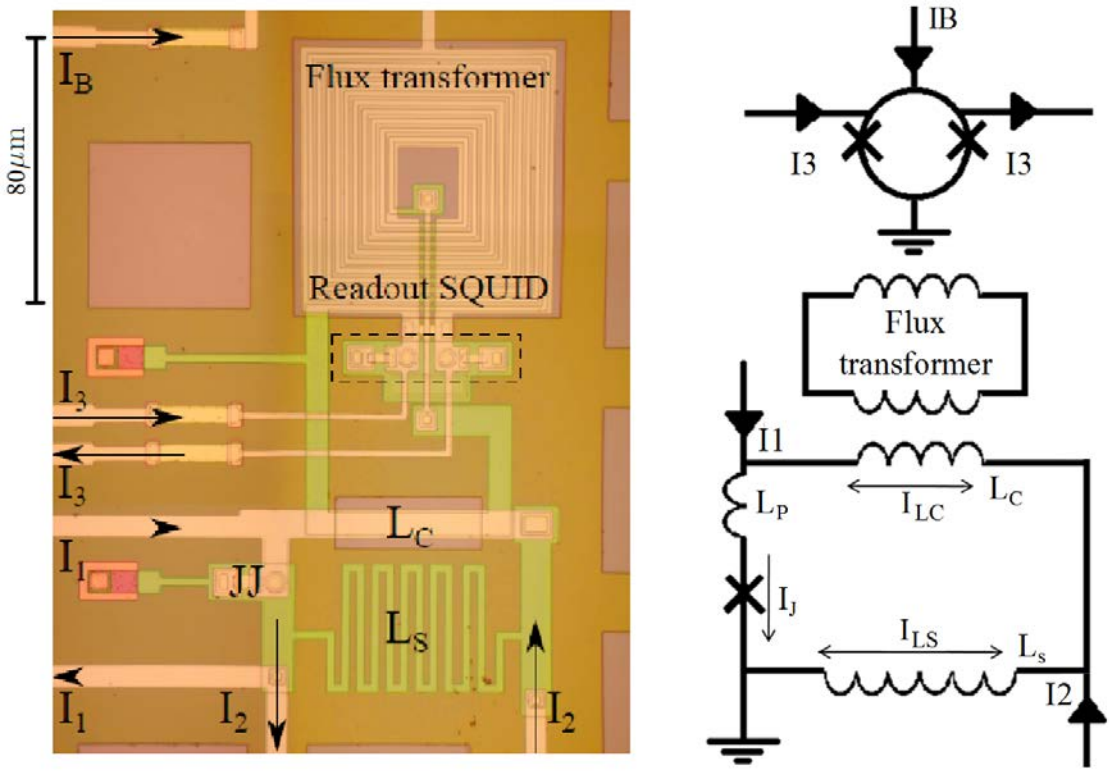

Figure 3.14: Photograph of the circuit used to measure the CPR of an SIS Josephson junction labelled JJ (left). The circuit is represented schematically (right) for ease of explanation and comparison with the Waldram-Lumley device shown in Fig. 3.13.

formed by micro striplines and the whole circuit (excluding the flux transformer) is above a superconducting ground plane.

3.2.1 The Current-Phase Relationship Measurement

The Waldram-Lumley device and the circuit shown in Fig. 3.14 both make use of the fact that, for a Josephson junction in a complete loop of superconducting material, 'the phase change measured around the loop must be the same as that across the junction' [4]. From the London equation for current including the effect of magnetic field, the phase difference across the junction is

$$\varphi_J = \theta_1 - \theta_2 = \frac{2e}{\hbar} \oint A \cdot dl = 2\pi \frac{\Phi}{\Phi_0} \tag{3.16}$$

where Φ is the flux through the loop around which one is integrating and $\Phi_0 = h/2e$, where h is Planck's constant and e is the electron charge, is the flux quantum.

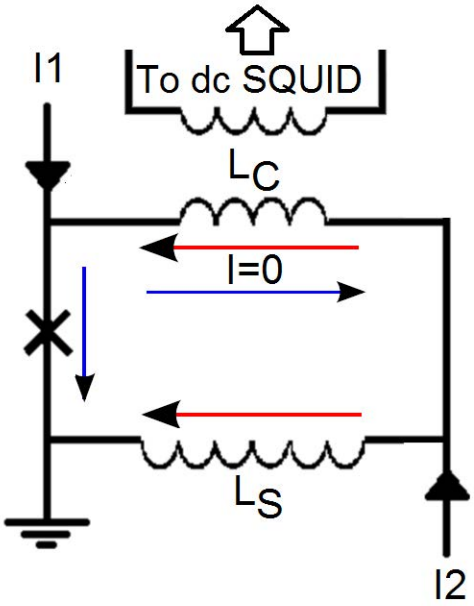

Figure 3.15: Waldram-Lumley method for a direct measurement of the CPR of a Josephson junction (denoted by a cross). For details, see text.

To measure the CPR in this geometry, a dc SQUID is coupled to the measurement

circuit via a flux transformer and used to sense magnetic fields produced by any current flowing through inductor L_C. In practice, the dc SQUID is brought to a optimal point of operation using current I_B such that $dV/d\Phi$ is maximal (current I_3 can also be used to apply flux directly to the SQUID loop). The dc SQUID is then used as a null detector through the observation of changes in the SQUID voltage, V_{SQ}, in response to current flow in the coupled inductor by the following method, as illustrated in Fig. 3.15:

- A measurement begins on the assumption that there is no current flowing through inductor L_C. In practice, there may be but since the CPR is periodic, any current that is flowing simply adds an offset to the measurement.
- A small current I_1 is fed to the left hand side of the circuit. The current will split such that some will flow through the Josephson junction and some will flow through inductor L_C. The dc SQUID will have a measurable response due to the magnetic field produced by the current in L_C.
- A small current I_2 is then fed to the right hand side of the circuit. Again, it will split so that some will flow through L_C and some will flow through the large inductance L_S provided by the meander line.
- For each value of I_1, a particular value of I_2 of the correct sign will exactly cancel the current flowing in L_C. At this point, the dc SQUID response will return to the initial value prior to increasing I_1.

At this point, there is no current flowing through L_C. I_1 flows entirely through the Josephson junction ($I_J = I_1$), and I_2 flows entirely through the large meander line L_S where the flux $\Phi = I_2 L_S$. Ignoring any mutual inductances other than between L_C and the flux transformer, the phase difference across the junction is then the same as the phase across L_S, given by

$$\varphi_J = 2\pi\Phi/\Phi_0 = 2\pi\left(\frac{L_S I_2}{\Phi_0}\right). \tag{3.17}$$

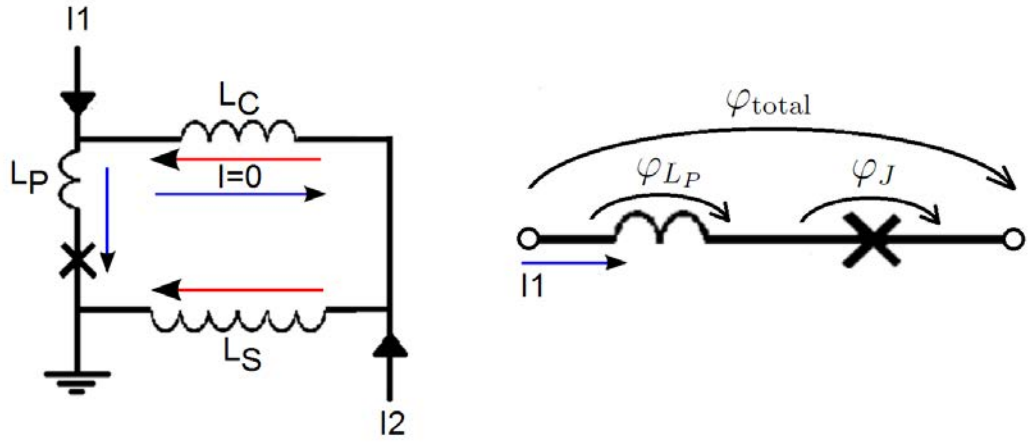

Figure 3.16: Waldram-Lumley method (left) for a direct measurement of the CPR of a Josephson junction with an additional inductance, L_P, in series with the junction. The Waldram-Lumley method measures the total phase difference across the Josephson junction *and* L_P (right). For details, see text.

For the device with planar geometry described here, there is an additional complication that arises from the value of inductance of the small piece of stripline that is in series with the Josephson junction. A more complete diagram of the Waldram-Lumley method as applied to the planar device is shown in Fig. 3.16 (left), which shows that I_1 now not only flows through the junction but also creates some flux in inductor L_P that opposes the flux created by the current flowing through L_S. The Waldram-Lumley method as described by the bullet points above will then give a measurement of the CPR not just across the junction, but across the *combination* of the junction and L_P, shown in Fig. 3.16 (right).

It is important to determine the influence of the value of L_P on the CPR. If a sinusoidal CPR is assumed, the total phase difference across the structure shown in Fig. 3.16 (right) can be written as

$$\varphi_{\text{total}} = \varphi_J + \varphi_{L_P} = \arcsin\frac{I}{I_C} + f\frac{I}{I_C} \tag{3.18}$$

where

$$f = \frac{L_P}{L_J}. \tag{3.19}$$

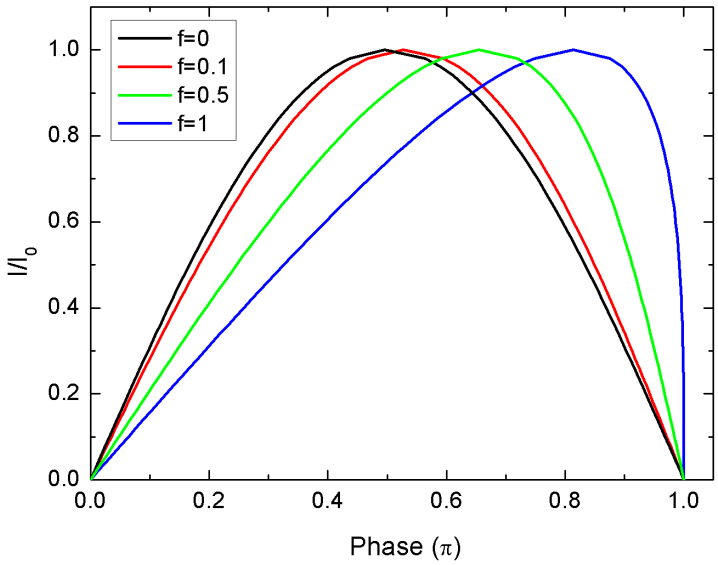

Figure 3.17: CPR for a series of values of f, as defined by equation (3.19).

Fig. 3.17 plots the CPR for a structure shown in Fig. 3.16 (right) as described by equation (3.18) for a range of values of f. As the ratio of inductances becomes larger, the CPR moves further away from the ideal case where $L_P = 0$. For the device described here, the value of L_P cannot be reduced[1] and it will be shown that the small current limit of the Josephson inductance, L_{J0}, is of a similar magnitude to L_P. The measurement device is intended for use with a Josephson junction with a small I_C (and hence large L_J) and therefore one could ignore the influence of L_P on the CPR. For the junction used for test purposes it will be shown that L_P cannot be ignored and therefore an adjustment to equation (3.17) has to be made. The phase difference across the junction as determined by the Waldram-Lumley method can now be written as

$$\varphi_J = 2\pi\Phi/\Phi_0 = 2\pi\left(\frac{L_S I_2 - L_P I_1}{\Phi_0}\right) \tag{3.20}$$

[1]IPHT design rules, available at `www.ipht-jena.de`.

where the flux produced by current flowing through the small piece of track in series with the Josephson junction is accounted for. The CPR is then gained by plotting I_1 (the current through the junction) as a function of the phase difference given by equation 3.20, where it is shown that values of I_2, L_S and L_P are needed. For this circuit design, there is no easy way to determine L_P so this was initially determined through fitting to the data and assuming a sinusoidal CPR. A method for determining the value of L_S will be given below.

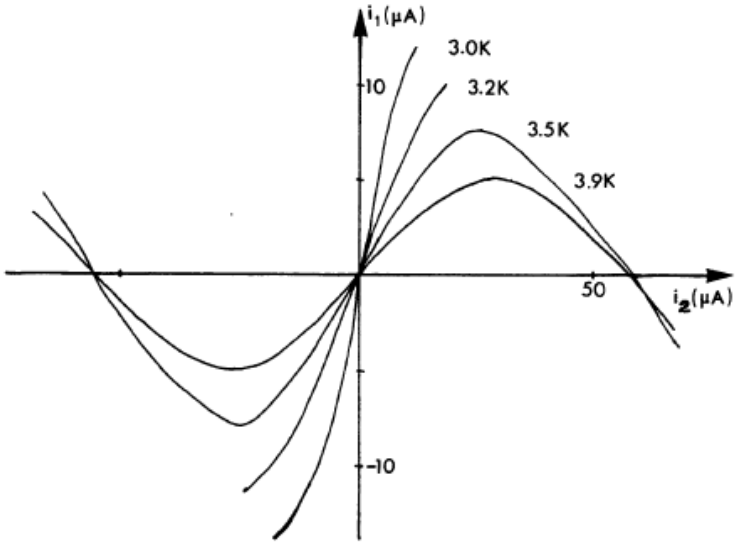

Figure 3.18: Experimental data for $T < 4.2$ K for the Waldram-Lumley device from Ref. [4]. For $T < 3.5$ K, it is impossible to view the whole CPR since $\beta_L > 1$.

In principle, many cycles of the CPR could be measured as it is a periodic function. As with the rf SQUID, however, there will be flux jumps in the measurement loop if $\beta_L > 1$ where β_L was discussed in section 3.1.3 and reproduced here:

$$\beta_L = \frac{2\pi L I_C}{\Phi_0}.$$

In the Waldram-Lumley device, the inductances were optimised such that $\beta_L < 1$. In that situation, the CPR may be observed continuously over many cycles since the circuit response is non-hysteretic. This is well illustrated by the data in Fig. 3.18 from Ref. [4] for temperatures that provided a value of I_C such that $\beta_L < 1$ (in this

case for $T \geq 3.5$ K). As will be shown by the experimental results in section 3.5, the device shown in Fig. 3.14 has $\beta_L \gg 1$ owing to the high-I_C SIS Josephson junction. Replacing the present junction with a Josephson junction with a lower I_C would allow the two circuits to become comparable in their operation.

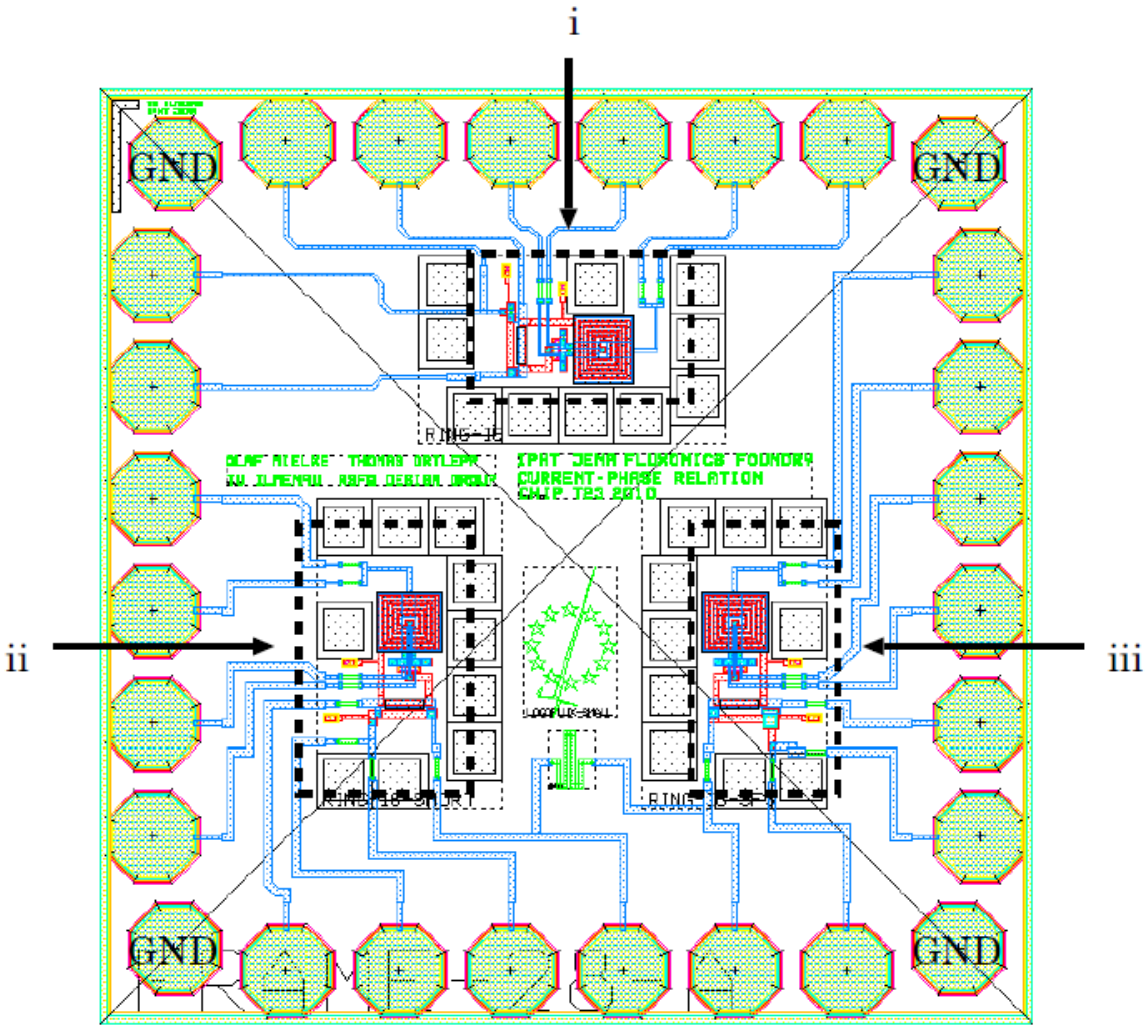

Figure 3.19: Full layout for the measurement chip. The measurement circuit is replicated three times with the following differences in the measurement loop: i) SIS Josephson junction ii) Short circuit iii) Window for SIFS Josephson junction deposition.

The measurement chip comprises three separate measurement circuits for calibration purposes, each having identical properties except for the measurement loop itself. The full chip layout is shown in Fig. 3.19. The first circuit contains an SIS Josephson

junction[2] ($J_C = 1$ kA/cm^2), the second has the junction removed to leave a short length of superconducting track in its place, and the third has the junction removed to leave a window creating an open circuit in its place. This window is useful in terms of circuit characterisation but is also the key to the versatility of this design; it could eventually contain an SIFS Josephson junction or indeed any kind of junction that can be successfully deposited in this space.

3.3 Circuit Characterisation

Equation (3.20) showed that the CPR measurement requires a detailed knowledge of the values of inductances L_S and L_P; methods for determining these circuit parameters will now be presented. Since the measurement circuit consists of a loop of superconducting material interrupted by a Josephson junction, the circuit has an rf SQUID configuration. The determination of circuit parameters can be explained in this context.

3.3.1 Determination of L_S

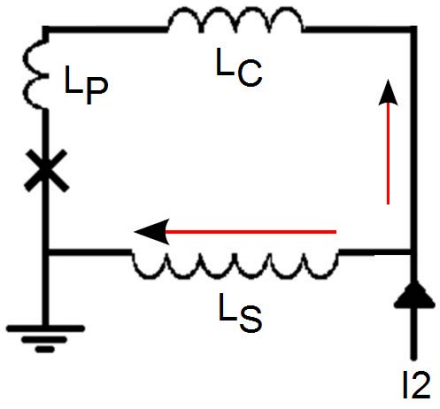

Figure 3.20: Measurement scheme for determining L_S using current I_2 only.

The method used to determine L_S is shown in Fig. 3.20 and involves the use of

[2]IPHT design rules, available at `www.ipht-jena.de`.

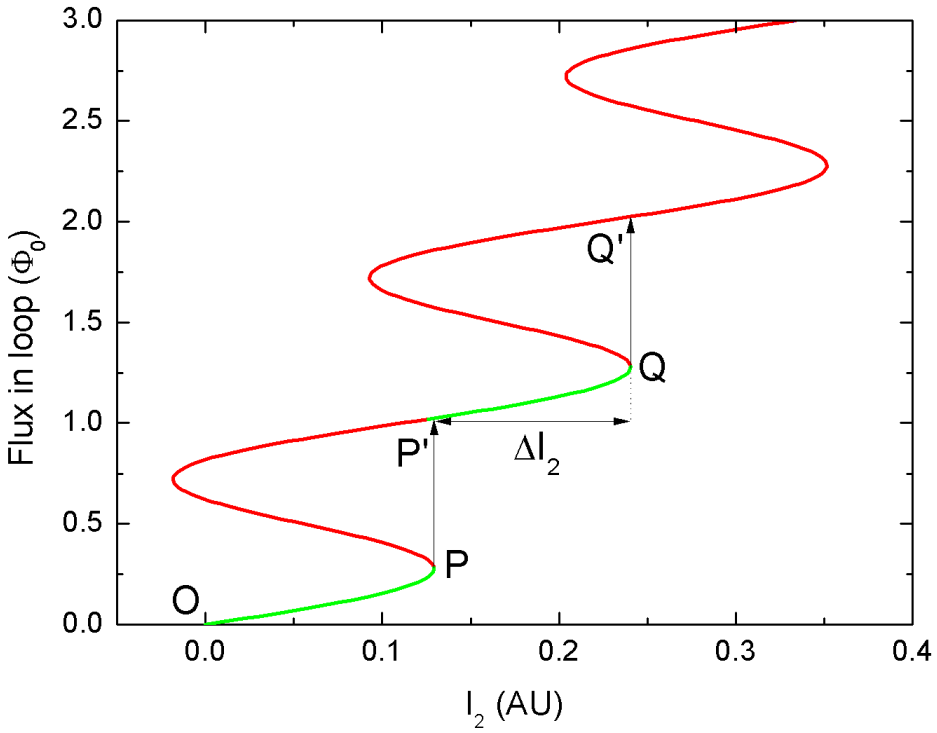

Figure 3.21: Flux in the measurement loop as a function of I_2 to illustrate the determination of L_S. The measurement begins at point O whereupon I_2 is increased along the green curve until a flux jump is observed at P. From P', I_2 is increased further along the green curve until a second flux jump is observed at Q. Since the state of the junction is identical for $P = Q$ and $P' = Q'$, the inductance L_S is given by $\Delta I_2 = \Phi_0/L_S$.

current source I_2 only. An applied I_2 will split between the two branches of the measurement loop to ground and, as with the rf SQUID, the total flux in the loop can be written as

$$\Phi = L_S I_2 - (L_S + L_P + L_C) I_C \sin\left(2\pi \frac{\Phi}{\Phi_0}\right) \tag{3.21}$$

where $L_S I_2$ now plays the role of the applied flux, Φ_{ext} (c.f. equation (3.11)). Therefore the flux inside the measurement loop can be plotted as a function of I_2, as shown in Fig. 3.21 for $\beta_L > 1$.

Using Fig. 3.21 as a reference, experimental determination of L_S begins at point O with current I_1 disconnected. Current I_2 is increased along the green portion of the curve to point P where a flux jump will occur to point P'. In practice, flux jumps are observed as small jumps in the dc SQUID voltage as it measures the current flowing through inductor L_C. I_2 is increased further until a second flux jump occurs from point Q to Q'. The graph shows behaviour that is repetitive in Φ_0 such that the state of the junction is identical for $P = Q$ and $P' = Q'$ (and any other equivalent points Φ_0 apart). The extra current in the measurement loop from I_2 must therefore flow through L_S only. With knowledge of ΔI_2 between two consecutive flux jumps, L_S can therefore be calculated as

$$\Delta I_2 = \frac{\Phi_0}{L_S}. \tag{3.22}$$

3.3.2 Determination of L_C

Equation (3.20) shows that knowledge of L_C is not important for the CPR measurement. It will be seen, however, that it is needed for other purposes. The determination of L_C is similar to the procedure described in detail for the determination of L_S. Here, current source I_1 is used with I_2 disconnected and the total flux in the

measurement loop can now be written as

$$\Phi = (L_S + L_C)I_1 - (L_S + L_P + L_C)I_C \sin\left(2\pi\frac{\Phi}{\Phi_0}\right) \tag{3.23}$$

where, by contrast, the applied flux is now given by $(L_S + L_C)I_1$. For this measurement I_1 is increased to observe two consecutive flux jumps such that

$$\Delta I_1 = \frac{\Phi_0}{(L_S + L_C)}. \tag{3.24}$$

From the previously determined value of L_S and knowledge of ΔI_1, the value of L_C can be deduced. By measuring the current required to cause an 'upward' and a 'downward' jump it is also possible to make an estimation of the critical current of the junction, I_C, and therefore deduce the value of β_L.

3.3.3 Estimation of L_P

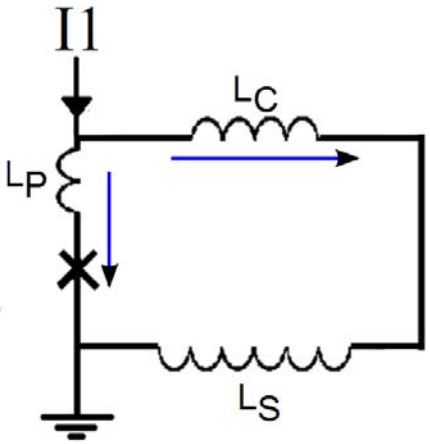

Figure 3.22: Measurement scheme for determining L_P using current I_1 only.

Fig. 3.22 shows that L_P is in series with the Josephson junction; in the absence of any other connections to the circuit, L_P cannot be measured directly. An estimate of L_P can be made through fitting a theoretical expression to experimental measurements

of $I_1(I_2)$, however, an estimate of L_P can be made in an alternative manner as described here.

With I_2 disconnected, the applied current I_1 splits between the two branches of the measurement loop in inverse proportion to the value of inductance in each branch. The fraction of I_1 that flows to the right (through L_C) is given by

$$\frac{\Delta I_{L_C}}{\Delta I_1} = \frac{(L_P + L_J)}{(L_S + L_C) + (L_P + L_J)}. \tag{3.25}$$

To estimate $(L_P + L_J)$, a method of determining $\Delta I_{L_C}/\Delta I_1$ is therefore required.

For points P' and Q' in Fig. 3.21, the state of the junction is identical, i.e. the same amount of current, I_J, flows through the junction. Since P' and Q' are identical in terms of the junction, ΔI_1 between these points must flow entirely through L_C and therefore can be measured via the dc SQUID. The total current I_1 sent to the measurement circuit is known directly and the role of current I_3 is to apply flux to the dc SQUID. Therefore, to determine the *fraction* of I_1 that flows through L_C, a calibration in terms of I_3 can be made by measuring ΔI_3 required to restore the dc SQUID voltage from $V_{SQ}(Q')$ to $V_{SQ}(P')$ following a flux jump caused by I_1, i.e.

$$\frac{\Delta I_3}{\Delta I_1} = \frac{\Delta I_3}{\Delta I_{L_C}}. \tag{3.26}$$

Earlier discussion showed that although a Josephson junction has a highly nonlinear inductance, for $I \ll I_C$ it has an approximately constant value of inductance, L_{J0} (see Fig. 3.3). Therefore, for small values of current, each branch of the measurement loop can be considered as being made of simple linear inductances. If the amount of current that passes into branch $(L_C + L_S)$ can be determined for small values of I_1 then, through subtraction, $(L_P + L_J)$ can also be determined. To do this, a measurement of $I_3(I_1)$ can be made in a similar manner to a CPR measurement, shown schematically in Fig. 3.23 where the goal is to measure between points R and

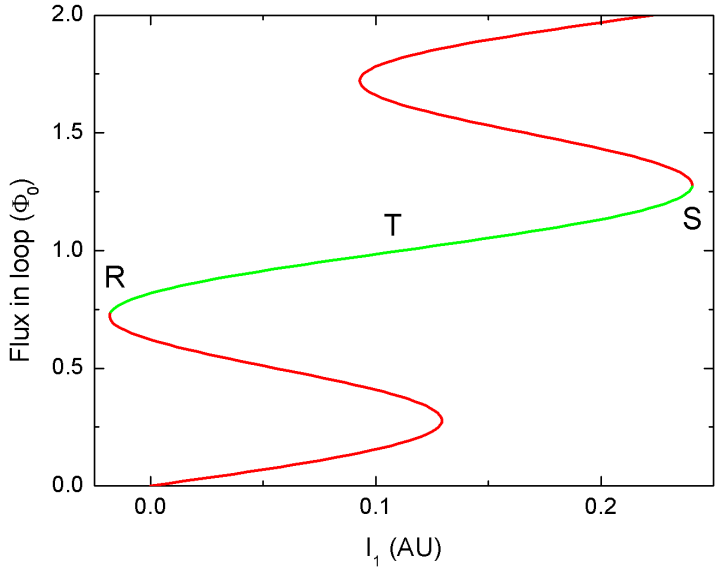

Figure 3.23: Flux in the measurement loop as a function of I_1 to illustrate the determination of L_P. A measurement of $I_3(I_1)$ is made between points R and S. A linear fit to the data around T gives $\Delta I_3/\Delta I_1$ which, together with equation 3.26, provides a method of determining $(L_P + L_J)$.

S.

Around point T is the region of small current flow through the junction and therefore the data serve two purposes. Firstly, such a measurement would confirm the linearity of the response to small I_J and secondly, by performing a linear fit to the data around T, a measurement of $\Delta I_3/\Delta I_1$ for small I_J is gained. With the results of these two experiments, the fraction of I_1 flowing through inductor L_C can be found by

$$\frac{\Delta I_{L_C}}{\Delta I_1} = \frac{\Delta I_{L_C}}{\Delta I_3} \cdot \frac{\Delta I_3}{\Delta I_1} = \frac{(L_P + L_J)}{(L_S + L_C) + (L_P + L_J)}. \tag{3.27}$$

3.4 Experimental Method

The sample box

The CPR measurement chip was mounted onto a custom made chip carrier using OptiClean lens cleaner as a glue. The chip carrier alone is shown in Fig. 3.24 (left) where small copper tracks were defined on flexible PCB and bonded to a larger piece of copper using Stycast. Aluminium wirebonds were made between the chip bonding pads and copper tracks on the chip carrier which lead to a 0.1″ socket strip. The entire chip carrier was then carefully secured inside a brass sample box, as shown in Fig. 3.24 (right) with the lid removed. A stripped down ten-pin LEMO connector with labelled flying leads with plugs at the end was built into the wall of the sample box inside the box; the plugs were then connected to the relevant sockets on the chip carrier before fitting the lid on the box.

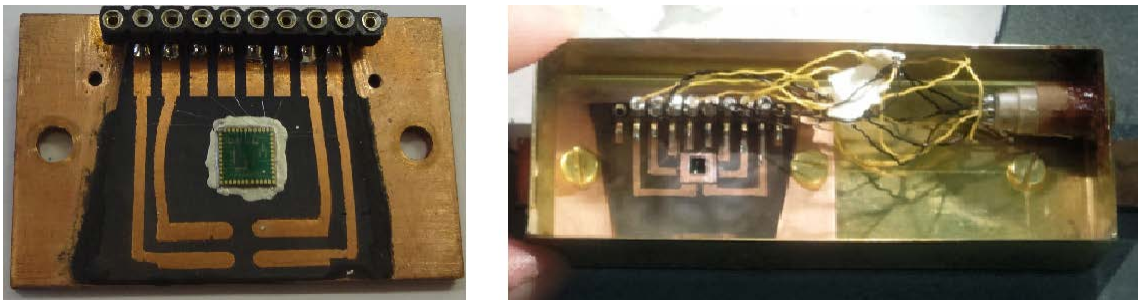

Figure 3.24: The chip carrier (left) and a prepared CPR measurement chip inside the sample box where the lid is not shown (right).

The sample box was screwed onto a copper bar which was tightly attached to the ^{3}He pot of a Oxford Instruments Heliox system. The lower end of the cryostat wiring was soldered to a corresponding stripped LEMO plug which was connected to the sample box socket and the cryostat wiring was checked for continuity before cooling. Finally, the Inner Vacuum Chamber (IVC) of the cryostat was fitted and evacuated to a pressure of no greater that 1×10^{-3} mbar (typically much lower). In an attempt to reduce interference from external electromagnetic signals, the IVC was also fitted with a superconducting lead shield. The cryostat wiring passed upwards to a 24-pin

Fischer connector.

Cooling Apparatus

The chip must be cooled to $T < T_C$ to characterise the measurement circuit and to observe the CPR. To do this, an Oxford Instruments Heliox ^{3}He system[3] was used with a base temperature of ∼250 mK. There are two phases to reaching this low temperature. Firstly, ^{3}He gas is released from the ^{3}He sorption pump (sorb) and allowed to condense in the region of a 1 K plate (achieved by pumping on a small amount of ^{4}He taken from the bath via a needle valve). The liquid ^{3}He then runs down into the ^{3}He pot. Following this, the sorb is used to reduce the pressure above the liquid in the pot which allows cooling to the base temperature.

In practice, most experiments were actually conducted at a temperature of 4.2 K due to the high I_C of the SIS Josephson junction. To achieve this, the IVC was simply filled with helium exchange gas after evacuation and lowered into the liquid ^{4}He bath. This allowed for a very stable temperature with which to perform all circuit characterisation measurements. The thermometer used to determine the sample temperature was a ruthenium oxide sensor mounted directly onto the ^{3}He pot. The sample housing bolted directly onto the ^{3}He pot using a copper rod; since all measurements were typically made at 4.2 K there was no concern about thermal lags in the system and the sample was assumed to be at the same temperature as the ^{3}He pot.

Room Temperature Readout System

Characterisation and CPR measurements were made as described in sections 3.2.1 and 3.3. The schematic diagram of the circuit in Fig. 3.14 (right) shows that multiple current sources were needed, each with a separate readout. A block diagram of the

[3]Oxford Instruments Heliox VL, `www.oxford-instruments.com`.

entire readout system is shown in Fig. 3.25.

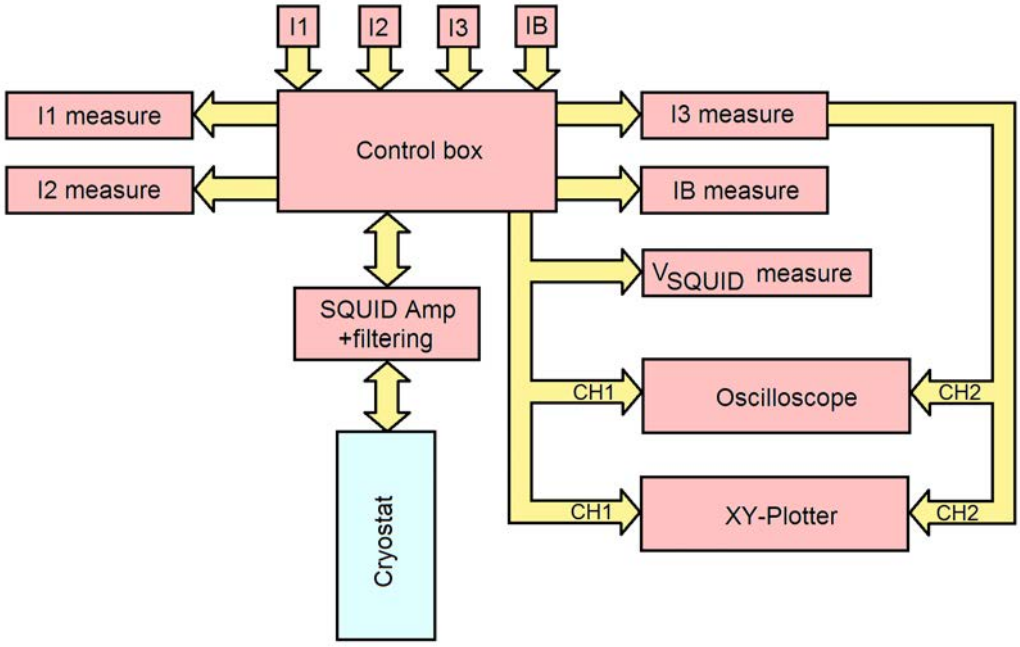

Figure 3.25: Block diagram of the room temperature readout system. For details, see text.

Broadly, the control box contains four current sources: two for the measurement loop (I_1 and I_2) and two for the dc SQUID used to detect current flowing through L_C (I_B and I_3). To avoid earth loops, each current source had a separate battery power supply and was monitored using a battery operated multimeter (labelled as 'I_x measure', where x is the current supply in question). The currents passed to the chip were arranged into balanced twisted pairs and passed through partitioned filters within the dc SQUID amplifier box. To make measurements of the current flowing from inductor L_C, the dc SQUID voltage was amplified and monitored using an oscilloscope. The dc SQUID was first brought to an optimal point of operation by initialising I_B. The same signal was also sent to an xy-plotter to provide a mechanical readout. The advantage of this readout scheme was that flux jumps within the cryogenic measurement loop were immediately obvious and could otherwise have been easily missed if only using the oscilloscope trace. By watching the xy-plotter pen, the dc SQUID voltage was easily initialised and returned to a set point by application of I_1 and I_2 during a CPR measurement.

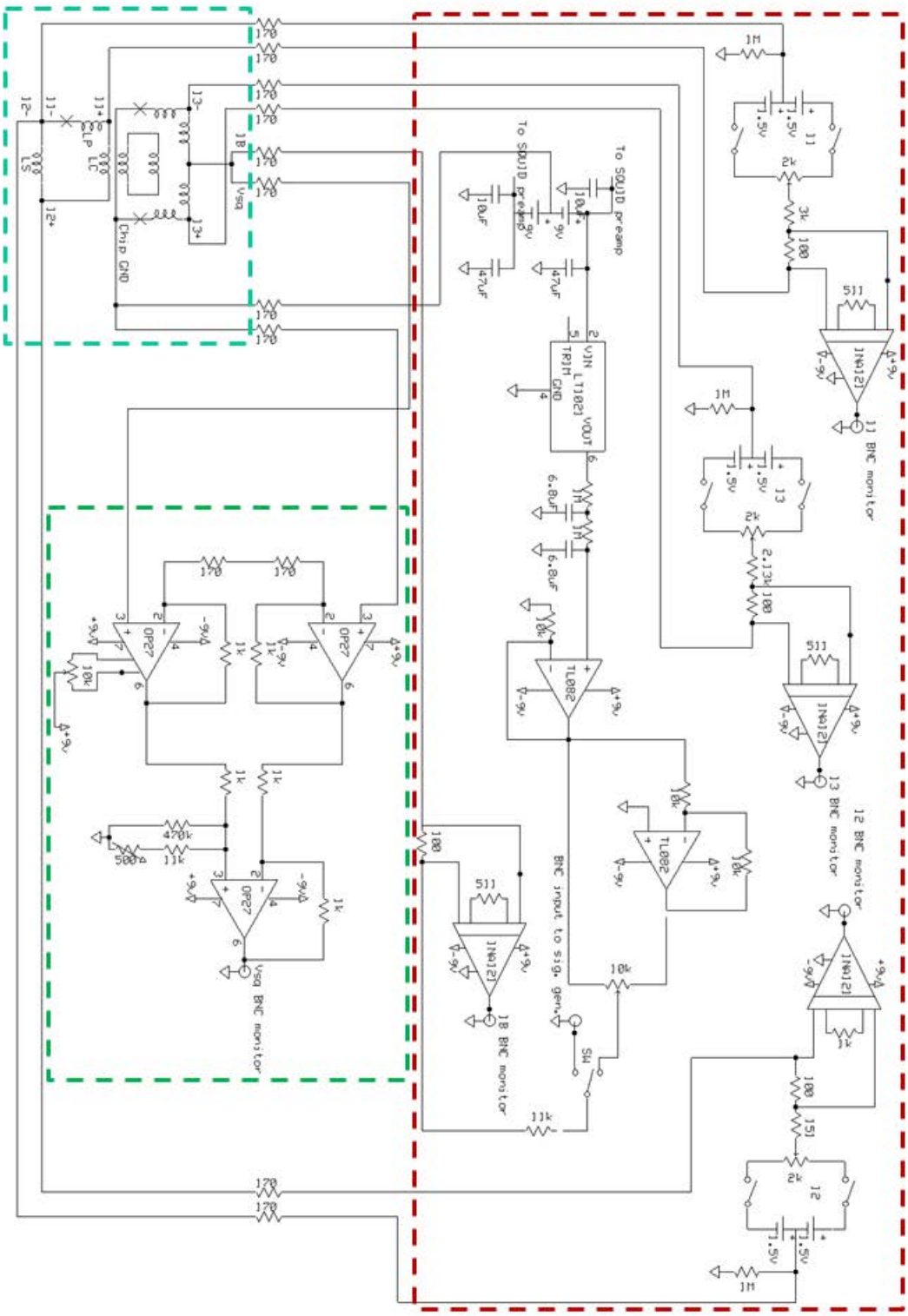

Figure 3.26: Room temperature electronics inside the control box (red) and dc SQUID amplifier box (green) as shown in Fig. 3.25. Diagram also includes a schematic representation of the low temperature chip (blue). For details, see text.

The custom electronics that were kept inside diecast 'control' and 'dc SQUID amplifier' boxes are shown in Fig. 3.26. The diagram also includes a schematic representation of the low temperature chip to fully illustrate which pairs of wires were twisted inside the cryostat (wire resistance shown as 170 Ω) and the complete path taken by each signal (Josephson junctions are represented by a cross). Each twisted pair was balanced (e.g. I_1+/I_1-) to minimise the effect of external electromagnetic interference on the measurements. A regulated, filtered ±9 V battery supply was used to power the electronics and the dc SQUID bias current, I_B. Efforts were made to ensure that each current source was well isolated; I_1, I_2 and I_3 each had a separate ±5 V battery power supply. Each current was set manually via a potentiometer (or an alternative BNC input from a signal generator) which lead to a current-limiting resistor and further filtering (not shown) before entering the cryostat. To measure each applied current, differential amplifiers measured the potential difference across 100 Ω resistors and readout to a separate battery-operated multimeter.

The dc SQUID on the measurement chip was used to sense the magnetic field associated with the current flowing through inductor L_C. The dc SQUID voltage, V_{SQ}, was measured across the device by a three op-amp differential amplifier with a gain of ∼1000. This part of the electronics resided in a separate diecast box that plugged directly into a 24-pin Fischer connector on top of the cryostat. The inside of this box was partitioned and each signal was passed through a 1000 pF feedthrough capacitor (not shown in the schematic wiring diagram). From this box, the signals were passed through shielded twisted pairs via D-connectors into the control box, as described above.

3.5 Experimentally Determined Circuit Parameters

The CPR measurement chip shown in Fig. 3.14 (left) was the first of two generations and had an experimentally determined value of $\beta_L \approx 88$. Due to the large value of β_L, a second chip was designed where the meander line providing inductance

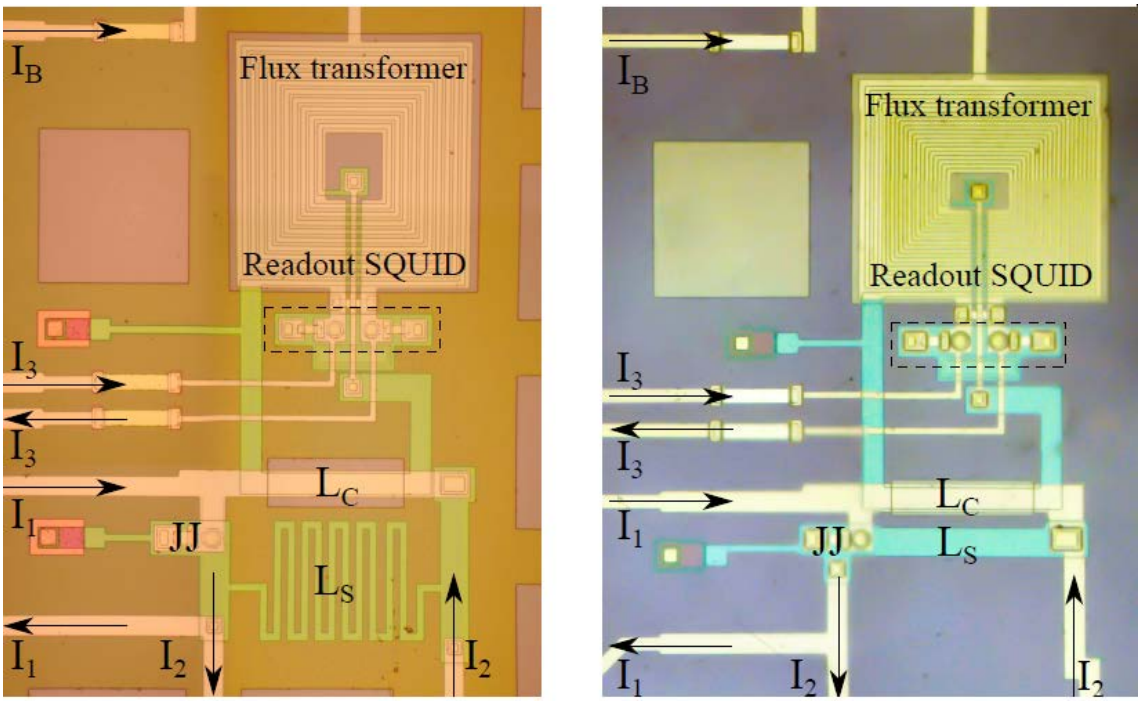

Figure 3.27: Left: Chip #1 – first design of the CPR measurement circuit with a large meander line for inductor L_S. Right: Chip #2 – second design of the measurement circuit where the value of L_S is reduced.

L_S was greatly reduced, as shown in Fig. 3.27 (right). As such, the experimental results presented here will focus on the measurements made on chip #2. It should be emphasised again that this circuit was designed to be compatible with a low-I_C Josephson junction and as such suffers from some problems as a result of the high-I_C junction already in the loop. These problems will be discussed further in section 3.6.

3.5.1 Circuit Parameters

Table 3.1 provides the circuit parameters as determined for chip #2 following the methods described in section 3.3. A more detailed discussion will be presented regarding the determination of L_P that is in series with the Josephson junction in the measurement loop.

Table 3.1: Circuit parameters determined for chip #2 using the methods described in section 3.3 at $T = 4.24$ K.

Circuit Parameter	Measured Value
I_C	109.21±0.51 μA
L_{J0}	3.04±0.01 pH
L_C	33.52±0.65 pH
L_S	3.29±0.01 pH
L_P	1.42±0.02 pH
β_L	12.60±0.23

3.5.2 Determination of L_P

As noted in section 3.3.3, there is no direct way to measure the value of L_P and yet it is an important parameter that can have a significant influence on the measured CPR. A method of experimental determination was provided to estimate $(L_P + L_J)$; through knowledge of I_C and assuming a sinusoidal CPR, L_J and hence L_P can be deduced. The results of experiments to determine L_P will now be given. Following that, an indirect method of determination will be presented where a theoretical model is fitted to an experimental measurement of $I_1(I_2)$.

Determination through Fitting: Fixed L_P

By following the method detailed in section 3.3.3, it was found that $\Delta I_3/\Delta I_{L_C} = 0.075\pm0.001$. Following the second step of this method, a measurement of $I_3(I_1)$ gave the result shown in Fig. 3.28. There are two pieces of information to take from this graph. Firstly, for small values of I_1, the junction behaviour is linear and therefore the Josephson junction can be treated as a fixed value inductor over this range. Deviation from linear behaviour occurs toward the end of the working I_1 range as the Josephson inductance diverges as per equation (3.6). Secondly, a linear fit across the linear region of the graph provides a measure of $\Delta I_3/\Delta I_1 = 0.013 \pm (1 \times 10^{-4})$.

The measured values of $\Delta I_3/\Delta I_{L_C}$ and $\Delta I_3/\Delta I_1$ allow an experimental determination of L_P using equation (3.27). The result of this analysis gives $L_P = 4.50 \pm$

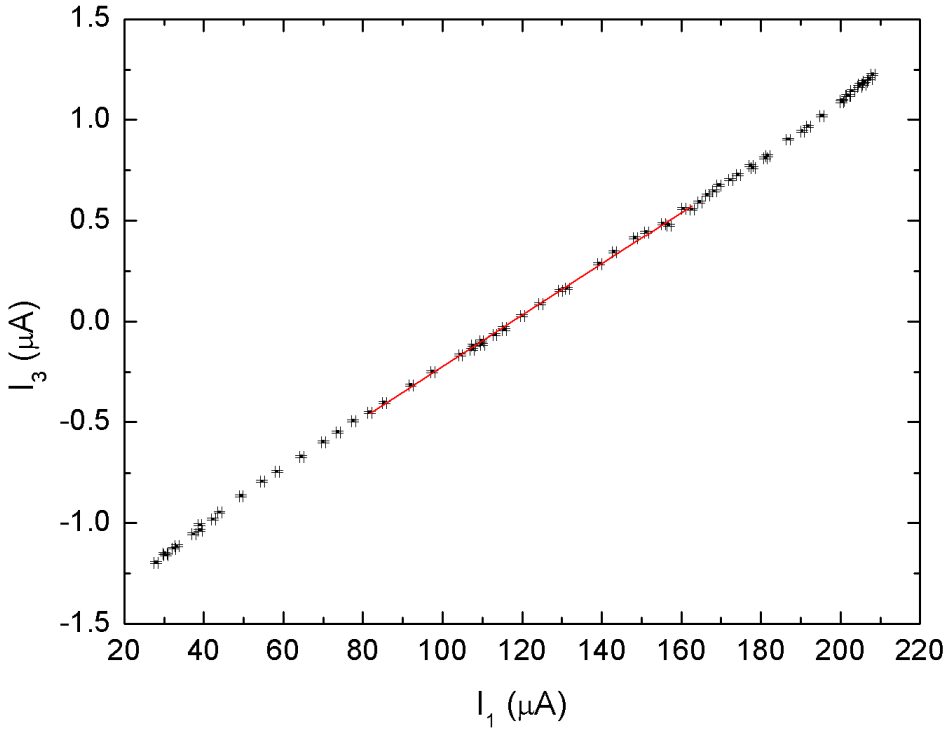

Figure 3.28: $I_3(I_1)$ measured on chip #2 at $T = 4.2$ K where the symbol size represents the error. A linear fit to the data is given by the red line.

0.28 pH. To check the validity of this result, this value of L_P was used to fit equation (3.29) to a measurement of $I_1(I_2)$ (further details given below). The result is shown below in Fig. 3.29 where this value does not provide a good fit to the data when all variables are fixed to experimentally determined values.

Determination through Fitting: Variable L_P

The result presented above followed a direct experimental method of determining L_P, but an estimate of can also be made by treating L_P as a variable parameter during a fitting process. The Waldram-Lumley method for direct CPR measurement involves balancing a measurement circuit using two currents labelled I_1 and I_2. To reiterate, when no current flows through inductor L_C, I_1 flows entirely through the Josephson junction such that $I_1 = I_J$. By assuming a sinusoidal CPR, from the dc Josephson equation and the phase across the junction (given by equation (3.20)), I_1

can be written in terms of I_2 as

$$I_1 = I_C \sin\left(\frac{2\pi}{\Phi_0}\left(L_S I_2 - L_P I_1\right)\right). \tag{3.28}$$

Rearranging for I_2 in terms of I_1 gives

$$\left(\frac{I_2}{I_C}\right) = \left(\frac{L_P}{L_S}\right)\left(\frac{I_1}{I_C}\right) + \left(\frac{\Phi_0}{2\pi I_C L_S}\right)\arcsin\left(\frac{I_1}{I_C}\right). \tag{3.29}$$

By using the experimentally measured values of L_S, and plotting the balancing currents normalised by I_C, an estimate of L_P can be made.

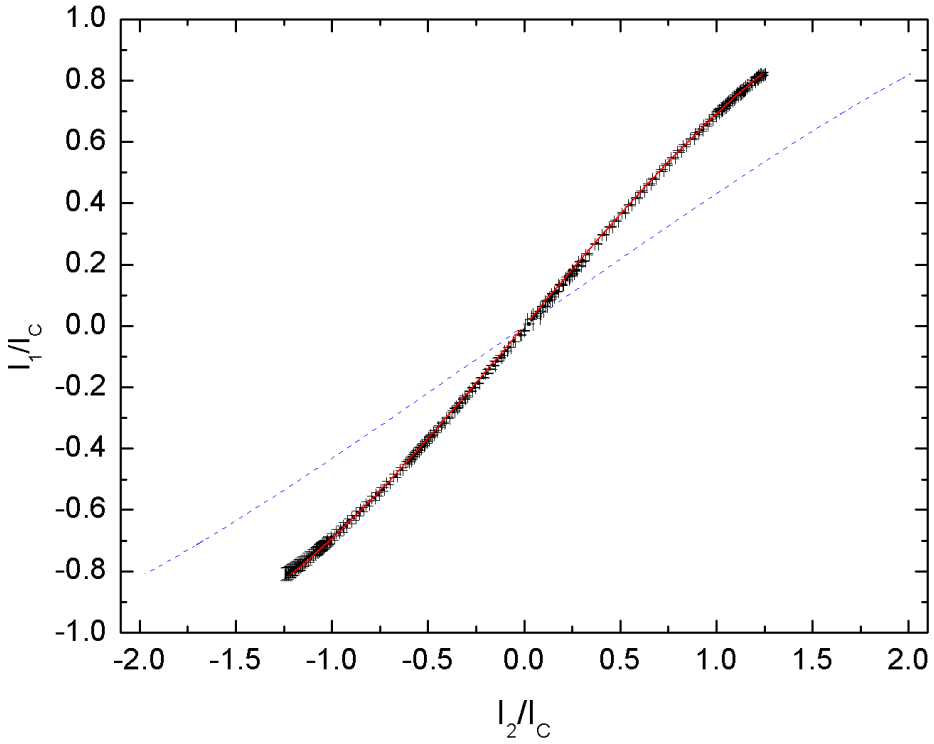

Figure 3.29: $I_1(I_2)$ (normalised to I_C of the junction in the measurement loop) for $T = 4.24$ K with a theoretical fits to the data. The red line is a fit where L_P was used as the only fitting parameter. The blue line is a fit where all parameters are fixed to experimentally determined values.

Fig. 3.29 plots $I_1(I_2)$ where each current is normalised by the critical current of the Josephson junction ($I_C = 109.21 \pm 0.51$ μA at $T = 4.24$ K). The red line is a fit to

the data using equation (3.29) where the result of using L_P as a fitting parameter gives $L_P = 1.42 \pm 0.02$ pH. By comparison, the blue line plots equation (3.29) where all parameters were fixed to those determined experimentally. Clearly there is a large discrepancy in the values of L_P as determined by experimental deduction and by fitting equation (3.29) to $I_1(I_2)$. An investigation of the possible origins of this discrepancy was conducted where the results will be presented in section 3.6

3.5.3 The Current-Phase Relationship Measurement

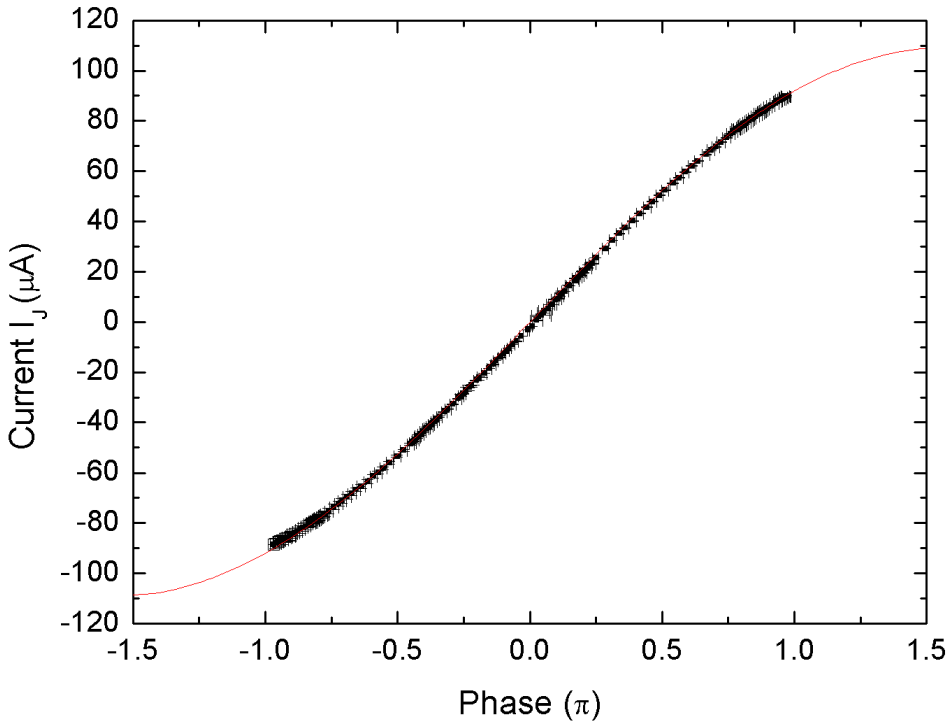

Figure 3.30: The CPR measured for the SIS Josephson junction on chip #2 at $T = 4.26$ K. The red line is the CPR expected for a sinusoidal dc Josephson relationship.

To complete the characterisation of chip #2, a typical CPR measurement is shown in Fig. 3.30. The red line is the CPR calculated using equation (3.28) where the values of L_S and L_P are given in table 3.1. Since $\beta_L \gg 1$, the whole CPR is not accessible. It is noted that $2I_C$ measured with a single current source results in $I_C = 109.21 \pm 0.51$ μA; while the values of inductance used provide a good fit to the experimentally measured CPR, only 85% of I_C is reached in either direction before

a flux jump in the loop occurs. Similar behaviour is observed in the measurement of $I_3(I_1)$ shown in Fig. 3.28, which also uses two current sources to conduct the experiment. There are two obvious possible reasons why it was not possible to reach the previously observed value of I_C: the effects of temperature and of electromagnetic interference. Since these two factors are present for every measurement, they can be eliminated as the sole cause. The reduction of the observed I_C for experiments involving two current sources, together with the discrepancies in the estimated value of L_P, indicate significant issues with the present circuit design.

3.6 Circuit Design Problems

Large Josephson junction I_C

It was noted in section 3.2.1 that unless $L_P \ll L_J$, the influence of L_P can cause a significant distortion of the measured CPR. Two indirect methods of measuring L_P were presented and it was found that each method gave a different value of L_P outside of experimental error. The value of f is in the range $0.47 - 1.33$ which, from Fig. 3.17, causes a considerable distortion of the measured CPR. Without a good knowledge of L_P, it is impossible to remove its influence and measure small deviations away from an ideal sinusoidal CPR.

It should be stressed that this CPR measurement circuit was designed to measure the CPR of a low-I_C Josephson junction with an intended I_C of $\sim$1% of the SIS junction used to test and characterise the circuit. A low-I_C junction would have a value of L_{J0} ($L_J \gg L_P$) such that the influence of L_P on the CPR would be negligible and the whole CPR would be accessible. The collaborators for this project, whose job it was to incorporate a low-I_C junction into the measurement loop, reported technical difficulties such that this was not achieved. As will be discussed below, however, there are more serious problems with this circuit design.

Mutual Inductances

For the circuit analysis presented in section 3.2, it was stated that on-chip mutual inductances other than between L_C and the dc SQUID were ignored. Simulations performed by the Ilmenau group showed that, since the majority of the measurement circuit is fabricated on a superconducting ground plane, any parasitic on-chip mutual inductances would be negligibly small[4]. The inconsistencies observed in the measurement of L_P and I_C prompted suspicions to the contrary, as it is implied that there is a direct coupling of fields created by current flowing in nearby wires into the measurement loop, possibly via flux coupled directly into the flux transformer.

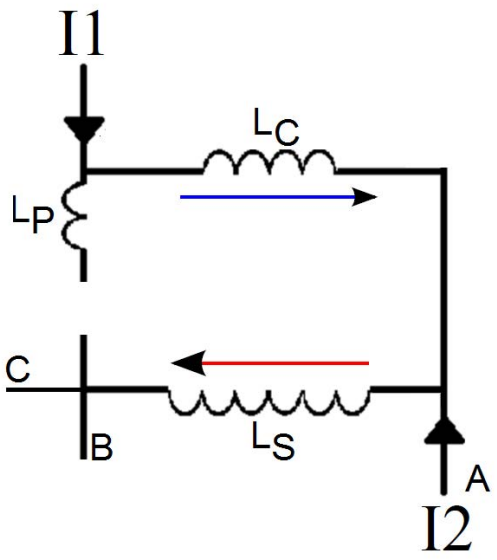

Figure 3.31: Schematic diagram of the CPR measurement circuit used to investigate parasitic mutual inductances. The Josephson junction is absent to prevent current flow in the left hand side of the circuit.

Circuit (*iii*) on chip #2 was used (see Fig. 3.19) to investigate parasitic mutual inductances. Circuit (*iii*) is identical to circuit (*i*) except that the Josephson junction is absent from the measurement loop to leave a 'window' (an open circuit), shown schematically in Fig. 3.31. The primary purpose of this circuit was to enable deposition of a low-I_C SIFS Josephson junction into the measurement loop but it also served as a useful diagnostic tool. For this circuit, current I_1 can only pass through

[4]Mielke, O. and Ortlepp, T. – private communication.

inductor L_C to ground and inductor L_P should have no influence on the results. Since there is no path for current I_2 to take through L_C, the application of I_2 should not result in a change in the dc SQUID voltage, V_{SQ}.

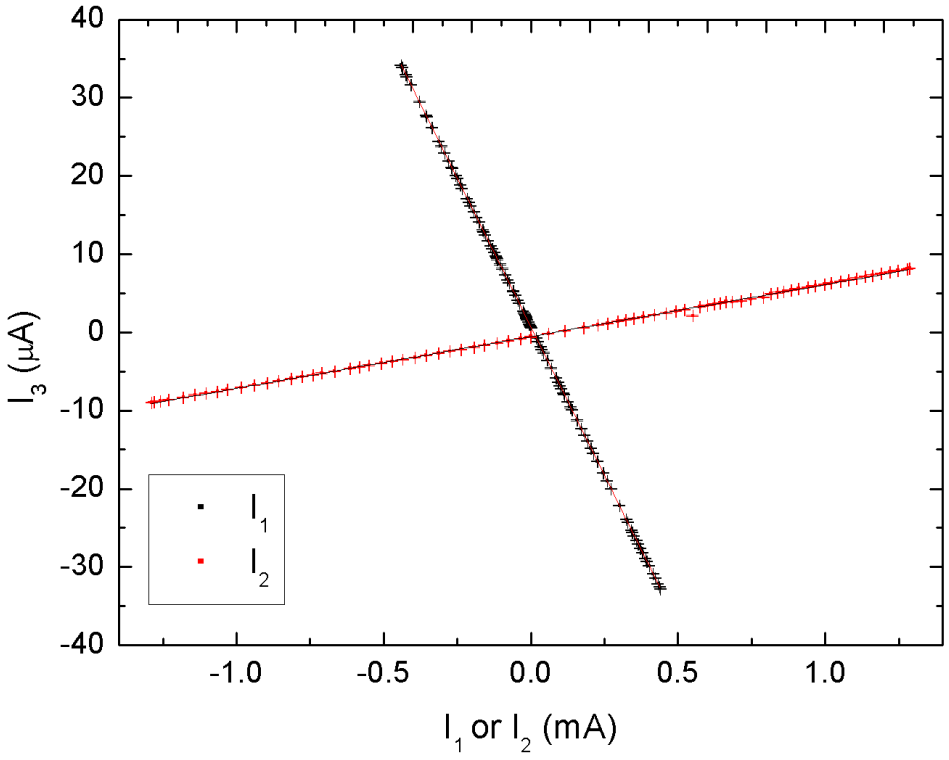

Figure 3.32: I_3 measured as a function of I_1 and I_2 for the CPR measurement circuit where the Josephson junction was removed (shown in Fig. 3.31).

In practice, a significant change in V_{SQ} was observed as a result of I_2 flow through inductor L_S. Fig. 3.32 shows $I_1(I_3)$ and $I_2(I_3)$ measured for the circuit where the Josephson junction was absent, as shown in Fig. 3.31. The role of I_3 is to apply flux directly to the dc SQUID. Fig. 3.32 shows that the amount of I_3 required to restore V_{SQ} following a change in I_1 is larger for this circuit; this is to be expected since there is now no current path other than through L_C ($I_1 = I_{L_C}$). Also shown is that, despite the superconducting ground plane, there is a significant change in V_{SQ} in response to current I_2 flowing through inductor L_S only. Extensive testing of the electronics shown in Fig. 3.26 gave no reason to believe this to be the source of the problem. Extreme care was also taken throughout the experimental setup to reduce electromagnetic interference, however, at the level of the low temperature

wirebonds this was impossible (i.e. although the wires that interfaced with the CPR measurement chip from room temperature were carefully arranged into twisted pairs, it is impossible to twist wirebonds together and as such there is an area enclosed by current-carrying wires close to the chip). Since there is no current path for I_2 other than through L_S only, it is deduced that there is either an on-chip mutual inductance between L_S and L_C, or that magnetic field created by the flow of I_2 through the nearby wirebonds is sensed by the dc SQUID.

To investigate the cause of the anomalous V_{SQ} response, a set of experiments were conducted such that I_2 was passed in various paths both on- and off-chip of progressively greater physical distances away from the measurement circuit. It is again noted that there must be current-carrying wires attached to the chip to make a CPR measurement and there is inevitably a significant enclosed area close the chip. The schematic diagram of the circuit with the junction removed was shown in Fig. 3.31 where different points in the circuit were labeled A, B, and C. Fig. 3.33 illustrates four different experiments that were conducted; (i) passed current around the loop $A \rightarrow B$ directly through L_S, (ii) passed current in an on-chip loop around $B \rightarrow C$, (iii) shows that the two wirebonds were connected to the same bonding pad such that no current would flow through the measurement circuit, and (iv) shows that the wirebonds were connected to a point off-chip. Current I_2 was used for this series of experiments though what is true of I_2 will presumably also be true for all other current sources including I_1 and I_3.

The results of this series of experiments are shown in Fig. 3.34. It was found that the response of V_{SQ} to the current I_2 was present but reduced as the wirebonds were moved physically further away from the measurement circuit and the current passed around progressively smaller loops. The implication of these data is that, although there may indeed be some parasitic mutual inductance between L_S and L_C, there is direct pickup of the magnetic field created by current flow in nearby wires both on-*and* off-chip, and it can be concluded that the dc SQUID is insufficiently shielded. Clearly this is a significant problem in terms of the Waldram-Lumley method of

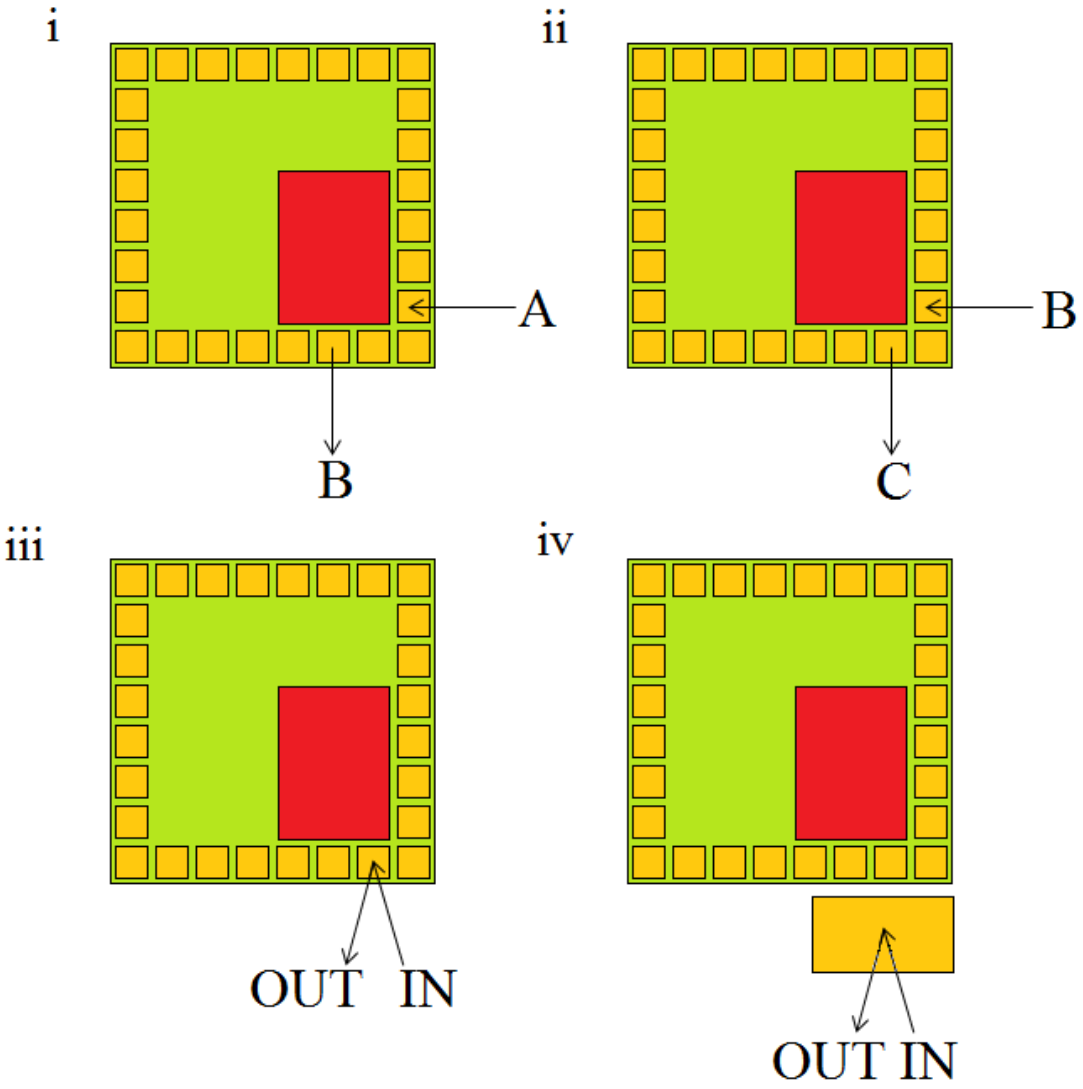

Figure 3.33: Diagram to show the placement of wirebonds (black arrows) to create current paths of a varying distance from the measurement circuit (red) – see Fig. 3.32 for a closer picture of paths $A \rightarrow B$ and $B \rightarrow C$. The wirebond pads are shown by the yellow blocks and the isolated block in (iv) represents a copper track on the sample holder.

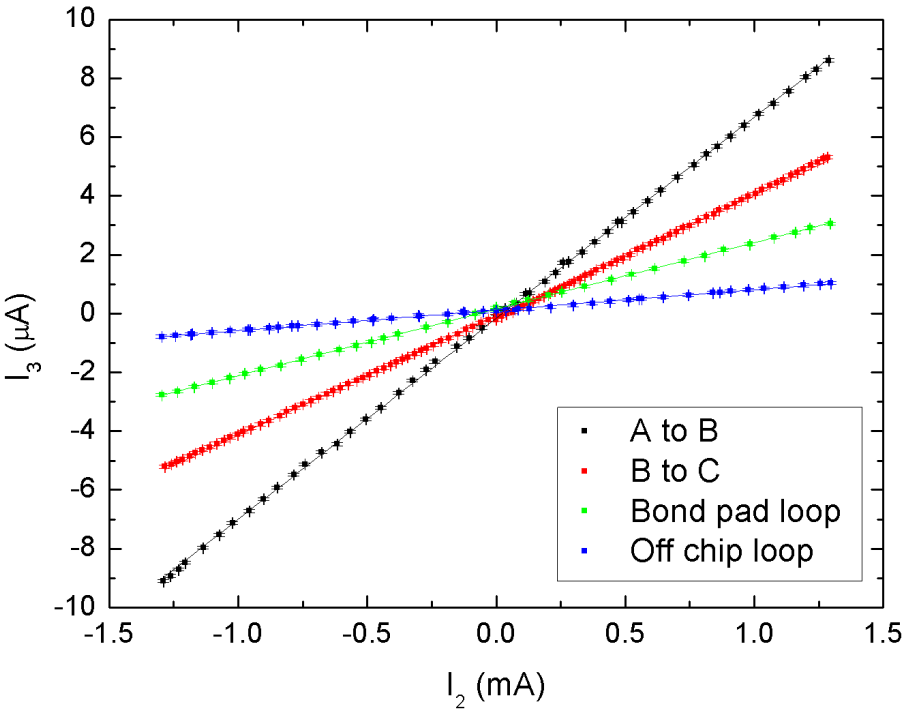

Figure 3.34: Current I_3 required to maintain the dc SQUID voltage in response to current I_2 passed in loops as they are moved further away from the measurement circuit. See Fig. 3.32 and 3.33 as a reference for points on the circuit labeled A, B and C.

measuring the CPR as it relies on accurately sensing the point at which zero current passes through L_C.

A further experiment was conducted which attempted to reduce the amount of pickup from nearby current-carrying wires by fitting a superconducting shield directly over the measurement circuit, but this did little to reduce the magnitude of the dc SQUID response. This result may indicate another problem with the planar geometry used here; a current that flows through a stripline will induce a return current in the superconducting groundplane that it resides upon. The return current must take a circular path that could enclose parts of the measurement circuit including the flux transformer. Without thorough modelling of the structure, however, it is difficult to say if this is the case. Through the observation of a significant dc SQUID response to nearby current flow and on-chip parasitic mutual inductances, it was concluded that this particular circuit design could not be used to measure the CPR using the method first employed by Waldram and Lumley, or indeed by any other sequence of measurements.

3.7 Conclusions

Early discussion showed that there exist Josephson junction structures that can have a preferential phase difference of π across the junction in the ground state or exhibit deviations away from a sinusoidal CPR. Both of these properties can be investigated through an experimental observation of the CPR. A device that measures the CPR directly under static conditions using a planar geometry was shown in Fig. 3.27 (right). This chapter documented the work that was undertaken to characterise the measurement circuit with the results summarised below:

- The CPR measurement device was designed by Dr E. Tarte of the University of Birmingham and Dr T. Ortlepp of Ilmenau University of Technology. The chips were made at the Institute of Photonic Technology by Dr J. Kunert.

- A means of interfacing with the measurement device was designed and built. The room temperature electronics consisted of separate current sources each with a floating readout.

- The principle of CPR measurement required a good knowledge of the values of on-chip inductances, particularly for the case of a high-I_C Josephson junction. A detailed method for the determination of important circuit parameters was developed and the result of measurement was summarised in table 3.1. Despite the superconducting ground plane, inconsistencies were found in the estimation of L_P which was in series with the Josephson junction.

- The high value of I_C for the Josephson junction used for test purposes limited the accessible CPR. Furthermore, it was observed that measurements involving two current sources caused flux jumps in the measurement loop at 85% of the I_C determined by a single current source.

- The inconsistency in circuit parameter estimation and the reduction in accessible CPR prompted an investigation of circuit characteristics using a measurement circuit which had the Josephson junction removed. Direct evidence of a mutual inductance between off-chip currents and the dc SQUID was found.

The results presented in this chapter show that there are significant issues that would need to be resolved before a reliable CPR measurement can be made with this circuit design, particularly if small deviations away from a sinusoidal CPR are to be measured. As stated, the circuit was designed for use with an SIFS junction with $I_C \approx 1$ μA. This would reduce the value of $\beta_L < 1$ and mean that the influence of L_P on the CPR would be negligibly small. Unfortunately, our collaborators reported difficulties in the fabrication of SIFS junctions into the small on-chip window intended for this exact purpose such that appropriate samples were not produced.

The more serious problem was a measurable change of V_{SQ} in response to a current flowing through L_S and to off-chip current flow through nearby wirebonds as mea-

sured with a CPR measurement circuit without a Josephson junction. The causes of this are on-chip mutual inductances and/or an improperly shielded dc SQUID. The result of off-chip signal pickup and parasitic mutual inductances is to introduce uncertainty in determining the point at which $I_{L_C} = 0$, which is crucial to the Waldram-Lumley method. Furthermore, it is not clear that the effect of parasitic mutual inductances would be avoided by the deposition of a low-I_C junction in the measurement loop. Some other groups who have measured the CPR using devices with a similar geometry [5–7] make little or no reference to an investigation of parasitic mutual inductances and therefore there is some potential doubt cast upon the results of these experiments. Further adjustments to the CPR measurement circuit shown in Fig. 3.27 (right) were considered but it was deemed to be unfeasible to produce them with speed and reliability.

The main result of the work documented in this chapter was to highlight serious design flaws that could not have been easily remedied within the allocated time frame. Therefore, a second measurement device is proposed that would help to combat the complications of Josephson junction fabrication and the need for the extensive circuit characterisation described here. This device proposal makes use of superconducting coplanar resonators and a feasibility study of this method will be the focus of chapters 4 and 7.

CHAPTER 4

MICROWAVE CURRENT-PHASE RELATIONSHIP MEASUREMENT SCHEME

The previous chapter highlighted problems encountered in the use of a dc CPR measurement device with a planar geometry. In this chapter, an alternative measurement device will be proposed whereby CPR measurements are made in the microwave regime. The proposed structure is a variant of the GHz SQUID that was studied extensively in the 1990's (see Ref. [77] for a review). The device relies on the use of a superconducting coplanar resonator to interact with a nearby rf SQUID that contains an SFS Josephson junction. Before the device is described fully and results of the device feasibility study are presented, it is first necessary to build upon the introductory material presented in chapter 2 to give a more detailed discussion of the relevant physics.

4.1 Microwave Properties of Superconductors

4.1.1 Complex Conductivity of Superconductors

The Two-Fluid Model

Before the formulation of BCS theory, Gorter and Casimir [15] proposed a 'two-fluid model' to phenomenologically account for the properties of superconductivity. The fraction of superconducting electrons, n_s/n, was assumed to vary from 1 at $T = 0$ to zero at T_C. For low temperature superconductors, the best agreement with the observations was given when

$$\frac{n_s}{n} = 1 - \left(\frac{T}{T_C}\right)^4 \tag{4.1}$$

where n is the total number density of conduction electrons. The temperature dependent change in n_s is shown in Fig. 4.1 showing that below T_C there is some fraction of the conduction electrons that exist in the superconducting state with the remainder in the normal state. From equation (2.4), it is seen that $\lambda_L \propto 1/\sqrt{n_s}$, so the penetration depth varies as shown by the red line in Fig. 4.1. For dc signals, even a small fraction of n_s will give rise to a sharp resistive transition as the sample is cooled below T_C. By contrast, a description of the ac properties of superconductors based on the two-fluid model must include the presence of normal electrons since an electric field, $\mathbf{E}$, will act upon both parts of the conduction electron fluid.

By including the two parts of the fluid in the response, a complex conductivity model can be described. The superconducting pairs experience a force from an applied electric field of frequency, ω, and move without dissipation. The normal electrons move under the same influence but experience dissipation through collisions with a momentum relaxation time, τ. Assuming a sinusoidal time dependence, the total current density, $\mathbf{J}$, and hence the conductivity, σ, can be written as a sum of

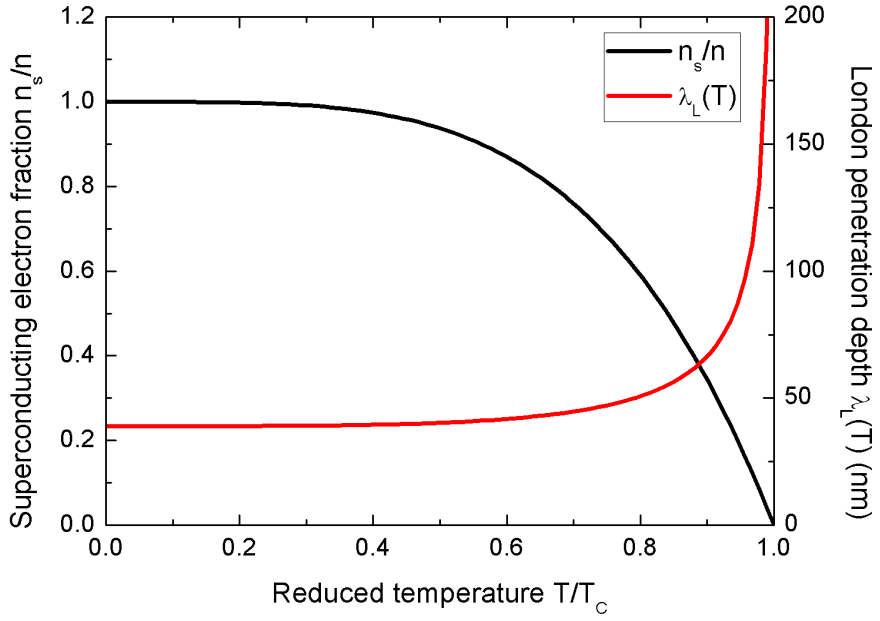

Figure 4.1: Temperature dependence of the superconducting electron fraction n_s/n (black line, left y-axis) and the London penetration depth (red line, right y-axis) where $\lambda_L(0) = 39$ nm.

the normal and superconducting contributions (denoted by the subscripts n and s respectively):

$$\mathbf{J} = \mathbf{J_n} + \mathbf{J_s} = (\sigma_1 - i\sigma_2)\mathbf{E}. \tag{4.2}$$

This equation relates the current density to the applied electric field by a complex conductivity where the real part, σ_1, depends only on the normal electrons,

$$\sigma_1 = \frac{n_n e^2 \tau}{m(1+\omega^2\tau^2)} \tag{4.3}$$

and the imaginary part of the conductivity, σ_2, contains inertial contributions from both the normal (which can usually be neglected) and the superconducting electrons:

$$\sigma_2 = \frac{n_s e^2}{m\omega} + \frac{n_n e^2(\omega\tau)^2}{m\omega(1+\omega^2\tau^2)}. \tag{4.4}$$

Here, n_n and n_s are the number densities of the normal and superconducting charge carriers respectively and m denotes their mass. The complex conductivity can be drawn as an equivalent circuit diagram, shown in Fig. 4.2 (left), where the temperature dependent behaviour of σ_1 and σ_2 is shown in Fig. 4.2 (right). Provided $\omega^2\tau^2 \ll 1$, an effective conductivity, σ_{eff}, can be written as

$$\sigma_{\text{eff}} \cong \sigma_n \left(\frac{n_n}{n}\right) - i\left(\frac{1}{\omega\mu_0\lambda^2}\right) \tag{4.5}$$

where $\sigma_n = ne^2\tau/m$, which provides the normal state conductivity.

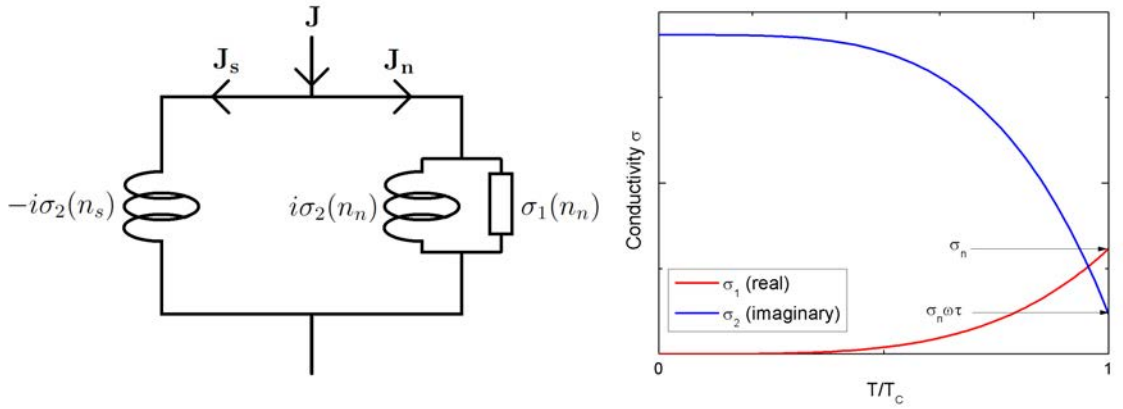

Figure 4.2: Left: Two-fluid model circuit diagram for $\omega > 0$. Right: Real and imaginary components of the conductivity for $\omega^2\tau^2 \ll 1$ as a function of temperature.

The temperature dependence of the complex conductivity arises due to the change in the relative number densities of the charge carriers given by equation (4.1). For $T > T_C$, equation (4.1) shows that $n_s = 0$ and the model simply becomes the Drude conductivity for a normal metal. In a superconductor (with $n_s > 0$) for $\omega = 0$ the current flows only through the inductive path with no associated resistive loss. However, for $\omega > 0$ current flows in both conductive channels (with the ratio dictated by the value of n_s/n). Therefore, since there are always some normal electrons present for $T \neq 0$, there is always dissipation in superconductors for $\omega \neq 0$. This provides the limitation for the quality factor of a superconducting resonator.

Mattis-Bardeen Theory

While the conductivity can be approximated using equations (4.3) and (4.4) from the two-fluid model, there are inherent problems with this approach in that the effect of the energy gap is not considered (which includes, for example, pair breaking by incident radiation on the material when $\hbar\omega > 2\Delta$) [78]. Furthermore, the two-fluid model treats the movement of electron pairs in a similar way to normal electrons rather than treating them as having a finite size given by the coherence length.

A more accurate description of the complex conductivity for superconductors was proposed by Mattis and Bardeen in 1958 [79] (henceforth referred to as the 'Mattis-Bardeen theory'). Their analysis derived the complex conductivity function using the microscopic theory of superconductivity and, although more complicated than the two-fluid model, more accurately describes the normal and paired electron contributions to the conductivity at all frequencies. The result of Mattis-Bardeen theory gives the following integrals:

$$\begin{aligned}\frac{\sigma_1}{\sigma_n} = \frac{2}{\hbar\omega}\int_{\Delta}^{\infty}\left[f(E)-f(E+\hbar\omega)\right]g(E)dE \\ +\frac{1}{\hbar\omega}\int_{\Delta-\hbar\omega}^{-\Delta}\left[1-2f(E+\hbar\omega)\right]g(E)d(E)\end{aligned} \tag{4.6}$$

and

$$\frac{\sigma_2}{\sigma_n} = \frac{1}{\hbar\omega}\int_{\max\{\Delta-\hbar\omega,-\Delta\}}^{\Delta}\frac{\left[1-2f(E+\hbar\omega)\right]\left(E^2+\Delta^2+\hbar\omega E\right)}{\left(\Delta^2-E^2\right)^{1/2}\left[(E+\hbar\omega)^2-\Delta^2\right]^{1/2}}dE \tag{4.7}$$

where

$$g(E) = \frac{E^2+\Delta^2+\hbar\omega E}{\left(E^2-\Delta^2\right)^{1/2}\left[(E+\hbar\omega)^2-\Delta^2\right]^{1/2}}. \tag{4.8}$$

σ_n is the conductivity of the normal state just after T_C is exceeded and $f(E)$ is the Fermi function given by

$$f(E) = \frac{1}{1 + \exp(E/k_B T)}. \tag{4.9}$$

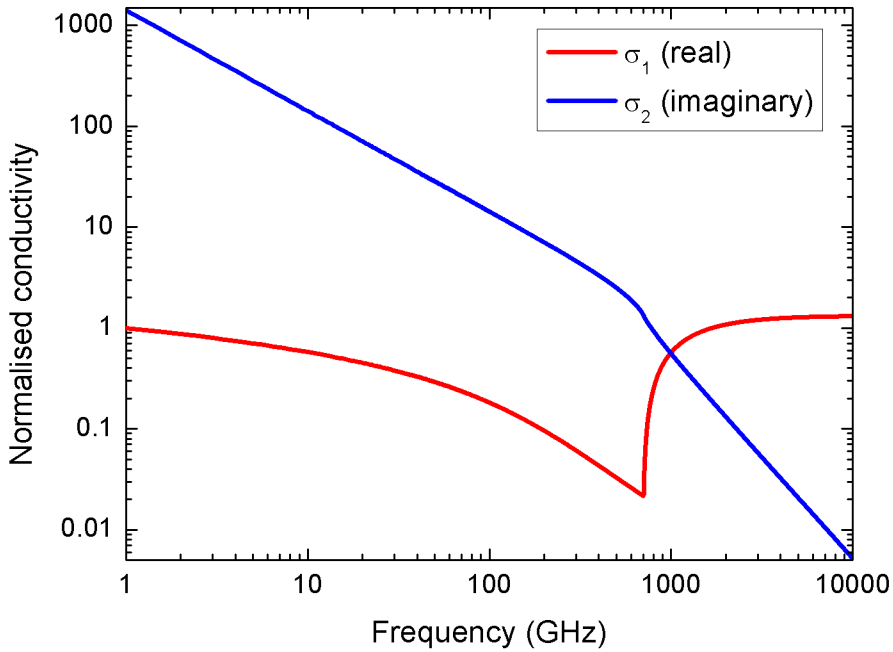

Figure 4.3: Real and imaginary parts of the conductivity plotted as a function of frequency for $T/T_C = 0.5$ and $2\Delta = 3$ meV. The conductivity was calculated using Mattis-Bardeen theory with the program 'MB_Fit.cc' (described in section 6.2.3).

The Mattis-Bardeen integrals describe the frequency and temperature dependence of the conductivity of superconductors, including the effect of a gap parameter, Δ, which has a temperature dependence that was shown in Fig. 2.2. There are two integrals in equation (4.6); the first represents quasiparticles that arise from thermal excitations (existing only for $T > 0$) and the second represents the effect of quasiparticles arising from an applied external field which do not appear for $\hbar\omega < 2\Delta$. The real part of the conductivity therefore increases sharply above this frequency. Equation (4.7) describes the behaviour of the paired electrons only and the lower limit is set to $-\Delta$ if the applied frequency exceeds the gap frequency ($\hbar\omega > 2\Delta$). Fig. 4.3 illustrates how the Mattis-Bardeen integrals include the effect

of paired electrons by plotting the real and imaginary parts of the conductivity as a function of frequency. A discontinuity is observed in the conductivity at a frequency that corresponds to the gap frequency; the two-fluid model does not include the effect of pair breaking at high frequencies and therefore shows no similar discontinuities.

The Mattis-Bardeen theory more correctly handles the nature of the charge carriers than does the two-fluid model and has also shown to provide good agreement with experimental results for a variety of superconductors (see [20] and references therein). For the purposes of the experiments described here, the Mattis-Bardeen theory will be used as part of the analysis for calculating the kinetic inductance fraction of superconducting coplanar resonators.

4.1.2 Kinetic Inductance

The proposed device is made of thin film superconducting material. Along with a geometric inductance from the energy stored by the magnetic field produced as a consequence of current flow, there is an additional *kinetic* inductance associated with the inertial mass of the superconducting electron pairs. The normal electrons also have a kinetic inductance caused by the finite acceleration time in response to a changing field but it remains negligibly small unless τ is extremely large; as such, this term is usually ignored for normal metals. The kinetic energy density stored in the paired electrons that cannot be dissipated is

$$K.E. = n_s \frac{1}{2} m v_s^2 \tag{4.10}$$

where m and v_s are the mass and velocity of the superconducting charge carriers respectively. Substitution of the velocity with the supercurrent density ($J_s = -n_s e v_s$) gives

$$K.E. = \frac{1}{2}\mu_0 {\lambda_L}^2 J_s^2 \tag{4.11}$$

where λ_L is the London penetration depth given by equation (2.4). Therefore, the total kinetic inductance per unit length of a superconducting strip, L_K, is given by

$$\frac{1}{2}L_K I^2 = \frac{1}{2}\mu_0 \lambda_L^2 \int J_s^2 ds \tag{4.12}$$

where I is the total current and a non-uniform current distribution is taken into account by the surface integral. The fast changing electric field of an ac signal acts on the charge carriers but, due to their finite mass, the change is resisted. Therefore the response to a change in field is not instantaneous and results in a phase lag in the voltage (i.e. indistinguishable from an inductance). It is also noted that L_K is dependent on both the geometry and on $\lambda_L \propto 1/\sqrt{n_s}$, where the London penetration depth is analogous to the skin depth for a normal metal.

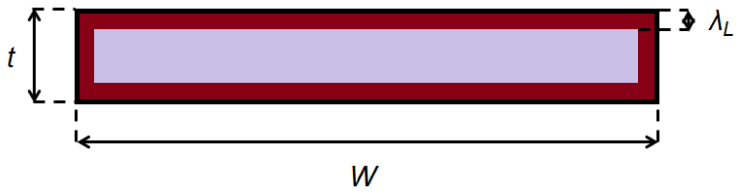

Figure 4.4: Schematic diagram of an isolated superconducting strip where the current flow is into the plane. The approximate current distribution is shown (red indicates the region with the highest current density) for a piece of superconductor of thickness t and width W such that $W \gg t \gg \lambda_L$.

Since the kinetic inductance is dependent on the penetration depth, there are now two limiting situations to be considered that depend upon the conductor thickness. Fig. 4.4 illustrates a piece of superconductor of thickness t and width W where $W \gg t \gg \lambda_L$. Let J_s be considered to be constant over the red region which indicates areas of majority current flow and given by $J_s = I/A$, where I is the current and A is the area it is distributed over. The surface integral in equation (4.12) can now be replaced by A such that

$$\frac{1}{2}L_K I^2 = \frac{1}{2}\mu_0 \lambda_L^2 J_s^2 A. \tag{4.13}$$

For the case shown in Fig. 4.4, $A = 2W\lambda_L$ so for $t \gg \lambda_L$:

$$L_K = \frac{\mu_0 \lambda_L}{2W}. \tag{4.14}$$

If the superconductor is now made to be very thin, such that $t \ll \lambda_L$, there will now be no region of the superconductor that does not carry some part of the current and the area is now simply given by $A = Wt$. Now the kinetic inductance has the form

$$L_K = \frac{\mu_0 \lambda_L^2}{Wt} \tag{4.15}$$

where the previously linear dependence on the penetration depth becomes quadratic as the film thickness decreases [80] and, for samples with small dimensions, the kinetic inductance can become a significant fraction of the total inductance. The discussion here deals with an idealised system geometry; it will be shown in chapter 7 that a non-ideal sample geometry (for example, a non-rectangular cross section) can alter these results dramatically.

4.2 Coplanar Resonators

The proposal for a microwave CPR measurement device uses a coplanar resonator to probe a nearby Josephson junction structure. In the literature, coplanar resonator devices are widely used in the fields of radiation detection [81, 82], material characterisation [83–92], tunable resonators [93–99], quantum computing [96, 98, 100–110], and for the readout of nanoscale mechanical beam motion [111, 112]. Before describing the proposed CPR measurement device, it is first necessary to outline the design

and operation of a coplanar resonator structure. Further information can be found in Refs. [9, 113, 114].

4.2.1 Geometric Properties

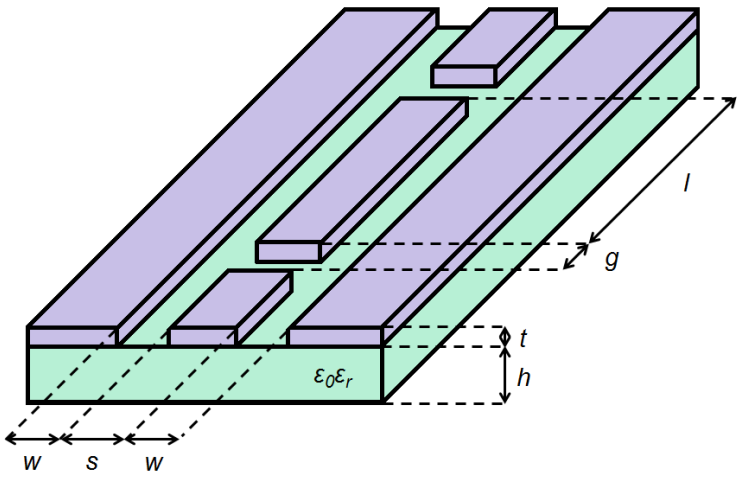

Figure 4.5: Schematic diagram of a coplanar resonator with a centre conductor of length l and width s fabricated from a conductor of thickness t. The conductor resides on top of a substrate of thickness h with relative permittivity ϵ_r. The coupling gap of size g separates the centre conductor from the signal feedlines, and gap of size w separates the centre conductor from the ground planes.

A coplanar resonator is a distributed element device that is fabricated on a single metallised side of a dielectric substrate with relative permittivity ϵ_r. A strip of centre conductor is laterally separated from two ground planes to form a transmission line and, for an integral number of half-wavelengths to fit into the resonator, is open circuit at either end such that a resonant structure is formed. This is shown schematically in Fig. 4.5 where, for the work presented in this thesis, the substrate material was sapphire, the conductor was niobium, and the work focuses on the fundamental $\lambda/2$ resonance.

A coplanar resonator allows standing wave formation at frequencies determined by the device length in a way that is analogous to standing sound wave formation in a pipe. A signal can be coupled to the centre conductor from feedlines via 'coupling gaps' such that there is maximal signal transmission through the device at resonance.

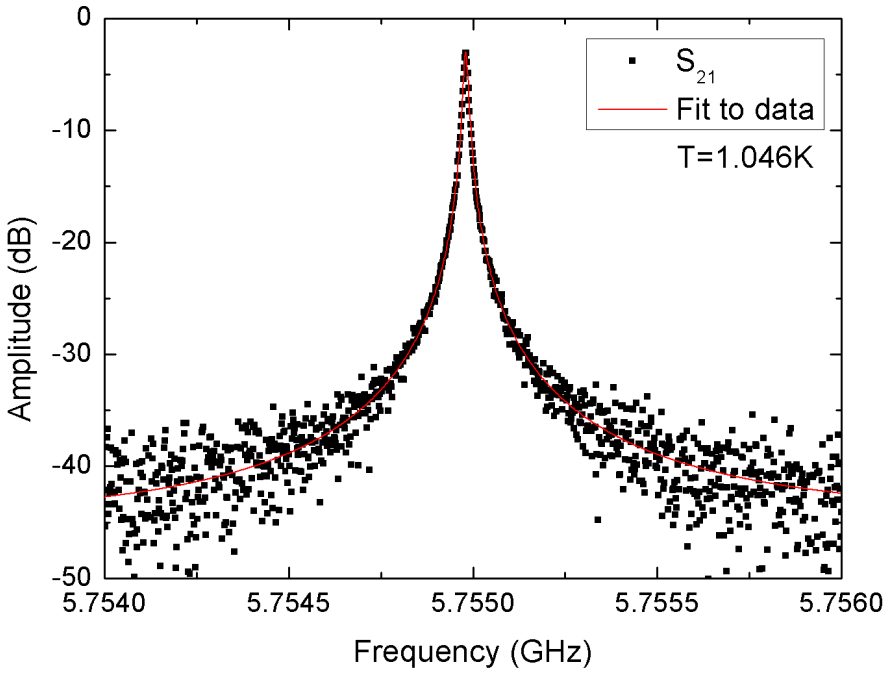

Figure 4.6: Microwave response of a niobium $\lambda/2$ coplanar resonator on a sapphire substrate at $T = 1.05$ K. The red line is a theoretical fit to the data which gives $f_0 = (5.7550 \pm 0.0001)$ GHz with $Q = 409,863 \pm 1798$.

Away from resonance, the transmitted signal power remains small. An example of signal transmission at resonance is shown in Fig. 4.6 for a niobium coplanar resonator on a sapphire substrate at $T = 1.05$ K.

The resonant frequency of the n^{th} mode is determined by the inductance and capacitance per unit length of the conducting strip and can be found by

$$f_n = \frac{n\nu_{ph}}{2l} = \frac{nc}{2l\sqrt{\epsilon_{\text{eff}}}} = \frac{n}{2l\sqrt{L'C'}} \tag{4.16}$$

where ν_{ph} is the phase velocity of the propagating wave, L' and C' are the inductance and capacitance per unit length and c is the speed of light in a vacuum. Here, ϵ_{eff} is the effective permittivity of the structure and is given by

$$\epsilon_{\text{eff}} = \frac{1}{2}(\epsilon_r + 1) \tag{4.17}$$

i.e. an average value of the permittivites of the substrate and the space above (typically vacuum). Although Fig. 4.5 shows a straight centre conductor, the wavelength for microwaves is in the millimeter range and it is quite common for the resonant structure with f_0 in the microwave regime to include meanders to further miniaturise the design.

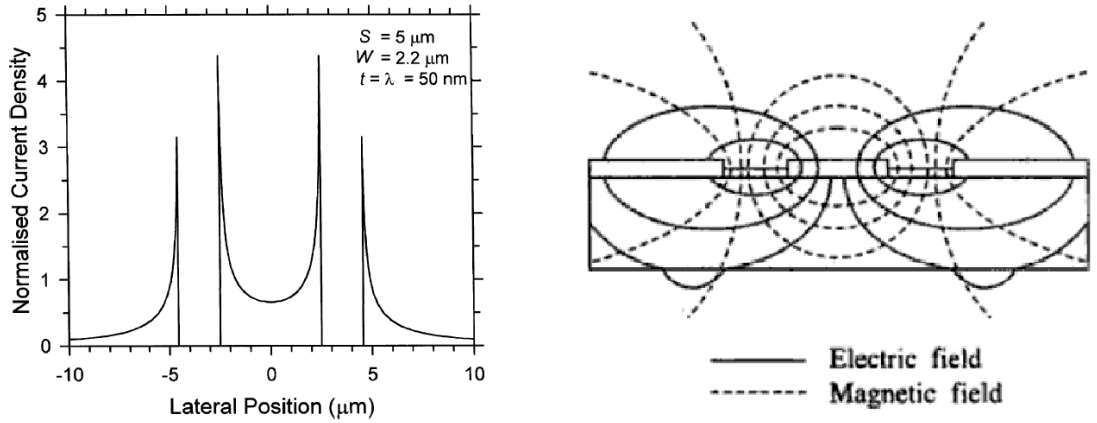

Figure 4.7: Left: Cross sectional current density for a coplanar resonator (adapted from Fig. 3 in Ref. [80]) normalised by the average current density. Right: Cross sectional electric and magnetic field distribution (image from Ref. [115]).

Determination of the geometric L' and C' is provided via conformal mapping techniques as outlined by Simons and Göppl [114, 116] and allows for the nonuniform current distribution across the coplanar resonator as shown in Fig. 4.7 with the resulting cross sectional electric and magnetic field distribution. The current distribution tends to crowd at the edges over a distance given by λ_L when the width of the centre conductor $W \gg \lambda_L$. This current distribution persists along the length of the centre track, though modulated by the longitudinal current distribution shown in Fig. 4.8. The inductance and capacitance per unit length of a coplanar transmission line are given by

$$L' = \frac{\mu_0 K(k_0')}{4K(k_0)} \tag{4.18}$$

and

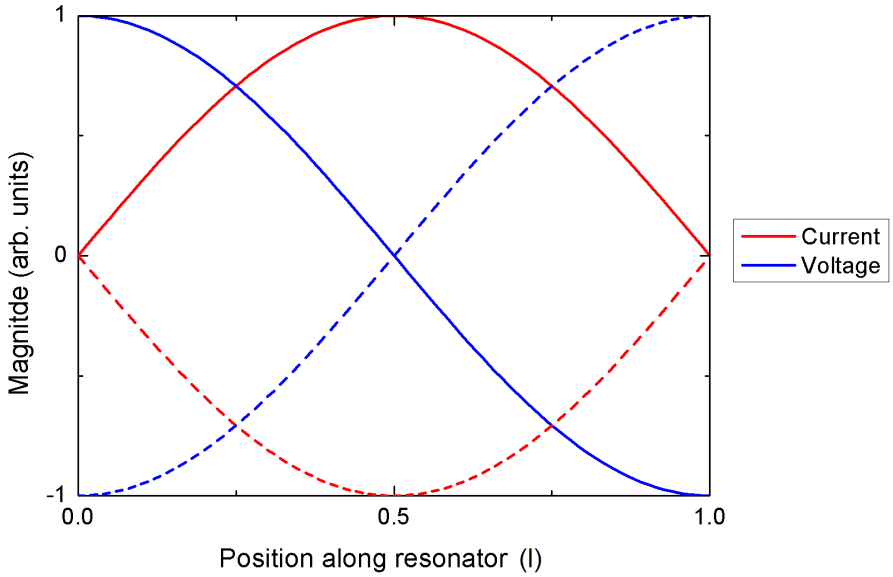

Figure 4.8: Current (red) and voltage (blue) of the fundamental resonance along the length of a $\lambda/2$ resonator at time $t = 0$ and at $t = T/2$ (dashed lines), where T is the period of the wave.

$$C' = 4\epsilon_0\epsilon_{\text{eff}}\frac{K(k_0)}{K(k_0')} \tag{4.19}$$

where ϵ_0 is the vacuum permittivity, K is the complete elliptic integral of the first kind, $k_0 = s/(s+2w)$ and $k_0' = \sqrt{1-k_0^2}$. For the total geometric inductance, L_G, or capacitance, C_G, the above expressions must each be multiplied by the resonator length, l. The characteristic impedance of the coplanar resonator is then given by

$$Z_0 = \sqrt{\frac{L'}{C'}} = \frac{30\pi}{\sqrt{\epsilon_{\text{eff}}}}\frac{K(k_0')}{K(k_0)}. \tag{4.20}$$

For the feedlines in particular, this is usually chosen as 50 Ω to minimise reflection of the drive signal. For the samples measured here, a design by Dr J. E. Healey [117] was used which gave $f_0 \approx 6$ GHz. Through application of the equations given here, the estimated resonator properties are given in table 4.1.

Table 4.1: Design parameters of the coplanar resonator used for the experiments described in this thesis (design by Dr J. E. Healey [117]).

Item	Symbol	Size
Length of central conductor	l	$\sim$1 cm
Coupling gap	g	4 μm
Width of central conductor	w	10 μm
Separation from ground plane	s	5 μm
Inductance per unit length	L'	0.40 μH/m
Capacitance per unit length	C'	0.15 nF/m
Characteristic impedance	Z_0	51.38 Ω
Fundamental resonant frequency	f_0	6.38 GHz

The Quality Factor

Along with f_0, another measurable parameter that is used as a figure of merit for a resonant system is the quality factor, Q. This is a dimensionless quantity that describes how narrow the resonant peak is and can be defined as

$$Q = 2\pi \frac{\text{stored energy}}{\text{energy dissipated per cycle}}. \tag{4.21}$$

The Q of a coplanar resonator can be determined through measurement of the transmission properties of the device at resonance by

$$Q = \frac{f_0}{\Delta f_0} \tag{4.22}$$

where Δf_0 is the full width at half maximum and $1/Q$ is also a measure of the losses in the system. There are a number of loss mechanisms but generally the quality factor associated with the resonant system alone, Q_0 (also called the unloaded quality factor), is

$$\frac{1}{Q_0} = \frac{1}{Q_c} + \frac{1}{Q_d} + \frac{1}{Q_r} \tag{4.23}$$

where Q_c, Q_d and Q_r are the quality factors associated with the conducting material, the dielectric material and radiation respectively. Superconductors are able to provide much higher Q resonators than those made of normal metals due to the extreme reduction of resistive losses. The temperature dependence of the normal electron fraction in the two-fluid model plotted in Fig. 4.1 implies that Q decreases as the temperature increases for superconducting resonators. The observed quality factor, Q_L (also called the loaded quality factor), is

$$\frac{1}{Q_L} = \frac{1}{Q_0} + \frac{1}{Q_e} \tag{4.24}$$

where Q_e encompasses contributions to the loss that are external to the resonator, e.g. losses through connections made to the network analyser. Coupling to external circuitry can be the dominant source of losses for superconducting coplanar resonators; Göppl et al [116] showed that the size of the coupling gap is an important parameter that can be used to limit the interaction with the external environment. The coupling gap size used here was selected on the basis of previous experiments conducted within the research group [117]. Further discussion of contributions to the losses will be given in section 7.1.1.

4.2.2 Changes to the Resonant Frequency

For superconducting samples, there are two contributions to the total inductance, L_T, such that

$$L_T = L_G + L_K \tag{4.25}$$

where $L_G = L'l$ is the geometric inductance and L_K is the kinetic inductance as discussed in section 4.1.2 where the kinetic inductance fraction can be defined as

$$\alpha = \frac{L_K}{L_T}. \tag{4.26}$$

The kinetic inductance of a coplanar resonator can be affected by the sample temperature and by the application of an external magnetic field. The change in L_K can be measured experimentally and used to study properties of the materials used in the resonator fabrication.

Temperature Dependence

While it can be assumed that the *capacitance* is temperature independent over the range covered in the experiments described here [118, 119], the temperature dependence of the *kinetic inductance* cannot be neglected. The temperature dependence of the fundamental resonant frequency can be written as

$$f_0(T) = \frac{1}{2l\sqrt{(L_G + L_K(T))C_G}} \tag{4.27}$$

where $C_G = C'l$ is the geometric capacitance. Equation (4.27) shows that material properties affecting L_K ($\propto \lambda_L \propto 1/\sqrt{n_s}$) of a coplanar resonator can be studied by monitoring the resonant frequency as a function of temperature if it is assumed that no other variable is temperature dependent. Since $f_0 \propto 1/\sqrt{LC}$, a small change in f_0 is

$$\frac{\delta f_0}{f_0} = -\frac{1}{2}\frac{\delta L_T}{L_T} \tag{4.28}$$

since C_G is assumed to be temperature independent. L_T is given by equation (4.25) so

$$\frac{\delta f_0}{f_0} = -\frac{1}{2}\frac{L_K}{L_G + L_K}\frac{\delta L_K}{L_K} = -\frac{\alpha}{2}\frac{\delta L_K}{L_K} \tag{4.29}$$

by substitution of equation (4.26) for the kinetic inductance fraction. In section 4.1.2 it was shown that $L_K \propto \lambda_L$ in the thick film limit and $L_K \propto \lambda_L^2$ in the thin film limit. Equation (2.4) shows that $\lambda_L \propto \sigma_2^{-1/2}$; for both cases of interest it can be said that $L_K \propto \lambda_L^\beta$ where $\beta = 1$ for $t \gg \lambda_L$, and $\beta = 2$ for $t \ll \lambda_L$ (or more generally, $L_K \propto \lambda_L^\beta$ where $1 < \beta < 2$). Therefore, $L_K \propto \sigma_2^{-\beta/2}$ which means that equation (4.29) can be written

$$\frac{\delta f_0}{f_0} = \frac{\alpha\beta}{4}\frac{\delta\sigma_2}{\sigma_2} \tag{4.30}$$

where σ_2 can be calculated from the Mattis-Bardeen integral given in section 4.1.1. The fractional change in the frequency for a superconducting resonator with a high Q can be easily measured as a function of temperature [120]. The kinetic inductance fraction can then be determined through fitting equation (4.30) to $f_0(T)$; this has been reported by a number of groups and observed values have ranged from $\alpha = 0.04$ [81] to α=0.35 [86] for varying materials and resonator designs. For some applications, such as kinetic inductance detectors, it is often desirable to maximise this value. To achieve this, the superconducting film thickness may be reduced [80] or the geometry of the device can be altered [87].

Field Dependence

The application of a magnetic field to a superconductor results in a change in the number density of Cooper pairs [121]. Due to the Meissner effect, the screening current density on the superconductor surface is increased to exclude the field, which causes a corresponding increase in the penetration depth $\lambda_L \propto 1/\sqrt{n_s}$. As was already stated in equations (4.14) and (4.15), the kinetic inductance $L_K \propto \lambda_L$ for films where the thickness $t \gg \lambda_L$ and $L_K \propto \lambda_L^2$ for films where the thickness

$t \ll \lambda_L$. Therefore the application of a magnetic field to a coplanar resonator device is expected to change the resonant frequency.

To describe the field dependence of the penetration depth, a phenomenological model can be constructed in a similar manner to Ginzburg-Landau theory, i.e. by considering only the symmetry of the system. It is known that there is a critical magnetic field, H_C, above which the superconductivity is destroyed so all field strengths should be measured with respect to this. It is also known that the functional dependence of λ_L on H/H_C cannot depend on the direction of H and therefore there will be no linear dependence on the applied field. Given this, the general behaviour for $H \ll H_C$ is

$$\frac{\delta\lambda_L(T,H)}{\lambda_L(T,0)} \propto \frac{H^2}{H_C^2}. \tag{4.31}$$

This is an established result that was notably reported by Pippard in 1950 [93, 122, 123].

Early work performed by Oates et al [94] in the context of tunable filters involved altering the magnetisation of a ferrite in close proximity to the superconducting resonator, though the device performance was limited by the materials. Later experimental work by Healey et al [93,124] involved the application of a small magnetic field directly to the device. The results shown in these references show that the shift in f_0 has a quadratic dependence on the applied field and is given by

$$f(T,H) = f(T,0)\left(1 - \frac{L_K(T,0)}{L_T}\eta(T)\frac{H^2}{H_C^2}\right) \tag{4.32}$$

where $L_K(T,0)$ is the kinetic inductance for zero applied field, H is the applied field, H_C is the thermodynamic critical field and $\eta(T)$ is a temperature dependent scaling factor that depends upon the quasiparticle density (i.e. $\eta(T) \to 0$ as $T \to 0$). For the origin of this expression see Refs. [93, 117] and references therein.

Previous work on this topic has shown that a relatively small applied field can result in large shifts in f_0 without any signficant reduction in Q. Upon increasing the field further, hysteresis begins above a threshold field strength where the Q finally drops. A likely explanation for the large shift in f_0 due to a small applied field is due to flux focusing effects resulting from the device geometry (which is supported by the change in $\delta f_0(H)$ as a function of the angle at which the field is applied observed by Healey et al [93]), while the observation of hysteresis is thought to be related to vortices entering the film and moving under the influence of the oscillating current in the resonator [125, 126].

Power Dependence

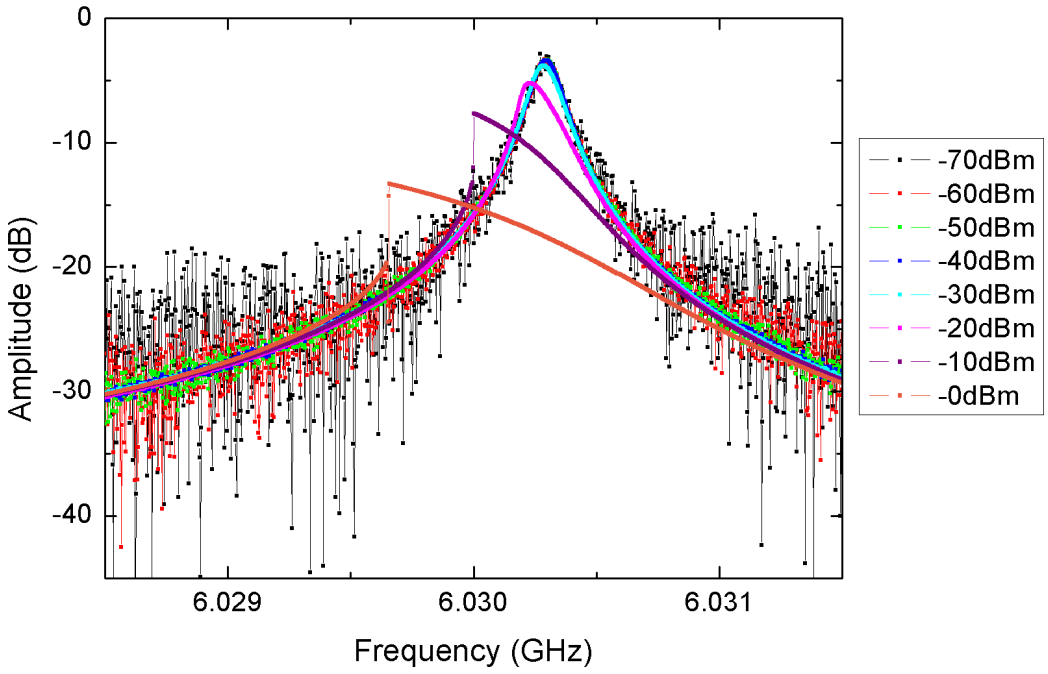

Figure 4.9: Microwave transmission as a function of drive power for a $\lambda/2$ niobium resonator with 6 μm coupling gaps on a sapphire substrate measured at $T = 1.3$ K (sample fabricated by A. Bannykh).

Fig. 4.9 shows the power dependence of the fundamental resonant frequency of a $\lambda/2$ niobium coplanar resonator on a sapphire substrate. For low input powers, the resonant peak is approximately symmetric about the resonant frequency and

is easily fitted by a modified Lorenztian form provided by equation (6.10) (as will be described in section 6.2.2). As the drive power is increased, the noise decreases but the response exhibits nonlinearity showing an asymmetric lineshape (noticeably between -30 dBm and -20 dBm). For f_0(-70 dBm), Q ≈51,000 but increasing the drive power to 0 dBm results in a dramatic drop in the quality factor and a shift in the measured resonant frequency. The decrease in the resonant frequency with increasing drive power is due to a positive feedback mechanism associated with an increase in the kinetic inductance.

If the resonator response is driven nonlinear by a high input power, fitting the resonant peak to a theoretical model requires a modified approach to the analysis [127,128]. In order to avoid this complication in the analysis, drive signal powers were used that were low enough to avoid nonlinearity in the microwave response.

4.3 Alternative CPR Measurement Scheme

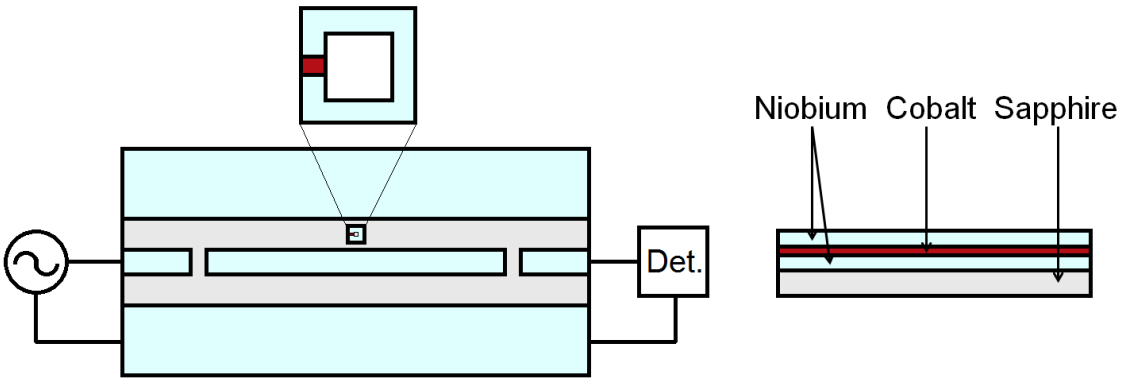

Figure 4.10: Schematic diagram showing the proposed microwave CPR measurement device where the Josephson junction (shown symbolically in red in the expanded view) is fabricated as part of an rf SQUID located between the ground plane and centre track of a coplanar resonator. The entire device is made from a superconductor-ferromagnet-superconductor thin film.

Chapter 3 described the inherent problems associated with a dc CPR measurement device with a planar geometry. A novel alternative device for the measurement of the Josephson junction CPR is to use coplanar resonators as a probe for the behaviour

of a nearby junction. The proposed measurement device is shown in Fig. 4.10. The device draws inspiration from the Rifkin-Deaver [8] method of CPR measurement that was outlined in section 3.1.4 and from so-called 'GHz SQUIDs' – rf SQUIDs operated at microwave frequencies where a coplanar resonator serves as the tank circuit [77, 129]. Using this approach, a coplanar resonator would be patterned from a multilayered thin film with a superconductor-ferromagnet-superconductor (SFS) or superconductor-insulator-ferromagnet-superconductor (SIFS) sandwich structure such that the intermediate layer is the desired junction barrier material. The collaborators for the work presented in this thesis reported difficulties in film deposition and junction fabrication within a defined area on the CPR measurement chip shown in Fig. 3.14 – the proposed device could be more easily fabricated using a single deposition run.

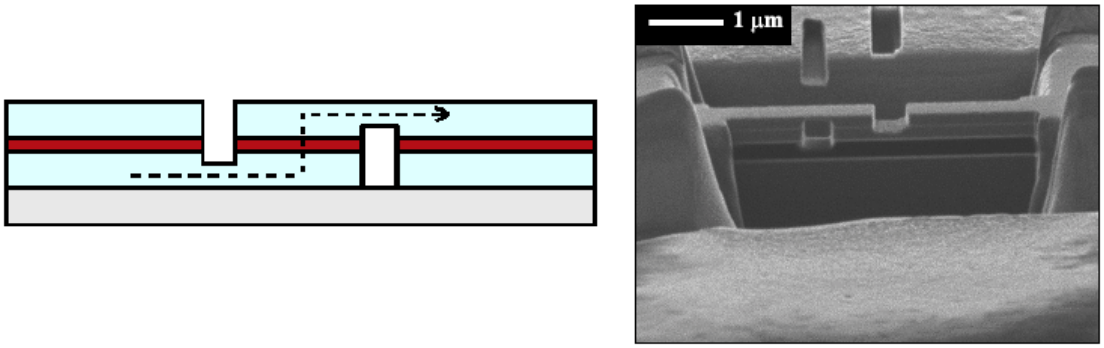

Figure 4.11: Left: Diagram of the junction structure that would be patterned into the block shown in Fig. 4.10. Right: Image of a junction (Nb-CuNi-Nb) produced by FIB as demonstrated by Bell et al [130].

Device fabrication would require leaving a small block of material in the gap between one side of the centre conductor and the ground plane of a coplanar resonator. Using Focused Ion Beam (FIB) milling, this block would then be patterned into an rf SQUID structure, with the junction fabrication style shown in Fig. 4.11, using a technique that has been demonstrated by Bell et al [130] and Golod et al [54] for SFS junctions. The measurement procedure would then be to monitor the microwave response of the coplanar resonator as a small magnetic field is applied perpendicular to the device.

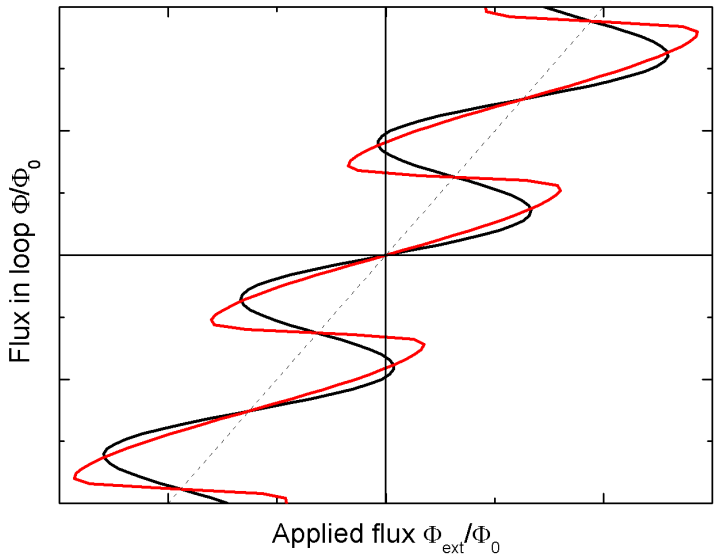

Figure 4.12: Response of an rf SQUID ($\beta_L = 5$) to an applied magnetic field for a device containing a Josephson junction with a sinusoidal (black) and nonsinusoidal (red) CPR (skewed CPR plotted for a double-barrier Josephson junction as given in Ref. [73]).

The response of an ideal rf SQUID to an applied magnetic field was shown in Fig. 3.8 and is reproduced for a non-sinusoidal CPR in Fig. 4.12 for $\beta_L = 5$ (though the proposed device would have $\beta_L < 1$ such that the rf SQUID is non-hysteretic). This shows that the internal flux of the SQUID is periodically modulated between diamagnetic and paramagnetic behaviour as the external field is increased and this would affect the field dependence of resonant frequency of the superconducting coplanar resonator by modifying the magnetic field distribution created as a result of the oscillating current in the coplanar resonator. By affecting the transmission line inductance, a periodic shift in the resonant frequency is expected that would reflect the CPR of the Josephson junction.

As an example, a ring of superconducting material of diameter of 20 μm provides an inductance of 25 pH. According to equation (3.12), a critical current of < 13 μA is then required to keep the SQUID response non-hysteretic. If it is assumed that the rf SQUID exhibits a maximum of 20% perfect diamagnetism and is placed next to a resonator of length 1 cm such that $f_0 = 6$ GHz, a maximum resonant frequency shift of 1.2 MHz is expected due to the effect of an applied magnetic field on the rf SQUID

alone. To produce a single flux quantum in the SQUID structure, an estimated static field of 5 μT is required. Previous investigation of field tuned superconducting coplanar resonators by Healey et al [93] and the results to be shown in chapter 7 indicate that this magnitude of field applied perpendicularly to the resonator would produce a negligible shift in a niobium resonator due to the effects discussed in relation to equation (4.32).

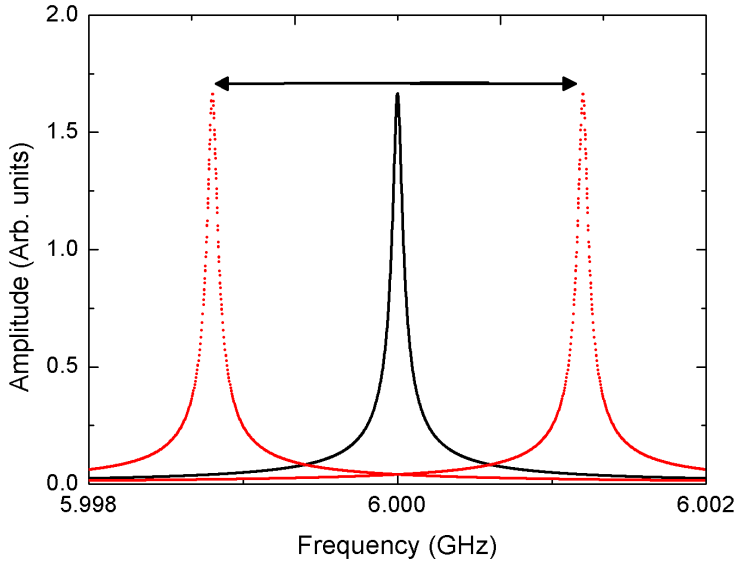

Figure 4.13: Simulated data showing the estimated shift in the resonant frequency of a coplanar resonator coupled to an rf SQUID as a dc magnetic field is applied and increased.

The application of a small but increasing magnetic field would result in the modulation of the resonant frequency of the coplanar resonator as shown by the arrow in Fig. 4.13. This could be easily detected by monitoring the transmission of microwave signal through the resonator using a network analyser. By observing how the resonant frequency shifts with applied field, the CPR could be deduced in a manner similar to that demonstrated by Rifkin and Deaver [8]. Departures from sinusoidal behaviour, as shown in Fig. 4.12, would be reflected in the movement of the resonant frequency but accurate determination of the CPR again relies on good knowledge of the device parameters and so would require careful modelling of the structure.

For niobium coplanar resonators, quality factors $\gg 100,000$ are achievable [95]; this proposal requires that the entire device - both the resonator and the rf SQUID - be made from the same thin film structure which incorporates a non-superconducting (i.e. lossy) material. It is therefore necessary to first establish if the presence of a ferromagnetic layer degrades the performance of the resonator to such an extent as to render this proposal unfeasible. Furthermore, in light of studies on superconductor-ferromagnet bilayers [39, 131], it is also necessary to investigate whether the ferromagnetic layer produces a similar observable influence on the microwave response of the superconductor that would change the interpretation of the data used to extract the CPR.

Part II

Microwave Investigation of Superconductor-Ferromagnet Bilayers: A Feasibility Study

CHAPTER 5

SAMPLE PREPARATION AND CHARACTERISATION

This chapter describes the preparation and characterisation of samples fabricated to assess the suitability of the chosen materials to the device proposed at the end of the previous chapter, and how the combination of superconductors and ferromagnets would affect the performance of a microwave CPR device. Superconductor-ferromagnet thin film multilayers were deposited onto sapphire substrates and used to fabricate half wavelength coplanar resonators. The result of fabrication was investigated using AFM and the magnetic and superconducting properties of the films were characterised by low temperature SQUID magnetometry; the results of this are presented here.

5.1 Sample Preparation

5.1.1 Thin Film Deposition

Sets of multilayered superconductor-ferromagnet films were deposited by A. Bannykh, a member of the Department of Materials Science at the University of Cambridge. Single crystal sapphire substrates were diced into 10×5 mm pieces using a circular diamond saw and cleaned using the following process: 30 minute acetone ultrasonic bath (twice), 45 minute IPA ultrasonic bath, followed by careful drying with a nitrogen gun. The substrates were then immediately loaded into the deposition system.

The films were prepared in an Ultra-High Vacuum (UHV) system by dc magnetron sputtering, as described in detail in Ref. [31] and shown photographed in Fig. 5.1. This system allows preparation of up to 15 samples in a single deposition run without breaking vacuum, where the layer thicknesses for each sample can be independently varied. To achieve this, the blank substrates were loaded onto a rotating disc equidistant from one another (labelled (d) in Fig. 5.1). The rotation speed of the disc is controlled with a programmable stepper motor (a). Inside the system are three magnetrons (b) of which only a single one sputters material (niobium, cobalt or platinum) at any time. Above the rotating disc is a barrier (c) that physically separated the blank substrates from the magnetrons, except for a small cut away directly underneath each magnetron.

The purpose of this arrangement is to allow sputtered material to be deposited only onto a single substrate at a time as it is passed directly beneath the magnetron. To control the film thickness, the individual layer material was sputtered at a constant rate and the stepper motor was programmed to vary the disc rotation speed over a single revolution, thereby controlling how long each substrate spent below the exposed magnetron. In this way, a substrate that moves more slowly beneath the sputtering target would have a thicker layer of deposited material. Through knowl-

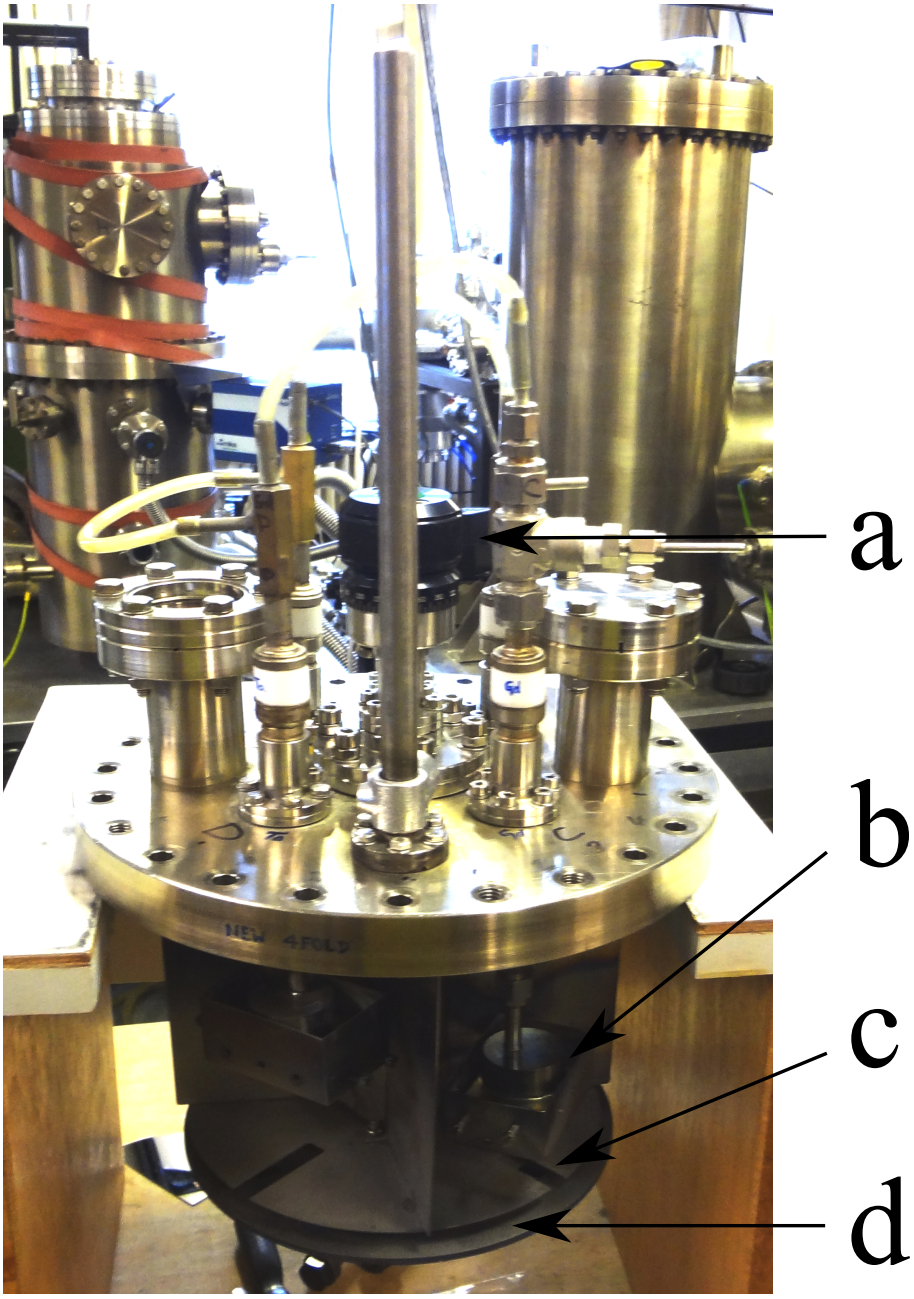

Figure 5.1: Photograph of dc magnetron sputtering system used to produce multi-layered thin films at the University of Cambridge. A programmable stepper motor (a) rotates the bottom plate that holds the substrates (d). The barrier with cut away sections (c) is fixed and allows sputtered material from the magnetron (b) only onto the substrate directly underneath.

edge of each individual substrate location on the rotating disc, a set of multilayered thin films were deposited where the cobalt layer thickness was varied systematically across the set. This system design ensures that each sample in the same run, and therefore the interface between layers, is exposed to the same conditions; this particular system has been reported to give an estimated error in the calculated film thickness of $\sim$0.2 nm [31, 32].

Three deposition runs yielded three sets of thin film multilayers. The sequence of layers for each set of films are given in table 5.1 where the purpose of the platinum layer in sets #1 and #2 was to prevent oxidation of the cobalt layer. After each deposition run, the system was vented and the thin films were removed and stored in cleaned and labelled sample boxes ready to be patterned in coplanar resonator devices.

Table 5.1: Summary of the thin film structures produced by A. Bannykh. The numbers in parentheses indicate the expected layer thickness in nanometers where x denotes a variable thickness.

Set number	Structure
#1	Al_2O_3 – Nb(5) – Nb(200) – Co(x) – Pt(5)
#2	Al_2O_3 – Nb(5) – Nb(200) – Co(x) – Pt(5)
#3	Al_2O_3 – Nb(5) – Co(x) – Nb(200)

Prior to patterning the thin films, a four-point measurement for a single sample from each set was conducted to measure the resistance as a function of temperature and thereby determine T_C. These measurements were made by A. Bannykh using a dip probe at the University of Cambridge. Fig. 5.2 shows such a measurement for a sample from set #1 with a cobalt layer thickness of 0.8 nm with the result $T_C \sim 8.85$ K. Although the data does not extend to room temperature, the film shows an estimated Residual Resistance Ratio (RRR) of 3.94 (between 300 K and 10 K), which compares favourably with other reported RRR's of niobium films of a similar thickness [132].

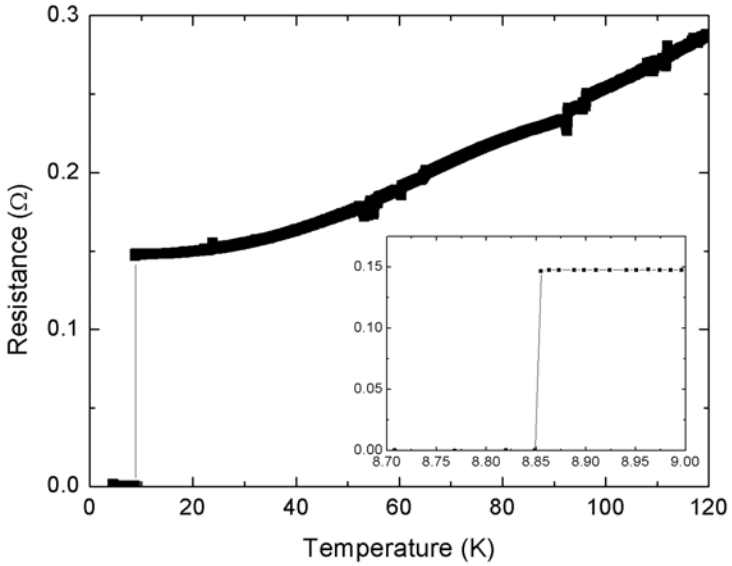

Figure 5.2: $R(T)$ of sample from set #1 with a cobalt layer thickness of 0.8 nm showing T_C=8.85 K (measurement made by A. Bannykh).

5.1.2 Coplanar Resonator Fabrication by Optical Lithography

Coplanar resonator devices were fabricated from the thin film structures described in the previous section. The resonators were either fabricated by the author or by A. Bannykh (see table 5.2 in section 5.1.3 for sample nomenclature); this section summarises the fabrication process used by the author.

The first stage in the fabrication process was careful cleaning of the thin films. The samples were placed in an acetone ultrasonic bath to loosen and remove any particulate matter that had adhered to the surface, followed by flooding with acetone/IPA and careful drying with a nitrogen gun. Some films appeared to have poor adhesion to the substrate; it was found that the ultrasonic bath was able to remove parts of the film so this technique was limited in use to short bursts followed by close optical inspection. After cleaning with solvents, the samples were dried thoroughly and inspected under a microscope to ensure the surface was free from contaminants.

Once cleaned, the films were patterned into coplanar resonators by standard pho-

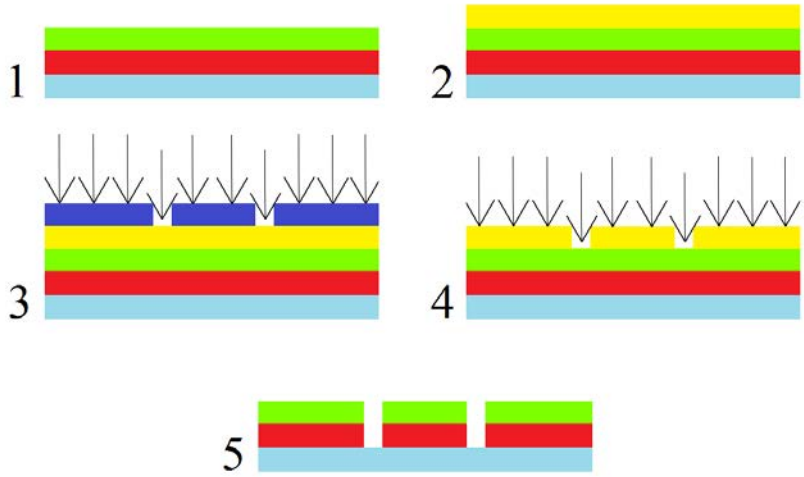

Figure 5.3: A step by step illustration of the photolithographic process. (1) Cleaned thin film multilayer (Al_2O_3 = light blue, Nb = red, Co = green), (2) Photoresist spun onto surface (yellow), (3) Mask (dark blue) brought into contact with photoresist and exposed to UV light, (4) Photoresist developed and sample ion beam milled to remove the exposed thin film material, (5) Photoresist removed to reveal pattern.

tolithographic processes. The method described here is the result of careful experimentation and optimisation to give a process that was reproducible and provided the best results from the photolithograhpy. Fig. 5.3 summarises the steps used in the fabrication process.

Each sample was first given a dehydration bake at 110°C on a hot plate to ensure that there was no moisture present on the film surface. This is an important step as it helps photoresist-surface adhesion and prevents unwanted lifting of small features during photoresist development. The sample was removed from the hot plate and installed onto a spin-coater and allowed to cool briefly. The sample was covered with photoresist using a pipette and spun at 5500 rpm for 45 seconds. The photoresist was AZ5214E used as a positive photoresist, i.e. the area exposed to UV light becomes more soluble in the developer solution. The estimated photoresist thickness for this spin speed[1] was ∼1.2 μm. The spin coating was followed by a prebake of 50 seconds at 110°C to remove excess solvent from the photoresist prior to exposure.

The next step in the process was to produce the coplanar resonator pattern in the

[1]Clariant AZ5214E photoresist datasheet, available at `www.microchemicals.com`

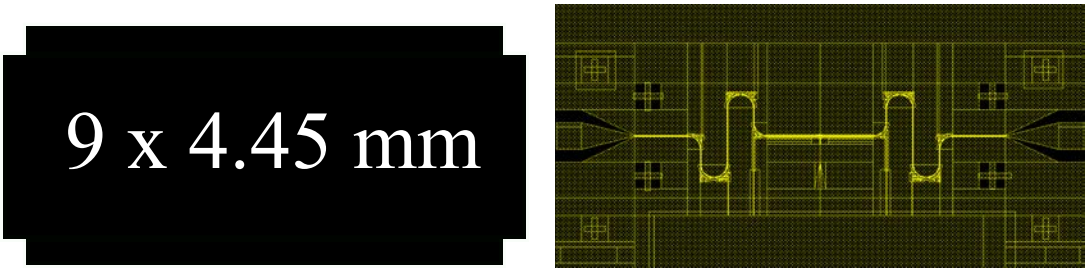

Figure 5.4: Left: Edge bead removal mask (not to scale). Right: Coplanar resonator mask (coupling capacitor gap = 4 μm, see Fig. 4.5 for more detail. Design by Dr J. E. Healey [117]).

photoresist. Two masks were used to accomplish this; Fig. 5.4 (left) shows the shape and dimensions of the edge bead mask used to remove the thicker photoresist from the sample perimeter that would otherwise have prevented good contact between the photoresist surface and the coplanar resonator mask. The photoresist was exposed using a Karl Süss MJB3 mask aligner in contact mode (i.e. the photoresist surface is brought into close physical contact with the mask). This mode has the advantage of being able to achieve small feature sizes, though it is vitally important that any dust/debris is removed from the mask before exposure. OptiClean peel-off lens cleaner was used to remove particulate matter that may have built up on the mask surface. For edge bead removal, an exposure time of 40 seconds was used. The photoresist was then developed using undiluted AZ726 MIF for 50 seconds followed by a thorough rinse in deionised water.

The coplanar resonator structure was then patterned into the photoresist. Fig. 5.4 (right) shows the mask design used by both the author and A. Bannykh to produce all coplanar resonator devices; this mask was originally designed and used in experiments by Dr J. E. Healey [117]. The dimensions of this resonator were given in table 4.1. The sample was brought into close contact with the resonator mask, exposed for 7 seconds, and developed for 30 seconds. At this stage it was crucial to inspect the resulting pattern under a high magnification microscope to look for potential short circuits between the central conductor and the ground planes and to decide whether or not to proceed based upon the quality of the resonator edges

defined in the photoresist. If there were any short circuits or the edge quality was deemed to be inadequate, the photoresist was washed from the surface with acetone and the entire process was repeated. If the photolithography results were satisfactory, the sample was baked at 110°C for 3 minutes before being placed into an argon ion beam miller.

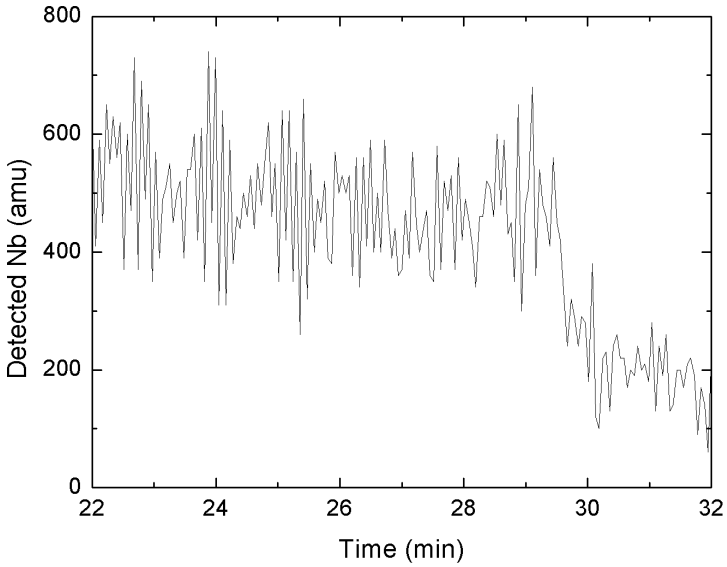

Figure 5.5: End point detection of 200 nm niobium milled at an angle of 45°.

The patterned films were milled using an Oxford Applied Research IM150 argon ion beam miller. The samples were stuck to the miller platform with vacuum grease. The platform is cooled, rotates, and can be tilted with respect to the ion beam; for consistency, all samples were milled at an angle of 45°. To estimate the milling time required, a mass spectrometer with end point detection software attached to the chamber was used to detect the amount of niobium removed from a 200 nm thick thin film over time. The result of this experiment is shown in Fig. 5.5 and shows that, for ions with an energy of approximately 500 eV, the niobium was removed from the substrate within 29 minutes. Since cobalt could not be detected by the mass spectrometer, a standard milling time of 50 minutes was used for each sample to allow for the extra film thickness. After milling, the samples were removed and inspected under a microscope. If there was no evidence of incomplete milling, the photoresist was removed with acetone.

5.1.3 Sample Nomenclature

As stated, samples were either fabricated by the author or by A. Bannykh of the University of Cambridge. In the following sections, each sample will be referred to using the following system:

$$S_X Y Z$$

where X is the sample set number which contains information about the structure, Y refers to the person who patterned the sample and Z is the cobalt layer thickness in nanometers. For example, $S_1G2.0$ refers to a sample made in deposition run #1 (where the structure for set #1 was defined in table 5.1), patterned by GMK (the author) with a cobalt layer thickness of 2 nm. It will become apparent in the discussion following the results that the fabricator is of some importance. A table summarising the properties of all samples measured is now given and should be referred back to if needed.

Table 5.2: Summary of all samples measured in this report where GMK is the author, AB is A. Bannykh from the University of Cambridge, and X is unpatterned.

Sample	Deposition number	Fabricator	Cobalt thickness (nm)
$S_1G0.0$	1	GMK	0.0
$S_1G0.4$	1	GMK	0.4
$S_1G0.8$	1	GMK	0.8
$S_1A1.2$	1	AB	1.2
$S_2G1.4$	2	GMK	1.4
$S_3A1.4$	3	AB	1.4
$S_1A1.6$	1	AB	1.6
$S_1G1.6$	1	GMK	1.6
$S_1G2.0$	1	GMK	2.0
$S_2G2.0$	2	GMK	2.0
$S_1A2.4$	1	AB	2.4
$S_3A2.6$	3	AB	2.6
$S_1G2.8$	1	GMK	2.8
$S_1G3.2$	1	GMK	3.2
$S_2X6.0$	2	Unpatterned	6.0
$S_2A10.0$	2	AB	10.0
$S_3A10.0$	3	AB	10.0

5.2 AFM Measurements

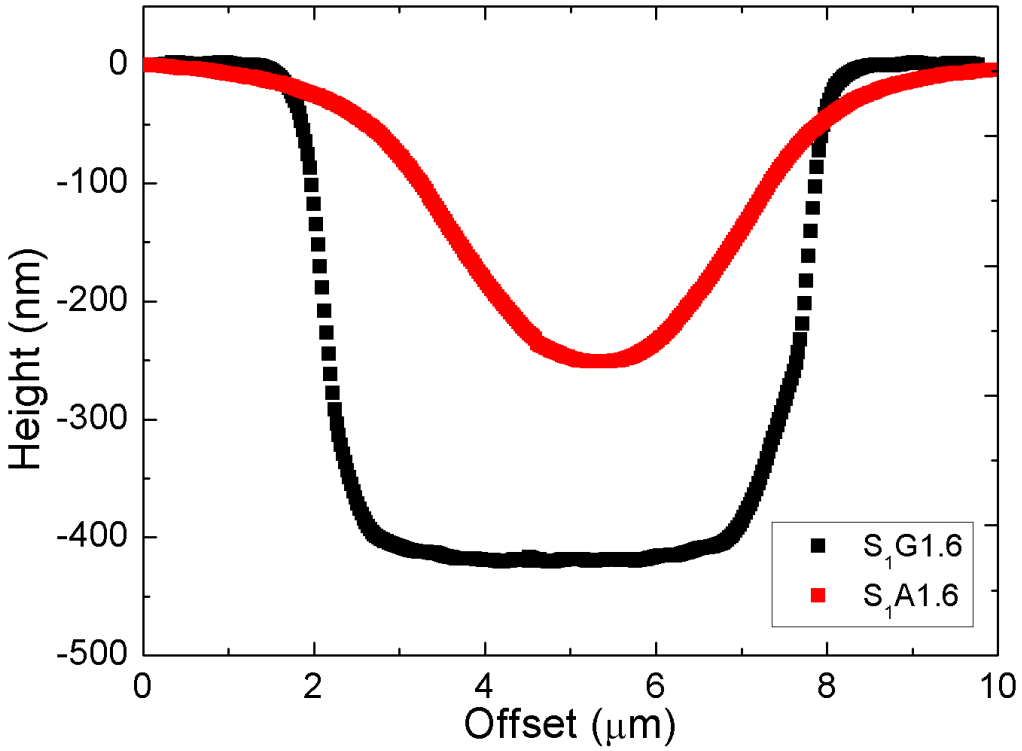

Figure 5.6: Examples of AFM step height measurements of the superconducting resonator centre track edges made in collaboration with Dr J. Bowen (Department of Chemical Engineering, University of Birmingham).

Step height measurements of the centre track edges of the patterned samples were made using Atomic Force Microscopy (AFM) to observe the quality of the fabrication. It was found that there was a marked difference in the edge profile of samples fabricated at the different research institutions. Fig. 5.6 shows step height measurements of two samples that are representative of the common difference in fabrication. In this figure, the top of the conducting films has been shifted to a measured height of 0 nm and the width of the milled dip is representative of w in Fig. 4.5. The black data points show the edge profile of sample $S_1G1.6$ and the red data points are the same measurement on sample $S_1A1.6$. For $S_1G1.6$, the slight change in step gradient shows where the substrate has been milled below the level of the surface where the thin film resides.

It will be shown in section 7.2.1 that the observed difference in the style of fabrication has a significant effect on the temperature dependence of the resonant frequency of a coplanar resonator and that differences in the edge profile must be accounted for when comparing the change in the resonant frequency as a function of temperature to Mattis-Bardeen theory.

5.3 Sample Material Characterisation

Three sets of films were deposited with differing structures and layer thicknesses as shown in table 5.1. Although the niobium thickness was maintained at 200 nm, the cobalt layer thickness was varied in the nanometer range (0 – 10 nm). While the deposition method ensured that the layer interfaces were subject to identical conditions within the same deposition run, the conditions may not have been consistent across different runs and may have lead to a variation in the material properties (either superconducting or ferromagnetic). Measuring how the magnetic moment scales with cobalt thickness can also provide information about the deposition conditions, film quality, and error in the estimated film thickness. With this in mind, material characterisation of the thin films structures was undertaken to enable a better comparison of the films within a single set and of those deposited over different runs.

A limited number of measurements were conducted by A. Bannykh at the University of Cambridge. The magnetic properties of a selection of samples were measured using a Vibrating Sample Magnetometer (VSM) at room temperature (results shown in Fig. 5.10) and T_C was observed for a single sample per set. Since the microwave measurements were made at low temperatures, it was felt necessary to measure the magnetic properties at a similar temperature. A Quantum Design MPMS-XL (Magnetic Property Measurement System-XL) was used by the author to investigate both the superconducting and the magnetic properties of the samples over a wide range of temperatures.

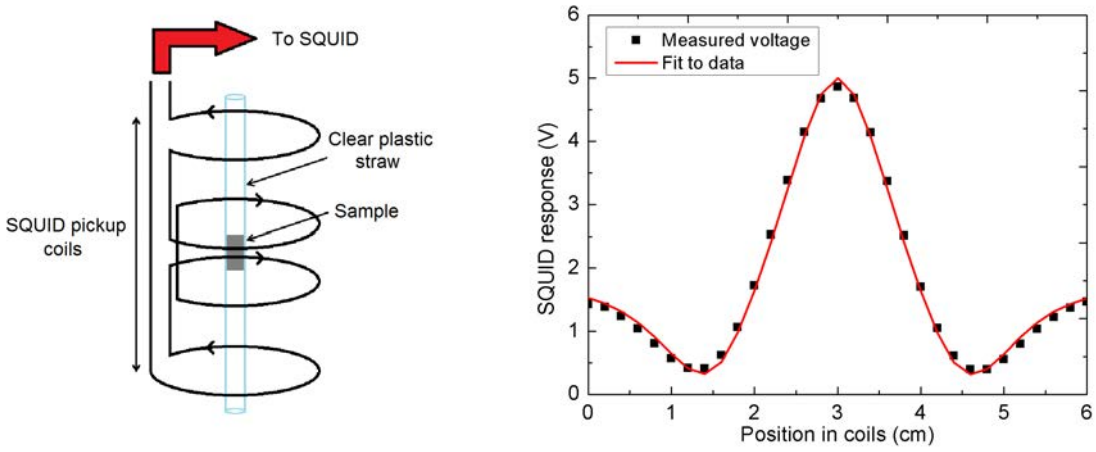

Figure 5.7: Left: Schematic diagram of the MPMS-XL measurement technique. Right: An example of the resulting SQUID response as sample moves through the coils (sample $S_2A10.0$ at 12 K and H_{app}=0 Oe).

The MPMS is a SQUID magnetometer with a quoted sensitivity of 5×10^{-9} emu when operated in Reciprocating Sample Option (RSO) mode[2]. To make a measurement, the samples were held upright in a clear plastic drinking straw and positioned such that a magnetic field was applied parallel to the film. In RSO mode, the sample is moved up and down in a rapid, continuous and sinusoidal fashion through a second-order superconducting gradiometer that forms a closed flux-transformer coupled to a SQUID, as shown in Fig. 5.7 (left). The output voltage of the SQUID in response to the sample movement is measured as a function of sample position and fitted to an ideal dipole response to provide the sample magnetic moment, as shown in Fig. 5.7 (right). The amplitude of the response is used to determine the magnitude of the magnetic moment. To improve the signal-to-noise ratio of the measurement, a number of scans were averaged for each data point taken.

5.3.1 Magnetic Characterisation

For superconductor-ferromagnet multilayered systems there are many reports of a small thickness of the ferromagnet at the interface that does not contribute magnetically, often called a 'dead layer' [133–135]. Early experimental work by Lieber-

[2]Quantum Design, Inc. `www.qdusa.com`

mann et al [136] showed a dead layer thickness, d_{DL}, of two atomic layers on iron films grown by electrodeposition; the work was soon extended to the study of dead layers in nickel and cobalt [137]. The thickness of d_{DL} is material dependent; typical d_{DL} of cobalt, for example, ranges from $0.7-1.2$ nm while d_{DL} for a dilute ferromagnet can be much thicker (for example $5-8$ nm for Ni_3Al [33]). SFS junctions with a strong ferromagnetic barrier will inevitably be more sensitive to variation in d_{DL} as the barrier layer must be thin compared to weaker ferromagnets to allow Josephson coupling. The magnetic properties, particularly the dead layer, appear to be hard to control during deposition, meaning that devices fabricated from thin films from different deposition runs may suffer from irreproducibility in junction behaviour, as was noted by Bell et al [60].

To investigate the properties of the cobalt layer alone, hysteresis loops for each sample were measured at both 12 K and 300 K. These temperatures were selected for several reasons; the microwave measurements were made at low temperatures and therefore a measurement of the saturation magnetisation, M_S, was necessary at a similar temperature. Covering a large temperature range allowed investigation of the magnetic dead layer properties; a temperature dependent d_{DL} might indicate a region of material with a reduced Curie temperature compared to the rest of the thin film layer.

Fig. 5.8 shows an example of (uncorrected) hysteresis loops measured at 12 K and 300 K for sample $S_1A1.6$ over a range of applied field of ± 10 kOe. The data shown are representative of all samples measured and illustrates two important factors that were taken into account when deducing M_S/area (shown in final form in Fig. 5.10). Firstly, Fig. 5.8 shows that the data consist of a ferromagnetic signal in combination with a diamagnetic background signal that provided an overall negative slope that was similar across all samples. The source of this background signal is believed to mainly originate from the substrate though will also include any other signals present (diamagnetic or otherwise). The extracted value of M_S(sample) from Fig. 5.8 was given by linear fits to data points $> \pm 5$ kOe. Above this field the sample

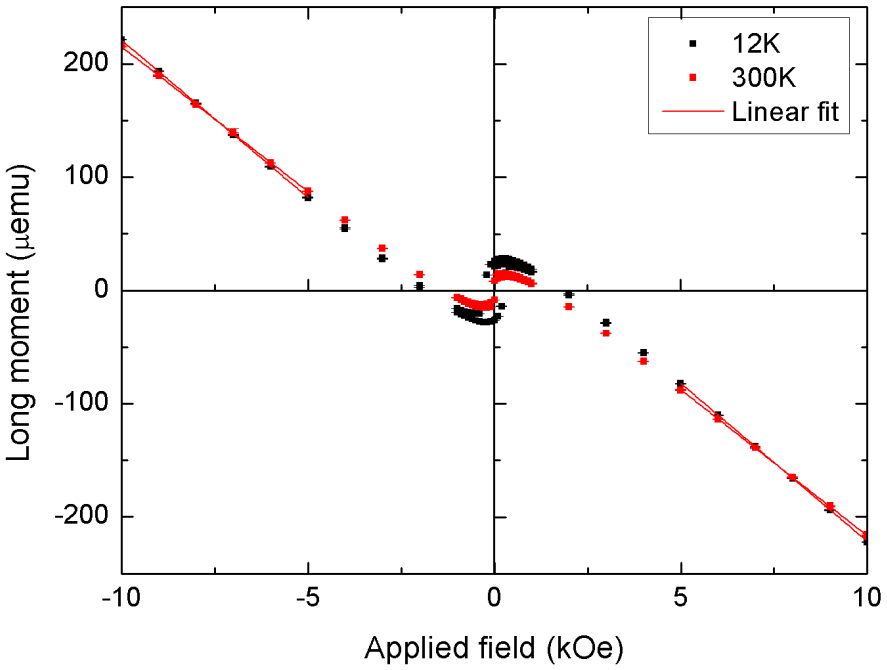

Figure 5.8: Hysteresis loops measured at 12 K and 300 K on sample $S_1A1.6$ with linear fits for $H > \pm 5$ kOe used to determine M_S(sample).

magnetisation is fully saturated and the response is linear and reversible; linear fits were performed for positive and negative applied fields and averaged to deduce M_S(sample).

The second feature illustrated by Fig. 5.8 is that the uncorrected data show that M_S(sample) was temperature dependent and changed by (1.69±0.12) μemu between 12 K and 300 K; a similar temperature dependence was shown by all samples. This temperature dependence could be attributed to a change in the magnetic behaviour of the dead layer. However, the measurement temperatures used here are well below T_{Curie} of bulk cobalt such that the magnetisation would be expected to be constant over this range. All films were deposited onto sapphire substrates and it was shown by Salzer et al [138] that ferromagnetic-like behaviour is often observed in sapphire due to impurities and surface contaminants. The magnitude of M_S of sapphire samples was reportedly reduced by more than half after careful cleaning using an acid or acetone ultrasonic bath for up to a day. Thorough cleaning of the samples measured here proved to be difficult due to film adhesion problems; vigorous cleaning

with an ultrasonic bath often resulted in film lift-off. Each sample was cleaned gently prior to magnetic measurement whilst avoiding film lift-off.

As shown schematically in Fig. 5.7 (left), a plastic drinking straw was used to hold the samples. To fit the samples inside, a 'door' was cut into the straw and bent around the sample which was then held in place with PTFE tape. Contamination through the use of stainless steel tools is known to give a small ferromagnetic response to an otherwise non-magnetic material [139] and it is noted that any deformation of the straw used to hold the sample can produce a small background signal [140]. Sample manipulation with stainless steel tweezers was unavoidable and, as noted above, vigorous cleaning proved to be problematic. To account for any signal from contamination, the same straw was used for each measurement with a similar amount of clean PTFE tape, and it was assumed that a similar level of contamination would be present on each measurement.

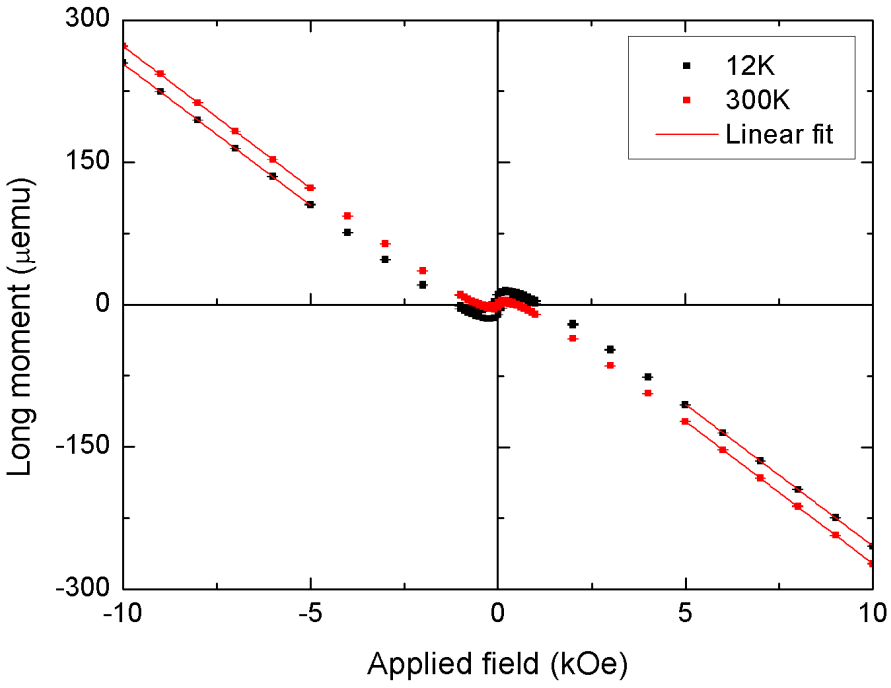

Figure 5.9: Hysteresis loops of the addenda (straw, PTFE and blank substrate) at 12 K and 300 K with linear fits for applied fields $> \pm 5$ kOe used to determine M_S(addenda).

A measurement of M_S(addenda) (straw, PTFE and a blank sapphire substrate)

is shown in Fig. 5.9, which shows a temperature dependent ferromagnetic signal combined with a diamagnetic background. Investigation of the contamination confirmed the manipulated straw as a source; measurement of an uncontaminated straw yielded a magnetic moment of < 0.1 μemu and cutting the straw with stainless steel scissors immediately produced a measurable signal. To correct and normalise values of M_S the estimated film area, A, was used as follows:

$$M_S/\text{area} = \frac{\text{M}_\text{S}(\text{sample}) - \text{M}_\text{S}(\text{addenda})}{\text{A}}. \tag{5.1}$$

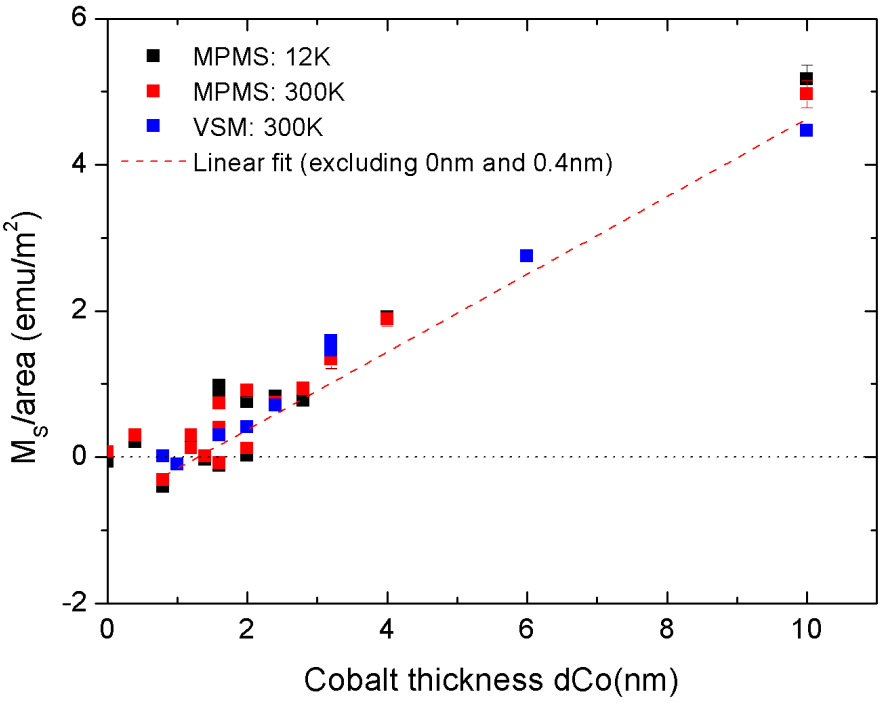

Figure 5.10: Normalised M_S for thin film superconductor-ferromagnet samples at 12 K and 300 K with a linear fit to all data excluding samples $S_1G0.0$ and $S_1G0.4$. The black dotted line shows the level of zero magnetisation. All samples belong to set #1 excluding samples $S_2G1.4$, $S_2G2.0$ (lower M_S/area), $S_2X6.0$ and $S_2A10.0$ (VSM).

Values of M_S/area are presented in Fig. 5.10, which shows the saturation magnetisation per unit area for samples taken from sets #1 and #2[3]. The graph shows measurements made at 12 K and 300 K and compares measurements made using

[3]Samples taken from set #2: $S_2G1.4$, $S_2G2.0$ (lower M_S/area), $S_2X6.0$ and $S_2A10.0$ (VSM).

the MPMS to those made by A. Bannykh using VSM at room temperature. The two measurement techniques gave results that are in good agreement. A linear fit to the data is shown for all samples excluding $S_1G0.0$ and $S_1G0.4$. It is believed that these two samples have a significantly thicker cobalt layer above the quoted error of ± 0.2 nm reported in Ref. [31] (for further discussion and complementary evidence to support this hypothesis see section 7.1.2).

Fig. 5.10 shows that M_S/area increases linearly with increasing cobalt thickness and decreases to zero magnetisation at a finite cobalt thickness. This is taken as the thickness of the magnetic dead layer, d_{DL}. A linear fit that excludes samples $S_1G0.0$ and $S_1G0.4$ finds that $d_{\mathrm{DL}} \sim 1.3$ nm. This result is similar to other reported measurements [37], including for films produced using the same deposition system [31, 32]. By contrast, Fig. 5.10 shows more scatter on the data points. This partially arises from the broad subtraction of M_S(addenda) taken from a single measurement which is similar in magnitude to M_S(sample) in the case of the thinner layers. Accordingly, as the layer thickness increases the scatter decreases.

It is noted, however, that the overall scatter may not entirely be the result of measurement inaccuracy. Repeat measurements of sample $S_1A1.2$ made several months apart gave values of M_S/area(12 K) of (1.45 ± 0.17) μemu and (1.45 ± 0.71) μemu (data points in Fig. 5.10 are almost exactly overlaid). This shows that the measurement itself and the subsequent analysis provides a good degree of reproducibility and that the cobalt layer magnetisation does not change or degrade over this timescale. It is also noted that the photolithographic process did not change the ferromagnetic properties of the films. Sample $S_1G1.6$ was measured before ((1.92 ± 0.17) μemu) and after ((1.93 ± 0.12) μemu) patterning which showed that M_S/area agrees to within experimental error. Fig. 5.10 also shows that samples measured from set #2 generally have a lower M_S/area than similar samples from set #1. This is also reflected in later measurements (see section 7.1.2).

The overall scatter on M_S/area(dCo) could be an indication of low quality cobalt leading to a reduced value for the bulk magnetisation, M_B. To gain an estimate of

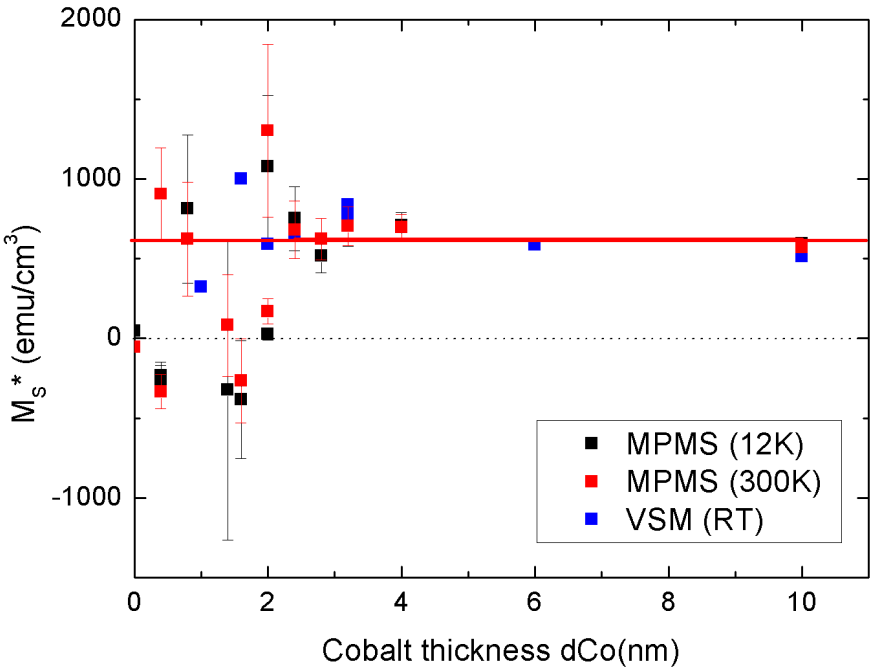

Figure 5.11: Saturation magnetisation per unit active volume for 12 K and 300 K with outliers removed (see text). The solid red line shows a horizontal linear fit to data points where $d_{\mathrm{Co}} > 2$ nm which gives an estimate of the bulk magnetisation of (622 ± 25) emu/cm^3.

M_B, the analysis in Ref. [31] was followed. Fig. 5.11 shows the magnetisation per unit *active* volume as a function of the cobalt thickness given by

$$M_S^* = \frac{M_S}{A(d_{\mathrm{Co}} - d_{\mathrm{DL}})} \tag{5.2}$$

where A is the estimated surface area of the film, d_{Co} is the quoted cobalt thickness and d_{DL} is the dead layer thickness as estimated from the dashed red line in Fig. 5.10). The magnetisation increased for small d_{Co} before plateauing at a value corresponding to the bulk magnetisation. For thin films made in the same deposition system, $M_B \sim 1000$ emu/cm^3 has been reported [31]. The quoted value of M_B for bulk cobalt is 1422 emu/cm^3 [141]. Fig. 5.11 provides an estimate of $M_B = (622 \pm 25)$ emu/cm^3 given by a horizontal linear fit to data points where $d_{\mathrm{Co}} > 2$ nm. Some outlying data points were removed in the regime where $d_{\mathrm{Co}} \approx d_{\mathrm{DL}}$. The estimated value of M_B implies that the ferromagnetism in these samples is com-

paratively weak. Magnetic measurements made using different techniques (MPMS and VSM) agree well so it can be concluded that the cobalt deposited on the samples measured here does indeed show a reduced value of M_B.

The main conclusions to draw from the results of magnetic characterisation of these samples can now be summarised:

- A magnetic dead layer thickness of $d_{\mathrm{DL}} \sim 1.3$ nm is observed.
- d_{DL} is temperature independent and does not change over a timescale of at least months.
- Patterning does not affect the ferromagnetic properties of the samples.
- A reduced value of $M_B = (622 \pm 25)$ emu/cm^3 is found which is low compared to the value quoted in the literature [141].

5.3.2 Superconductor Characterisation

The superconducting properties of the samples were also measured using the MPMS. The proposal for CPR measurement via a coplanar resonator relies on good quality niobium to provide a high Q resonator; due to the antagonistic nature of superconductors and ferromagnets, T_C can be rapidly suppressed due to the breaking of the Cooper pairs through the exchange interaction. T_C measurements were made to ensure that the presence of a thin ferromagnetic layer did not degrade the superconducting properties to such an extent that would lead to poor device performance.

There are numerous publications that show that varying the thickness of a ferromagnetic layer in close proximity to thin superconducting layers can lead to the observation of an oscillating T_C. This has been shown to occur in both multilayer [142, 143] and bilayer systems [40, 131] but it should be noted that publications reporting a nonmonotonic dependence of T_C on the ferromagnetic thickness typically involve thin superconducting layer thicknesses (typically < 50 nm). Zdravkov et al [38]

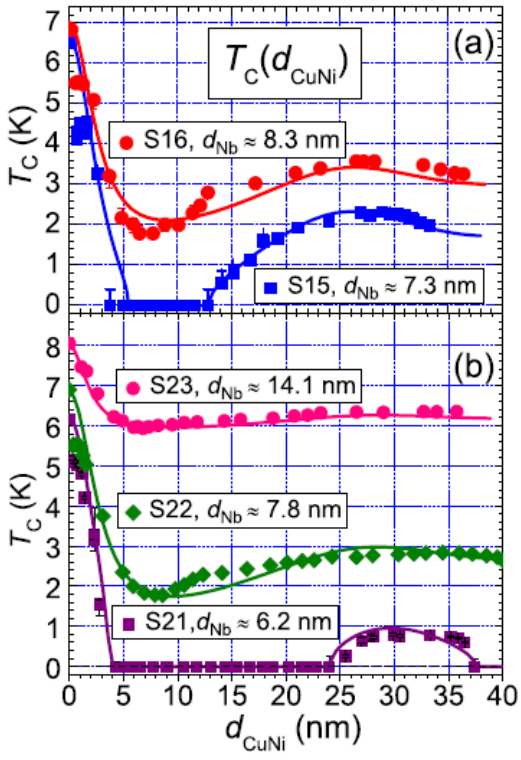

Figure 5.12: Results by Zdravkov et al [38] showing T_C for bilayer samples with varying niobium thicknesses as $d_{Cu_{41}Ni_{59}}$ was varied. The solid lines are fits to theory as discussed in the publication.

studied reentrant superconductivity in superconductor/ferromagnetic alloy bilayers with select results shown in Fig. 5.12; by observing T_C as the ferromagnetic layer thickness was varied on niobium films of varying thickness, behaviour moved from strong T_C suppression and convincing reentrant behaviour to relatively weak T_C suppression and a shallow minimum (i.e. the effect of the ferromagnet on the superconductor appeared to be reduced). It is therefore noted that the amplitude oscillation in T_C is strongly sensitive to the superconductor thickness.

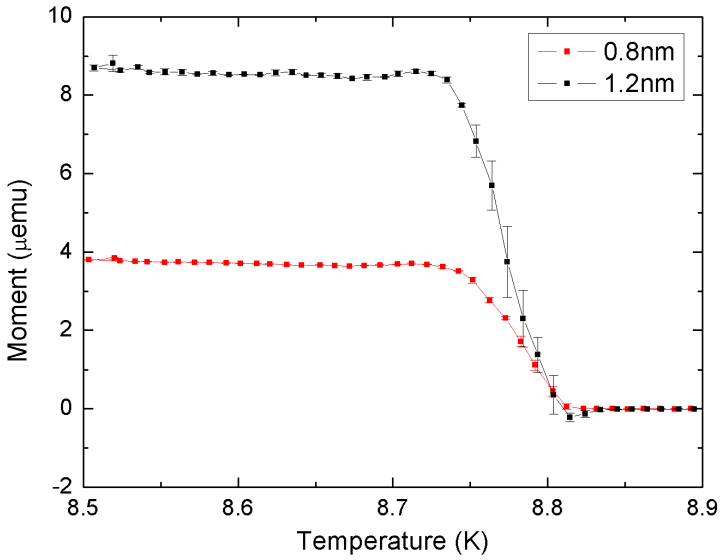

Figure 5.13: T_C measurements for samples $S_1G0.8$ (red) and $S_1A1.2$ (black) where the cobalt thickness is given in the legend. Due to a large overall difference in the moment of the samples (from the cobalt), the data have been shifted vertically to clearly show T_C for both samples simultaneously.

Fig. 5.13 shows representative data of T_C measurements for samples $S_1G0.8$ and $S_1A1.2$ made using the MPMS in an applied field of 0.1 Oe. The absolute value of the signal is dependent on the magnetic history of the cobalt; to clearly show the superconducting transition of both samples, the data sets have been shifted to agree at 0 μemu above T_C. There is a clear step between superconducting and normal behaviour. Determination of T_C via magnetic measurement can be more difficult to interpret than measuring resistance as a function of temperature particularly due to the presence of a ferromagnetic layer; while this measurement is not as well defined as an $R(T)$ measurement, here T_C is taken as 50% of the transition. Comparing the

values of T_C deduced from the MPMS to the $R(T)$ measurement shown in Fig. 5.2, it can be seen that the latter measurement provides a slightly higher $T_C = 8.85$ K. The difference could be explained by the method of measurement; it is expected that a magnetic measurement might produce a lower value of T_C with a larger transition width as this method interrogates the entire sample rather than a single superconducting pathway within the film.

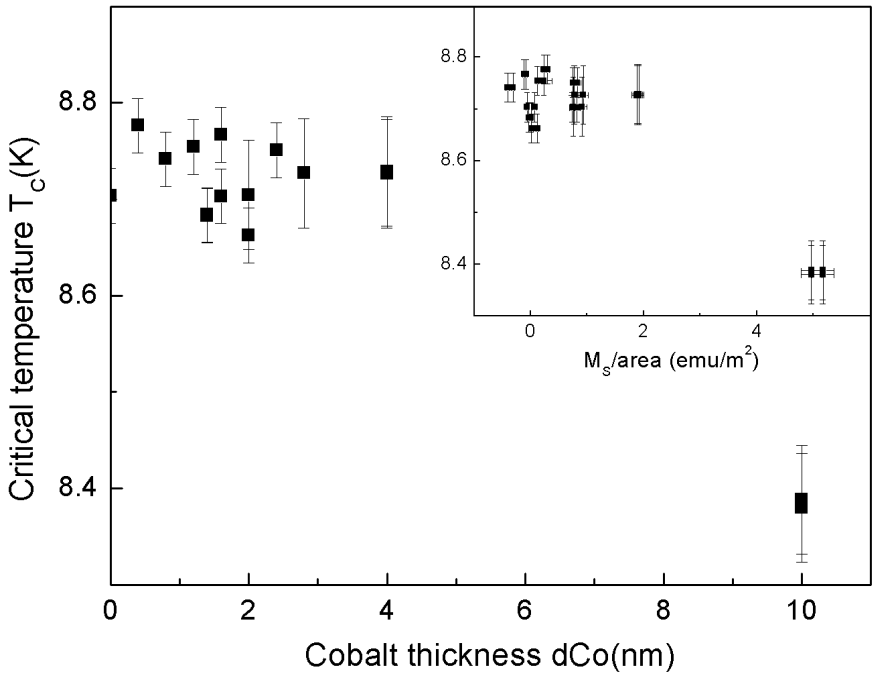

Figure 5.14: T_C for samples (sets #1 and #2) measured using the MPMS. Samples from set #2 are $S_2G1.4$ and $S_2G2.0$ (lower). Inset: T_C as a function of the saturation magnetisation per unit area as shown in Fig. 5.10.

As d_{Co} was varied in the range $0 - 4$ nm there was no systematic variation in T_C to within experimental error, as shown in Fig. 5.14 as a function of d_{Co} and M_S/area. This should not be surprising given the results presented by Zdravkov et al in Fig. 5.12 since d_{Nb} was maintained at 200 nm for all samples. T_C measurements typically followed the completion of a hysteresis loop (which ended at 10 kOe) but not in all cases. It has been shown by Kinsey et al [144] that the magnetic history of cobalt on niobium can influence T_C through domain formation; here the aim was simply to gain an estimate of T_C to assess the material suitability for device fabrication rather than to make a detailed study of the superconductor-ferromagnet

interaction. Measurement of $T_C(d_{\mathrm{Co}})$ does show that for thicker cobalt layers, T_C shows signs of suppression (for $d_{\mathrm{Co}} = 10$ nm). For the purposes of the CPR measurement device, this is inconsequential as the cobalt thickness range of interest is < 4 nm where no suppression was observed [31, 37].

Although material characterisation measurements made using the MPMS are often difficult to interpret, the great advantage is one of automation and these results show that a thin cobalt layer on 200 nm of niobium does not suppress T_C to such a degree that the materials would not be useful for fabricating resonator devices.

CHAPTER 6

MICROWAVE MEASUREMENT AND DATA ANALYSIS TECHNIQUES

This chapter describes the experimental and data analysis techniques used to perform microwave measurements on coplanar resonator samples. The method of sample mounting and the low temperature experimental setup are first documented before a method of extracting the resonant frequency and quality factor from an asymmetric lineshape is presented. This was a necessary step in the complete data analysis process due to the low quality factor of the majority of samples measured. Finally, the method used to compare the temperature dependence of the resonant frequency to Mattis-Bardeen frequency is described.

6.1 Experimental Method for Microwave Measurements

6.1.1 Sample Mounting

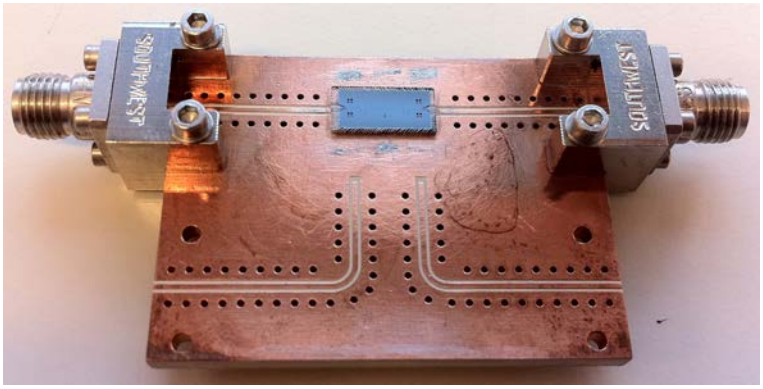

Figure 6.1: Patterned launcher board with soldered board-mounting SMA connectors and a wirebonded sample (lower two lines not used) [117].

To measure the microwave properties of the thin film structures, the launcher board shown in Fig. 6.1 was used to hold the sample and enabled direct wirebond connections to be made to the fan-like structure patterned into the film which allowed microwaves to be coupled to the centre conductor of the resonator (see Fig. 5.4 (right)). The board[1] was designed and used in experiments by Dr J. E. Healey [117]; it also has a coplanar transmission line structure so that microwaves can be passed to and collected from the sample via board-mounting stainless steel SMA connectors and was designed with a 50 Ω impedance to avoid reflection of the microwave signal. The inner pins of the SMA connectors were soldered to the inner conductor of the coplanar transmission line etched into the launcher board and the outer of the SMA connector was screwed onto the ground plane. The connectors also acted as mechanical support for the sample housing; its gold plated copper box is shown in Fig. 6.2.

The samples were mounted onto the launcher board using the peel-off lens cleaning solution OptiClean which, along with being an excellent tool for cleaning masks used in photolithography, proved to be an effective low temperature adhesive. Ini-

[1]Rogers Corporation Advanced Circuit Materials, RT/Duroid 6010 LM

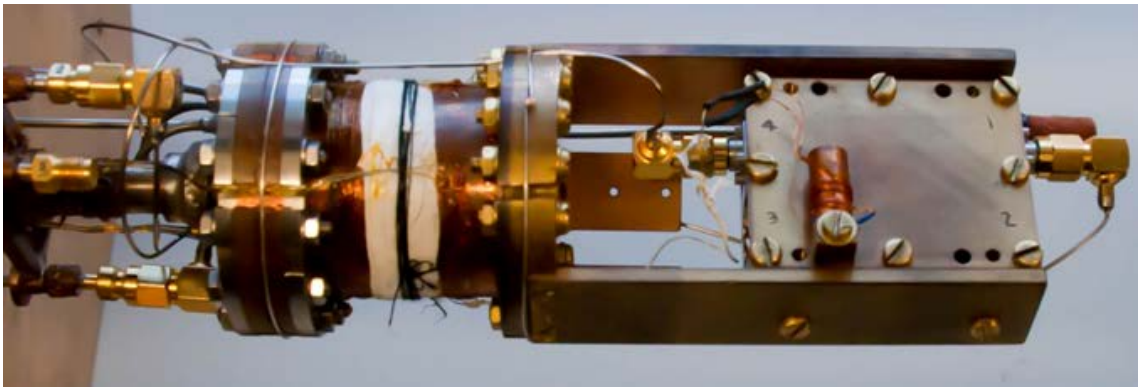

Figure 6.2: Photograph of the sample box with a ruthenium oxide thermometer mounted onto the cryostat.

tially, varnish was used as the bonding agent but was found to crack readily under thermal cycling. As it was unclear at which time the cracking occurred, the sample may then have only been cooled by thermal conduction through the wirebonds. OptiClean acted as an effective quick-drying adhesive that appeared to remain slightly malleable after many thermal cycles.

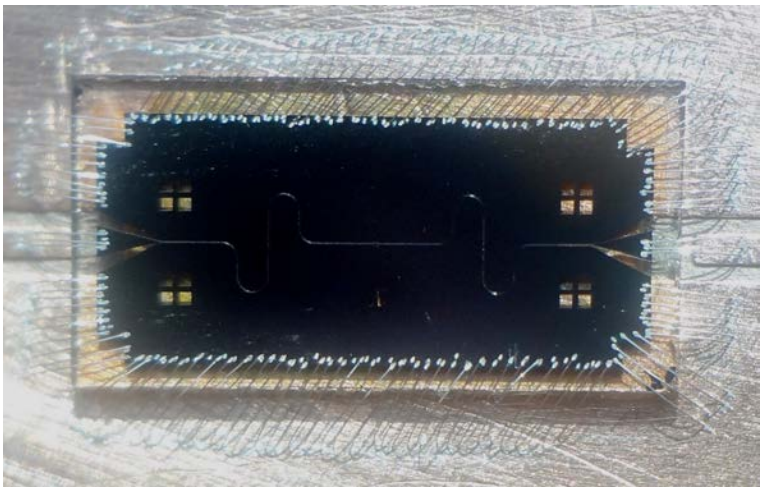

Figure 6.3: Photograph of a coplanar resonator sample to show the number and spacing of the wirebonds used.

Once a sample was mounted and the adhesive had dried, many aluminium wirebonds (each with a diameter of 25 μm) were used to connect the ground planes of the sample and board together, and the centre conductor of the board's coplanar transmission line to the fan-like structure on the patterned sample that couples microwaves to the resonator via a capacitive gap. It was noted by Wenner et al [145] that best

performance is provided by many uniformly spaced, closely packed short wirebonds. Efforts were made to adhere to this style; a total of approximately 130 wirebonds were used per sample as shown in Fig. 6.3.

6.1.2 Low Temperature and Microwave Apparatus

Figure 6.4: Photograph of the microwave measurement system. The glass fibre dewar houses the sample and a pair of slightly separated Helmholtz coils can be used to apply a magnetic field. The laptop controls the network analyser and temperature controller. The pump (shown right) is connected to the 1 K pot.

A photograph of the apparatus used to measure the microwave response of the coplanar resonators is shown in Fig. 6.4. The equipment shown here was initially used for other experiments involving coplanar resonator samples conducted within the research group [117]. The setup consisted of a means of cooling the devices to $\sim$1 K and reliably changing the temperature thereafter, a network analyser to initiate and measure the resulting microwaves that passed through the sample, and a set of coils either side of the dewar were used to apply a magnetic field perpendicular to the sample. A LabView program was written by the author to automate the experiment. A block diagram to illustrate the connections made between the pieces

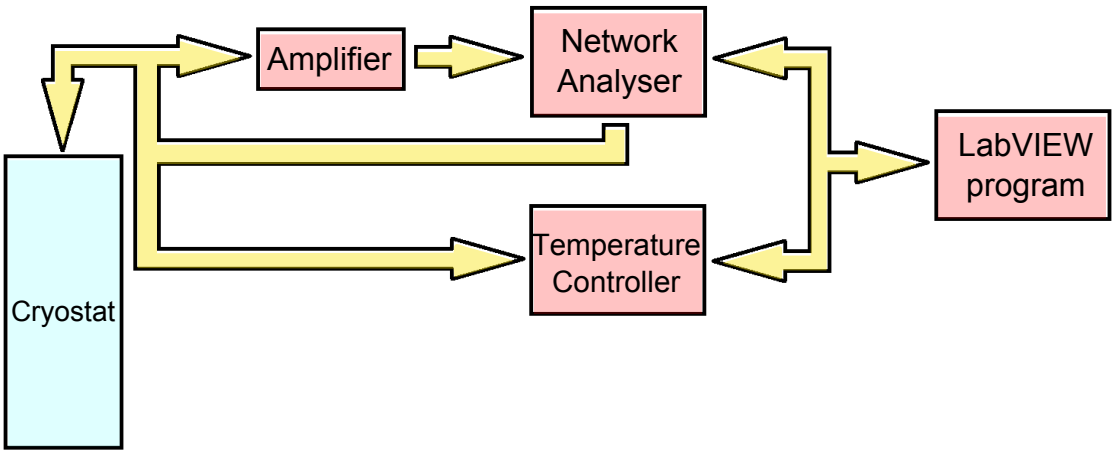

Figure 6.5: Block diagram of the measurement system shown photographed in Fig. 6.4.

of equipment is shown in Fig. 6.5.

Cooling Apparatus

The glass fibre helium dewar shown in Fig. 6.4 holds a cryostat that carries a vacuum can, the insides of which are separated from the liquid ^{4}He bath by an indium seal. Inside the vacuum can is a 1 K pot; to achieve low temperatures, this pot can be filled with a small amount of ^{4}He by pumping liquid from the dewar via a needle valve. Once filled, the needle valve is closed and the pressure above the liquid helium is reduced by continuing to pump on the liquid, thereby lowering the temperature to $\sim$1 K by evaporative cooling. The sample box was secured between two copper supports attached to the 1 K pot (shown in detail in Fig. 6.2) such that the superconducting resonators were cooled by conduction through the cryostat materials. The advantage of this method is that the samples were not in direct contact with the ^{4}He bath.

The temperature of the 1 K pot was monitored, changed and stabilised using a Lakeshore 340 temperature controller. A cernox thermometer (with a calibrated range of 100 mK – 300 K) and a heater wire mounted directly onto the pot allowed fine control of the temperature. A set point temperature can be entered into

the temperature controller and, using pre-programmed PID settings[2], a current is passed through the heater wire to reach and maintain the chosen temperature. The temperature controller interfaced with a LabView program[3] which was developed to record the microwave response of the devices as a function of temperature. A temperature range could be specified along with the value that the temperature should be incremented by. The program contained a 'wait' period to allow for thermal lag in the system before recording microwave transmission data from the network analyser, along with the sample temperature that was measured using a ruthenium oxide thermometer attached directly to the sample box.

Microwave Apparatus

Upon reaching the required temperature and being prompted by the LabView program to do so, the microwave response of a sample was measured using a two-port HP 8720D network analyzer. A microwave signal was passed from the first port of the network analyser via semi-flexible coaxial cable to an SMA connector at the top of the cryostat. From there, the signal was passed down the cryostat through rigid 2.2 mm cupronickel coaxial cable to the top of the vacuum can. Inside the can, the microwave signal was then carried by 1 mm brass coaxial cable before being passed into the sample box via the board mounting SMA connectors shown in Fig. 6.1. Once through the sample, the signal was passed up the other side of the cryostat and through a Miteq amplifier with a gain of 36 dB at 6 GHz and a noise figure of 5 dB. Finally, the signal was collected by the second port of the network analyser (further information about microwave measurements will be given in section 6.2.1). Each measurement was averaged 16 times before being sent to the computer where it was saved in labelled files for further analysis.

The microwave response of the cryostat cables alone is shown in Fig. 6.6, along with the network analyser noise floor and a measurement of the signal (∼10 dB

[2] $P = 1000$, $I = 200$, $D = 2$.

[3] Written in collaboration with Dr A. Frommhold, Department of Electronic, Electrical and Computer Engineering, University of Birmingham (2010).

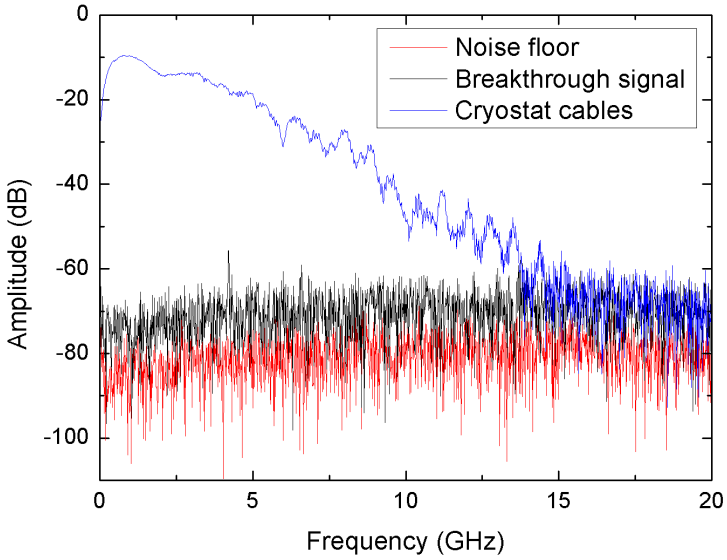

Figure 6.6: $S_{21}(f)$ of the the network analyser noise floor, signal transmitted across the launcher board in the absence of a sample, and the attenuation properties of the cryostat cables for a signal power of -30 dBm (all at room temperature).

above the noise floor) that is transmitted across the launcher board in the absence of a sample at room temperature. It is beneficial to keep this 'breakthrough signal' to a minimum so as to maintain a Lorentzian lineshape in the resonant peak of the superconducting device [146]; a detailed discussion on the subject of dealing with this breakthrough signal during data analysis will be given in section 6.2.2. The cables alone showed approximately 20 dB of attenuation at 6 GHz; this was consistently removed from the sample measurements using the network analyser's memory function.

Magnetic Field Application

An external magnetic field of ± 0.2 mT could be applied to the samples which were centrally located between (slightly separated) Helmholtz coils. The coils were mounted on a rotating platform to enable orientation of the field while the sample remained at low temperatures (inherited from experiments by Dr J. E. Healey [117]). Due to the sample geometry, the resonant frequency of a superconducting coplanar resonator is maximally perturbed when the field is applied perpendicular to the

film [93]. While the sample orientation was clearly marked on the cryostat, the coils were rotated as a field of 0.12 mT was applied to find the angle which provided the maximum shift of f_0 for $T < T_C$. Once properly orientated, the field was removed and the sample was warmed above T_C and subsequently re-cooled in zero applied field to $T = 1.12$ K to begin field dependence measurements.

6.2 Data Analysis Techniques

Microwave measurement of coplanar resonators yielded a large amount of data for which the analysis process was largely automated. The LabView program described in section 6.1.2 tabulated f_0 and Q as determined by the network analyser, though this is only useful for samples that exhibit a symmetric resonant peak with a high quality factor. The presence of a normal metal layer dramatically increased the losses of the superconducting resonator and resulted in a lowered Q, often with an asymmetric resonant peak. This section describes how f_0 and Q were extracted from $S_{21}(f)$ collected during the experiments and how, by plotting $f_0(T)$, a comparison was made with Mattis-Bardeen theory.

6.2.1 Data Collection: Scattering Parameters

To investigate the properties of superconductor-ferromagnet bilayer coplanar resonators, $S_{21}(f)$ was collected using a network analyser. The quality factor was typically $< 10,000$ and resonant peaks were often found to be asymmetric. Parasitic resonances may produce phase shifts which can create these asymmetries and make parameter extraction by the network analyser inaccurate. It is therefore important to understand the basics of network analyser operation in order to fit a theoretical model to the data to enable an accurate determination of the resonant frequency and the quality factor.

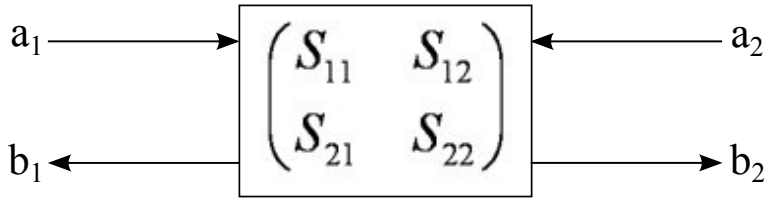

Figure 6.7: Diagram of a two-port network where a_n is the incoming voltage wave at each port, b_n is the outgoing voltage wave and n is the port number.

Network analysers measure scattering parameters (s-parameters), which contain information about the magnitude and the phase of signals as they interact with the network. Fig. 6.7 shows a schematic diagram of a two-port measurement system; s-parameters describe how an n-port network responds to propagating signals.

From Fig. 6.7, the scattering matrix can be defined as:

$$\begin{pmatrix} b_1 \\ b_2 \end{pmatrix} = \begin{pmatrix} S_{11} & S_{12} \\ S_{21} & S_{22} \end{pmatrix} \begin{pmatrix} a_1 \\ a_2 \end{pmatrix} \tag{6.1}$$

S-parameters are written as S_{ij}, for which i is the responsive port and j is the port that initiates the signal. Expanding the scattering matrix gives the following equations:

$$b_1 = S_{11}a_1 + S_{12}a_2 \tag{6.2}$$

and

$$b_2 = S_{21}a_1 + S_{22}a_2. \tag{6.3}$$

S_{21} is therefore

$$S_{21} = \frac{b_2}{a_1}, \tag{6.4}$$

which shows that S_{21} is the ratio of the signal emerging from port 2 as a result of a signal that has passed through the sample after being initiated by port 1. Since a_n and b_n are vectors, this allows the measurement of the magnitude and the phase of the signals. The magnitude (a voltage ratio) of s-parameters is given in decibels by

$$S_{ij}(\text{dB}) = 20\log_{10}(|S_{ij}|) = 20\log_{10}\left(\frac{|V|}{V_0}\right). \tag{6.5}$$

The experiments described in chapter 7 provided $S_{21}(f)$ for a range of temperatures; a theoretical model of $|V|$ can be fitted to the data after the antilog of S_{21} is calculated, as will be described in the following section.

6.2.2 Fitting to Resonant Peaks

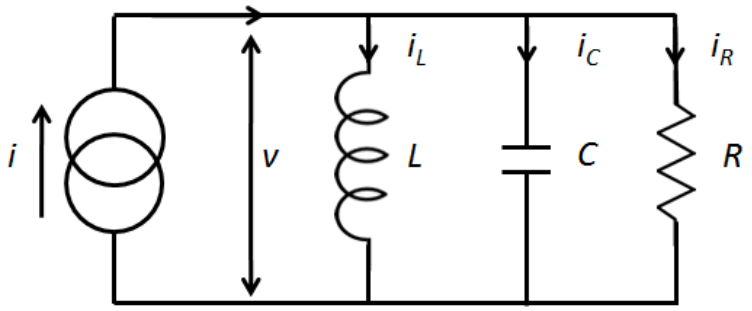

Figure 6.8: Schematic circuit diagram of a coplanar resonator modeled as a parallel LCR circuit.

A theoretical model was developed to accurately determine f_0 and Q from $S_{21}(f)$ where the results of this analysis were used to assess the performance of the materials and their application to a microwave CPR measurement device. All measurements of the resonant peak were made at signal powers low enough to avoid nonlinearity in the microwave response. To derive an expression for $|V|$ in the linear regime, the coplanar resonator was modeled as a parallel LCR circuit, shown in Fig. 6.8.

If the circuit is driven by a current $Ie^{i\omega t}$, which has amplitude I and frequency ω, the voltage V is given as follows:

$$V = \frac{i\omega I/C}{(\omega_0^2 - \omega^2) + i\omega/\tau} \tag{6.6}$$

where $\tau = RC$ and $\omega_0^2 = 1/LC$. The real part of the voltage is

$$V_{Re} = \frac{\omega^2 I/C\tau}{((\omega_0^2 - \omega^2)^2 + \omega^2/\tau^2)} \tag{6.7}$$

and the imaginary part of the voltage is

$$V_{Im} = \frac{I\omega/C(\omega_0^2 - \omega^2)}{((\omega_0^2 - \omega^2)^2 + \omega^2/\tau^2)}. \tag{6.8}$$

Therefore the magnitude of the voltage is

$$|V| = \sqrt{\left[\frac{\omega^2 I/C\tau}{((\omega_0^2 - \omega^2)^2 + \omega^2/\tau^2)}\right]^2 + \left[\frac{I\omega/C(\omega_0^2 - \omega^2)}{((\omega_0^2 - \omega^2)^2 + \omega^2/\tau^2)}\right]^2}. \tag{6.9}$$

So far, the model assumes no additional signal incident at the detector port. For the range of Q values found in the samples measured here, fitting the resonant peak to a Lorentzian lineshape is sufficient in the case where no other coupling between ports is present [95,116,147]. In practice, an asymmetric resonant peak is often observed that cannot be described by a simple Lorentzian function. Hornibrook et al [146] showed that parasitic coupling between ports is responsible for suppression of the quality factor and generation of a non-Lorentzian microwave response that necessitates a modified approach to the analysis.

For the multilayered resonators measured here, an asymmetric lineshape was typical though the origin of the asymmetry was unknown. To model these asymmetric peaks, a 'coupling signal' with components in and out of phase (defined as A and B respectively) with the driving current is assumed to exist along with the resonant signal. The coupling signal is also assumed to remain constant over the frequency

range unlike the rapid variation of the resonant signal. The magnitude of the complex voltage is then given as

$$|V| = \sqrt{\left[\frac{\omega^2 I/C\tau}{((\omega_0^2-\omega^2)^2+\omega^2/\tau^2)} + \frac{AI}{C}\right]^2 + \left[\frac{I\omega/C(\omega_0^2-\omega^2)}{((\omega_0^2-\omega^2)^2+\omega^2/\tau^2)} + \frac{BI}{C}\right]^2}. \quad (6.10)$$

where I/C is the height of the peak, τ is the inverse of the peak width, and ω_0 is the resonant frequency. Although initially assumed that this coupling signal should be fixed, in practice it was often found to be necessary to add a further two components of the coupling signal that were allowed to vary across the frequency range. These were labelled D and E and again represented the real and imaginary parts of the coupling. Using this analysis, the quality factor of the resonant signal is given by

$$Q = \frac{\omega_0}{1/\tau}. \quad (6.11)$$

The model given by equation (6.10) was used to fit to $S_{21}(f)$ collected during low temperature measurements. Rather than analyse the data as it was being collected using LabView, the data fitting program Extrema[4] was used to take in $S_{21}(f)$, fit the model to the data, determine values for each variable parameter with associated errors and output the tabulated information to a file for further analysis.

Testing The Model

Fig. 4.6 in section 4.2 showed the microwave response of a niobium-only resonator with a high quality factor ($> 400,000$). The resonant peak is symmetric about f_0 and could be described by a simple Lorentzian function (though the fit shown uses the model described above). To illustrate the need for the more complicated model given by equation (6.10), Fig. 6.9 shows $S_{21}(f)$ of sample $S_1G0.0$ taken $T = 1.02$ K.

[4]Extrema, `www.exsitewebware.com/extrema/`

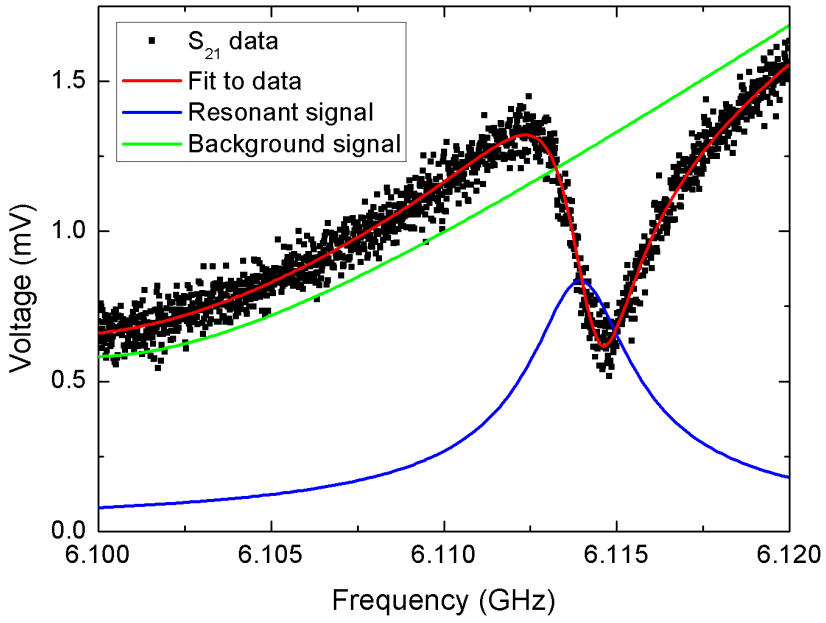

Figure 6.9: Example of fitting equation (6.10) to a low Q resonant peak (sample $S_1G0.0$ at $T = 1.02$ K). The theoretical fit to the data is composed of two components: the Lorentzian signal (blue line) and the coupling signal (green line). See text for the result of the fit.

The model is fit to the data using the extra parameters (D and E) that allow the coupling signal to vary across the frequency range. The result of the fit gives values of $f_0 = (6.11394 \pm 2 \times 10^{-5})$ GHz and $Q = 2290 \pm 32$, which is a typical quality factor for the multilayered samples measured here (i.e. $Q < 10,000$). For the particular example given in Fig. 6.9, it is unlikely that the network analyser would have been able to even provide an estimate of these values owing to the rising background across the frequency range.

To assess the accuracy to which f_0 and Q can be determined using equation (6.10), an asymmetric resonant peak was generated with a typical level of noise to test the model. An example of generated data is shown in Fig. 6.10. The parameter values used to generate the data, together with the values determined by fitting equation (6.10) to the data, are given in table 6.1.

While the coupling signal parameters (A, B, D and E) determined through fitting show a poor agreement with the generating parameters, the parameters that describe

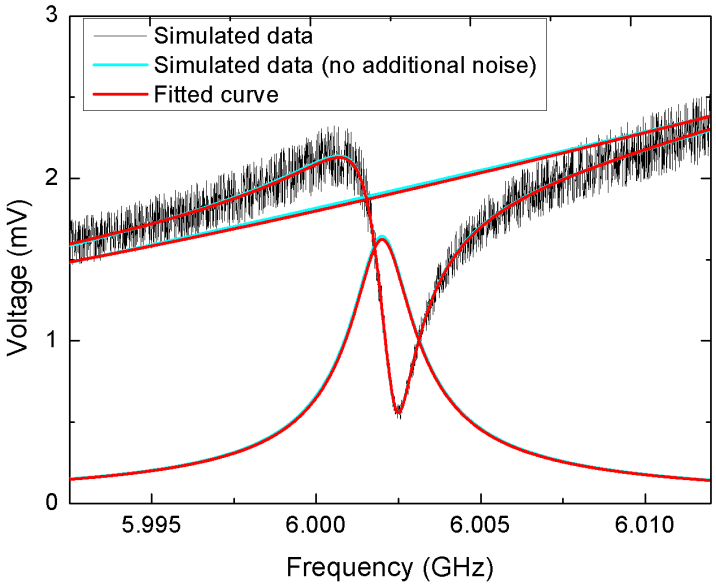

Figure 6.10: Theoretically generated data with noise and without noise. Equation (6.10) was fit to the simulated data to assess the accuracy of parameter determination.

the resonant peak (including the quality factor) differ from the generating values by amounts less than the estimated errors. This agreement is confirmed in Fig. 6.10 through a comparison of the fit result (blue line) with the simulated data minus the additional noise (red line); it is difficult to see both lines as they are almost exactly overlaid. Although the coupling parameters differ individually by amounts far greater than the errors, the combination almost exactly reproduces the original function.

The simulated data was intended to replicate the microwave response of a sample with a low quality factor at $T = 1$ K. As the temperature is raised, the quality factor drops as system losses increase and therefore it is even more important to be able to analyse the data with confidence by using the method described here.

Table 6.1: Parameters used used to generate the simulated data shown in Fig. 6.10 and the parameters with associated errors determined by fitting equation (6.10) to the data.

Parameter	Simulation Parameter	Fitted Parameter
I/C	2.84×10^{-3}	$(2.89 \pm 0.04) \times 10^{-3}$
τ	0.57	0.57 ± 0.01
ω_0	6.002	$6.00199 \pm (1 \times 10^{-5})$
A	121.64	101.79 ± 12.16
B	-4.282	-25.485 ± 0.002
D	-0.02	-0.02 ± 12.53
E	7.830×10^{-4}	$(4.314 \pm 0.002) \times 10^{-3}$
Quality factor, Q	3421	3412 ± 45

6.2.3 Comparison to Mattis-Bardeen Theory

After analysis of $S_{21}(f)$ for each sample over a range of temperatures, $f_0(T)$ was compared with the behaviour predicted by Mattis-Bardeen theory [79]. Similar to the analysis of Gao et al [120] and Barends et al [85], the kinetic inductance fraction of each sample was calculated by fitting equation (4.30) to the experimental data. Mattis-Bardeen theory has been noted to provide a good description of a range of superconductors [20]. Departures from this theory could necessitate modifications in the analysis of results from a microwave CPR measurement device.

To determine the kinetic inductance fraction of each sample, a program 'MB_fit.cc' was written in C++ which used the microwave simulation library 'SuperMix'[5] to numerically evaluate the complex part of the conductivity, σ_2, according to Mattis-Bardeen theory and subsequently fitted equation (4.30) to the measured $f_0(T)$. The developed program took in values of the resonant frequency, f_0, the sample temperature, T, the energy gap at $T = 0$, Δ_0, and the transition temperature, T_C, and returned $\delta\sigma_2(T)/\sigma_2(0)$ where $\sigma_2(0)$ is the complex conductivity at the lowest temperature achieved for each set of $f_0(T)$ data. The fit to the data was then performed[6] by treating β as an integer (with $\beta = 1$ or $\beta = 2$, depending on the chosen

[5]SuperMix, `www.submm.caltech.edu/supermix`

[6]ROOT: A Data Analysis Framework, `root.cern.ch/drupal/`

limit) and using α as a fitting parameter. This procedure allowed a quantitative measure of the kinetic inductance fraction of each sample which provided a means of direct comparison between samples with varying cobalt layer thicknesses.

The temperature dependent energy gap $\Delta(T)$ is calculated within the program by using a further subroutine from the SuperMix library which draws upon the experimental results of Mühlschlegel [148] for $T/T_C > 0.18$ to interpolate the low temperature values of $\Delta(T)$. The lowest temperature achieved in the experiments described in this chapter was ~ 1 K; for a low temperature approximation of $\Delta(T)$, the following expression was used (see Ref. [149]):

$$\frac{\Delta(T)}{\Delta_0} \approx \exp\left[-\sqrt{\frac{2\pi kT}{\Delta_0}}\exp\left(-\frac{\Delta_0}{kT}\right)\right] \approx \exp\left[-\sqrt{3.562x}\exp(-1.764/x)\right] \quad (6.12)$$

where x is the reduced temperature for values below those available in Ref. [148] (i.e. $T/T_C < 0.18$) and, using material parameters for niobium provided by Pöpel [20], the energy gap is assumed to be $2\Delta_0 = 3.80kT_C$. The experimental results analysed using this method will be shown in section 7.2.1.

CHAPTER 7

MICROWAVE MEASUREMENTS: RESULTS AND DISCUSSION

This chapter documents the experiments that were performed to assess the suitability of the chosen materials to the device proposed at the end of chapter 4, and discussion as to how the combination of superconductors and ferromagnets would affect the performance of a microwave CPR device. The microwave losses of the samples were measured as a function of the ferromagnetic layer thickness; the results are presented and discussed with the aid of computational simulation. The temperature and field dependence of the resonant frequency is given for both magnetically unsaturated and saturated samples. The chapter concludes with preliminary microwave measurement of superconductor-ferromagnet-superconductor films and how one should proceed toward the device proposed in chapter 4.

7.1 Resonator losses

The results presented in this section initially focus on sample sets #1 and #2 which have the same structure but were deposited in separate deposition runs (see table 5.1 for a summary). A limited number of measurements were also made on samples from set #3 which does not have a platinum capping layer and instead has a 'sandwich' structure that is closer to that required for the proposed microwave CPR measurement device. Results for sample set #3 will be presented in section 7.4.

7.1.1 Sources of Loss

The losses associated with the observed (loaded) quality factor in a coplanar resonator, Q_L, have many contributions. For sample sets #1 and #2, the following contributions are expected:

$$\frac{1}{Q_L} = \frac{1}{Q_e} + \frac{1}{Q_r} + \frac{1}{Q_{\text{sub}}} + \frac{1}{Q_{\text{TLS}}} + \frac{1}{Q_{\text{Nb}}} + \frac{1}{Q_{\text{Co}}} + \frac{1}{Q_{\text{Pt}}} + \dots \tag{7.1}$$

Here, Q_e is the quality factor attributed to external coupling (to the network analyser, for example) which is mainly influenced by the size of the coupling gap; Chen et al calculated $1/Q_e \sim 8 \times 10^{-7}$ for a 4 μm coupling gap [91]. If $Q_e \gg Q_0$ one can say $Q_L \approx Q_0$, where Q_0 is the unloaded quality factor. Q_r is due to radiation loss which has been shown to be strongly dependent on the resonator geometry [150]. Q_{sub} is inversely proportional to the intrinsic loss tangent of the substrate; sapphire is widely used as a substrate for microwave applications due to its very low loss tangent [132, 151]. The contribution of Q_{sub} to the total losses will be shown to be negligible.

Q_{TLS} is the loss contribution due to Two-Level Systems (TLS) that are unsaturated at low powers and temperatures and couple to the electric field of the resonator. These dipole TLS exist in dielectrics, either within the substrate or on oxides formed

on the conductor surface [86] (particularly on niobium [150]). Macha et al [119] observed that the influence of TLS on the measured losses became noticeable at $T < 800$ mK. The results to be shown in this section were taken at $T > 1$ K, on samples where the niobium is protected from oxidation by a capping layer, and at relatively high powers (≥ -40 dBm) and therefore the noise contribution of TLS can be ignored [79, 152]. Q_{Nb}, Q_{Co} and Q_{Pt} are related to losses in the conducting materials (Q_c in equation (4.23)): niobium, cobalt, and platinum respectively.

A typical quality factor for a superconducting resonator can be in the hundreds of thousands [124]. A typical Q for the multilayered samples will be shown to be $< 10,000$. A direct comparison can be drawn between the data presented here and the quality factor of a niobium resonator on sapphire substrate that was measured in the same cryostat ($S_{21}(f)$ shown in Fig. 4.6). The measured $1/Q_L$ for this particular sample at 1 K was $(2.44 \pm 0.01) \times 10^{-6}$ and therefore all terms other than the extra resonator materials (the cobalt and platinum layers) have a negligible contribution to the losses seen for the multilayered samples.

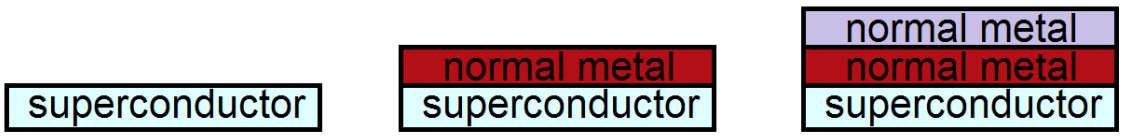

Figure 7.1: Cartoon showing a cross section of a centre track made of a superconductor (left), a bilayer structure (middle) and a multilayered structure with a fixed thickness capping layer (right).

The success of a microwave device used as a phase-sensitive probe is dependent upon maximising the quality factor of the resonator. It is now necessary to consider how the addition of a layer of normal metal affects the resonator losses; a cartoon of the structure is shown in Fig. 7.1 (middle). For a dc signal, the addition of a normal metal layer should not introduce extra losses as the current will flow entirely in the superconducting layer. For an ac signal, however, an oscillating voltage is induced along the length of the resonator. Currents will therefore be induced in the normal metal layer resulting in dissipation proportional to V^2/R. Thicker layers will have a smaller resistance and therefore will cause higher losses; it is therefore expected

that $1/Q \propto d_{\mathrm{Co}}$ and the losses will be in the limit $Q \ll Q_{d_{\mathrm{Co}}=0}$. It is also expected that a capping layer of a fixed thickness (Fig. 7.1 (right)) will simply add a vertical offset to the losses in the system.

7.1.2 Resonator Loss Measurements

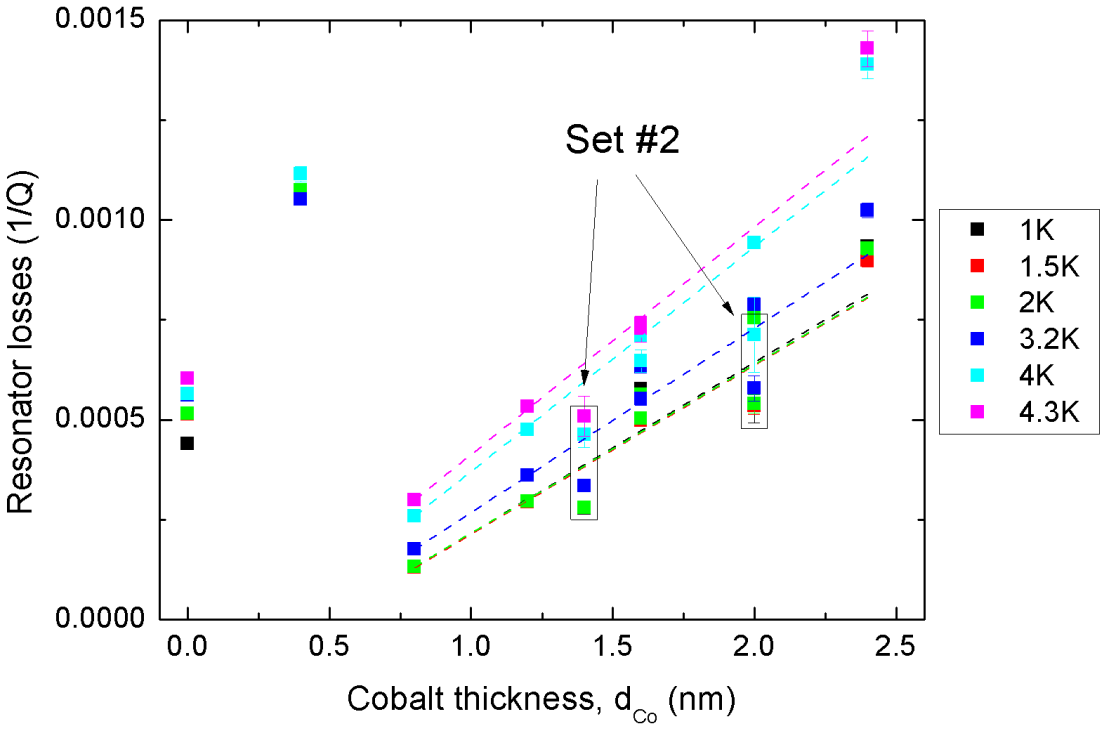

Figure 7.2: Resonator losses ($1/Q$) as a function of cobalt layer thickness, measured at different temperatures (indicated by the legend). Measured sample sets were #1 and #2 (as indicated). Dashed lines show linear fits to experimental data excluding samples $S_1G0.0$ and $S_1G0.4$. For further details, see text.

Following magnetic characterisation, resonator losses for sample sets #1 and #2 were measured as a function of cobalt thickness over a range of temperatures. The microwave losses are directly proportional to the reciprocal of the quality factor, as determined through fitting to $S_{21}(f)$ with equation (6.10). The results of these measurements are shown in Fig. 7.2. The dashed lines show linear fits to $1/Q(d_{\mathrm{Co}})$ at different temperatures. As in the analysis of the magnetic dead layer, the fits exclude samples $S_1G0.0$ and $S_1G0.4$ (discussed further below). It should be noted

that each sample had a similar magnetic history prior to these measurements.

The broad behaviour presented in Fig. 7.2 follows the predicted behaviour in that $1/Q$ depends linearly on d_{Co}. All samples in Fig. 7.2 have a fixed 5 nm thick platinum capping layer that is intended to preserve the magnetic properties of the cobalt over time and adds similar losses to each sample. As the temperature is increased, there is an associated increase in the losses. Similar behaviour is expected for superconductor-only resonators and can be understood in the context of the two-fluid model; as the temperature is increased, there is an increase in the dissipative quasiparticle density (and therefore the magnetic penetration depth) which results in a lower Q. For the multilayer samples, $1/Q(d_{\mathrm{Co}})$ scales linearly if $d_{\mathrm{Co}} \ll \delta$ where δ is the skin depth (δ(Co) at 5 GHz $\approx$ 200 nm). The samples measured here are always in this limit since samples with $d_{\mathrm{Co}} > 2.4$ nm exhibited $Q_L < 1000$ at ~ 1 K, i.e. $Q \to 0$ for large d_{Co}. It is expected that if the normal layer thickness could be increased with a measurable Q, the losses would eventually reach a plateau when $d_{\mathrm{Co}} > \delta$.

A feature of the data that was not predicted by this simple argument is the magnitude of the increase in losses with temperature is not the same for all d_{Co}. Each dashed line shows $1/Q(d_{\mathrm{Co}})$ where the colour is representative of temperature (from 1 – 4.3 K). For $T \leq 2$ K, $1/Q(d_{\mathrm{Co}})$ remains approximately constant; referring back to Fig. 4.1 this can be expected since the quasiparticle density does not change significantly over this temperature range. For $T > 2$ K, the losses are large and increase more rapidly with temperature. This behaviour implies an interaction between the superconductor and ferromagnetic/normal metal layers. There are two potential mechanisms that could account for this behaviour. Firstly, there may be a temperature dependent reduction of the effective d_{Co} through the proximity effect. This could lead to a reduction in losses in this region, which accounts for a greater fraction of the thinner cobalt films. Secondly, some region of the superconducting film may also be weakened by the presence of the ferromagnet.

Inconsistent Results

The results presented here suggest that the thin films received were either mislabeled or wrongly deposited in terms of the cobalt thickness. The linear fits in Fig. 7.2 exclude samples $S_1G0.0$ and $S_1G0.4$ as the losses appear to be anomalously high. The magnetic characterisation of these samples also revealed high values of M_S/area, shown in Fig. 5.10, where these samples were also excluded from the linear fit. The first conclusion that can be drawn is that observed losses seem to be consistent with a thickness of ferromagnet that is thicker than anticipated by the deposition conditions. If d_{Co} is estimated for these samples by extrapolating horizontally from the measured values of $1/Q$ or M_S/area to the linear fits for both characterisation methods, the result is a similar estimated d_{Co}. There may, however, also be a difference in the platinum layer that is only visible through microwave measurement. Despite this, the comparative features of the experimental results show that the magnetic and microwave characterisation methods are complementary and can allow qualitative comparison between the results. This is also evident in the comparison of the properties of sample sets #1 and #2. The data show that both $1/Q(d_{\mathrm{Co}})$ and $M_S/\mathrm{area}(\mathrm{d_{Co}})$ for samples $S_2G1.4$ and $S_2G2.0$ were low compared to similar measurements made on set #1.

Further conclusions can be drawn from the comparison $M_S/\mathrm{area}(\mathrm{d_{Co}})$ (Fig. 5.10) and $1/Q(d_{\mathrm{Co}})$ (Fig. 7.2). The scatter on $M_S/\mathrm{area}(\mathrm{d_{Co}})$ for very thin d_{Co} does not appear in the measurement of $1/Q(d_{\mathrm{Co}})$. This could be indicative of magnetic inhomogeneity in thin cobalt films; while there are less samples in this range, the scatter appears reduced for $d_{\mathrm{Co}} > 2$ nm. For the application of SFS Josephson junction fabrication, inhomogeneity is undesirable [53]. If the assumption of poor magnetic uniformity is correct, an improvement in film deposition is required to ensure predictable and repeatable device fabrication is possible, as demonstrated by Robinson et al [31]. The lack of similar scatter for $1/Q(d_{\mathrm{Co}})$ suggests that the effect of magnetic inhomogeneity is less influential on the broad microwave behaviour of the device, due in part to the thick platinum layer that also contributes a large part

to the losses.

7.1.3 Dead Layer Thickness

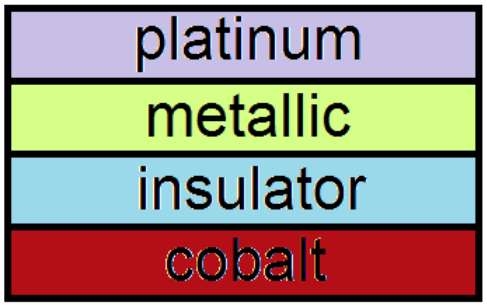

Figure 7.3: Expanded view of platinum-cobalt interface illustrating the proposed composition of the magnetic dead layer.

As already discussed, comparison of $1/Q(d_{\mathrm{Co}})$ and $M_S/\mathrm{area}(\mathrm{d_{Co}})$ allows some insight as to the material composition of the cobalt films which includes a thickness of magnetic dead layer, d_{DL}. $M_S/\mathrm{area}(\mathrm{d_{Co}})$ interrogates only magnetically active materials; magnetic characterisation measurements found d_{DL} to be ~ 1.3 nm. It is postulated that there exists a region of insulating material and/or a region of non-magnetic metallic material that make up all or part of the dead layer, as shown in Fig. 7.3.

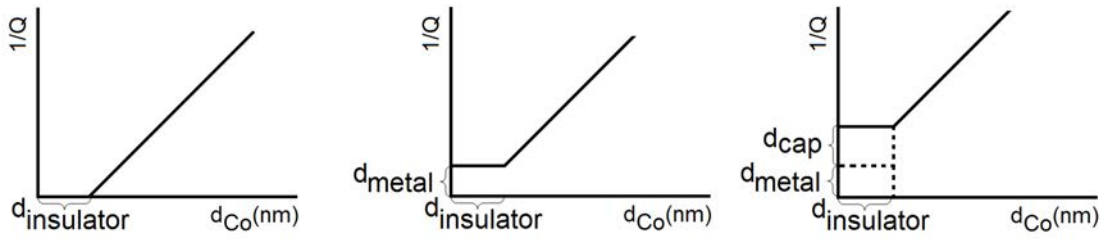

Figure 7.4: Predicted behaviour for resonator losses with an insulating layer with thickness $d_{\mathrm{insulator}}$ (left), the addition of a metallic non-magnetic layer of thickness d_{metal} (middle) and the whole structure including a metallic capping layer with thickness d_{cap} (right).

In Fig. 7.2, a backward extrapolation of $1/Q(d_{\mathrm{Co}})$ (1 K) finds that $1/Q \to 0$ at $d_{\mathrm{Co}} \approx 0.5$ nm. If there were no platinum layer, this thickness would be a measure of an

insulating layer, $d_{\text{insulator}}$ that would not be visible to magnetic characterisation and would not contribute to the microwave losses (Fig. 7.4 (left)). Generally, $1/Q(d_{\text{Co}})$ increases linearly but, for very small d_{Co} (metallic but not magnetic, d_{metal}), it is thought that there should be a region where the losses plateau (Fig. 7.4 (middle)). Lastly, the fixed 5 nm platinum layer, d_{cap} simply adds an offset to all measurement of loss by an amount related to the layer thickness (Fig. 7.4 (right)).

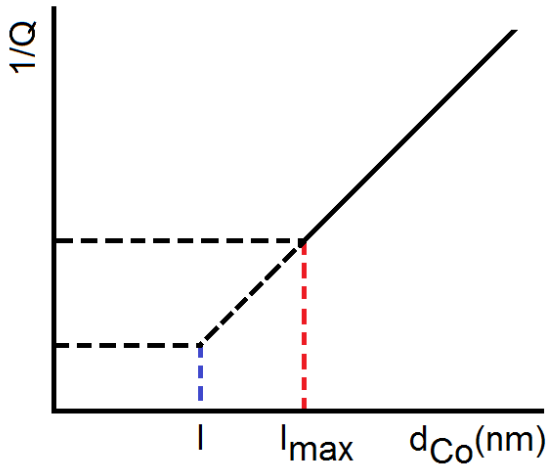

Figure 7.5: Illustration of $1/Q(d_{\text{Co}})$ data obtained (solid black line) with a plateau predicted for small d_{Co} (dashed black lines). I_{max} shows the maximum insulator thickness for the smallest d_{Co} measured (0.8 nm). I is the true insulator thickness (not observed for data shown in Fig. 7.2).

The measurements of $1/Q(d_{\text{Co}})$ presented in Fig. 7.2 did not show a plateau in the resonator losses and the quoted film thicknesses for samples $S_1G0.0$ and $S_1G0.4$ were thought to be unreliable. Despite this, some speculation can be made regarding the magnitude of d_{DL}. Using Fig. 7.5 as an illustration, a plateau should be observed beginning at $d_{\text{Co}} = d_{\text{I}}$ where d_{I} is the thickness of an insulating layer. The solid black line in this illustration represents experimental data for $1/Q(d_{\text{Co}})$ where $d_{\text{I}} = d_{I_{\text{max}}}$, i.e. there is no observed plateau so any insulating layer can be thought of as being at a maximum. By measuring $M_S/\text{area}(\text{d}_{\text{Co}})$, the dead layer thickness was found to be $d_{\text{DL}} \approx 1.3$ nm, which is a measure of the *total* thickness of non-magnetic material including any metallic material. The sample with the smallest d_{Co} measured was 0.8 nm ($=d_{I_{\text{max}}}$); therefore it can be concluded that $d_{\text{insulator}} = d_{\text{DL}} - d_{I_{\text{max}}}$ so there

is an insulating layer present that is at least 0.5 nm thick.

7.1.4 Quantitative Assessment of Losses: Simulation

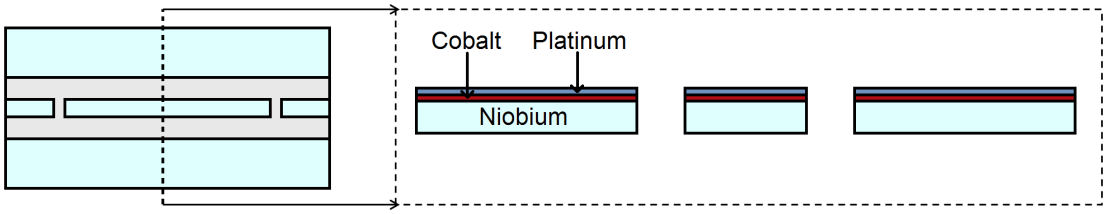

Figure 7.6: Diagram of the model created in COMSOL Multiphysics. The left image shows a top down view of the whole resonator structure where the vertical dashed line indicates the position of the cross sectional 2D model, shown right.

To progress toward a microwave CPR measurement device, a method of predicting the order of magnitude of losses in multilayered resonators is required. A time varying current in the superconducting layer will induce a current in a normal metal layer in close proximity; a model that assumes a simple current flow will not suffice here due to the complicated variation in current density along and across the track [80].

Full 3D modelling is not possible due to the large ratio of the dimensions of a coplanar resonator, therefore a diagram of the model used here is shown in the dashed box in Fig. 7.6. A 2D cross section of the coplanar resonator was simulated in COMSOL Multiphysics where it is assumed that the resonator length is infinite in the plane. Maxwell's equations are solved for the magnetic field in the plane and a uniform electric field perpendicular to the plane. The model computes the behaviour for a section chosen to be across the middle of the resonator (Fig. 7.6 (left)) where the described behaviour is well approximated.

The magnetic and electrical properties of each layer were defined within COMSOL using the AC/DC module with perpendicular induction currents. The software does not have facilities for a straightforward simulation of superconductors so a large negative imaginary conductivity was initially chosen to provide a skin depth $\delta \approx 50$ nm at the resonant frequency of 6 GHz (roughly equal to the value of the

bulk magnetic penetration depth, λ_L). The initial values of conductivity and relative permeability chosen for each material are given in table 7.1.

Table 7.1: Initial electrical and magnetic properties used to simulate a multilayered resonator.

Layer material	Conductivity (S/m)	Relative permeability
Niobium	$-i(1 \times 10^{10})$	1
Cobalt	2×10^{7}	100
Platinum	9×10^{6}	1

It is also necessary to define the time dependent voltage to drive the resonant system. The point in the resonant cycle at which the current in the centre track is maximal for the cross section shown in Fig. 7.6 is chosen such that the same voltage per unit length – 1 V/m at 6 GHz – is applied to all conductive layers in the centre track. The ground planes are held at a constant voltage and are therefore only subjected to currents induced as a result of the current in the centre track.

To test the model, a single layered superconducting resonator was first simulated, the result of which is shown in Fig. 7.7. The 2D surface plot (top) shows the magnetic energy density focused closely on the centre track, though the ground planes extend further laterally than is shown in this image. A cross section across the model shows that the total current density replicates the current distribution shown by Porch et al [80], which used a first principles approach to numerical simulation based on a solution of the London equations (also using a 2D geometry), so there is some confidence that this model should give a good approximation to a real resonator. Since the superconductor is treated as a perfect conductor, the result of a simulation involving only the niobium layer is the total absence of loss. There are many contributions to loss in a real system (especially those containing normal metal) that are not accounted for in this simplistic model, so the estimates of loss will naturally be low compared with experimental observations.

An attempt was made to model the experimental data shown in Fig. 7.2 by adding a platinum layer of fixed thickness and varying the cobalt layer thickness over the

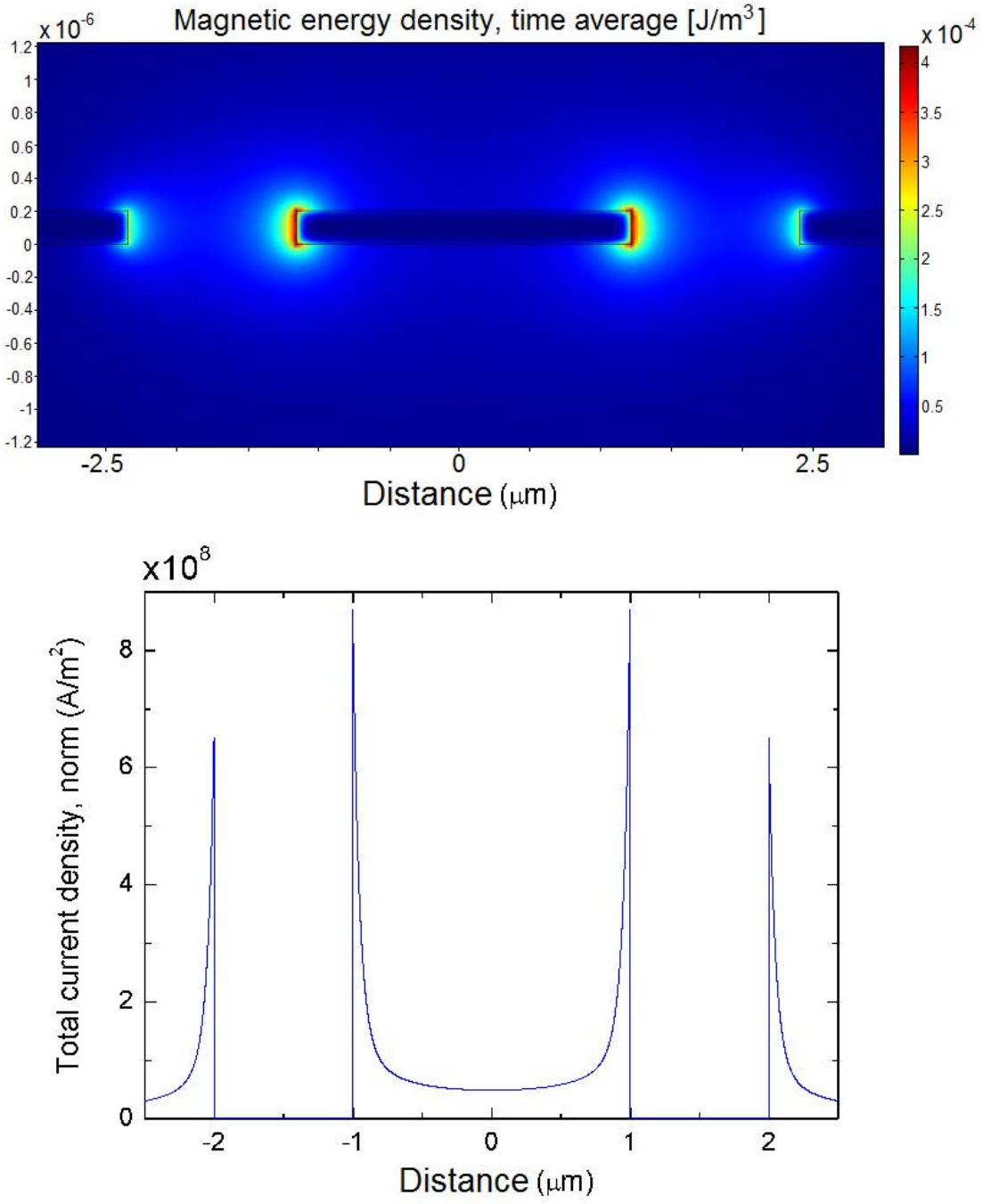

Figure 7.7: Simulation results for a niobium-only superconducting resonator. Top: Magnetic energy density surrounding a cross section of the centre track. Bottom: Cross section plot across the model of the current density in the coplanar resonator.

range $1 - 5$ nm at $T = 0$ K. It is assumed that the normal metal layers are in good electrical contact with the superconductor such that the application of the same 1 V/m for all layers in the centre track is justified. In reality, it is believed that there is a thin insulating layer resulting from the magnetic dead layer but since the capacitance between the superconducting centre track and the cobalt is much greater than between the centre track and the ground plane, the application of 1 V/m along the centre track for all layers is justified. COMSOL enables an estimate of the quality factor to be made by simulating the average energy per cycle, U_{avg}, and the total power loss per second, P_{avg}, from which the following is obtained:

$$Q = \frac{4\pi f U_{\text{avg}}}{P_{\text{avg}}} \tag{7.2}$$

where f is the frequency of the driving voltage.

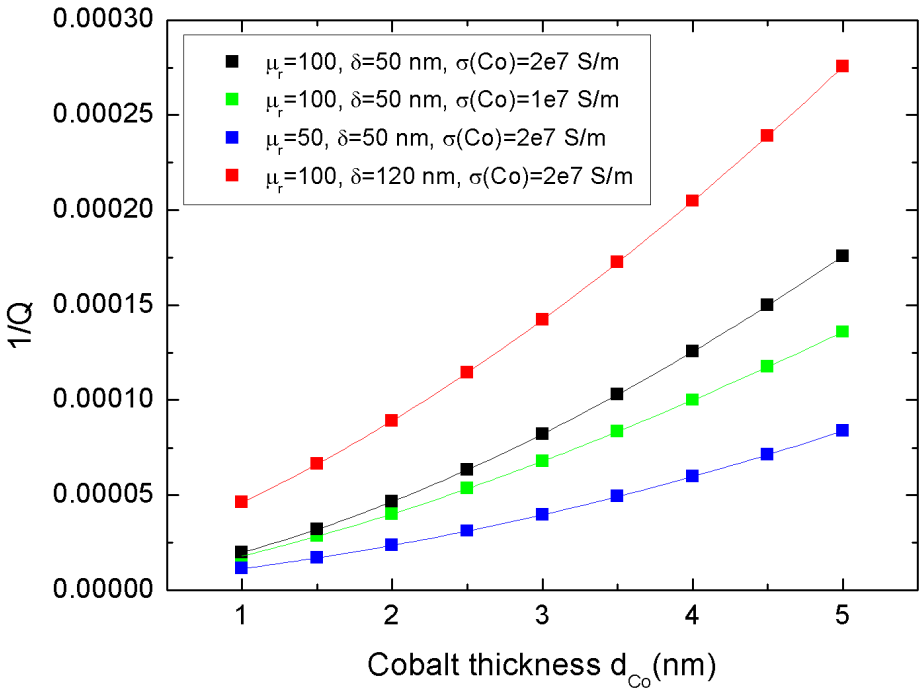

Figure 7.8: Simulated losses for the model shown in Fig 7.6 with 1 V/m at 6 GHz applied to all layers in the centre track. A variety of material parameters were simulated as indicated by the legend.

Results of simulation with a variety of material parameters – the London penetration

depth, λ_L, the relative permeability, μ_r, and the normal metal layer conductivities, σ – are shown in Fig. 7.8. The value of $1/Q$ is plotted as it is proportional to the losses in the system. There are two notable differences between the simulated losses and those observed experimentally. Firstly, despite adjustment of the electrical and magnetic parameters within reasonable physical limits, $1/Q$ is approximately 10 times smaller than experimental observations. Secondly, the simulated dependence of losses on the cobalt thickness is non-linear which is not seen experimentally.

To explain the low losses seen in the simulation, it is again noted that there is current induced in the cobalt layer as a result of the current in the superconductor. There are no losses for a niobium-only resonator in this model since this layer acts as an inductor driven by the applied voltage. For the model described, currents that flow in the normal layers arise from two sources – firstly the applied current that flows as a result of the applied oscillating voltage, and secondly a current flow in the *opposite* direction induced by the current in the niobium layer. Through simulation with the values in table 7.1, it is found that the induced current is approximately 96% of the current flow as a result of the applied voltage. The low simulated losses are a result of the near perfect balance between the two currents.

Since the losses are proportional to the square of the current, any substantial deviation from this near balance will result in a dramatic change in the simulated quality factor. To investigate this, the induced current in the cobalt layer was artificially suppressed such that the only current in the normal metal layers was the one induced by the applied voltage. The result of these simulations is shown in Fig. 7.9. It was found that reasonable adjustments to the layer conductivities (provided in the figure caption) gave a good agreement with the experimental data. Smaller deviations from the 96% balance of the two currents would provide similar results.

There is no method to determine whether deviation from an almost complete balance of applied and induced currents arises from sample inhomogeneity or from any other source that is is not properly accounted for in the model. In reality, it is expected that there are regions of the cobalt layer that are metallic but non-magnetic and

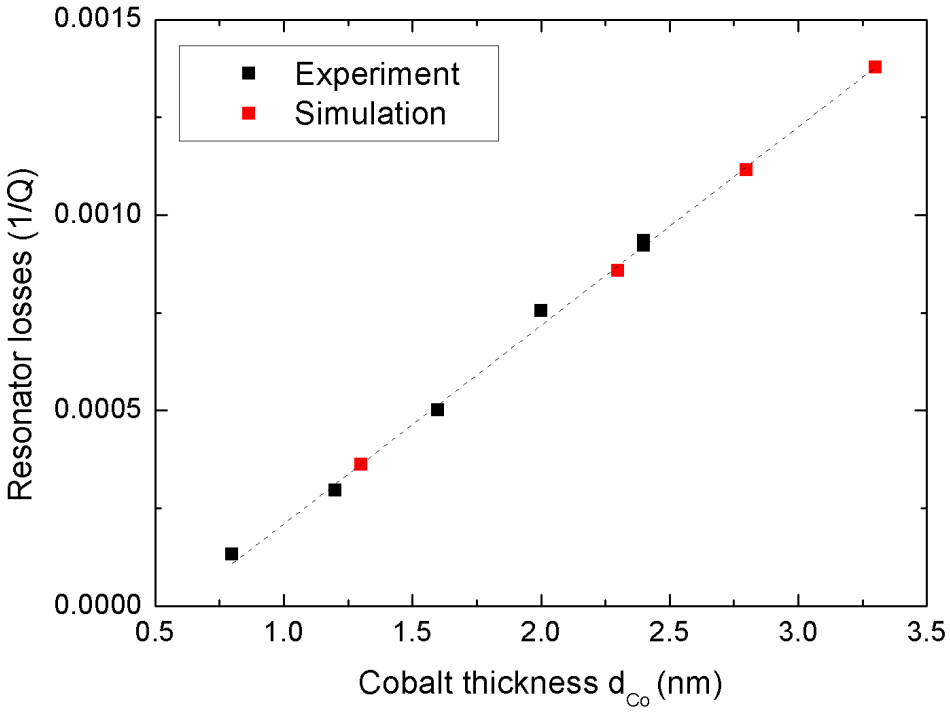

Figure 7.9: Simulated losses for the model shown in Fig 7.6 with the induced current in the normal metal layers artificially suppressed. The following values of layer conductivity were found to provide a good agreement with the experimental results: $\sigma_{\mathrm{Pt}} = 2.9 \times 10^6$ S/m, $\sigma_{\mathrm{Co}} = 1.85 \times 10^7$ S/m. The simulated losses are compared to experimental data.

some regions that are insulating. Without proper material characterisation, it is difficult to estimate the exact properties of the normal metal layers. Since there is no measure of the resistivity of the normal metal layers, it is difficult to take the modelling further. Nevertheless, to gain an order of magnitude estimate of the losses, it is found that a tenth of the simulated value for the cases where no attempt to suppress the induced current matches quite well with experiment but it should be stressed that this is not precise.

7.2 Kinetic Inductance Fraction Measurement

Equation (4.16) showed that the resonant frequency, f_0, is determined by the sample capacitance and inductance. If it is assumed that the capacitance is temperature independent over the range measured here (typically $1 - 5$ K) [119, 124], an observed change in f_0 is then due solely to the device inductance, L_T, as given by equation (4.25) and reproduced below:

$$L_T = L_G + L_K$$

where L_G is the geometric inductance and L_K is the kinetic inductance. L_G is fixed by the dimensions of the sample but $L_K \propto 1/\sqrt{n_s}$ and is therefore affected by variables such as the temperature [120] and an applied magnetic field [93]. The observation of a change in f_0 of a superconducting resonator therefore allows a quantitative determination of the kinetic inductance fraction of the samples. Earlier discussion in chapter 2 showed that the proximity effect in superconductor-ferromagnet bi- and multilayers can be responsible for changes in the superconducting state; measuring the kinetic inductance fraction provides a direct observation of the number density of the superconducting electrons.

If $f_0(T)$ and $f_0(H)$ agree well with the theoretical predictions outlined in sec-

tion 4.2.2, the resonator materials can then be applied to the measurement of the CPR with confidence. It has already been shown through observation of the CPR by Frolov et al [6] that if a weak ferromagnet is used as the barrier of a Josephson junction, one can observe a 0- to π-transition in the phase difference by changing the temperature. It is therefore important to establish any other unpredicted behaviour that may arise in microwave devices through the combined use of superconductors and ferromagnets. Furthermore, the microwave CPR measurement device relies on the application of a small magnetic field; it is important to know how much (if at all) these fields would shift the resonant frequency without the presence of the Josephson junction structure. By observing f_0 as a function of temperature and applied magnetic field, any departure from the theoretically predicted behaviour would become apparent and could be used to adjust the interpretation of the measurement scheme shown in Fig. 4.10.

7.2.1 Temperature Dependence of the Resonant Frequency

The temperature dependence of f_0 was measured for multilayered resonators made from thin films from sets #1 and #2 using the method described in section 5.1. The resulting data was analysed using techniques outlined in section 6.2. The resonators were cooled to the base temperature of the cryostat (~ 1 K) and warmed in small temperature steps while collecting $S_{21}(f)$ data. For each sample, equation (4.30) was fit to $f_0(T)$, which uses Mattis-Bardeen theory to numerically evaluate σ_2 for each temperature. The samples were first assumed to be in the thick film limit (i.e. $t \gg \lambda_L$ so $L_K \propto \lambda_L$ and $\beta = 1$).

Energy gap selection

The fitting program 'MB_Fit.cc' described in section 6.2.3 allows the value of the energy gap to be kept as a fixed parameter or to be used as a fitting parameter along with the kinetic inductance fraction, α. Fig. 7.10 shows experimental data from

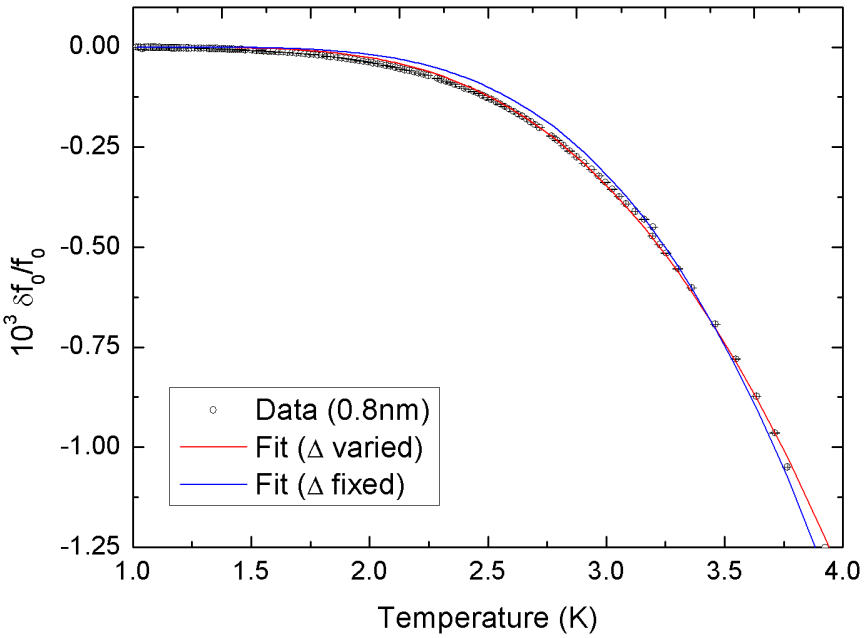

Figure 7.10: Fits to $f_0(T)$ data from sample $S_1G0.8$ using program 'MB_Fit.cc'. The blue line shows the fit performed with $2\Delta(0) = 3.01$ meV. The red line shows the fit where the energy gap was used as a fitting parameter giving the result $2\Delta(0) = (2.54 \pm 0.46)$ meV.

sample $S_1G0.8$ showing the resonant frequency shift as a function of temperature. The blue line shows equation (4.30) fitted to the data where the energy gap was kept at a fixed value of $2\Delta = 3.01$ meV as calculated assuming $T_C = 9.21$ K using $2\Delta(0) = 3.80 k_B T_C$ from Pöpel [20]. The red line shows a fit to the data where the energy gap was used as a second fitting parameter, which gave $2\Delta = (2.54 \pm 0.46)$ meV corresponding to a $T_C = (7.8 \pm 1.4)$ K.

Fig. 7.10 shows that allowing the energy gap to be used as a fitting parameter appears to provide a closer description of the data and gives a value of $2\Delta(0)$ that more accurately reflects the transition temperature of the superconducting sample. The measured value of T_C was (8.74 ± 0.03) K and the value of T_C as determined through fitting to the Mattis-Bardeen theory was (7.8 ± 1.4) K. It has been shown that these values can vary across samples and is dependent on the method of measurement [153] and, if the superconducting properties are reduced at the edges of the sample, this would potentially only be reflected by a coplanar resonator determination of T_C.

Fig. 5.14 showed T_C as determined by low temperature SQUID magnetometry; it was noted that this method potentially lacks the accuracy afforded by a four-point measurement and this could be reflected by the large amount of scatter on the data. If the scatter is an accurate representation of the spread on T_C, allowing $2\Delta(0)$ to be used as a fitting parameter during data analysis will take this spread into account and provide a better estimate of the kinetic inductance fraction. It was also shown by Barends et al [86] that niobium does not follow Mattis-Bardeen theory as closely as NbTiN at the lowest temperatures. It is therefore expected that there is some deviation from ideal behaviour shown by the materials used here.

Kinetic Inductance Fraction

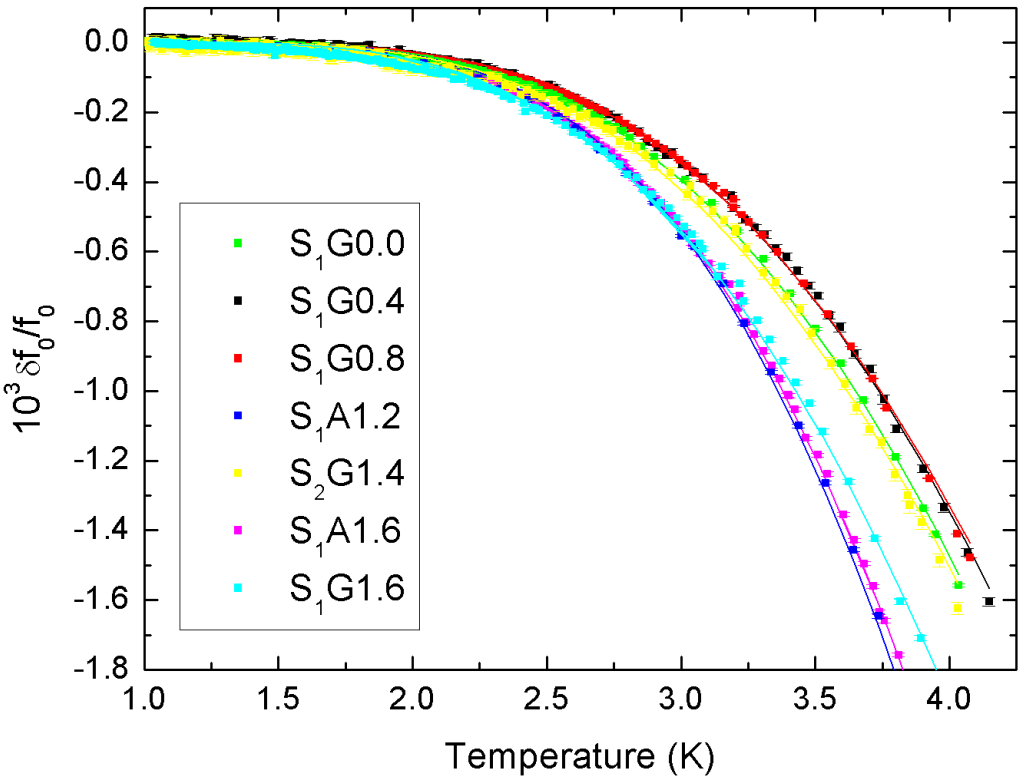

Figure 7.11: Examples of the change in resonant frequency as a function of temperature. The dashed lines are fits to the data using equation (4.30) where $2\Delta(0)$ and α are the fitting parameters and it is assumed that the films are in the thick film limit ($\beta = 1$). See table 5.2 for sample naming convention.

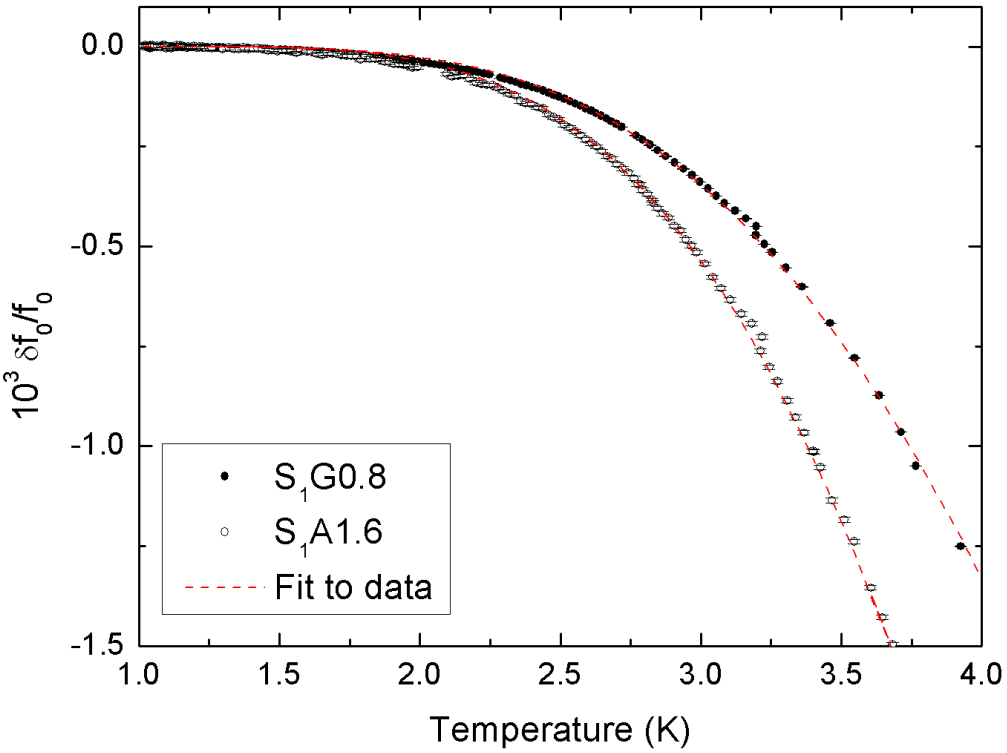

Figure 7.12: $f_0(T)$ as measured for samples $S_1G0.8$ and $S_1A1.6$ where the dashed lines are fits to the data using equation (4.30).

Fig. 7.11 shows examples of the fractional change in the resonant frequency as a function of temperature for samples measured with $d_{\mathrm{Co}} < 3$ nm (above this thickness the resonance was observable but with $Q \ll 1000$, which did not allow good fits to $S_{21}(f)$ to extract f_0 and Q). The dashed lines show fits to the data using equation (4.30) with the energy gap, $2\Delta(0)$, and the kinetic inductance fraction, α, as fitting parameters. It was observed that for samples with varying cobalt thickness, the rate of change of shift in resonant frequency is not constant. The graph is only intended to highlight the spread of behaviour that was observed across the resonators measured. Fig. 7.12 shows this effect more closely for samples $S_1G0.8$ and $S_1A1,6$, which have kinetic inductance fractions of $6.73 \pm (3.52 \times 10^{-3})\%$ and $12.59 \pm 0.05\%$ respectively, assuming both films are in the thick film limit.

The main result of this analysis is shown in Fig. 7.13 which plots the kinetic inductance fraction, α, as a function of cobalt thickness as estimated by the deposition conditions. The corresponding values for the energy gap are shown in Fig. 7.14. All black data points (for sets #1 and #2) indicate samples fabricated by the author where the analysis assumes that the films are in the thick film limit (i.e. $\beta = 1$ in equation (4.30)). The red data points are for samples from set #1 that were fabricated at the University of Cambridge. The top graph in Fig. 7.13 shows the result of analysis performed assuming the films were in the thick film limit where the α values appear to occupy two distinct bands; high values of $\alpha \sim 12\%$ and low values of $\alpha \sim 6\%$. A potential explanation for the emergence of these two bands is that it may reflect a periodic change in the properties superconducting state brought about by the cobalt layer (see sections 2.3.2 and 3.1.2, particularly Fig. 3.6 from Robinson et al [52] which showed 0-π transitions occuring in an SFS junction where the 'oscillation' period is approximately reflected here).

It is believed, however, that the observed 'oscillation' is *not* a result of the superconductor-ferromagnet interaction and instead is a consequence of a change in the film thickness at the edges of the coplanar resonators which necessitates a change in the analysis from the thick film to the thin film limit. As described in section 4.1.2, in

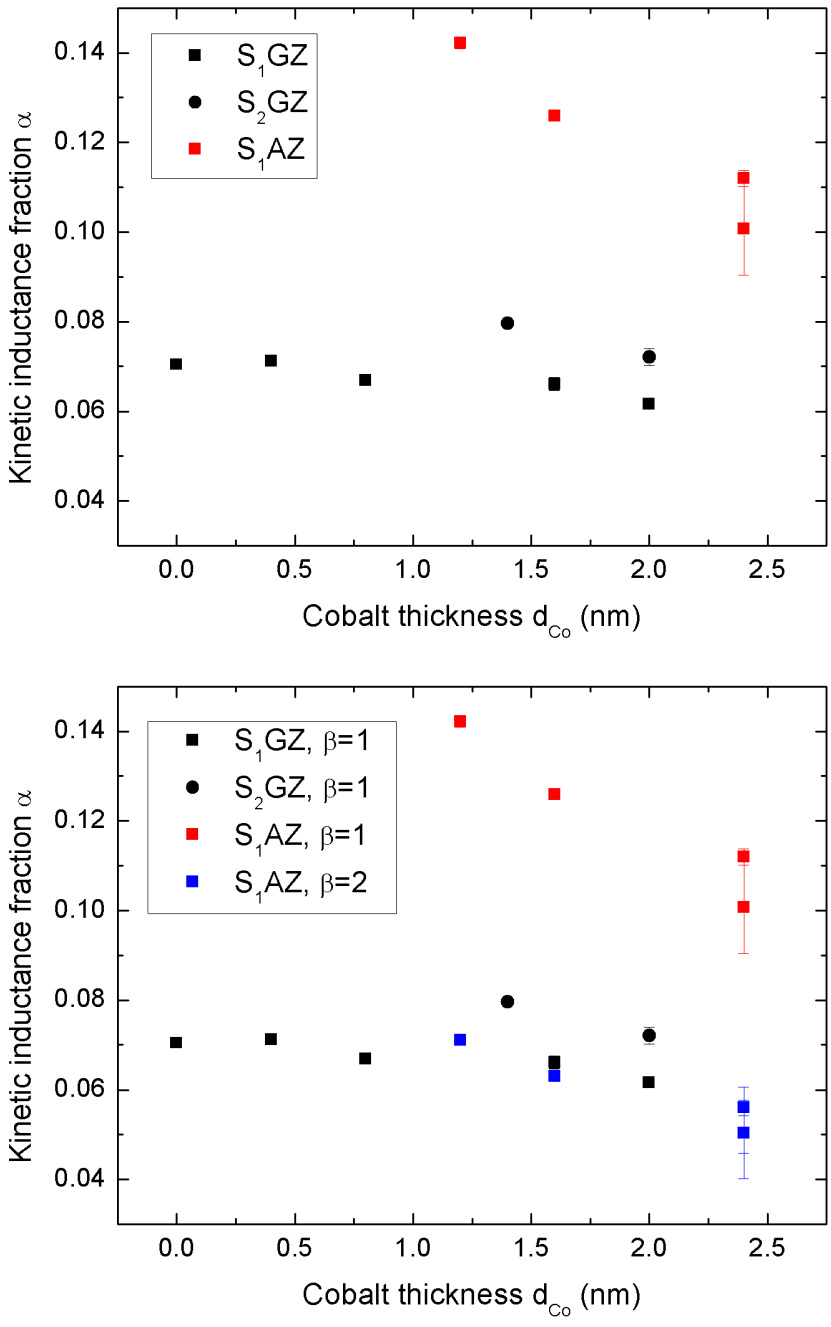

Figure 7.13: Kinetic inductance fraction, α, measured for samples with varying cobalt thickness (using the energy gap as a fitting parameter). The legend follows the naming convention defined in section 5.1.3 where Z is the cobalt thickness. Top: All samples analysed in the thick film limit ($\beta = 1$). Bottom: Samples S_2AZ analysed in the thick *and* thin ($\beta = 2$) limit as indicated by the legend.

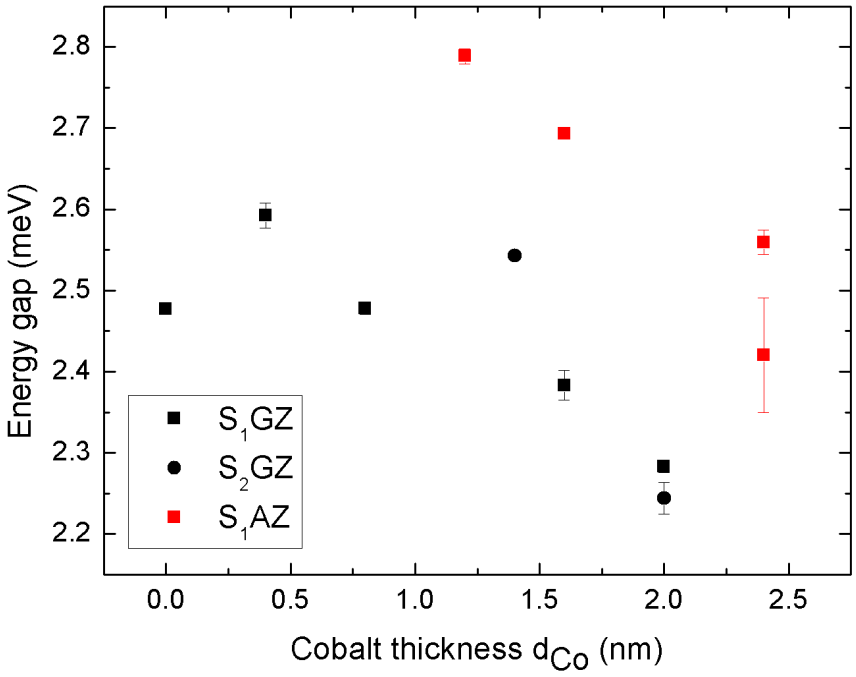

Figure 7.14: Values of the energy gap, $2\Delta(0)$, as a function of the cobalt layer thickness corresponding to the kinetic inductance fractions shown in Fig. 7.13. The legend follows the naming convention defined in section 5.1.3 where Z is the cobalt thickness.

the thick film limit $L_K \propto \lambda_L$ and in the thin film limit $L_K \propto \lambda_L^2$. The samples which showed a higher kinetic inductance fraction (red data points in Fig. 7.13) were then analysed assuming the thin film limit. It is then observed that all samples exhibit $\alpha \sim 6\%$. The kinetic inductance is a direct measurement of the number density of superconducting electrons ($L_K \propto 1/\sqrt{n_s}$) and it is observed that there is little variation in α as the cobalt thickness is increased. This is supported by the lack of variation in T_C of the same samples and by the evidence shown in Fig. 5.12 by Zdravkov et al [38], which shows that the overall effect of a ferromagnet on a superconductor is lessened as the superconductor is made thicker.

Further supporting evidence for this hypothesis is provided by the edge profile measurements that were shown in Fig. 5.6 in section 5.2. The figure showed step height measurements of the centre track edges of two samples which showed a large difference in the kinetic inductance fraction when both analysed in the thick film limit. It is noted that samples with a larger kinetic inductance fraction have a tapered edge profile while samples with a smaller kinetic inductance fraction have a more rectangular edge profile. The measurement also showed that the sample with a smaller kinetic inductance fraction had also been milled a significant way into the substrate. The effect of removing this area should be a change in the calculated resonant frequency from equation (4.17) and a potential reduction in the losses resulting from two-level systems should the resonator be operated at $T < 1$ K, as demonstrated by Barends et al [88] by substantial undercutting of the substrate in areas of high current density.

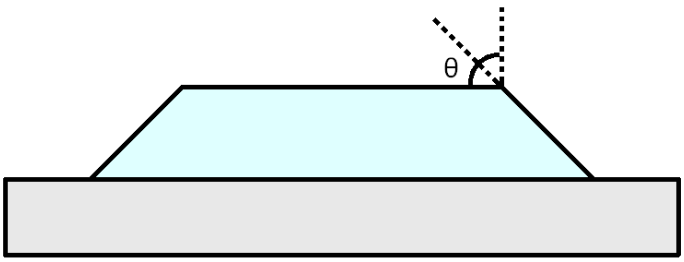

Figure 7.15: Schematic representation of the cross section of the centre track to highlight the quality of the edge profile, adapted from Ref. [154].

The step height measurements that were shown in Fig. 5.6 are representative of the difference between the style of fabrication of films showing low values of the kinetic inductance fraction when analysed in the thick film limit and those exhibiting higher values as shown in Fig. 7.13 (top). The current distribution in all coplanar resonators is such that the current density is higher at the edges; Benz et al [154] showed that a coplanar resonator structure where the edge walls have $\theta = 45°$ showed an increase of three times in the edge current density with a reduction in the observed quality factor compared to $\theta = 90°$ (where the difference in these edge profiles is shown schematically in Fig. 7.15). For the samples measured here, the overall effect of sloped edge walls was an increase in the kinetic inductance fraction. The technique of reducing the film thickness is well known to increase the kinetic inductance fraction [155, 156] and therefore can improve the performance of kinetic inductance detectors [81].

A large corresponding drop in the quality factor is not observed here, as was shown by the measured losses in Fig. 7.2 as a function of cobalt thickness and temperature. The exception to this is the sample $S_1A2.4$ though it is possible that this is a consequence of an overall lower quality factor which increased the uncertainty in the measurement. To explore small changes in the quality factor, a direct comparison can be drawn between samples $S_1G1.6$ and $S_1A1.6$ in terms of losses as a result of the edge profiles since the two samples were made in the same deposition run and have the same cobalt thickness as determined from the deposition conditions. The edge profiles of these samples were shown in Fig. 5.6 and the measured losses shown in Fig. 7.2 are reproduced in table 7.2.

Table 7.2: Quality factors measured at $T = 1.06$ K for samples $S_1G1.6$ and $S_1A1.6$.

Sample	Estimated θ	Measured quality factor	Measured f_0
$S_1G1.6$	90°	1994 ± 49	$6.34 \pm (2 \times 10^{-5})$ GHz
$S_1A1.6$	45°	1736 ± 15	$5.96 \pm (5 \times 10^{-5})$ GHz

Firstly, this shows that there is a difference of 380 MHz in the measured resonant frequency at $T = 1.06$ K, which is too large to be due to errors in the measurement

but is supportive of the reduction in substrate material causing a shift in the device resonant frequency. The measured quality factors, when compared to the estimated edge profile angles, also support the work of Benz et al [154,157]; the quality factor is reduced slightly as the θ is reduced from 90° to 45°. For these samples, a contributing factor for the increase in losses may simply be due to there being more material making up the device; i.e. the AFM edge profiles shown in Fig. 5.6 indicates that $S_1A1.6$ simply has more superconducting (and potentially ferromagnetic/normal) material present. Equally, measurements of the magnetic properties of these samples shown in Fig. 5.10 show that the thin films differ meaning that the normal metal layers may not be identical, which could contribute to a small difference in the losses.

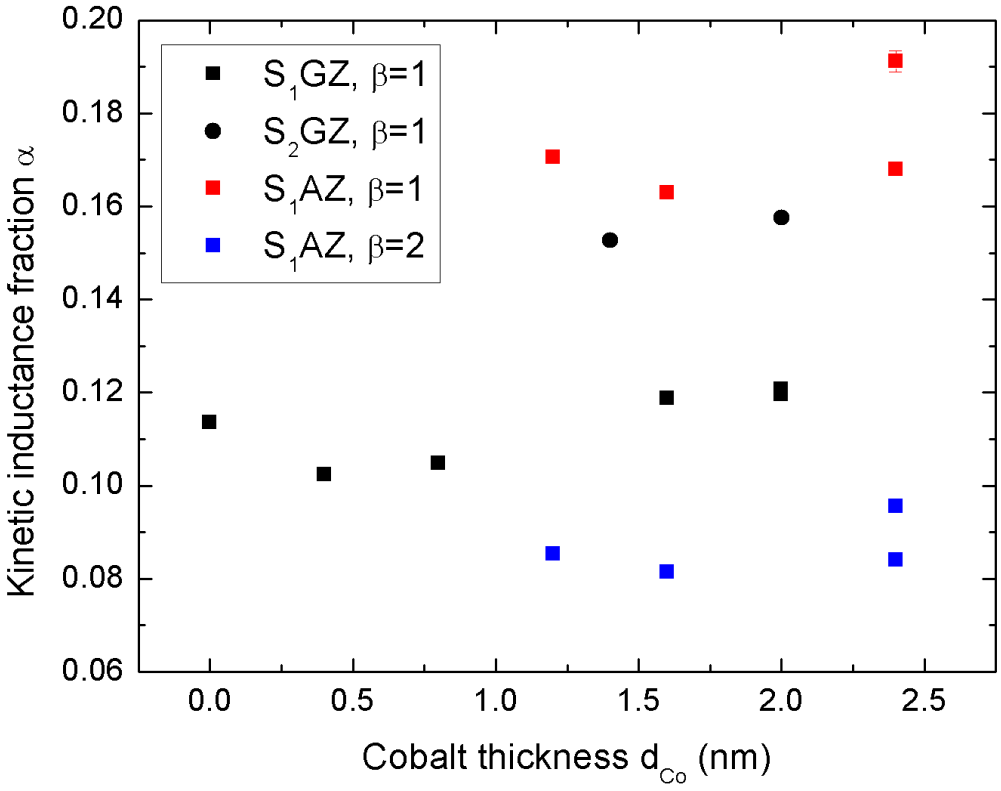

Figure 7.16: Kinetic inductance fraction, α, measured for samples with varying cobalt thickness (using a fixed energy gap of $2\Delta = 3.01$ meV in fit). The legend follows the naming convention defined in section 5.1.3 where Z is the cobalt thickness. Samples S_2AZ analysed in the thick ($\beta = 1$) *and* thin ($\beta = 2$) limit as indicated by the legend.

For completeness, the kinetic inductance fraction as a function of cobalt thickness is shown in Fig. 7.16 where α was determined by fitting equation (4.30) to $f_0(T)$ with

a fixed energy gap ($2\Delta = 3.01$ meV for all samples). This analysis showed a similar trend to that presented in Fig. 7.13 though samples from set #2 show slightly higher values of α. Although T_C measurements showed similar values across sample sets, a four-point measurement showed that sample set #2 had a higher value of T_C. Since the same energy gap was used to fit to all samples shown in Fig. 7.16, this may be a contributing reason for the comparatively high α values. This behaviour was also noted in the context of microwave losses as shown in Fig. 7.2.

Returning to Fig. 7.13, which used the energy gap as a fitting parameter, the value of the kinetic inductance fraction α decreased slightly for films with thicker cobalt layers; this could be interpreted as a consequence of a weakening of the superconducting state despite the niobium thickness. For samples with thicker cobalt layers, however, the quality factor was dramatically reduced (as shown in Fig. 7.2) which resulted in an increased uncertainty in the deduced values of both f_0 and Q. Furthermore, of particular relevance for $S_1A2.4$, the analysis was performed either in the thick or thin film limits; without a detailed knowledge of the edge profile and the microwave current distribution it is difficult to determine the exact value of β that should be used in equation (4.30) as it will almost certainly lie somewhere between the two limits. It can therefore be concluded that there appears to be little observable influence of the cobalt on the superconductor that affects the device behaviour for these thin film structures other than an increase in the losses as a function of cobalt thickness.

7.3 Field Dependence of the Resonant Frequency

To complement the investigation of $f_0(T)$, measurements were also made of the resonant frequency shift as a function of applied magnetic field, H. The proposed microwave CPR measurement device operates in small values of an applied magnetic field; it is therefore important to observe $f_0(H)$ without an inserted Josephson junction, so that this may be accounted for in later analysis. Furthermore, $f_0(H)$ follows

equation (4.32) [93]; i.e. the shift in f_0 due to an applied magnetic field is also dependent on the kinetic inductance fraction and therefore also contains information the number density of Cooper pairs.

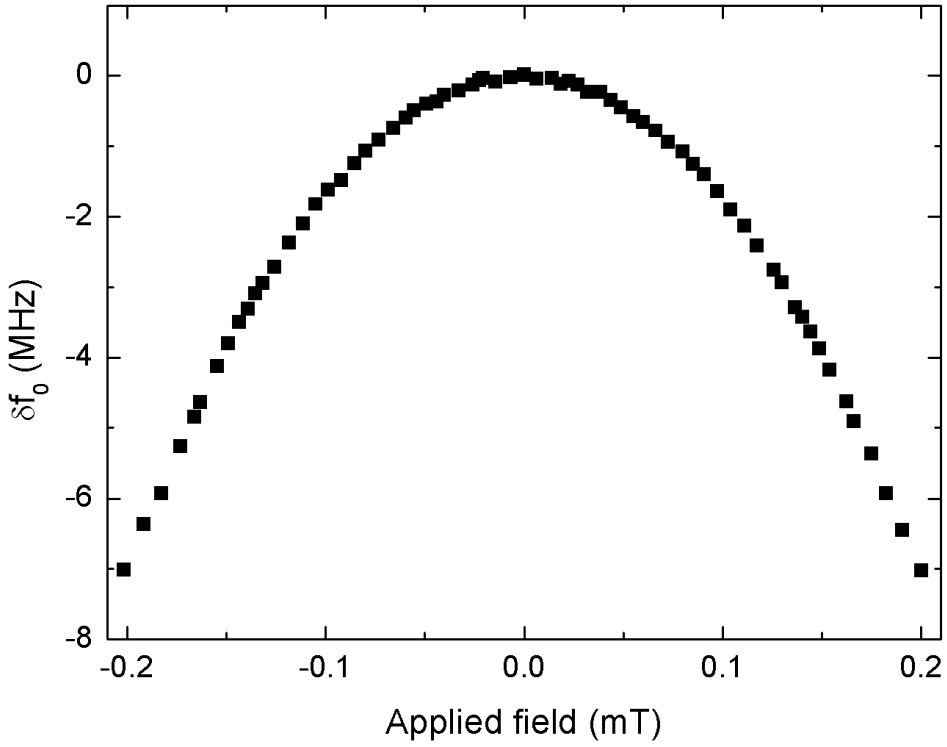

Figure 7.17: Change in the resonant frequency as a function of applied magnetic field, $\delta f_0(H)$, measured for sample $S_1G0.0$ at $T = 1.12$ K.

Fig. 7.17 shows an example of $f_0(H)$ as measured on sample $S_1G0.0$. The resonant frequency is quadratically dependent on the applied magnetic field as was explained in section 4.2.2 and predicted by equation (4.32). As with $f_0(T)$, the amount by which f_0 shifts is dependent on the kinetic inductance fraction since an applied magnetic field causes a corresponding increase in the screening current on the superconducting surface.

Fig. 7.18 provides another way of viewing the same data by plotting $\delta f_0(\mathrm{sgn(H)H^2})$. In this graph, $\mathrm{sgn(H)H^2}$ was plotted to highlight the symmetry of the data. This again shows the quadratic field dependence of the resonant frequency shift, as utilised by Pippard [122], where the gradient of $\delta f_0(\mathrm{sgn(H)H^2})$ gives an indication of the kinetic inductance fraction. Also shown is $Q(\mathrm{sgn(H)H^2})$; the quality factor remains

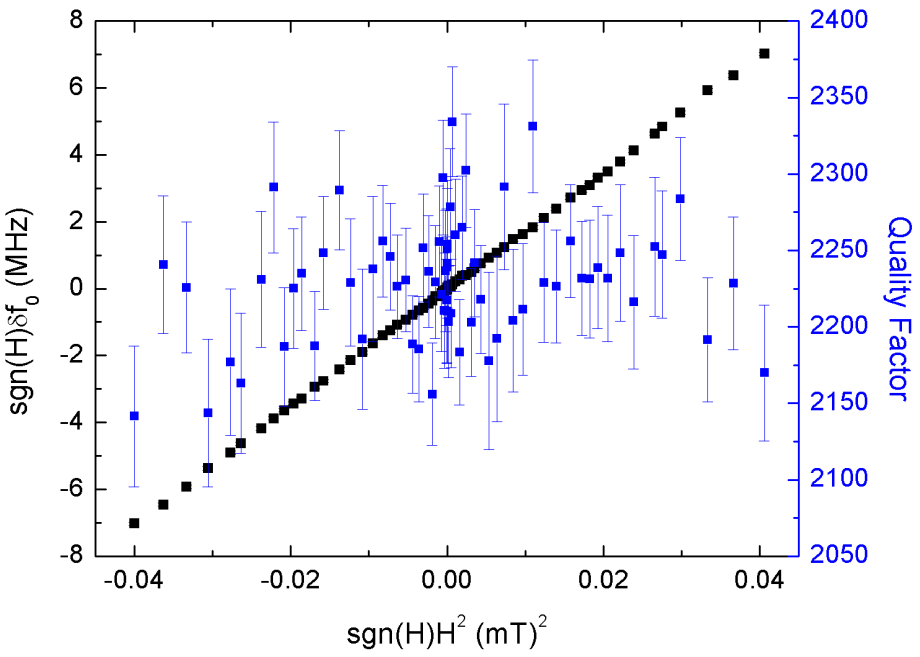

Figure 7.18: Change in the resonant frequency as a function of the square of the applied magnetic field, sgn(H)δf$_0$(sgn(H)H^2), and the quality factor as a function of the square of the applied magnetic field, Q(sgn(H)H^2), for sample $S_1G0.0$ at $T = 1.12$ K.

approximately constant across the range of magnetic field applied here, which was set by the limits of the experimental equipment. This shows that within this range of applied field no additional losses are introduced to the system, which makes this method an attractive way of tuning a coplanar resonator as opposed to some other methods suggested in the literature [93, 94].

Measurement of $f_0(H)$ was made for each sample as a way of comparing the relative device properties. Further illustrative examples of the are shown in Fig. 7.19 for samples $S_1G1.6$ and $S_1A1.6$. The errors are contained with the symbols in the figure and arise from fitting to $S_{21}(f)$ for each value of the applied field. The two samples shown in this example are chosen for direct comparison with the measurement of the temperature dependence of the resonant frequency shown in Fig. 7.13 which have edge profiles shown in Fig. 5.6.

Fig. 7.19 shows that $f_0(H)$ for sample $S_1G1.6$ follows the theoretically predicted re-

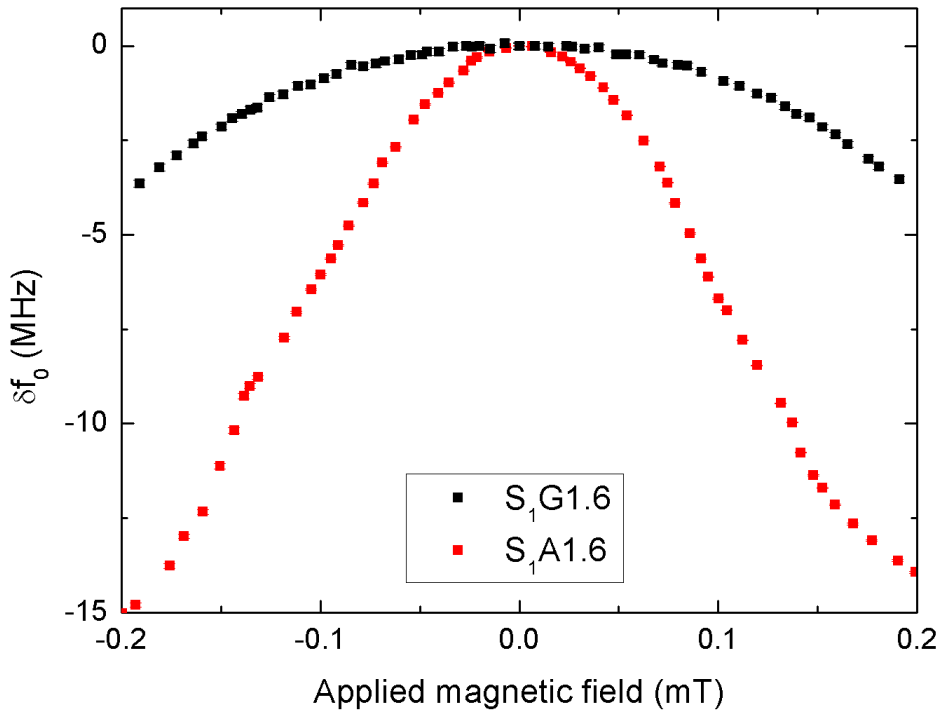

Figure 7.19: Change in the resonant frequency as a function of applied magnetic field, $\delta f_0(H)$, for samples $S_1G1.6$ (black) and $S_1A1.6$ (red).

sponse to an applied magnetic field for the full range of applied field whereas sample $S_1A1.6$ deviates from the quadratic response above ± 0.1 mT. It also shows the overall difference in response between the samples with a differing edge profile; $S_1A1.6$ has sloped edges and shows a much larger response to an applied field compared to a sample with a similar ferromagnetic layer thickness but with a different edge profile.

This behaviour can be explained by considering the effect of the superconducting material. The superconductor excludes the applied magnetic field from the material interior (neglecting that within a superconducting penetration depth of the edge) and focuses the magnetic field lines into the milled gaps in the coplanar resonator pattern. The edge profiles as measured by AFM show that for the sample with a large response to an applied magnetic field ($S_1A1.6$), the milled gap where the superconductor is removed is much smaller than the sample showing a smaller response ($S_1G1.6$) by several micrometers. It is therefore thought that for the same

applied field strength, the geometric flux focusing effect is greater which results in the larger resonant frequency shift observed here. Furthermore, since the edges of sample $S_1A1.6$ are sloped, and therefore thinner, flux lines are allowed into the interior at comparatively lower field strengths.

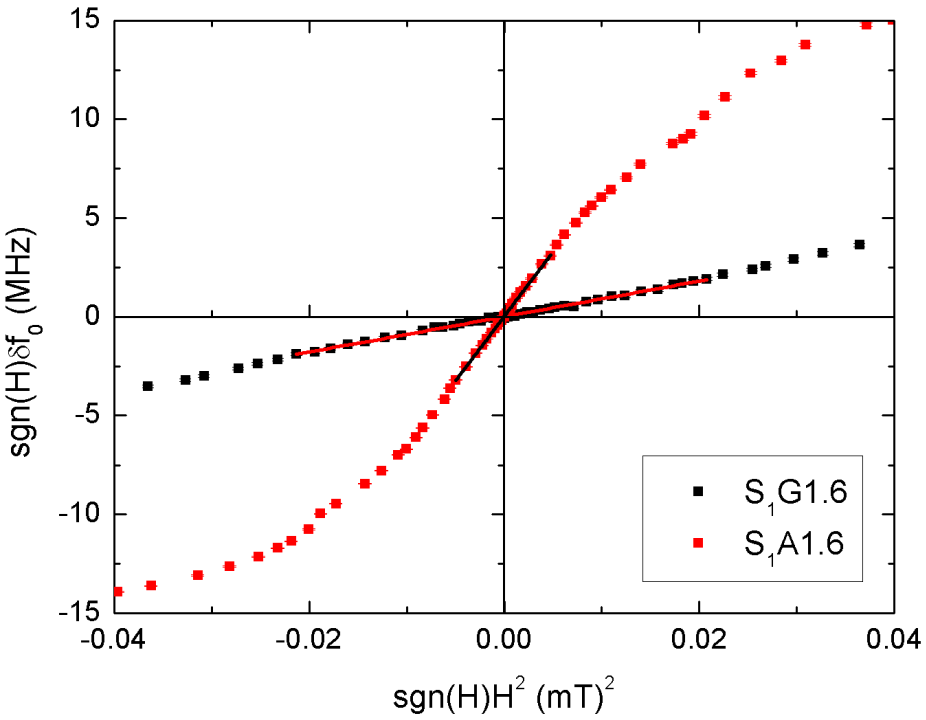

Figure 7.20: Change in the resonant frequency as a function of the square of the applied magnetic field, $\mathrm{sgn(H)}\delta \mathrm{f_0(sgn(H)H^2)}$, for samples $S_1G1.6$ and $S_1A1.6$. The straight lines are linear fits to the data.

This hypothesis is supported by the observed onset of hysteresis in the magnetic field response (not shown in entirety, see Refs. [95, 125] for examples) where extra loss is introduced to the system and is not immediately removed by reversing the magnetic field direction in small amounts. In Fig. 7.19, sample $S_1G1.6$ is seen to be approximately symmetric about zero applied field whereas $S_1A1.6$ shows deviation in the behaviour of the resonant frequency response. If $S_1G1.6$ had been measured at higher magnetic fields, eventually a similar effect would be seen. The deviation from a quadratic field dependence is shown more clearly by plotting $\delta f_0(\mathrm{sgn(H)H^2})$ as shown in Fig. 7.20.

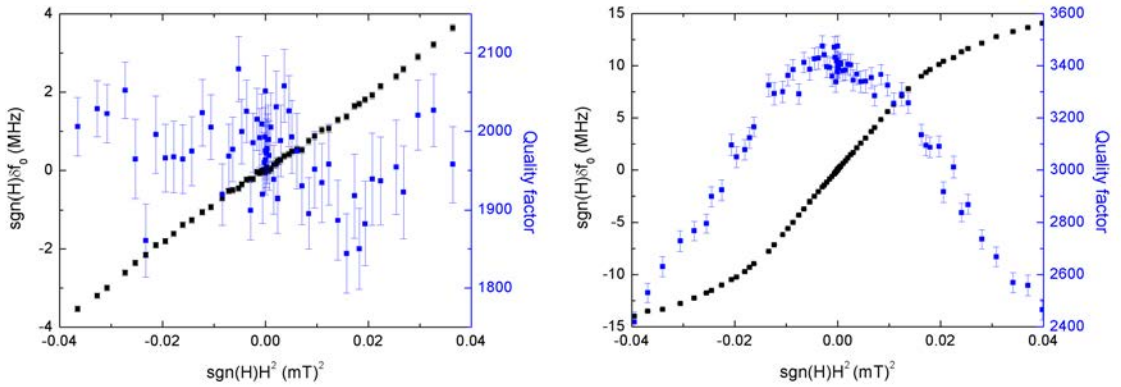

Figure 7.21: Change in the resonant frequency as a function of the square of the applied magnetic field, $\mathrm{sgn(H)}\delta f_0(\mathrm{sgn(H)H^2})$, and the quality factor as a function of the square of the applied magnetic field, $Q(\mathrm{sgn(H)H^2})$, for samples $S_1G1.6$ (left) and $S_1A1.2$ (right).

The deviation becomes even more apparent if the quality factor is also plotted with the change in the resonant frequency as shown in Fig. 7.21 for sample $S_1G1.6$ and $S_1A1.2$. For $S_1G1.6$, the quality factor remains approximately constant as the field is increased in either direction within this range; flux lines do not enter the thin film and introduce extra losses to the system. For $S_1A1.2$, which has a sloped edge profile and shows an increased responsivity, the quality factor remains constant across the linear response to H^2 and shows an immediate decrease as the resonant frequency response deviates from this. At this point, the effect of the sample geometry is such that the magnitude of the applied field exceeds the lower critical field and allows flux lines into the thin film which introduce losses. For sample $S_1A1.2$ the flux focusing factor is estimated to be $\sim$820 (assuming a lower critical field for niobium of 0.1 T and no alteration of behaviour due to thin film thickness). Sample $S_1G1.6$ does not show additional losses within the range of applied fields here but Healey et al [93] used samples of similar dimensions where the estimated flux focusing factor was given as 400.

The response of each sample to an applied magnetic field was studied. The resonant frequency shift caused by an applied magnetic field arises from the same mechanism as a shift caused by a change in temperature and therefore the overall behaviour in the field data across the sample set should be similar to that seen in the temperature

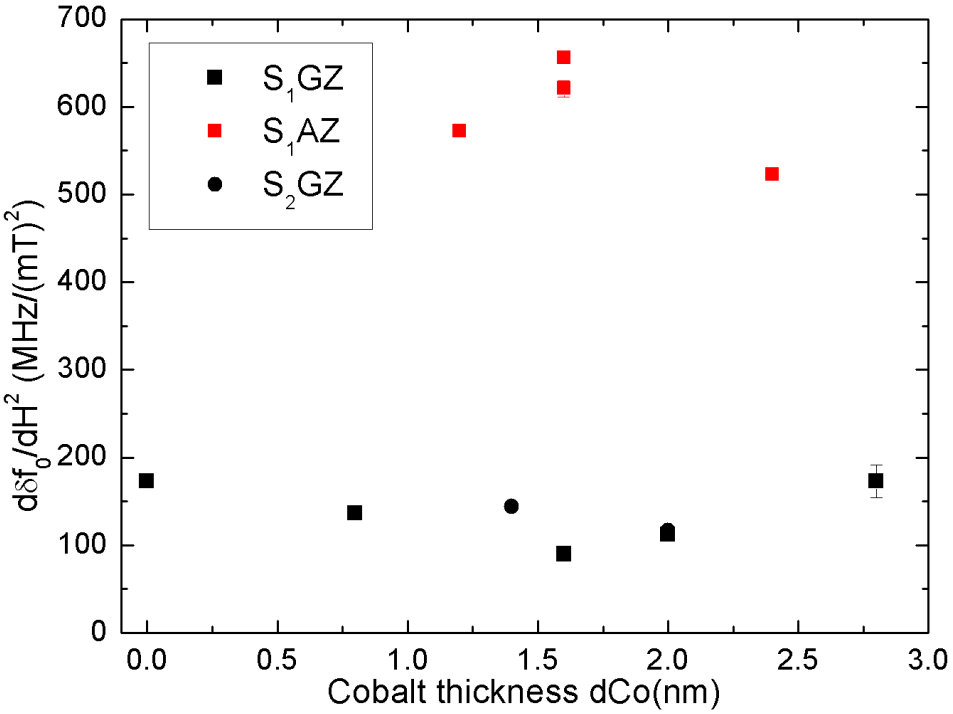

Figure 7.22: $d\delta f_0/dH^2(d_{\mathrm{Co}})$ for samples S_1GZ, S_1AZ and S_2GZ as determined by small magnetic field application in the non-hysteretic regime (see Fig. 7.20 for an example). The legend follows the naming convention defined in section 5.1.3 where Z is the cobalt thickness.

response. Fig. 7.22 shows $d\delta f_0/dH^2(d_{\mathrm{Co}})$ for all samples from sets #1 and #2 (measured *below* the onset of increased loss). By comparison with measurements of $f_0(T)$ shown in Fig. 7.13 it can be seen that those samples with sloped edge profiles do show an increased response to an applied magnetic field or temperature. There does not appear any systematic effect on the superconductivity from the presence of the ferromagnet and the samples showing an increased responsivity is again likely to be due to the effect of the film thickness on the kinetic inductance fraction [155].

7.3.1 Sample Magnetic History

It should be noted that the magnetic history of the samples was not a closely monitored variable since the primary aim of these experiments was to assess the feasibility of the proposed device from a losses perspective. During the majority of field dependence measurements, the cobalt layer was as deposited or had been through a degaussing sequence in the MPMS, i.e. the sample was not in a state of magnetic saturation. The field dependence of the quality factor shown in Fig. 7.21 shows typical results for samples measured before magnetic saturation. For sample $S_1A1.6$ however, a measurement of $f_0(H)$ was made *after* magnetic characterisation where the final sequence step was to apply a field of 1 T parallel to the thin film. The cobalt was therefore close to magnetic saturation before low temperature microwave testing. The maximum applied field from the coils was 0.2 mT so would do little to affect the overall sample magnetisation.

Fig. 7.23 shows the result of this measurement. $\delta f_0(H)$ and $Q(H)$ are shown (top) measured at $T = 1.12$ K. For clarity, $f_0(\mathrm{sgn(H)H^2})$ and $Q(\mathrm{sgn(H)H^2})$ are also shown (bottom). This sample showed a nonlinear $\delta f_0(\mathrm{sgn(H)H^2})$ above an average value of ± 0.04 mT^2 which gives an estimated flux focusing factor of $\sim$1500 (assuming no adjustment of H_C due to the sloping edge profile). Interestingly, when viewing $\delta f_0(H)$ and $Q(H)$ together, it can be seen that there is not simply a decrease in the quality factor as seen in Fig. 7.21 (right), which showed an example

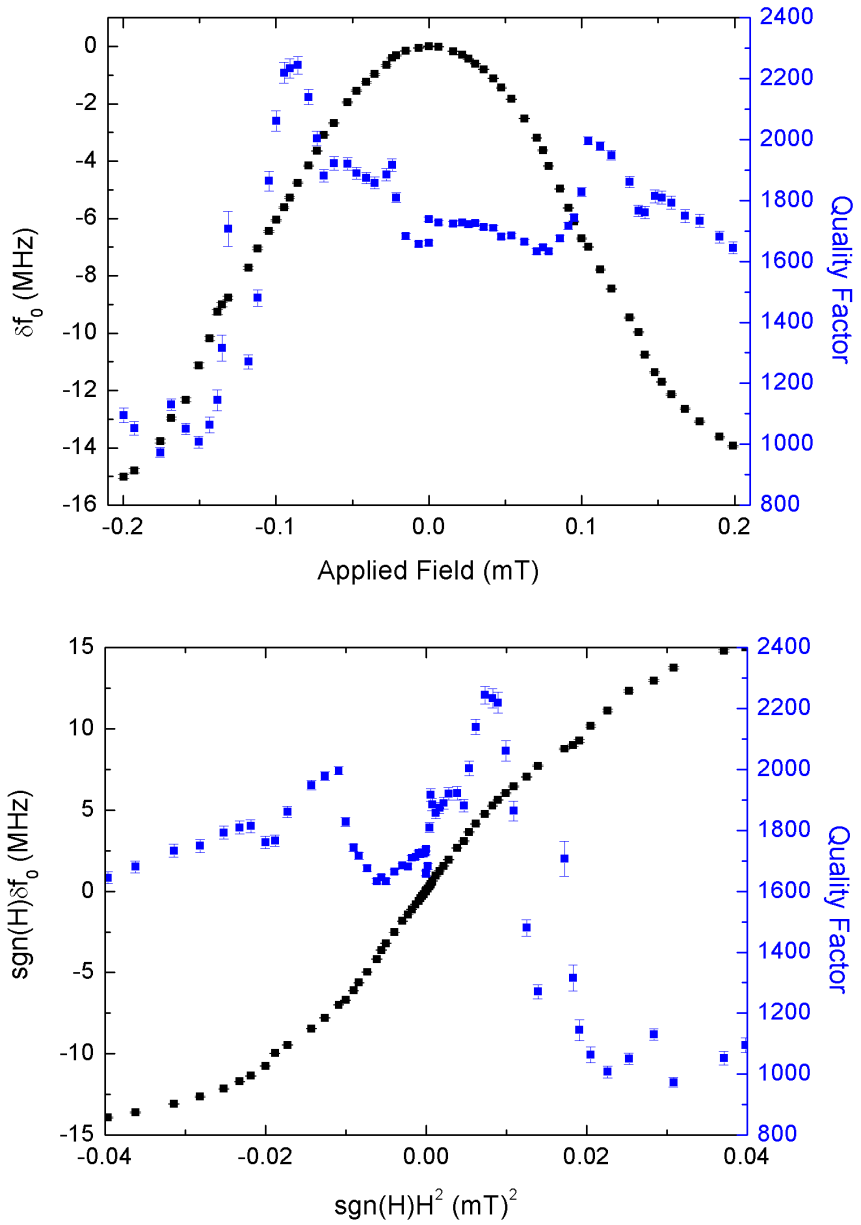

Figure 7.23: Top: Change in the resonant frequency as a function of the applied magnetic field, $\delta f_0(H)$, and the quality factor as a function of the applied magnetic field, $Q(H)$, for sample $S_1A1.6$ after magnetic saturation at $T = 1.12$ K. Bottom: sgn(H)δf$_0$(sgn(H)H^2) and Q(sgn(H)H^2) are also shown.

of a microwave measurement made on a sample before the cobalt was magnetically saturated. Across the linear region of $\delta f_0(\mathrm{sgn(H)H^2})$ there is a steady increase in the losses from low (negative) field to high (positive) field with a sharp decrease in the losses (both field directions) that appears to coincide with the initial onset of flux flow into the thin film denoted by a departure from linearity in $\delta f_0(\mathrm{sgn(H)H^2})$. There is a general slope in the quality factor values across the range of applied fields.

Similar 'peaked' behaviour has been experimentally observed in the electrical properties of superconductor-ferromagnet hybrid structures by Kinsey et al [144] for niobium-cobalt bilayers and in the magnetic properties of ferromagnet-superconductor core-shell structures by Müller et al [158]. Kinsey et al reported reentrant superconductivity that coincided with the coercive field of the ferromagnet. By way of explanation, it was proposed that neighbouring domains with an antiparallel spin alignment caused a reduction in the local exchange field of the ferromagnet which lead to islands of enhancement in T_C. By contrast, Müller et al reported measurements of $M(H)$ above and below T_C of the superconductor. They saw that the diamagnetic signal indicating superconductivity persisted well above H_C as the ferromagnetic shell became magnetically saturated. This was thought to be due to a local reduction of the applied magnetic field by the stray field of the shell. The result presented here is thought to have similarities with the work of Müller et al in that there is a compensation effect produced by the magnetically saturated cobalt.

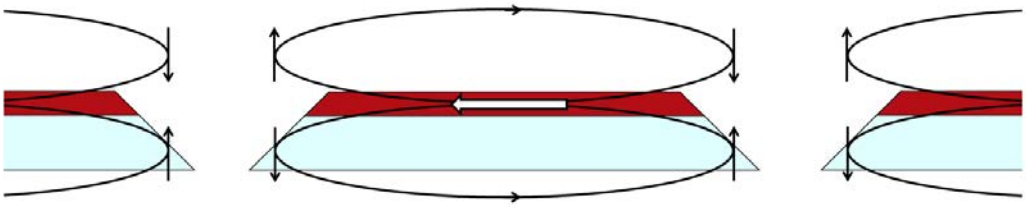

Figure 7.24: Cartoon cross section of a coplanar resonator. The magnetised cobalt layer (red) is on top of a niobium layer with sloped edges (blue) below T_C. The direction of the magnetisation of the cobalt is shown by the white arrow and the direction of the return field is indicated by the black arrows. At the thin superconducting edges, the return field can enter as flux lines and cause loss.

A proposed explanation for the observed behaviour is illustrated in Fig. 7.24 and is

unrelated to the coercive field of the cobalt. The diagram represents a cross section of a coplanar resonator device with an exaggerated sloped edge profile similar to that presented by sample $S_1A1.6$. The magnetically saturated cobalt (red) is on top of niobium (blue); below T_C, magnetic field lines are excluded from the superconductor interior but are permitted to enter at the edges. The sloped edge profile results in a reduced thickness niobium at the extremes; though the magnetisation is parallel to the superconductor, the return field lines of the cobalt produce perpendicular flux lines in the film in this region (with directionality shown by the black arrows). In zero applied field, microwave currents that flow predominantly in the edges move these flux lines which results in a lowered quality factor.

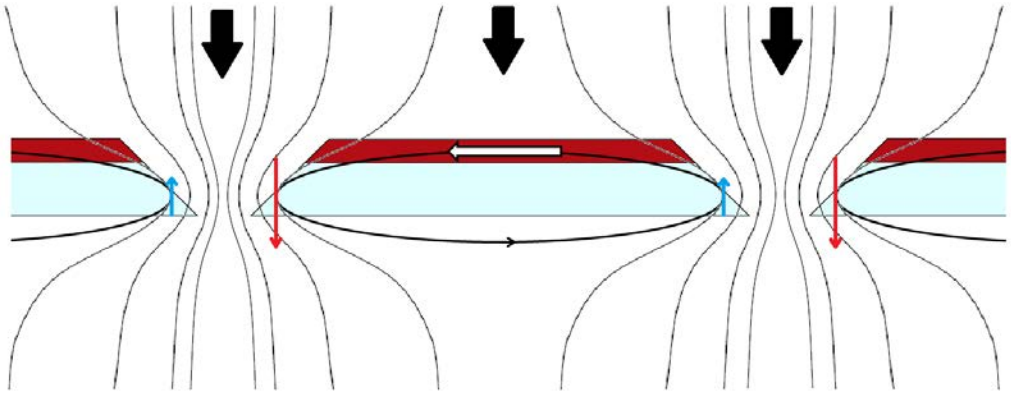

Figure 7.25: Cartoon cross section of a coplanar resonator with a perpendicularly applied magnetic field (direction shown by the black arrows). Small blue arrows indicate regions where there is a reduction is the flux line density, large red arrows show an area of enhanced flux line density.

This situation now is considered for the case of an applied magnetic field perpendicular to the sample in Fig. 7.25. For the edges with flux lines parallel to the applied field, it is proposed that there is an enhancement of the number of flux lines (though the density may remain constant if flux lines are simply pushed further into the film). For the edges with flux lines antiparallel to the applied field, opposite behaviour is anticipated resulting in an overall reduction in the losses, as observed at a field of ± 0.08 mT. This too will affect the kinetic inductance, as is seen by the small bumps in the data at $\mathrm{sgn(H)H^2} = \pm 0.02$ $\mathrm{mT^2}$. Though the cross sectional scenario is physically symmetric, it is noted that the current density is higher in

the centre track thereby causing the majority of the observed effects [80]. This behaviour continues up to a threshold where the effect of the applied magnetic field exceeds that of the return field of the cobalt. At this point, the quality factor is again reduced as before for applied fields of ± 0.1 mT.

The overall slope in the data is not expected given the symmetry though two possible explanations are offered. The above hypothesis assumes that the patterning is symmetric and uniform. This is unlikely to be true though this could present a very small effect on the observed behaviour. Perhaps a more likely explanation is a misalignment of the applied magnetic field relative to the sample, i.e. the applied field may not be exactly perpendicular to the film.

Field Dependence Conclusions

The proposed microwave CPR measurement device requires the application of a small magnetic field to shift the resonant frequency according to the state of the rf SQUID near to the centre track. In section 4.3, it was estimated that a field of ~ 5 μT would be necessary to produce a single flux quantum within the structure which would allow a complete cycle of the CPR to be observed. Fig. 7.22 showed $d\delta f_0/dH^2(d_{\mathrm{Co}})$; applying 5 μT to a sample that had a low response would cause a resonant frequency shift of ~ 5 kHz and a shift of ~ 16 kHz in a sample that had a larger response. Knowledge of $\delta f_0(H)$ is important in early device characterisation as it will allow any small changes of f_0 due to the applied field alone to be accounted for in later analysis. In the case of the samples measured here, the error on f_0 is larger than the expected resonant frequency shift for a sample without sloped edges though this will improve if the quality factor is increased.

7.4 Next Steps: Preliminary Results

The results of microwave measurement indicate that, for the thin film structures already studied, there appears to be little evidence that the ferromagnetic cobalt layer directly interacts in an observable way with the superconducting niobium in the temperature range that was accessible. This is contrary to some reported work in which T_C oscillations have been observed [37,40,131,142], though this is a positive result in terms of the CPR measurement device proposed as it will simplify later analysis.

To make further progress toward a microwave CPR measurement device, thin films with a superconductor-ferromagnet-superconductor sandwich structure should now be studied as shown schematically in Fig. 4.10 (right). The top layer of superconductor will prevent potential degradation of the cobalt and replace the platinum capping layer, which was one of the main sources of microwave loss in the thin films already studied. It is expected that the SFS device structure will therefore have much higher quality factors with some preliminary evidence for this shown here.

A third set of thin films were deposited (set #3) with the full structure: sapphire – Nb(5 nm) – Co(x) – Nb(200 nm), where x is the cobalt thickness in nanometers (see table 5.1). Fig. 3.6 (right) showed that cobalt thicknesses > 5 nm prevented good Josephson coupling between the superconducting electrodes evidenced by reduced values of $I_C R_N$, so it is unnecessary to study excessively thick ferromagnetic layers as it has already been established here that its presence does not interact with the microwave device in an unexpected way. Three samples from set #3 were fabricated and measured where the cobalt thickness and quality factors at $T = 1.12$ K are shown in table 7.3.

Sample $S_3A2.6$ was selected for further investigation. Temperature dependence of the resonant frequency showed similar behaviour to that for sample sets #1 and #2. A measurement of $f_0(H)$ showed some interesting behaviour, as presented in Fig. 7.26. The overall behaviour is similar to that shown by sets #1 and #2 in that

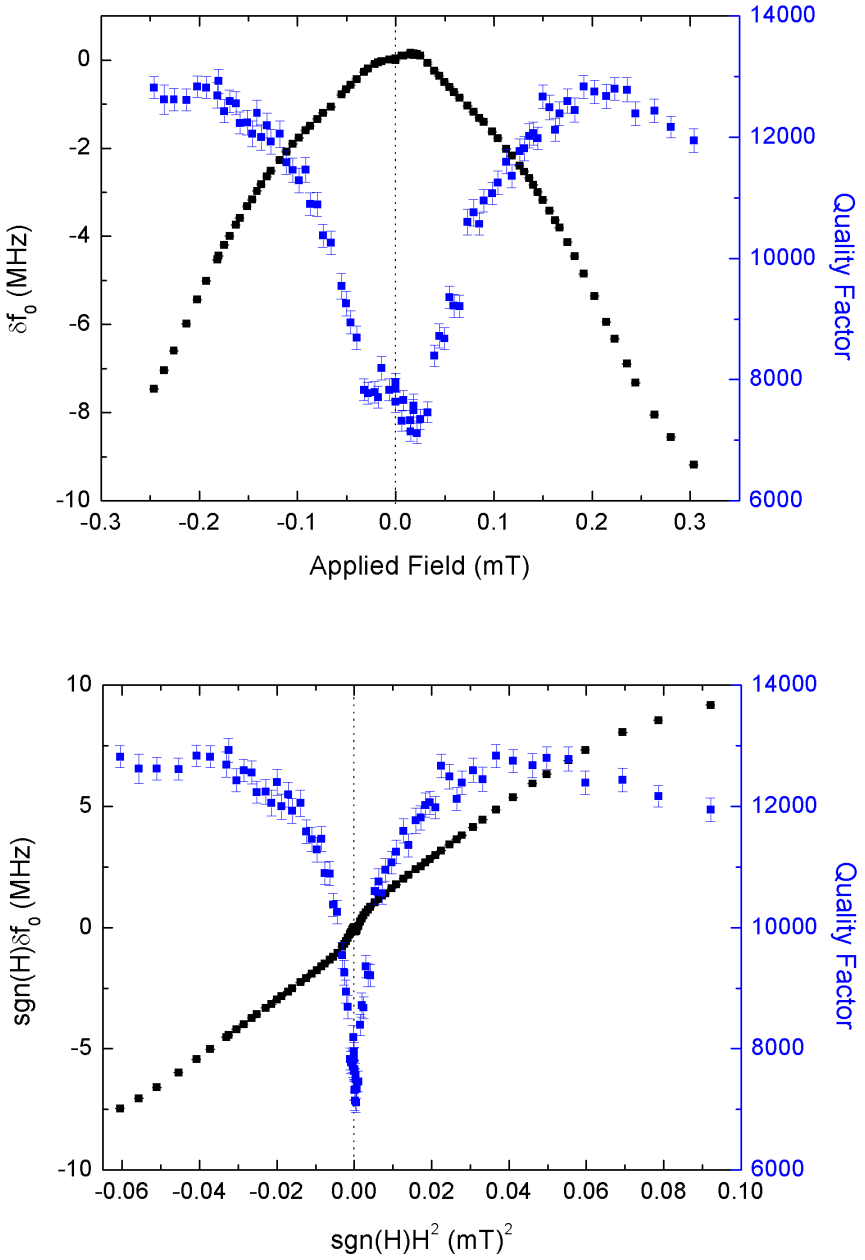

Figure 7.26: Top: Change in the resonant frequency as a function of the applied magnetic field, $\delta f_0(H)$, and the quality factor as a function of the applied magnetic field, $Q(H)$, for sample $S_3A2.6$ at $T = 1.12$ K. Bottom: sgn(H)δf$_0$(sgn(H)H^2) and Q(sgn(H)H^2) are also shown.

Table 7.3: Quality factors measured at $T = 1.12$ K for samples from set #3.

Cobalt thickness	Quality Factor
1.4 nm	$127,246 \pm 559$
2.6 nm	7947 ± 154
10 nm	Unobserved

there is a quadratic dependence of the resonant frequency shift to the applied magnetic field. The difference in this sample is shown in $f_0(H)$, though more clearly by $f_0(\mathrm{sgn(H)H^2})$ in Fig. 7.26 (bottom). For the region below ± 0.04 mT^2 there are two distinct regions in the resonant frequency responsivity. Between ± 0.03 mT^2 there is a region of enhanced responsivity that shows a reduced quality factor. Above this, $\pm 0.03 - 0.055$ mT^2, there is a region of $\delta f_0(\mathrm{sgn(H)H^2})$ with a distinctly different responsivity and an overall higher value of Q. Following this ($> \pm 0.055$ mT^2), familiar behaviour is seen as flux lines enter the film when $H > H_{C1}$ at the superconductor edges and lowers the quality factor as before.

It is thought that this behaviour is also a result of the film thickness in the structure [155, 156]. The central region could be thought of as the response of the lower niobium layer (5 nm) that dominates the overall behaviour. Above a critical value of applied field, the response of the upper niobium layer (200 nm) is seen with a gradient of $\delta f_0/\mathrm{sgn(H)H^2} = 117.21 \pm 0.36$, which is comparable with the results presented in Fig. 7.22. With a symmetric sandwich structure, this effect should not been seen and the quality factor should be much higher than observed in a bilayer system. This hypothesis arises from the initial results presented in table 7.3 and through further simulations performed with COMSOL, as described in section 7.1. For the thin film structure of set #3 with $d_{\mathrm{Co}} = 2.6$ nm, the speculative result of simulation provides $Q \approx 9000$, which agrees well with experimental observation. To simulate a symmetric SFS structure, the platinum layer was removed and replaced with a second 200 nm thick niobium layer. The result of this simulation (for the material properties listed in table 7.1) for $d_{Co} = 2$ nm is an expected quality factor of somewhere in the region of 500,000. This is quite large even for niobium resonators but since the simulation should be thought of as only providing an order of

magnitude estimate, this is promising nonetheless.

This initial work presented in this section paves the way for the development of a CPR measurement device that operates at microwave frequencies. It is seen that the quality factor is somewhat improved for an asymmetric sandwich structure and simulations indicate that this will increase further when using a symmetric structure.

7.5 Conclusions and Further Work

Following the initial work on dc measurement of the CPR of Josephson junctions presented in chapter 3, a feasibility study was conducted to assess the suitability of a microwave realisation for making this same measurement. The work presented in chapters 5–7 and the main results are summarised below:

- Thin film multilayer structures were deposited by A. Bannykh at the University of Cambridge by dc magnetron sputtering. An optical lithographic process was developed by the author to reliably pattern the films into $\lambda/2$ coplanar resonator structures.

- The samples were magnetically characterised using room temperature VSM (by A. Bannykh) and low temperature SQUID magnetometry (by the author). The results showed an overall increase in the saturation magnetisation as a function of the cobalt thickness as expected. The results of both measurement techniques agreed well. A magnetic dead layer of ~ 1.3 nm and a bulk magnetisation of (622 ± 25) emu/cm^3 were observed.

- T_C of the thin films was measured using a four-point measurement (by A. Bannykh) and low temperature SQUID magnetometry (by the author). For small cobalt thicknesses, a T_C of (8.74 ± 0.03) K was seen. For $d_{\mathrm{Co}} < 10$ nm there was no systematic variation in this value as the cobalt thickness increased.

- A theoretical model was developed to describe the microwave response of low quality factor resonators and a program was written by the author to extract the relevant parameters and enable fast data analysis. Automation software was developed in LabView to record $S_{21}(f)$ as a function of temperature and applied magnetic field. Finally, a program was written to compare the experimental results with Mattis-Bardeen theory which allowed determination of the kinetic inductance fraction of the films.

- Microwave losses as a function of cobalt thickness were measured over the range $1 - 4.2$ K. The losses increased linearly with cobalt thickness and increasing the temperature increased the rate of change of losses. The material properties of the magnetic dead layer were discussed with the result that there is at least 0.5 nm of insulating material present. Finally, simulations of the coplanar resonator were presented in an attempt to estimate the order of magnitude of the losses; simulated losses were a factor of ten lower than observed experimentally.

- AFM measurements were made to assess the edge profiles of the samples from sets #1 and #2. Samples that showed differences in responsivity to changes in temperature and applied magnetic field were found to have different edge profiles. Samples that exhibited a large responsivity had sloped edges while samples showing a smaller response had straighter edges.

- The kinetic inductance fraction was measured to be $\sim 6\%$ for all samples by comparing $f_0(T)$ to Mattis-Bardeen theory. It was found necessary to adjust the film thickness limit in which the analysis was conducted according to the fabrication style of each sample (determined through AFM measurement). The same behaviour was observed for $f_0(H)$ in terms of the film thickness dependence of the kinetic inductance fraction.

- The effect of the magnetic state of the cobalt was briefly studied for sample $S_1A1.6$ after the application of a magnetic field of 1 T. It was found that there was no obvious change in the behaviour of f_0 as a function of temperature or

applied magnetic field, but there was a surprising difference in the behaviour of $Q(H)$, which showed a sudden reduction in losses as $f_0(H)$ began to deviate from the behaviour predicted by equation (4.32). An explanation was proposed that followed the work of Müller et al [158] citing applied field compensation by the stray field of the magnetically saturated cobalt.

- The microwave properties of select coplanar resonators from set #3 were investigated. The quality factors were higher than those observed from sets #1 and #2. A measurement of $f_0(H)$ revealed two distinct regions of differing responsivity to the applied field where it is proposed to arise from the unequal niobium layer thicknesses. Simulation of a coplanar resonator fabricated from an SFS trilayer gave the order of magnitude of the quality factor in the hundreds of thousands.

Despite the high losses of the samples measured here (associated with the sample structure), it is thought that the materials studied here would be suitable for a microwave realisation of a CPR measurement device of an SFS Josephson junction. To progress further towards this device the following work should be conducted:

- Nb(200 nm) – Co(x) – Nb(200 nm) trilayer films should be deposited and checked for quality including substrate adhesion and material characterisation.
- A mask for photolithography should be designed to leave a block of trilayer material next to a current antinode in the superconducting resonator and an investigation should be conducted of its overall effect.
- A reliable fabrication process should be developed to integrate a Josephson junction structure into this block with further microwave property testing.
- Room temperature electronics should be designed and automation software developed to operate the device as a GHz rf SQUID in nonhysteretic mode for CPR readout.

If these steps can be completed successfully, this device could be used to measure any Josephson junction fabricated from high quality multilayered thin film structures patterned into a GHz resonator.

CHAPTER 8

CONCLUSIONS

Josephson junctions are of interest for the study of the fundamental physics that underpins their operation and for their practical applications. One such application is their potential role in creating the building blocks of quantum computers. The observation of the functional relationship between the current through the junction and the phase difference across it allows insight into the microscopic behaviour in the device, provides a test of the theoretical predictions for many exotic junctions, and allows more accurate modelling of large scale Josephson junction-containing systems. In this thesis, two experimental methods of measuring the CPR of Josephson junctions were investigated.

Chapter 3 documented the first of these methods. A low noise system for CPR measurement down to a temperature of 0.3 K was designed and thoroughly tested. Planar CPR measurement chips based on the Waldram-Lumley method were designed by Dr E. Tarte and Dr T. Ortlepp and fabricated at the Institute of Photonic Technology by Dr J. Kunert. There are two potential advantages of the design presented. The first is one of versatility; the CPR of any Josephson junction could be measured provided that it can be deposited onto the CPR measurement chip. Secondly, the CPR is measured directly and does not require complicated data anal-

ysis. The chip contained a high-I_C Josephson junction for test purposes; a detailed method for the determination of important circuit parameters was developed and experiments were conducted at $T = 4.2$ K. It was found that the CPR could not be measured using this chip for two reasons. Firstly, $L_P > L_{J0}$; since there is no way to accurately determine the value of L_P, there is no way to remove its influence from the measured CPR. This would have been resolved had the project collaborators been successful in the deposition of a low-I_C junction onto the CPR measurement circuit. The second problem was that it was found that this chip design was sensitive to pickup from current flowing through nearby wires and/or sensitive to return currents flowing in the superconducting ground plane. This problem is intrinsic to the planar design geometry and could not be resolved by further analysis, extra care taken in wiring, or by covering the chip with a superconducting shield. Since the Waldram-Lumley method relies on accurately measuring only the current through an inductor coupled to the dc SQUID, this last problem ultimately rendered CPR measurement with this chip invalid. Nonetheless, the experimental work conducted in the characterisation of this measurement device yielded a system with which to interface with further chip designs should the development continue.

Due to the problems encountered with the Waldram-Lumley method presented in chapter 3, an alternative CPR measurement method was proposed at the end of chapter 4 that drew inspiration from the Rifkin-Deaver method [8] and research from the field of GHz SQUIDs conducted in the early 1990's [77, 129]. This has the advantage of a less demanding fabrication process; rather than depositing a junction into a small area in the CPR device, the whole structure would be fabricated from a single multilayered film using single-step photolithography processing followed by Focused Ion Beam milling to define an rf SQUID. The method was found to be promising but the complete structure required to develop the device fully was not realised by the project collaborators. In the absence of the necessary thin films, attention was focused on assessing the suitability of the materials to the microwave CPR measurement method.

Chapter 7 presented the results of the feasibility study which focused on sets of niobium-cobalt-platinum films and a limited number of asymmetric niobium-cobalt-niobium sandwich structures where the cobalt layer thickness was systematically varied across each set. The in-plane magnetic moments of the films were measured as a function of the cobalt layer thickness with the results presented in chapter 5. It was found that the saturation magnetisation was proportional to the cobalt thickness but with an observable offset of ~ 1.3 nm, which is attributed to a magnetic dead layer. The measured magnetisation was found to be consistent with similar measurements made at the University of Cambridge using a different magnetometer. The microwave losses were also measured as a function of cobalt layer thickness and showed a similar pattern of behaviour observed in the magnetic measurements. A good agreement between losses simulated using COMSOL Multiphysics and experimental data is found if it is assumed that there is a reduced balance between the applied current in the normal metal layers and the opposing current induced by currents in the superconducting layer. It is suggested that this may be due to sample inhomogeneity but further investigation is clearly required. Further simulations showed a good agreement with the losses observed for an asymmetric sandwich structure and preliminary simulations suggest that, should a symmetric SFS film be fabricated into a coplanar resonator, one could expect a quality factor of the order of hundreds of thousands.

The dependence of the resonant frequency on temperature and field was also investigated as a function of cobalt thickness to search for possible oscillatory behaviour that would relate to the known variation of I_C in SFS Josephson junctions [31] or observed oscillatory behaviour of T_C in other systems [40,131]. Low quality factors and interaction with other system resonances yielded asymmetric resonant peaks that necessitated the development of a theoretical model and fitting routine to accurately determine the relevant parameters as documented in chapter 6. This, together with the development of a LabView program to automate low temperature microwave experiments, may prove of use for future work. The temperature dependence of f_0 was found to be in good agreement with Mattis-Bardeen theory for all cobalt thick-

nesses. Although the slopes of $f_0(T)$ were found to vary with cobalt thickness, this was explained by an increase in the kinetic inductance due to a tapered edge profile for samples prepared at the University of Cambridge and no oscillatory dependence of n_s of d_{Co} was observed within experimental error.

Previous work [93, 117] has shown that a small magnetic field of ~ 0.1 mT applied perpendicularly to a coplanar resonator can reversibility shift the resonant peak by ~ 2 MHz without introducing significant extra loss to the system. The shift is quadratically dependent on the size of the applied field until flux lines are forced into the film. It was therefore of interest to study how this behaviour would be modified by the presence of a ferromagnetic layer such that it may be applied to the microwave CPR measurement device. It was found that f_0 could be shifted by a factor of two more than for a niobium-only resonator; this was an unexpected result and further theoretical work is needed to assess the origin for the enhanced responsivity to an applied field. For the asymmetric sandwich structure, a measurement of $f_0(H)$ showed two regions of different responsivity to the field that was explained by the different niobium layer thicknesses. The observed result of increased responsivity arises from an enhancement of the kinetic inductance fraction for the thinner layer. This suggests that thin superconducting layers, or devices purposely made with a tapering edge profile, would be of use in field tuned devices. However, a tapered edge may suppress the value of H_C and therefore reduce the usable field range available to tune the device. At the end of chapter 7, a scheme of further work was presented that could be followed to complete the microwave CPR measurement device development.

As a final point, there are relatively few experimental papers in the literature that outline attempts to measure the CPR of a Josephson junction. Of those who have reported work in this field, the majority seem to favour the Rifkin-Deaver method despite the challenges involved in extracting the CPR from the experimental data. Some other groups who have been inspired by the Waldram-Lumley method, albeit with a planar geometry, do not mention careful investigations of the issues raised

by the work presented in chapter 3 and therefore some doubt could be potentially cast on the results. Certainly, the planar dc device presented here could not be used to make an accurate assessment of the CPR of a Josephson junction. It seems to the author that if one should implement this CPR measurement style, the original Waldram-Lumley device structure [4] provides the necessary protection against parasitic signal pick-up and yet the geometry reduces the versatility of the concept immensely. The Rifkin-Deaver style method does not suffer from the same problems yet, as all circuit elements are produced in a single film deposition, the applications are limited. However, there is some hope that the later work presented in chapter 7 can pave the way toward this alternative measurement scheme applied to SIFS Josephson junctions such that it could combine the ease of microwave component fabrication with the control of film thickness and junction fabrication that has been previously demonstrated by the collaborators for this project [31].

REFERENCES

[1] J. Clarke and F. K. Wilhelm, "Superconducting quantum bits," *Nature*, vol. 453, no. 7198, pp. 1031–1042, 2008.

[2] G. Wendin and V. S. Shumeiko, "Quantum bits with Josephson junctions," *Low Temperature Physics*, vol. 33, p. 724, 2007.

[3] K. K. Likharev, "Superconducting weak links," *Reviews of Modern Physics*, vol. 51, no. 1, p. 101, 1979.

[4] J. R. Waldram and J. M. Lumley, "Direct measurements of the current-phase relation in superconducting weak links," *Revue de Physique Appliquée*, vol. 10, no. 1, pp. 7–10, 1975.

[5] O. Mielke, T. Ortlepp, H. F. Uhlmann, and H. Toepfer, "Experimental evaluation of the current-phase relation of a Josephson junction," in *Theoretical Engineering (ISTET), 2009 XV International Symposium on*, pp. 1–5, VDE, 2009.

[6] S. M. Frolov, D. J. van Harlingen, V. A. Oboznov, V. V. Bolginov, and V. V. Ryazanov, "Measurement of the current-phase relation of superconductor/ferromagnet/superconductor π Josephson junctions," *Physical Review B*, vol. 70, no. 14, p. 144505, 2004.

[7] C. Chialvo, I. C. Moraru, D. J. van Harlingen, and N. Mason, "Current-phase relation of graphene Josephson junctions," *arXiv preprint arXiv:1005.2630*, 2010.

[8] R. Rifkin and B. S. Deaver Jr, "Current-phase relation and phase-dependent conductance of superconducting point contacts from rf impedance measurements," *Physical Review B*, vol. 13, no. 9, p. 3894, 1976.

[9] T. van Duzer and C. W. Turner, *Principles of superconductive devices and circuits*. Prentice Hall, 1999.

[10] M. Tinkham, *Introduction to superconductivity*. McGraw-Hill, 1975.

[11] H. K. Onnes, "The superconductivity of mercury," *Communications from the Physical Laboratory at the University of Leiden*, vol. 122, p. 124, 1911.

[12] W. Meissner and R. Ochsenfeld, "A new effect in penetration of superconductors," *Die Naturwissenschaften*, vol. 21, pp. 787–788, 1933.

[13] F. London and H. London, "The electromagnetic equations of the supraconductor," *Proceedings of the Royal Society of London. Series A-Mathematical and Physical Sciences*, vol. 149, no. 866, pp. 71–88, 1935.

[14] J. R. Hook and H. E. Hall, *Solid State Physics*. Manchester Physics Series, Wiley-Blackwell, 1991.

[15] C. J. Gorter and H. Casimir, "On supraconductivity I," *Physica*, vol. 1, no. 1, pp. 306–320, 1934.

[16] J. Bardeen, L. N. Cooper, and J. R. Schrieffer, "Theory of superconductivity," *Physical Review*, vol. 108, no. 5, p. 1175, 1957.

[17] H. Fröhlich, "Theory of the superconducting state. I. the ground state at the absolute zero of temperature," *Physical Review*, vol. 79, no. 5, pp. 845–856, 1950.

[18] P. Townsend and J. Sutton, "Investigation by electron tunneling of the superconducting energy gaps in Nb, Ta, Sn, and Pb," *Physical Review*, vol. 128, no. 2, p. 591, 1962.

[19] B. S. Deaver Jr and W. M. Fairbank, "Experimental evidence for quantized flux in superconducting cylinders," *Physical Review Letters*, vol. 7, no. 2, pp. 43–46, 1961.

[20] R. Pöpel, "Exact solutions of the Mattis Bardeen theory for thin superconducting films and bulk material," *Magnetics, IEEE Transactions on*, vol. 27, no. 2, pp. 1306–1309, 1991.

[21] S. Blundell, *Magnetism in Condensed Matter*. Oxford Master Series in Condensed Matter Physics, OUP Oxford, 2001.

[22] B. I. Bleaney and B. Bleaney, *Electricity and magnetism*. Oxford University Press, 1976.

[23] A. I. Buzdin, "Proximity effects in superconductor-ferromagnet heterostructures," *Reviews of Modern Physics*, vol. 77, no. 3, p. 935, 2005.

[24] N. R. Werthamer, "Theory of the superconducting transition temperature and energy gap function of superposed metal films," *Physical Review*, vol. 132, no. 6, p. 2440, 1963.

[25] A. K. Feofanov, V. A. Oboznov, V. V. Bol'ginov, J. Lisenfeld, S. Poletto, V. V. Ryazanov, A. N. Rossolenko, M. Khabipov, D. Balashov, A. B. Zorin, *et al.*, "Implementation of superconductor/ferromagnet/superconductor π-shifters in superconducting digital and quantum circuits," *Nature Physics*, vol. 6, no. 8, pp. 593–597, 2010.

[26] P. Fulde and R. A. Ferrell, "Superconductivity in a strong spin-exchange field," *Physical Review*, vol. 135, p. A550, 1964.

[27] A. I. Larkin and Y. N. Ovchinnikov, "Nonuniform state of superconductors," *Soviet Journal of Experimental and Theoretical Physics*, vol. 20, p. 762, 1965.

[28] E. A. Demler, G. B. Arnold, and M. R. Beasley, "Superconducting proximity effects in magnetic metals," *Physical Review B*, vol. 55, no. 22, p. 15174, 1997.

[29] V. V. Ryazanov, V. A. Oboznov, A. Y. Rusanov, A. V. Veretennikov, A. A. Golubov, and J. Aarts, "Coupling of two superconductors through a ferromagnet: evidence for a π junction," *Physical Review Letters*, vol. 86, no. 11, pp. 2427–2430, 2001.

[30] A. Golubov, M. Kupriyanov, and E. Il'ichev, "The current-phase relation in Josephson junctions," *Reviews of Modern Physics*, vol. 76, no. 2, p. 411, 2004.

[31] J. W. A. Robinson, S. Piano, G. Burnell, C. Bell, and M. G. Blamire, "Zero to π transition in superconductor-ferromagnet-superconductor junctions," *Physical Review B*, vol. 76, no. 9, p. 094522, 2007.

[32] J. W. A. Robinson, S. Piano, G. Burnell, C. Bell, and M. G. Blamire, "Critical current oscillations in strong ferromagnetic π junctions," *Physical Review Letters*, vol. 97, no. 17, p. 177003, 2006.

[33] F. Born, M. Siegel, E. K. Hollmann, H. Braak, A. A. Golubov, D. Y. Gusakova, and M. Y. Kupriyanov, "Multiple 0-π transitions in superconductor/insulator/ferromagnet/superconductor josephson tunnel junctions," *Physical Review B*, vol. 74, no. 14, p. 140501, 2006.

[34] A. S. Sidorenko, V. I. Zdravkov, A. A. Prepelitsa, C. Helbig, Y. Luo, S. Gsell, M. Schreck, S. Klimm, S. Horn, L. R. Tagirov, *et al.*, "Oscillations of the critical temperature in superconducting Nb/Ni bilayers," *Annalen der Physik*, vol. 12, no. 1-2, pp. 37–50, 2003.

[35] Z. Radović, M. Ledvij, L. Dobrosavljević-Grujić, A. I. Buzdin, and J. R. Clem, "Transition temperatures of superconductor-ferromagnet superlattices," *Physical Review B*, vol. 44, no. 2, p. 759, 1991.

[36] H. K. Wong, B. Y. Jin, H. Q. Yang, J. B. Ketterson, and J. E. Hilliard, "Superconducting properties of V/Fe superlattices," *Journal of Low Temperature Physics*, vol. 63, no. 3, pp. 307–315, 1986.

[37] Y. Obi, M. Ikebe, T. Kubo, and H. Fujimori, "Oscillation phenomenon of transition temperatures in Nb/Co and V/Co superconductor/ferromagnet multilayers," *Physica C: Superconductivity*, vol. 317, pp. 149–153, 1999.

[38] V. I. Zdravkov, J. Kehrle, G. Obermeier, S. Gsell, M. Schreck, C. Müller, H. A. K. von Nidda, J. Lindner, J. Moosburger-Will, E. Nold, *et al.*, "Reentrant superconductivity in superconductor/ferromagnetic-alloy bilayers," *Physical Review B*, vol. 82, no. 5, p. 054517, 2010.

[39] T. Mühge, N. N. Garif'yanov, Y. V. Goryunov, G. G. Khaliullin, L. R. Tagirov, K. Westerholt, I. A. Garifullin, and H. Zabel, "Possible origin for oscillatory superconducting transition temperature in superconductor/ferromagnet multilayers," *Physical Review Letters*, vol. 77, no. 9, pp. 1857–1860, 1996.

[40] T. Mühge, K. Theis-Bröhl, K. Westerholt, H. Zabel, N. N. Garif'yanov, Y. V. Goryunov, I. A. Garifullin, and G. G. Khaliullin, "Influence of magnetism on superconductivity in epitaxial Fe/Nb bilayer systems," *Physical Review B*, vol. 57, no. 9, p. 5071, 1998.

[41] V. Ambegaokar and A. Baratoff, "Tunneling between superconductors," *Physical Review Letters*, vol. 10, no. 11, pp. 486–489, 1963.

[42] B. D. Josephson, "Possible new effects in superconductive tunnelling," *Physics Letters*, vol. 1, pp. 251–253, 1962.

[43] P. W. Anderson and J. M. Rowell, "Probable observation of the Josephson superconducting tunneling effect," *Physical Review Letters*, vol. 10, no. 6, pp. 230–232, 1963.

[44] D. N. Langenberg, D. J. Scalapino, B. N. Taylor, and R. E. Eck, "Investigation of microwave radiation emitted by Josephson junctions," *Physical Review Letters*, vol. 15, no. 7, pp. 294–297, 1965.

[45] L. N. Bulaevskii, V. V. Kuzii, and A. A. Sobyanin, "Superconducting system with weak coupling to the current in the ground state," *JETP lett*, vol. 25, no. 7, pp. 290–294, 1977.

[46] H. Hilgenkamp, "Pi-phase shift Josephson structures," *Superconductor Science and Technology*, vol. 21, no. 3, p. 034011, 2008.

[47] J. van Dam, Y. V. Nazarov, E. P. A. M. Bakkers, S. De Franceschi, and L. P. Kouwenhoven, "Supercurrent reversal in quantum dots," *Nature*, vol. 442, no. 7103, pp. 667–670, 2006.

[48] J. J. A. Baselmans, A. F. Morpurgo, B. J. van Wees, and T. M. Klapwijk, "Reversing the direction of the supercurrent in a controllable Josephson junction," *Nature*, vol. 397, no. 6714, pp. 43–45, 1999.

[49] E. Il'ichev, M. Grajcar, R. Hlubina, R. P. J. IJsselsteijn, H. E. Hoenig, H. G. Meyer, A. Golubov, M. H. S. Amin, A. M. Zagoskin, A. N. Omelyanchouk, *et al.*, "Degenerate ground state in a mesoscopic $YBa_2Cu_3O_{7-x}$ grain boundary Josephson junction," *Physical Review Letters*, vol. 86, no. 23, pp. 5369–5372, 2001.

[50] G. Testa, A. Monaco, E. Esposito, E. Sarnelli, D. J. Kang, S. H. Mennema, E. J. Tarte, and M. G. Blamire, "Midgap state-based π-junctions for digital applications," *Applied Physics Letters*, vol. 85, no. 7, pp. 1202–1204, 2004.

[51] V. A. Oboznov, V. V. Bol'ginov, A. K. Feofanov, V. V. Ryazanov, and A. I. Buzdin, "Thickness dependence of the Josephson ground states of superconductor-ferromagnet-superconductor junctions," *Physical Review Letters*, vol. 96, no. 19, p. 197003, 2006.

[52] J. W. A. Robinson, S. Piano, G. Burnell, C. Bell, and M. G. Blamire, "Transport and magnetic properties of strong ferromagnetic pi-junctions," *Applied Superconductivity, IEEE Transactions on*, vol. 17, no. 2, pp. 641–644, 2007.

[53] M. Weides, M. Kemmler, E. Goldobin, D. Koelle, R. Kleiner, H. Kohlstedt, and A. Buzdin, "High quality ferromagnetic 0 and π josephson tunnel junctions," *Applied Physics Letters*, vol. 89, no. 12, pp. 122511–122511, 2006.

[54] T. Golod, H. Frederiksen, and V. M. Krasnov, "Nb-PtNi-Nb Josephson junctions made by 3D FIB nano-sculpturing," in *Journal of Physics: Conference Series*, vol. 150, p. 052062, 2009.

[55] M. Aprili, T. Kontos, W. Guichard, J. Lesueur, and P. Gandit, "Ferromagnetic π-junctions," *Physica C: Superconductivity*, vol. 408, pp. 606–609, 2004.

[56] T. Kontos, M. Aprili, J. Lesueur, F. Genet, B. Stephanidis, and R. Boursier, "Josephson junction through a thin ferromagnetic layer: negative coupling," *Physical Review Retters*, vol. 89, no. 13, p. 137007, 2002.

[57] W. Guichard, M. Aprili, O. Bourgeois, T. Kontos, J. Lesueur, and P. Gandit, "Phase sensitive experiments in ferromagnetic-based Josephson junctions," *Physical Review Letters*, vol. 90, no. 16, p. 167001, 2003.

[58] T. S. Khaire, W. P. Pratt Jr, and N. O. Birge, "Critical current behavior in Josephson junctions with the weak ferromagnet PdNi," *Physical Review B*, vol. 79, no. 9, p. 094523, 2009.

[59] I. A. Campbell, "Strong and weak ferromagnetism in Ni-Fe alloys," *Journal of Physics F: Metal Physics*, vol. 4, no. 8, p. L181, 2001.

[60] C. Bell, R. Loloee, G. Burnell, and M. G. Blamire, "Characteristics of strong ferromagnetic josephson junctions with epitaxial barriers," *Physical Review B*, vol. 71, no. 18, p. 180501, 2005.

[61] Y. Blum, A. Tsukernik, M. Karpovski, and A. Palevski, "Oscillations of the superconducting critical current in Nb-Cu-Ni-Cu-Nb junctions," *Physical Review Letters*, vol. 89, no. 18, p. 187004, 2002.

[62] A. A. Bannykh, J. Pfeiffer, V. S. Stolyarov, I. E. Batov, V. V. Ryazanov, and M. Weides, "Josephson tunnel junctions with a strong ferromagnetic interlayer," *Physical Review B*, vol. 79, no. 5, p. 054501, 2009.

[63] L. B. Ioffe, V. B. Geshkenbein, M. V. Feigel'man, A. L. Fauchère, and G. Blatter, "Environmentally decoupled sds-wave Josephson junctions for quantum computing," *Nature*, vol. 398, no. 6729, pp. 679–681, 1999.

[64] J. Pfeiffer, M. Kemmler, D. Koelle, R. Kleiner, E. Goldobin, M. Weides, A. K. Feofanov, J. Lisenfeld, and A. V. Ustinov, "Static and dynamic properties of 0, π, and 0-π ferromagnetic Josephson tunnel junctions," *Physical Review B*, vol. 77, no. 21, p. 214506, 2008.

[65] G. Wild, C. Probst, A. Marx, and R. Gross, "Josephson coupling and Fiske dynamics in ferromagnetic tunnel junctions," *The European Physical Journal B – Condensed Matter and Complex Systems*, vol. 78, no. 4, pp. 509–523, 2010.

[66] J. Clarke and A. I. Braginski, *The SQUID handbook*. Wiley Online Library, 2006.

[67] G. Blatter, V. B. Geshkenbein, and L. B. Ioffe, "Design aspects of superconducting-phase quantum bits," *Physical Review B*, vol. 63, no. 17, p. 174511, 2001.

[68] S. M. Frolov, M. J. A. Stoutimore, T. A. Crane, D. J. van Harlingen, V. A. Oboznov, V. V. Ryazanov, A. Ruosi, C. Granata, and M. Russo, "Imaging spontaneous currents in superconducting arrays of π-junctions," *Nature Physics*, vol. 4, no. 1, pp. 32–36, 2007.

[69] A. Bauer, J. Bentner, M. Aprili, M. L. Della Rocca, M. Reinwald, W. Wegscheider, and C. Strunk, "Spontaneous supercurrent induced by ferromagnetic π junctions," *Physical Review Letters*, vol. 92, no. 21, p. 217001, 2004.

[70] L. D. Jackel, J. M. Warlaumont, T. D. Clark, J. C. Brown, R. A. Buhrman, and M. T. Levinsen, "Superconducting weak-link current-phase relations," *Applied Physics Letters*, vol. 28, no. 6, pp. 353–355, 1976.

[71] T. A. Fulton and R. C. Dynes, "Current-phase relations in superconducting bridges," *Physical Review Letters*, vol. 25, no. 12, pp. 794–797, 1970.

[72] E. Il'ichev, V. Zakosarenko, R. P. J. IJsselsteijn, V. Schultze, H. G. Meyer, H. E. Hoenig, H. Hilgenkamp, and J. Mannhart, "Nonsinusoidal current-phase relationship of grain boundary josephson junctions in high-T_c superconductors," *Physical Review Letters*, vol. 81, no. 4, pp. 894–897, 1998.

[73] R. De Luca, "Skewness in the current-phase relation of double-barrier Josephson junctions," *Physics Letters A*, vol. 375, no. 24, pp. 2441–2443, 2011.

[74] E. Il'ichev, V. Zakosarenko, R. P. J. IJsselsteijn, H. E. Hoenig, V. Schultze, H. G. Meyer, M. Grajcar, and R. Hlubina, "Anomalous periodicity of the current-phase relationship of grain-boundary josephson junctions in high-T_c superconductors," *Physical Review B*, vol. 60, no. 5, p. 3096, 1999.

[75] D. J. van Harlingen, "Phase-sensitive tests of the symmetry of the pairing state in the high-temperature superconductors – evidence for $d_{x^2-y^2}$ symmetry," *Reviews of Modern Physics*, vol. 67, no. 2, p. 515, 1995.

[76] M. Ebel, C. Busch, U. Merkt, M. Grajcar, T. Plecenik, and E. Il'ichev, "Supercurrent-phase relationship of a Nb/ InAs (2DES)/ Nb Josephson junction in overlapping geometry," *Physical Review B*, vol. 71, no. 5, p. 052506, 2005.

[77] M. Mück, "Progress in rf-SQUIDs," *Applied Superconductivity, IEEE Transactions on*, vol. 3, no. 1, pp. 2003–2010, 1993.

[78] D. S. Linden, T. P. Orlando, and W. G. Lyons, "Modified two-fluid model for superconductor surface impedance calculation," *Applied Superconductivity, IEEE Transactions on*, vol. 4, no. 3, pp. 136–142, 1994.

[79] D. C. Mattis and J. Bardeen, "Theory of the anomalous skin effect in normal and superconducting metals," *Physical Review*, vol. 111, no. 2, p. 412, 1958.

[80] A. Porch, P. Mauskopf, S. Doyle, and C. Dunscombe, "Calculation of the characteristics of coplanar resonators for kinetic inductance detectors," *Applied Superconductivity, IEEE Transactions on*, vol. 15, no. 2, pp. 552–555, 2005.

[81] P. K. Day, H. G. LeDuc, B. A. Mazin, A. Vayonakis, and J. Zmuidzinas, "A broadband superconducting detector suitable for use in large arrays," *Nature*, vol. 425, pp. 817–821, 2003.

[82] B. A. Mazin, P. K. Day, H. G. LeDuc, A. Vayonakis, and J. Zmuidzinas, "Superconducting kinetic inductance photon detectors," in *Society of Photo-Optical Instrumentation Engineers (SPIE) Conference Series*, vol. 4849, pp. 283–293, 2002.

[83] J. Gao, J. Zmuidzinas, B. A. Mazin, H. G. LeDuc, and P. K. Day, "Noise properties of superconducting coplanar waveguide microwave resonators," *Applied Physics Letters*, vol. 90, no. 10, pp. 102507–102507, 2007.

[84] R. Barends, J. J. A. Baselmans, J. N. Hovenier, J. R. Gao, S. J. C. Yates, T. M. Klapwijk, and H. F. C. Hoevers, "Niobium and Tantalum high Q resonators for photon detectors," *Applied Superconductivity, IEEE Transactions on*, vol. 17, no. 2, pp. 263–266, 2007.

[85] R. Barends, H. L. Hortensius, T. Zijlstra, J. J. A. Baselmans, S. J. C. Yates, J. R. Gao, and T. M. Klapwijk, "Noise in NbTiN, Al, and Ta superconducting resonators on silicon and sapphire substrates," *Applied Superconductivity, IEEE Transactions on*, vol. 19, no. 3, pp. 936–939, 2009.

[86] R. Barends, H. L. Hortensius, T. Zijlstra, J. J. A. Baselmans, S. J. C. Yates, J. R. Gao, and T. M. Klapwijk, "Contribution of dielectrics to frequency and noise of NbTiN superconducting resonators," *Applied Physics Letters*, vol. 92, no. 22, pp. 223502–223502, 2008.

[87] J. Gao, M. Daal, A. Vayonakis, S. Kumar, J. Zmuidzinas, B. Sadoulet, B. A. Mazin, P. K. Day, and H. G. Leduc, "Experimental evidence for a surface distribution of two-level systems in superconducting lithographed microwave resonators," *Applied Physics Letters*, vol. 92, no. 15, pp. 152505–152505, 2008.

[88] R. Barends, N. Vercruyssen, A. Endo, P. J. De Visser, T. Zijlstra, T. M. Klapwijk, and J. J. A. Baselmans, "Reduced frequency noise in superconducting resonators," *Applied Physics Letters*, vol. 97, no. 3, pp. 033507–033507, 2010.

[89] J. M. Martinis, K. B. Cooper, R. McDermott, M. Steffen, M. Ansmann, K. D. Osborn, K. Cicak, S. Oh, D. P. Pappas, R. W. Simmonds, *et al.*, "Decoherence in Josephson qubits from dielectric loss," *Physical Review Letters*, vol. 95, no. 21, p. 210503, 2005.

[90] D. P. Pappas, M. R. Vissers, D. S. Wisbey, J. S. Kline, and J. Gao, "Two level system loss in superconducting microwave resonators," *Applied Superconductivity, IEEE Transactions on*, vol. 21, no. 3, pp. 871–874, 2011.

[91] W. Chen, D. A. Bennett, V. Patel, and J. E. Lukens, "Substrate and process dependent losses in superconducting thin film resonators," *Superconductor Science and Technology*, vol. 21, no. 7, p. 075013, 2008.

[92] E. F. C. Driessen, P. Coumou, R. R. Tromp, P. J. de Visser, and T. M. Klapwijk, "Strongly disordered s-wave superconductors probed by microwave electrodynamics," *arXiv preprint arXiv:1205.2463*, 2012.

[93] J. E. Healey, T. Lindström, M. S. Colclough, C. M. Muirhead, and A. Y. Tzalenchuk, "Magnetic field tuning of coplanar waveguide resonators," *Applied Physics Letters*, vol. 93, no. 4, p. 043513, 2008.

[94] D. E. Oates and G. F. Dionne, "Magnetically tunable superconducting resonators and filters," *Applied Superconductivity, IEEE Transactions on*, vol. 9, no. 2, pp. 4170–4175, 1999.

[95] L. Frunzio, A. Wallraff, D. Schuster, J. Majer, and R. Schoelkopf, "Fabrication and characterization of superconducting circuit QED devices for quantum computation," *Applied Superconductivity, IEEE Transactions on*, vol. 15, no. 2, pp. 860–863, 2005.

[96] Y. Kubo, F. R. Ong, P. Bertet, D. Vion, V. Jacques, D. Zheng, A. Dréau, J. F. Roch, A. Auffèves, F. Jelezko, *et al.*, "Strong coupling of a spin ensemble to a superconducting resonator," *Physical Review Letters*, vol. 105, no. 14, p. 140502, 2010.

[97] A. Palacios-Laloy, F. Nguyen, F. Mallet, P. Bertet, D. Vion, and D. Esteve, "Tunable resonators for quantum circuits," *Journal of Low Temperature Physics*, vol. 151, no. 3, pp. 1034–1042, 2008.

[98] A. Wallraff, D. I. Schuster, A. Blais, L. Frunzio, R. S. Huang, J. Majer, S. Kumar, S. M. Girvin, and R. J. Schoelkopf, "Strong coupling of a single photon to a superconducting qubit using circuit quantum electrodynamics," *Nature*, vol. 431, no. 7005, pp. 162–167, 2004.

[99] R. Barends, N. Vercruyssen, A. Endo, P. J. De Visser, T. Zijlstra, T. M. Klapwijk, P. Diener, S. J. C. Yates, and J. J. A. Baselmans, "Minimal resonator loss for circuit quantum electrodynamics," *Applied Physics Letters*, vol. 97, no. 2, pp. 023508–023508, 2010.

[100] T. Lindström, C. H. Webster, J. E. Healey, M. S. Colclough, C. M. Muirhead, and A. Y. Tzalenchuk, "Circuit QED with a flux qubit strongly coupled to a coplanar transmission line resonator," *Superconductor Science and Technology*, vol. 20, no. 8, p. 814, 2007.

[101] R. J. Schoelkopf, S. M. Girvin, *et al.*, "Wiring up quantum systems," *Nature*, vol. 451, no. 7179, p. 664, 2008.

[102] I. Chiorescu, P. Bertet, K. Semba, Y. Nakamura, C. Harmans, and J. E. Mooij, "Coherent dynamics of a flux qubit coupled to a harmonic oscillator," *Nature*, vol. 431, no. 7005, pp. 159–162, 2004.

[103] A. Blais, R. S. Huang, A. Wallraff, S. M. Girvin, and R. J. Schoelkopf, "Cavity quantum electrodynamics for superconducting electrical circuits: An architecture for quantum computation," *Physical Review A*, vol. 69, no. 6, p. 062320, 2004.

[104] D. I. Schuster, A. Wallraff, A. Blais, L. Frunzio, R. S. Huang, J. Majer, S. M. Girvin, and R. J. Schoelkopf, "ac stark shift and dephasing of a superconducting qubit strongly coupled to a cavity field," *Physical Review Letters*, vol. 94, no. 12, p. 123602, 2005.

[105] J. Majer, J. M. Chow, J. M. Gambetta, J. Koch, B. R. Johnson, J. A. Schreier, L. Frunzio, D. I. Schuster, A. A. Houck, A. Wallraff, *et al.*, "Coupling superconducting qubits via a cavity bus," *Nature*, vol. 449, no. 7161, pp. 443–447, 2007.

[106] M. A. Sillanpää, J. I. Park, and R. W. Simmonds, "Coherent quantum state storage and transfer between two phase qubits via a resonant cavity," *Nature*, vol. 449, no. 7161, pp. 438–442, 2007.

[107] P. Rabl, D. DeMille, J. M. Doyle, M. D. Lukin, R. J. Schoelkopf, and P. Zoller, "Hybrid quantum processors: molecular ensembles as quantum memory for solid state circuits," *Physical Review Letters*, vol. 97, no. 3, p. 33003, 2006.

[108] D. Petrosyan, G. Bensky, G. Kurizki, I. Mazets, J. Majer, and J. Schmiedmayer, "Reversible state transfer between superconducting qubits and atomic ensembles," *Physical Review A*, vol. 79, no. 4, p. 040304, 2009.

[109] J. H. Wesenberg, A. Ardavan, G. A. D. Briggs, J. J. L. Morton, R. J. Schoelkopf, D. I. Schuster, and K. Mølmer, "Quantum computing with an electron spin ensemble," *Physical Review Letters*, vol. 103, no. 7, p. 70502, 2009.

[110] D. I. Schuster, A. P. Sears, E. Ginossar, L. DiCarlo, L. Frunzio, J. J. L. Morton, H. Wu, G. A. D. Briggs, B. B. Buckley, D. D. Awschalom, *et al.*, "High-cooperativity coupling of electron-spin ensembles to superconducting cavities," *Physical Review Letters*, vol. 105, no. 14, p. 140501, 2010.

[111] C. A. Regal, J. D. Teufel, and K. W. Lehnert, "Measuring nanomechanical motion with a microwave cavity interferometer," *Nature Physics*, vol. 4, no. 7, pp. 555–560, 2008.

[112] J. D. Teufel, T. Donner, M. A. Castellanos-Beltran, J. W. Harlow, and K. W. Lehnert, "Nanomechanical motion measured with an imprecision below that at the standard quantum limit," *Nature nanotechnology*, vol. 4, no. 12, pp. 820–823, 2009.

[113] M. J. Lancaster, *Passive Microwave Device Applications of High-Temperature Superconductors*. Cambridge University Press, 2006.

[114] R. Simons, *Coplanar Waveguide Circuits, Components, and Systems*. Wiley Series in Microwave and Optical Engineering, Wiley, 2004.

[115] G. P. Srivastava and V. L. Gupta, *Microwave devices and circuit design*. PHI Learning Pvt. Ltd., 2006.

[116] M. Göppl, A. Fragner, M. Baur, R. Bianchetti, S. Filipp, J. M. Fink, P. J. Leek, G. Puebla, L. Steffen, and A. Wallraff, "Coplanar waveguide resonators for circuit quantum electrodynamics," *Journal of Applied Physics*, vol. 104, no. 11, pp. 113904–113904, 2008.

[117] J. E. Healey, *Experiments to develop High Q and tunable superconducting coplanar resonators applicable for quantum bit technology*. PhD thesis, University of Birmingham, 2010.

[118] T. Lindström, J. E. Healey, M. S. Colclough, C. M. Muirhead, and A. Y. Tzalenchuk, "Properties of superconducting planar resonators at millikelvin temperatures," *Physical Review B*, vol. 80, no. 13, p. 132501, 2009.

[119] P. Macha, S. H. W. van der Ploeg, G. Oelsner, E. Ilichev, H. G. Meyer, S. Wunsch, and M. Siegel, "Losses in coplanar waveguide resonators at millikelvin temperatures," *Applied Physics Letters*, vol. 96, no. 6, pp. 062503–062503, 2010.

[120] J. Gao, J. Zmuidzinas, B. A. Mazin, P. K. Day, and H. G. Leduc, "Experimental study of the kinetic inductance fraction of superconducting coplanar waveguide," *Nuclear Instruments and Methods in Physics Research Section A: Accelerators, Spectrometers, Detectors and Associated Equipment*, vol. 559, no. 2, pp. 585–587, 2006.

[121] J. Bardeen, "Critical fields and currents in superconductors," *Reviews of Modern Physics (US)*, vol. 34, 1962.

[122] A. B. Pippard and A. B. Pippard, "Field variation of the superconducting penetration depth," *Proceedings of the Royal Society of London. Series A. Mathematical and Physical Sciences*, vol. 203, no. 1073, pp. 210–223, 1950.

[123] J. Bardeen, "Field variation of superconducting penetration depth," *Physical Review*, vol. 81, no. 6, p. 1070, 1951.

[124] T. Lindström, J. Healey, M. Colclough, C. Webster, C. Muirhead, and A. Tzalenchuk, "Properties of high-quality coplanar waveguide resonators for QIP and detector applications," vol. 150, no. 5, p. 052140, 2009.

[125] D. Bothner, T. Gaber, M. Kemmler, D. Koelle, R. Kleiner, S. Wünsch, and M. Siegel, "Magnetic hysteresis effects in superconducting coplanar microwave resonators," *Physical Review B*, vol. 86, no. 1, p. 014517, 2012.

[126] C. Song, M. P. DeFeo, K. Yu, and B. L. T. Plourde, "Reducing microwave loss in superconducting resonators due to trapped vortices," *Applied Physics Letters*, vol. 95, no. 23, pp. 232501–232501, 2009.

[127] X. S. Rao, C. K. Ong, and Y. P. Feng, "Q-factor measurement of nonlinear superconducting resonators," *Electronics Letters*, vol. 36, no. 3, pp. 271–273, 2000.

[128] J. H. Oates, R. T. Shin, D. E. Oates, M. J. Tsuk, and P. P. Nguyen, "A nonlinear transmission line model for superconducting stripline resonators," *Applied Superconductivity, IEEE Transactions on*, vol. 3, no. 1, pp. 17–22, 1993.

[129] Y. Zhang, M. Mück, A. I. Braginski, and H. Topfer, "High-sensitivity microwave rf SQUID operating at 77 k," *Superconductor Science and Technology*, vol. 7, no. 5, p. 269, 1994.

[130] C. Bell, G. Burnell, D. J. Kang, R. H. Hadfield, M. J. Kappers, and M. G. Blamire, "Fabrication of nanoscale heterostructure devices with a focused ion beam microscope," *Nanotechnology*, vol. 14, no. 6, p. 630, 2003.

[131] V. I. Zdravkov, J. Kehrle, G. Obermeier, A. Ullrich, S. Gsell, D. Lenk, C. Müller, R. Morari, A. S. Sidorenko, V. V. Ryazanov, *et al.*, "Interference effects of the superconducting pairing wavefunction due to the Fulde–Ferrell–Larkin–Ovchinnikov like state in ferromagnet/superconductor bilayers," *Superconductor Science and Technology*, vol. 24, no. 9, p. 095004, 2011.

[132] G. Hammer, S. Wuensch, M. Roesch, K. Ilin, E. Crocoll, and M. Siegel, "Superconducting coplanar waveguide resonators for detector applications," *Superconductor Science and Technology*, vol. 20, no. 11, p. S408, 2007.

[133] Š. Pick, I. Turek, and H. Dreyssé, "On magnetically dead layers at Nb–Co interface," *Solid State Communications*, vol. 124, no. 1, pp. 21–23, 2002.

[134] K. Hayashi, M. Sawada, H. Yamagami, A. Kimura, and A. Kakizaki, "Magnetic dead layers in Fe films induced by a lattice mismatch at an interface," *Physica B: Condensed Matter*, vol. 351, no. 3, pp. 324–327, 2004.

[135] Q. Leng, H. Han, M. Mao, C. Hiner, and F. Ryan, "Magnetic dead layers in NiFe/Ta and NiFe/Si/diamond-like carbon films," *Journal of Applied Physics*, vol. 87, no. 9, pp. 6621–6623, 2000.

[136] L. N. Liebermann, D. R. Fredkin, and H. B. Shore, "Two-dimensional 'ferromagnetism' in iron," *Physical Review Letters*, vol. 22, no. 11, pp. 539–541, 1969.

[137] L. Liebermann, J. Clinton, D. M. Edwards, and J. Mathon, "'Dead' layers in ferromagnetic transition metals," *Physical Review Letters*, vol. 25, no. 4, pp. 232–235, 1970.

[138] R. Salzer, D. Spemann, P. Esquinazi, R. Höhne, A. Setzer, K. Schindler, H. Schmidt, and T. Butz, "Possible pitfalls in search of magnetic order in thin films deposited on single crystalline sapphire substrates," *Journal of Magnetism and Magnetic Materials*, vol. 317, no. 1, pp. 53–60, 2007.

[139] D. W. Abraham, M. M. Frank, and S. Guha, "Absence of magnetism in hafnium oxide films," *Applied Physics Letters*, vol. 87, no. 25, pp. 252502–252502, 2005.

[140] M. Sawicki, W. Stefanowicz, and A. Ney, "Sensitive SQUID magnetometry for studying nanomagnetism," *Semiconductor Science and Technology*, vol. 26, no. 6, p. 064006, 2011.

[141] D. R. Lide, *CRC Handbook of Chemistry and Physics*. CRC Handbook of Chemistry & Physics, Taylor & Francis Group, 2012.

[142] F. Y. Ogrin, S. L. Lee, A. D. Hillier, A. Mitchell, and T. H. Shen, "Interplay between magnetism and superconductivity in Nb/Co multilayers," *Physical Review B*, vol. 62, no. 9, p. 6021, 2000.

[143] V. Shelukhin, A. Tsukernik, M. Karpovski, Y. Blum, K. B. Efetov, A. F. Volkov, T. Champel, M. Eschrig, T. Löfwander, G. Schoen, *et al.*, "Observation of periodic π-phase shifts in ferromagnet-superconductor multilayers," *Physical Review B*, vol. 73, no. 17, p. 174506, 2006.

[144] R. J. Kinsey, G. Burnell, and M. G. Blamire, "Active supercurrent control in superconductor/ferromagnet heterostructures," *Applied Superconductivity, IEEE Transactions on*, vol. 11, no. 1, pp. 904–907, 2001.

[145] J. Wenner, M. Neeley, R. C. Bialczak, M. Lenander, E. Lucero, A. D. O'Connell, D. Sank, H. Wang, M. Weides, A. N. Cleland, *et al.*, "Wirebond crosstalk and cavity modes in large chip mounts for superconducting qubits," *Superconductor Science and Technology*, vol. 24, no. 6, p. 065001, 2011.

[146] J. Hornibrook, E. Mitchell, and D. Reilly, "Superconducting resonators with parasitic electromagnetic environments," *Bulletin of the American Physical Society*, vol. 57, 2012.

[147] G. Vardulakis, S. Withington, D. J. Goldie, and D. M. Glowacka, "Superconducting kinetic inductance detectors for astrophysics," *Measurement Science and Technology*, vol. 19, no. 1, p. 015509, 2007.

[148] B. Mühlschlegel, "Die thermodynamischen funktionen des supraleiters," *Zeitschrift für Physik A Hadrons and Nuclei*, vol. 155, no. 3, pp. 313–327, 1959.

[149] J. Gao, *The physics of superconducting microwave resonators*. PhD thesis, California Institute of Technology, 2008.

[150] J. M. Sage, V. Bolkhovsky, W. D. Oliver, B. Turek, and P. B. Welander, "Study of loss in superconducting coplanar waveguide resonators," *Journal of Applied Physics*, vol. 109, no. 6, pp. 063915–063915, 2011.

[151] V. Braginsky and V. Panov, "Superconducting resonators on sapphire," *IEEE Transactions on Magnetics*, vol. 15, no. 1, pp. 30–32, 1979.

[152] A. D. O'Connell, M. Ansmann, R. C. Bialczak, M. Hofheinz, N. Katz, E. Lucero, C. McKenney, M. Neeley, H. Wang, E. M. Weig, *et al.*, "Microwave dielectric loss at single photon energies and millikelvin temperatures," *Applied Physics Letters*, vol. 92, no. 11, pp. 112903–112903, 2008.

[153] S. M. Wasim and N. H. Zebouni, "Thermal conductivity of superconducting niobium," *Physical Review*, vol. 187, no. 2, p. 539, 1969.

[154] G. Benz, T. A. Scherer, M. Neuhaus, and W. Jutzi, "Quality factor and intermodulation product of superconducting coplanar wave guides with slots in a DC magnetic field," *Applied Superconductivity, IEEE Transactions on*, vol. 9, no. 2, pp. 3046–3049, 1999.

[155] K. Inomata, T. Yamamoto, M. Watanabe, K. Matsuba, and J. S. Tsai, "Film-thickness dependence of 10 GHz Nb coplanar-waveguide resonators," *Journal of Vacuum Science & Technology B: Microelectronics and Nanometer Structures*, vol. 27, no. 5, pp. 2286–2291, 2009.

[156] A. I. Gubin, K. S. Il'in, S. A. Vitusevich, M. Siegel, and N. Klein, "Dependence of magnetic penetration depth on the thickness of superconducting Nb thin films," *Physical Review B*, vol. 72, no. 6, p. 064503, 2005.

[157] G. Benz, T. A. Scherer, M. Neuhaus, and W. Jutzi, "Quality factors of coplanar niobium resonators on $LaAlO_3$ substrates with different cross-sectional geometries," *Cryogenics*, vol. 38, no. 6, pp. 697–700, 1998.

[158] A. Müller, S. E. C. Dale, M. A. Engbarth, S. J. Bending, L. M. Peter, A. Knittel, and H. Fangohr, "Field-tuneable diamagnetism in ferromagnetic–superconducting core–shell structures," *Advanced Functional Materials*, vol. 21, no. 10, pp. 1874–1880, 2011.